Cover Page

![Universiteit Leiden logo]
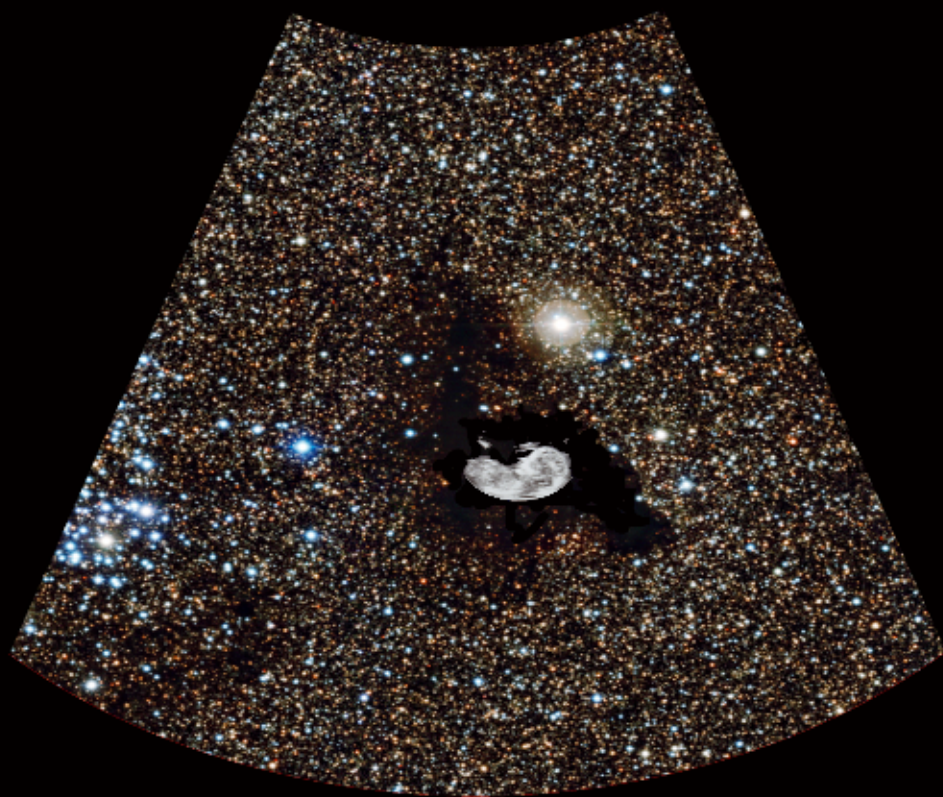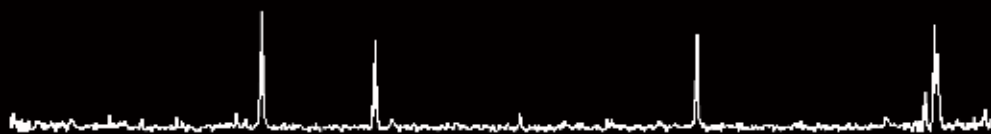
Universiteit Leiden

Author: Yildiz, Umut
Title: Warm and cold gas in low-mass protostars : Herschel Space Observatory and ground-based surveys
Issue Date: 2013-05-01

Warm and Cold Gas in Low-Mass Protostars

Herschel Space Observatory and *G*round-Based Surveys

Umut Yıldız

Warm and Cold Gas in Low-Mass Protostars

Umut Yıldız

WARM AND COLD GAS IN LOW-MASS PROTOSTARS

HERSCHEL SPACE OBSERVATORY AND GROUND-BASED SURVEYS

Universiteit Leiden

Warm and Cold Gas in Low-Mass Protostars

Herschel Space Observatory and Ground-Based Surveys

PROEFSCHRIFT

ter verkrijging van
de graad van Doctor aan de Universiteit Leiden,
op gezag van de Rector Magnificus prof. mr. C. J. J. M. Stolker,
volgens besluit van het College voor Promoties
te verdedigen op woensdag 1 mei 2013
klokke 16.15 uur

door

Umut Yıldız
geboren te Istanbul, Turkije
op 28 februari 1980

Promotiecommisie

Promotor:	Prof. dr. E. F. van Dishoeck	
Co-promotor	Dr. L. E. Kristensen	(Harvard-Smithsonian Center for Astrophysics)
Overige leden:	Prof. dr. P. F. Goldsmith	(NASA Jet Propulsion Laboratory; California Institute of Technology)
	Prof. dr. P. Caselli	(University of Leeds)
	Prof. dr. A. G. G. M. Tielens	
	Prof. dr. H. Röttgering	
	Dr. M. R. Hogerheijde	
	Dr. F. P. Helmich	(SRON Netherlands Institute for Space Research; Kapteyn Institute, University of Groningen)

for Fatime, Duru, Annem & Babam

Front Cover: Image of the dark cloud Barnard 86 in the neighbourhood of the bright star cluster NGC 6520. The image is taken by MPG/ESO 2.2-metre telescope at ESO's La Silla Observatory in Chile. The image is modified and a forming baby as displayed in a womb with an echo is put inside. The analogy resembles that stars are born in those dark molecular clouds and can be observed at long wavelengths. The displayed spectrum is the HIFI spectrum centered at O_2 487 GHz toward NGC1333 IRAS 4A from Chapter 6.

Back Cover: Contour map of bipolar outflows driven by two protostars, NGC1333 IRAS 4A and IRAS 4B from Chapter 4. Solid contours represent the red outflow lobe whereas dashed contours represent the blue outflow lobe.

Wordle: Each chapter begins with a *Wordle* image showing 150 words proportional to the frequency of their usage in each of the chapters, which indirectly acts as summary of that chapter (`www.wordle.net`).

"Staying steady is going back."
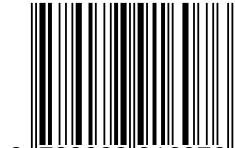– Anonymous

Contents

Contents

1

Introduction

1.1 Low-mass star formation

The query of where we come from or how our Solar System formed are ancient questions. During human history, many different types of people including philosophers, religious leaders, and scientists have tried to come up with different suggestions to address these questions. Today, even with our advanced engineering tools and our improved scientific methods, we are still trying to find at least some clues. Especially after the invention of radio astronomy in the 1930s by Karl Jansky and the detection of the first molecule –the methylidyne radical (CH)– in the interstellar medium in 1937 by optical absorption lines (Swings & Rosenfeld 1937, McKellar 1940), a lot of progress has been made during the course of time. Many new molecules have been discovered in a variety of astronomical sources, which span a large range of conditions.

The Sun is a G2 V-type main-sequence star comprising about 99.86% of the total mass of the Solar System. It largely consists of simple elements, like hydrogen and helium. Molecules, including some complex ones, are found throughout our Solar System. Most importantly, planets like our Earth and their atmospheres contain species like water that are key to the origin of life. To better understand their formation, low-mass stars similar to our Sun need to be studied at different evolutionary stages. This thesis addresses the *formation of the earliest stages of low-mass protostars*.

1.1.1 Molecular clouds

Two forces in the Universe play an important role in the birth and death of the celestial sources. These are: first, *gravity*, which tends to compress material and second, *pressure*, which oppositely pushes the interstellar material apart. At the very outset of star formation, in order for a cloud to collapse, the force of *gravity* must overcome the *thermal pressure* so that the clouds must be cold. The only regions in the *interstellar medium* that are dense enough for the force of gravity to overcome the relatively weak thermal pressure from low gas temperature and thus to allow star formation are the *dark molecular clouds*.

The simplest of those clouds are the *Bok globules*. Their temperatures are around 10 K, the densities range from 10^4 to 10^5 cm^{-3}, and their masses range from 10 to 100 M$_\odot$. While Bok globules have typical sizes of a few parsec, dark clouds or cloud complexes can be significantly larger with sizes of tens of parsecs. These places are the ideal sites for low-mass star formation. Due to the high extinction ($A_V > 100$ mag), the earliest protostellar phase can only be observed at longer wavelengths, e.g., far-infrared, submillimeter, and millimeter. Fig. 1.1 shows the *Herschel* Space Observatory image of the Eagle Nebula (also known as the Pillars of Creation) taken with the PACS/SPIRE instruments. The three color composite image shows the areas of active star birth, where the tips of the pillars also contain protostars. In our Milky Way galaxy, there are many similar molecular clouds that harbor star-forming regions, which form new stars with planets surrounding them.

Observations show that stars form in these collapsing dense and dark molecular clouds either in *isolated* or in *clustered* environments (reviews by Shu et al. 1987, Bergin & Tafalla 2007, Kennicutt & Evans 2012). The outcome of the star formation process may depend on this initial environment. For example, clusters of massive stars together with thousands of low mass stars are formed in giant molecular clouds (GMCs) like those in Orion. However, isolated low-mass stars form in smaller condensations, e.g., B68 in the Pipe Nebula.

Figure 1.1 – *Herschel*-PACS/SPIRE image of the Eagle Nebula. This is a three colour composite with colours assigned as (blue=70μm, green=160μm, red=250μm). The 70 μm and 160 μm data are from PACS and the 250 μm from SPIRE. Credits: ESA/PACS & SPIRE Consortium, T. Hill, F. Motte, CEA/IRFU - CNRS/INSU - Uni. Paris Diderot, HOBYS Key Program Consortium.

1.1.2   Stages of young stellar objects

Low-mass YSOs have been classified by various methods, e.g., based on the infrared slope, $\alpha_{IR} = d\log(\lambda F_\lambda)/d\log\lambda$, of the spectral energy distribution at wavelengths from 2 μm to 20 μm (Lada & Wilking 1984),

$$\alpha_{IR} : \xrightarrow{\text{Stage I}} 0.3 \xrightarrow{\text{Flat}} -0.3 \xrightarrow{\text{Stage II}} -1.6 \xrightarrow{\text{Stage III}} \tag{1.1}$$

or based on their bolometric temperature T_{bol}, (Myers & Ladd 1993, Chen et al. 1995),

$$T_{bol} : \xrightarrow{\text{Class 0}} 70 \text{ K} \xrightarrow{\text{Class I}} 650 \text{ K} \xrightarrow{\text{Class II}} 2800 \text{ K} \xrightarrow{\text{Class III}} \tag{1.2}$$

This sequence reflects that with the evolution of the protostellar phase from molecular clouds to protoplanetary disks, the peak emission shifts from longer to shorter wavelengths.

According to Lada (1987) and André et al. (2000), YSOs are characterized by four different evolutionary classes (Class 0–III) during their formation (Fig. 1.2; Evans et al. 2009, Dunham et al. 2013).

Class 0 — is the earliest and deeply-embedded stage of YSOs, where the *protostar* is surrounded by a collapsing *envelope* and a *circumstellar disk*, from which material is accreted onto the protostar. The mass of the envelope is much larger than that of the central protostar ($M_{env} >> M_*$) and the lifetime of this stage is typically 10^4 - 10^5 years. Very strong *jets* and *winds* erupt from both poles of the protostars and inner disks, which push and entrain the material in the envelope outward
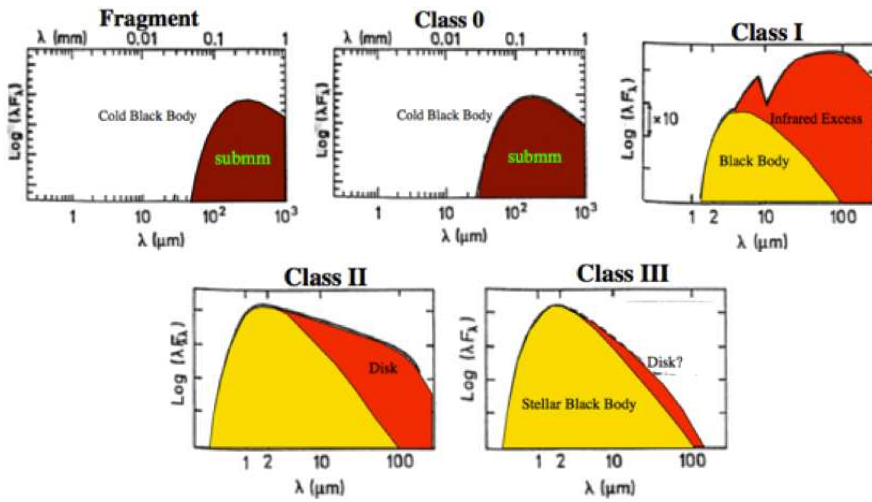
Figure 1.2 – Low mass star formation sequence according to their evolving SEDs. Adapted from André et al. (2000).

Figure 1.3 – Artist impression of the birth of a star. With submillimeter instruments, it is possible to penetrate the surrounding dust of a forming star. While matter accretes on the protostar, bipolar jets and molecular outflows erupt on both sides. Image credit: NASA/JPL-Caltech.

in the form of a collimated *outflow*. These outflows are important for removing angular momentum and mass and helping the accretion process to be more efficient (Fig. 1.3; e.g., Tafalla et al. 2000, Arce et al. 2007). The interaction of the outflows with the surrounding envelope also heats up the material and leads to the formation of many molecules. The spectral energy distribution (SED) of this phase peaks at far-infrared and submillimeter wavelengths.

Class I — is the next stage in the evolution, where the envelope is being dispersed by the outflows while the circumstellar disk grows. This phase lasts a few $\times 10^5$ years and the mass of the envelope is now less than the central protostar ($M_* > M_{\mathrm{env}}$). The bipolar outflows are still seen in this stage, however their strength is much lower than in the Class 0 phase. Due to the lower extinction, the SED now consists of two components; blackbody emission from the protostar and infrared excess from the surrounding disk.

Class II — is the phase where the envelope is almost completely dissipated into the protostellar disk ($M_{\mathrm{disk}} > M_{\mathrm{env}}$). The lifetime of this phase is a few $\times 10^6$ years and the black body radiation is shifted to near-infrared wavelengths, while the disk emission is still seen in the mid-to far-infrared wavelengths. The sources which are observed in this phase are also called *Classical T Tauri stars* (CTTSs), with possible *planet* formation.

Class III — is the phase where the accretion stops and the jets and outflows are entirely gone (Walter 1987). The sources are called *Weak-line T-Tauri stars* (WTTS) with a debris disk or planetary system that may have formed.

Toward the end of the Class III stage, the turning point of becoming a *star* is reached by burning hydrogen in its core through fusion reactions, which then leads to the *hydrostatic equilibrium* of stars. The new-born star appears in the Hertzsprung-Russell Diagram in its so-called *zero-age main-sequence* (ZAMS) period (Hayashi et al. 1962). After this period, the star joins the main sequence stellar evolution phase, which is very stable due to constant processing of Hydrogen into other elements.

Star-formation is a complex process with the components in each of those stages interacting. A good understanding of them is needed both individually and globally. In this thesis, I focus on the early Class 0 and Class I phases by using observations from ground- and space-based submillimeter telescopes, especially the new *Herschel* Space Observatory. Understanding the structure of molecular outflows, which are an integral part of these phases, has made significant progress over the last few decades since the first discovery in a low-mass protostar "L1551-IRS5" by Snell et al. (1980). Although the formation of jets, winds and outflows is not fully understood, it is thought that they result from the interaction of the magnetic field of the central object with the surrounding circumstellar disk. The amount of gas in the outflows in different temperatures can be traced using CO rotational transition observations (see Sect. 1.2). In this thesis, we quantify the cold ($T < 100$ K) and warm ($T > 100$ K) gas via rotational transitions of CO. The accretion also leads to heating of the surrounding envelope with increasing luminosity, leading to evaporation of the molecules that were frozen out during the earliest cold phases (e.g., van Dishoeck & Blake 1998, Ceccarelli et al. 2007, Caselli & Ceccarelli 2012). These detailed studies of the physical and chemical structure of low–mass protostars are important for a complete understanding of the evolution of young stellar objects (YSOs).

1.2 Molecules

The interstellar medium (ISM) consists of ~99% of gas and 1% dust by mass. Approximately 90% of this gas is in the form of H or H_2, 8% in He and ~1-2% is heavier elements by number. More than 170 different molecular species have been detected in various interstellar and

circumstellar media from nearby objects to distant galaxies. About 50 of those molecules contain 6 or more atoms and are called complex molecules (Herbst & van Dishoeck 2009). Deep inside molecular clouds, most of the carbon is in the form of CO and the hydrogen is in the form of H_2.

The other main constituent of molecular clouds is dust grains, and they typically make up 1% of the cloud by mass. Dust grains are key players when it comes to the chemistry in the sense that their surfaces can act as "*catalysts*" of chemical reactions (Herbst & van Dishoeck 2009). However, in order for the surfaces to aid chemical complexity, molecules need to meet and attach themselves to the surface of a grain, a process which is known as *freeze out*.

In dense clouds, the probability of a molecule to meet a grain surface and stick to it is so high that essentially all molecules except H_2 are frozen out. Typically this requires densities greater than $\sim 10^5$ cm^{-3}; if the density is lower, the time it takes for a molecule to randomly meet a dust grain is longer than the lifetime of molecular clouds and so no or little freeze out takes place (Jørgensen et al. 2005c). When the molecules are stuck to the surface, they can meet and react with other molecules. In particular, this is how water is expected to form, from successive reactions of O, O_2, O_3 with H and H_2 (Tielens & Hagen 1982, Ioppolo et al. 2008, Cuppen et al. 2010).

When dust grains heat up, molecules eventually evaporate depending on the binding energy of the molecule to the surface. H_2 has a very low binding energy and evaporates already at ~ 4 K, CO and O_2 are slightly more tightly bound and laboratory experiments show that they evaporate at ~ 20 K (Acharyya et al. 2007). H_2O and CH_3OH have higher binding energies and only thermally evaporate once the grains reach temperaures of 100 K or more. These values are all based on high-quality laboratory experiments carried out under controlled conditions.

The density and temperature constraints imply that the abundances of different molecules vary through the envelopes surrounding the forming protostars (Jørgensen et al. 2002). In this thesis, Chapters 2, 3, 4, and 6 discuss the variation of CO abundances in the protostellar envelopes and demonstrate the necessity of a freeze-out zone below the evaporation temperature of CO.

1.2.1 Molecular transitions

By observing molecules, we obtain information on the physical and chemical conditions of their past, today, and future. These molecules are observed through their discrete energy levels, where the transition between two levels emit or absorb radiation which corresponds to a frequency/wavelength that telescopes can detect. This radiation is like a specific blueprint of each species.

Three types of transitions can be observed: *Electronic Transitions* are the transitions among the electronic quantum states in the atoms or molecules, leading to emission of radiation in the visible and UV part of the spectrum. *Vibrational Transitions* are due to the vibrational states within every electronic state and occur due to the oscillatory motion of the nuclei. Regions with temperatures around ~ 1000 K emit at infrared wavelengths. *Rotational Transitions* are due to the end-over-end tumbling of the molecule and the torque exerted on the molecular dipole. Regions with temperatures <300 K emit mostly at millimeter and submillimeter wavelengths.

In this thesis, rotational transitions of the CO and O_2 molecules are used to characterize the physics and chemistry of the protostellar environments. Rotational transitions are possible when the atoms in a molecule have different electronegativity, so that it has a permanent dipole moment. CO is an asymmetric molecule with a small permanent dipole moment (0.112 Debye), which radiates in rotational transitions effectively. Homonuclear symmetric molecules, such as H_2, do not have a permanent electric dipole moment and only forbidden quadrupole transitions are possible. The pure rotational and rovibrational transitions of H_2 can be observed in regions with high kinetic temperatures of a few hundred to a few thousand Kelvins, e.g., shocked gas. O_2 is also a homonu-
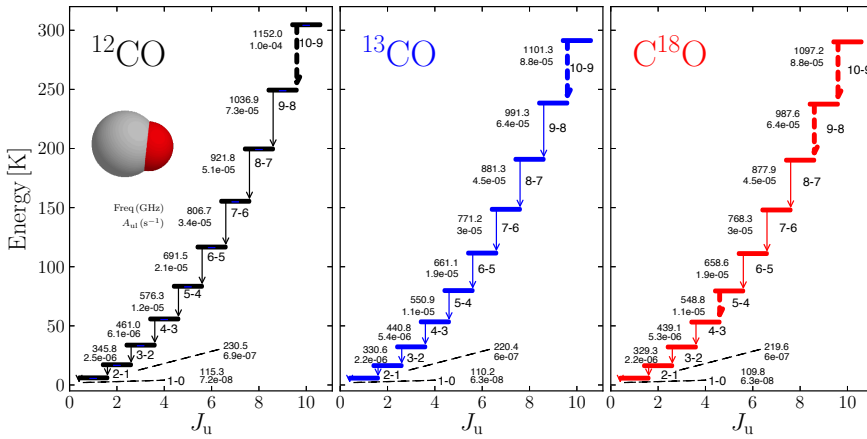
Figure 1.4 – *Right:* ^{12}CO (*left, black*), ^{13}CO (*middle, blue*) and C^{18}O (*right, red*) energy diagrams. Dashed transitions are targeted with *Herschel*-HIFI. The frequencies (in GHz) and Einstein A coefficients (in s^{-1}) are also given next to the transitions. Dashed transitions refer to those observed with *Herschel*-HIFI. In this thesis, we use the term "low-J" lines to be $J_{up} \leq 3$ and "high-J" lines with $J_{up} \geq 6$.
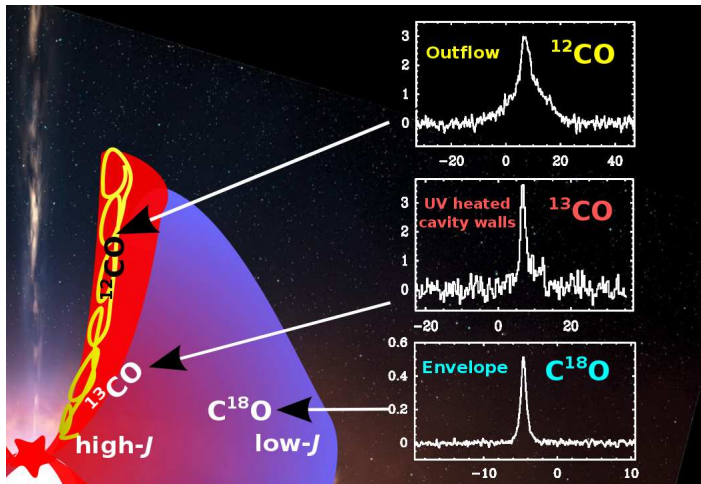
Figure 1.5 – Sketch showing the importance of high angular and spectral resolution to quantify the location and origin of warm and cold gas traced by CO. Background image is adapted from a NASA/JPL-Caltech image.

clear molecule like H$_2$, but it possesses a magnetic dipole moment, which allows it to radiate weakly at submillimeter wavelengths.

1.2.2   Carbon monoxide - CO

Spectral lines in the millimeter and submillimeter range are tracers of the dense molecular gas, which reveal the kinematic characteristics of collapse in the envelope and the high velocity gas in protostellar outflows. The CO molecule is the second most abundant molecule under most conditions in the interstellar medium after H_2, with a very simple level structure and the different isotopologues (^{13}CO, $C^{18}O$, $C^{17}O$) are detectable at sub-/mm wavelengths. Because of its small dipole moment, CO has the characteristics of being rotationally excited very easily at low densities, and therefore the excitation measurements provide an excellent estimate of the gas kinetic temperature and, by assuming a CO/H_2 abundance, of the molecular gas mass as well. In Fig. 1.4, the energy level diagrams for ^{12}CO, ^{13}CO, and $C^{18}O$ are shown. The rotational levels are more closely spaced than for H_2 because the moment of inertia is greater.

Since its discovery in the Orion molecular cloud (Wilson et al. 1970), CO has served as the primary tracer of molecular gas, both in our own and in external galaxies (e.g., Maloney & Black 1988, Lada 1987, Neininger et al. 1998, Kennicutt & Evans 2012). The most abundant isotope, $^{12}C^{16}O$, is naturally the easiest to detect, but ^{13}CO, $C^{18}O$, and occasionally $C^{17}O$ and $^{13}C^{18}O$, have also proved useful in tracing different environments. Important usage of CO is to characterize the swept-up gas in protostellar outflows where the temperature is relatively low (a few hundred Kelvins). Therefore CO maps have been widely used to identify the physical properties of these outflows. $C^{18}O$ lines are mainly used to probe the quiescent envelope gas, whereas ^{13}CO is found to be good tracer for UV heated gas (Fig. 1.5; Spaans et al. 1995, van Kempen et al. 2009a, Yıldız et al. 2012). In this thesis, Chapters 2–5 discuss the analysis of CO and isotopologue lines observed toward low-mass protostars.

1.2.3   Molecular oxygen - O_2

Oxygen is the third most abundant element in the Universe after hydrogen and helium, but it is still unclear what the main gas-phase reservoir is in dense molecular clouds. It is important to search for O_2 in order to understand the origin of this and other vital molecules for life that are chemically related, such as H_2O. The O_2 in our atmosphere causes strong absorption, therefore interstellar O_2 needs to be observed by space instruments (Goldsmith et al. 2011). In Fig. 1.6, the rotational energy level diagram of O_2 with the corresponding frequencies and Einstein A coefficients to each level are presented (adopted from Goldsmith et al. 2011). Until recently, efforts to detect interstellar molecular oxygen had failed due to its very low abundance. Two earlier space missions (*SWAS* and *Odin*) had dedicated instruments to detect O_2, but provided mostly upper limits. *SWAS* did not obtain a definitive detection of O_2 at 487 GHz toward nearby clouds (Goldsmith et al. 2000), whereas *Odin* observations of O_2 at 119 GHz gave upper limits of $\leq 10^{-7}$ (Pagani et al. 2003), except for a tentative detection toward the ρ Ophiuchi A cloud ($X(O_2) \sim 5 \times 10^{-8}$; Larsson et al. 2007).

In the *Herschel* Oxygen Project (HOP) key program, among the seven transitions shown in the Fig. 1.6, three relatively strong transitions at 487, 774, and 1121 GHz were targeted with *Herschel*-HIFI on various star-forming regions and dark clouds, and detected conclusively toward the Orion molecular cloud (Goldsmith et al. 2011) and ρ Ophiuchi A (Liseau et al. 2012). In this thesis, a deep O_2 observation at 487 GHz toward the deeply embedded protostar NGC 1333 IRAS 4A, also studied in CO, is discussed in Chapter 6.
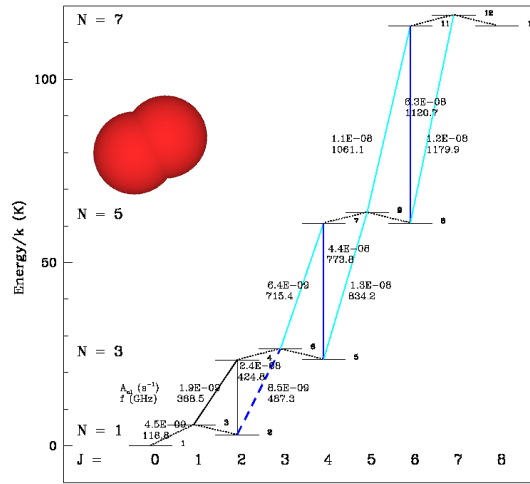
Figure 1.6 – Lower rotational energy level diagram of the O_2 molecule with the corresponding frequencies and Einstein A coefficients to each level (Goldsmith et al. 2011). The 487 GHz transition observed with *Herschel* HIFI toward IRAS 4A is shown with dashed blue line. The 774 GHz and 1121 GHz transitions are observed and detected in Orion.

1.3 Observations

I n this thesis, observations from different ground- and space-based telescopes were used to obtain the relevant data to study the protostellar environment. The space-based observations are centered on the the *Herschel* Space Observatory, whereas for the ground-based observations, Atacama Pathfinder EXperiment (APEX), James Clerk Maxwell Telescope (JCMT), IRAM 30m telescope, and Onsala 20m Radiotelescope are used. Information about the sample and the observing program (WISH) is given in Sect. 1.4.

1.3.1 *Herschel* Space Observatory

The *Herschel* Space Observatory[1] is a cornerstone mission of European Space Agency (ESA) that aims to study the Universe at far-infrared and submillimeter wavelengths (Pilbratt et al. 2010). Its main objectives are: to study the formation of galaxies in the early universe and their subsequent evolution; study the formation of stars and their interaction with the interstellar medium; observe the chemical composition of the atmospheres and surfaces of comets, planets and satellites; and investigate the molecular chemistry of the universe. The telescope has a Cassegrain design 3.5 meter diameter primary mirror, which is the largest single mirror ever built and launched into space for astronomy to date. The mirror is made of silicon carbide (SiC), which is a ceramic material with a good level of thermal conductivity and a small thermal expansion coefficient (Lemke 2008).

---

[1] This section is based on the general information over *Herschel* Space Observatory and its instruments, as presented on ESA, NASA and SRON's public web pages.

Herschel was launched together with the *Planck* Observatory from French Guyana by an Ariane–5 rocket on May 14, 2009. Both are currently located in Lissajous orbits about the second Lagrange point of the Sun-Earth system (L2), which is around 1.5 million kilometers away from the Earth. The L2 point is one of the ideal locations, where the observatory uses the Earth's gravity to put the telescope in a stable orbit, and the Earth and the Moon are distant enough to add negligible heating. Having these sources in approximately the same direction as the Sun allows enhanced observation efficiency and flexibility. Its large single-sided radiation shield blocks the thermal radiation from the Sun and the Earth, and by using the fact that space is intrinsically cold allows passive cooling of the telescope mirror to approximately 80 K. The instruments operate at much lower temperatures, which is achieved by cooling via Helium-3 (^{3}He) to reduce the temperature to close to absolute zero temperatures, e.g., 300 mK to use for the PACS and SPIRE bolometers. The HIFI mixers on the other hand operate between 2–4 K.

The liquid helium tank holds 2400 litres, which weighs 335 kg and the whole probe weighs 3.3 tons. The vaporisation rate is 2 mg/sec, meaning that it is aimed to supply a four-year mission with about 7000 hours of science time per year (see review from Lemke 2008). Three science instruments are located in the cryo-vacuum of the helium container, which have different wavelength coverages (Fig. 1.7):

- HIFI (Heterodyne Instrument for the Far Infrared) is a very high resolution heterodyne spectrometer sensitive to 480–1250 and 1410–1910 GHz (157–625 microns) built by a consortium of institutes under leadership of SRON Netherlands Institute for Space Research (Groningen, The Netherlands; de Graauw et al. 2010). The details of this instrument follow in Section 1.3.2.

- PACS (Photodetector Array Camera and Spectrometer) is an imaging photometer and medium resolution grating spectrometer sensitive to the wavelength range from 60 to 210 μm, built under leadership of the Max Planck Institute for Extraterrestrial Physics (Garching, Germany; Poglitsch et al. 2010). PACS consists of 5×5 spatial-pixels (spaxels) with a field-of-view covering 47″ at the resolution of 9.4″.

- SPIRE (Spectral and Photometric Imaging Receiver) is an imaging photometer and an imaging Fourier transform spectrometer sensitive to the wavelength range from 200–670 μm built under leadership of the University of Wales (Cardiff, UK; Griffin et al. 2010).

These instruments complement each other in terms of their capabilities. In this thesis, primarily HIFI observations are used, therefore the following section continues with detailed information on the HIFI instrument and its data reduction.

1.3.2   Heterodyne Instrument for the Far-Infrared (HIFI)

The Heterodyne Instrument for the Far-Infrared (HIFI[2]) is an ultra high spectral resolution heterodyne spectrometer with frequency ranges covering from 480–1250 GHz and 1400–1900 GHz (Fig. 1.8). Due to the high water content of the Earth's atmosphere, these wavelengths mostly cannot be observed with ground-based telescopes. HIFI's core scientific goals are to study the ISM in the Milky Way and other galaxies; stellar evolution, especially the formation and the late stages; and Solar System. Some of the key molecules that are targeted are H_2O, O_2, CO, OH, and HDO.

---

[2] Technical information about HIFI can be found in the "HIFI Observers Manual" and "HIFI Users Manual" from the ESA website.
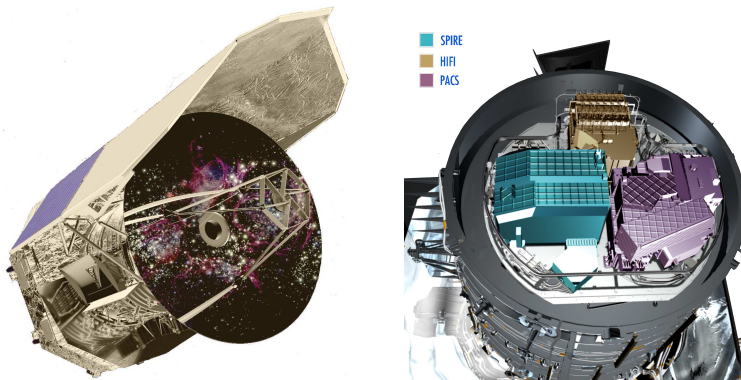
Figure 1.7 – *(Left:) Herschel* Space Observatory and *(right:)* its three on-board instruments, HIFI, PACS, and SPIRE (Image Credits: ESA).
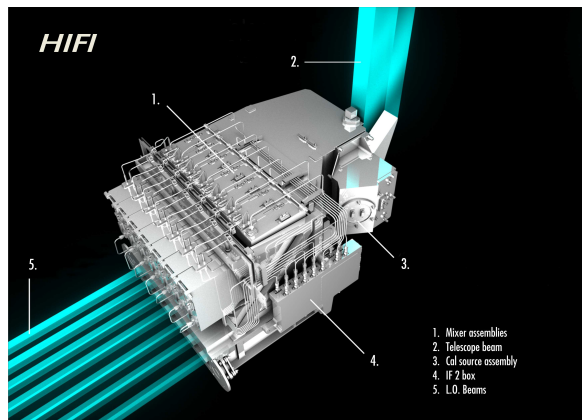
Figure 1.8 – Focal plane unit of the Heterodyne Instrument for the Far-Infrared (HIFI) instrument. Image Credit: ESA

HIFI has seven mixer bands (Bands 1–7) with horizontal (H) and vertical (V) polarizations. Bands 1 to 5 are using heterodyne SIS (Superconductor-Insulator-Superconductor) mixers to operate at 480–1250 GHz. Bands 6 and 7 use HEB (Hot Electron Bolometer) mixers for covering 1400–1900 GHz, which is better suited to detect radiation above 1000 GHz. In Table 1.1, the frequency ranges of the HIFI bands, the type of the mixers used, and the observed transitions that were used in this thesis are tabulated.

An instantaneous frequency coverage of 4 GHz is provided for Bands 1 to 5 and 2.4 GHz in Bands 6 and 7. The data are obtained as dual sideband data (DSB), which means that each channel of the spectrometers is sensitive to two frequencies (separated by 4.8 to 16 GHz) at the same time. This principle is explained in the next subsection. There are four spectrometers on board HIFI;

11

Table 1.1 – Overview of the HIFI bands

HIFI Band	Frequency (Min)[GHz]	Frequency (Max) [GHz]	Mixer	Observed Molecules[a]	HPBW (Min)["]
Band 1a	487.6	553.4	SIS	O_2, $C^{18}O$ 5–4	44
Band 1b	562.6	628.4	SIS	...	38
Band 2a	634.1	717.9	SIS	...	34
Band 2b	722.1	793.9	SIS	...	30
Band 3a	807.1	851.9	SIS, Diplexer	...	27
Band 3b	866.1	952.9	SIS, Diplexer	^{13}CO 8–7	25
Band 4a	957.2	1052.8	SIS, Diplexer	$C^{18}O$ 9–8	22
Band 4b	1054.7	1113.8	SIS, Diplexer	^{13}CO, $C^{18}O$ 10–9	20
Band 5a	1116.2	1235.8	SIS	^{12}CO 10–9	19
Band 5b	1235.2	1271.8	SIS	...	17
Band 6a	1430.2	1557.8	HEB, Diplexer	...	15
Band 6b	1578.2	1697.8	HEB, Diplexer	...	13
Band 7a	1701.2	1793.8	HEB, Diplexer	...	13
Band 7b	1793.2	1901.8	HEB, Diplexer	...	12

Notes: [a] The molecules that are observed and analysed in this thesis.

two Wide-Band Acousto-Optical Spectrometers (WBS) and two High Resolution Autocorrelation Spectrometers (HRS) each with H- and V polarizations. The observations are conducted for each of the spectrometers simultaneously. The WBS covers the full intermediate frequency bandwidth of 2.4 GHz in the highest frequency bands (Bands 6 and 7) and 4 GHz in all other bands at a single resolution (1.1 MHz ~0.2–0.7 km s^{-1}). The HRS have variable resolution from 0.125 to 1.00 MHz with subbands sampling up to half the 4 GHz intermediate frequency range. Subbands have the flexibility of being placed anywhere within the 4 GHz range. The HRS can be split up to allow the sampling of more than one part of the available range (for detailed information, see "*HIFI Users Manual*[3]" and "*HIFI Observers Manual*[4]"). The beam size (HPBW) of HIFI ranges from 42″ at 480 GHz to 12″ at 1900 GHz (Table 1.1). The in-flight performance and the calibration of HIFI are described in Roelfsema et al. (2012).

Heterodyne principle

Submillimeter wavelengths lie in between IR and radio wavelengths. The optical technology is very good in the near-IR side of the spectrum and on the other hand, electronics are quite advanced on the radio side of the spectrum. However, there is no direct method to amplify weak signals at submillimeter wavelengths. The solution to this problem is accomplished with the *heterodyne technique*, by bringing the signal down in frequency to radio wavelengths without losing its information from the original sky signal.

HIFI uses heterodyne technology in order to observe at far-infrared and submillimeter wavelengths at very high spectral resolution (resolving power of $\lambda/\Delta\lambda \sim 10^6$). In Fig. 1.9, a basic diagram of a submillimeter telescope is shown. In principle, the signal from an astronomical source at a frequency ν_{sky} (e.g., 812 GHz) is caught by the highly accurate mirror (dish), and it is mixed with

---

[3] http://www.sron.rug.nl/hifi_icc/hifi-um/hifi-um.html
[4] http://herschel.esac.esa.int/Docs/HIFI/html/hifi_om.html
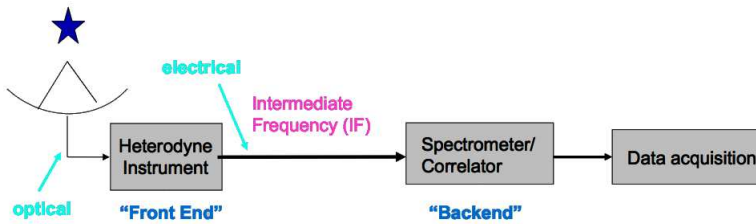
Figure 1.9 – Representative basic diagram of a submillimeter telescope.

a constant signal that is artificially generated by the local oscillator (LO) ν_{LO} (e.g., 807 GHz). The mixing is done in the heterodyne receiver via high technology mixers at superconducting temperatures. The output electrical signals contain the sum and the difference frequencies at $\nu_{LO}+\nu_{sky}$ and $\nu_{LO}-\nu_{sky}$. Although the sum frequency component is filtered away, however, the difference frequency component produces the intermediate frequency ν_{IF} (e.g., 5 GHz), which is then sent to HIFI's WBS and HRS spectrometers for the spectral analysis (de Graauw et al. 2010, Roelfsema et al. 2012).

Observing modes

In HIFI, three *Astronomical Observing Templates* (AOTs) are available in order to perform observations: *Single Pointing:* (AOT I) for observing astronomical sources at one position on the sky; *Mapping:* (AOT II) for observing extended regions; and *Spectral Scanning:* (AOT III) for surveying a single position on the sky over a continuous range of frequencies selected within the same LO band. Each of these AOT's can be used in a variety of different observing modes to provide the best quality data. The HIFI observing modes are:

Dual Beam Switch (DBS): Internal chopper mirror within HIFI is used to move the beam to a reference position up to 3 arcmin away from the target position. It is best used for non-crowded regions.

Position Switch (PSw): The HIFI beam is pointed to clean reference position, which is selected in a nearby region to the target.

Frequency Switch (FSw): The LO frequency is shifted by a small amount (a few tens of MHz), and the lines of interest still remain observable at two LO frequencies.

Load Chop: An internal cold source is used as a reference and the chopping mirror alternately looks at the target on the sky and an internal source of radiation.

In this thesis, we only used data of single pointing observations conducted primarily with "Dual Beam Switch (DBS)" or "Position Switch" observing modes.

HIFI noise characteristics

In this subsection, some tests of the data quality are presented. The aim was to quantify the behavior of the noise with increasing integration time in HIFI via analysing deep single pointing observations of different bands. In particular, the *rms* is expected to decrease with increasing integration time as $\sqrt{1/t}$ so several samples of long integration observations were used to test this. The observations are re-pipelined to Level 2 stage by removing the `doAvg` step in Level 1 tasks,
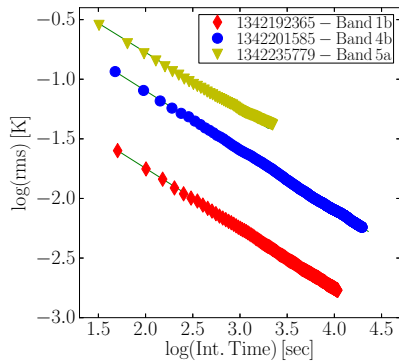
Figure 1.10 – Slopes show the decreasing *rms* with increasing integration time. The green lines behind the observed points show the expected *rms* evolution following $\sqrt{1/t}$ to indicate the expected behavior.

which then process all individual on-target data into Level 2 spectra with proper frequency scale and calibration. Since all individual on-target spectra are consecutive in time, the applied method is as follows: the first observed spectrum is taken and the *rms* is calculated, then the next spectrum is averaged with the first two ($1^{st}+2^{nd}$) and the *rms* is calculated again. Then the third spectrum is averaged with the previously averaged spectra ($1^{st}+2^{nd}$) and the *rms* is calculated, and so on. This process is continued by adding the next spectrum to the previously averaged spectra until the final spectrum. Figure 1.10 shows examples of *rms* versus integration time on three observations; e.g, obsid-1342192365 is a Band 1b observation, obsid-1342201585 is a Band 4b observation, and obsid-1342235779 is a Band 5a observation. All these observations are conducted in DBS FastChop mode. The green line shows the expected *rms* evolution following $\sqrt{1/t}$ for easy comparison. The slopes clearly show that the noise goes down with the increasing integration time, even long integrations of several hours. This is important to reach many of the HIFI science goals, including the search for O_2.

1.3.3 Ground-based telescopes

Atacama Pathfinder EXperiment

The Atacama Pathfinder EXperiment (APEX[5]) is a 12-meter submillimeter telescope at an altitude of 5100 meters at Llano de Chajnantor in Chile (Fig 1.11 *left*). It has various instruments operating from ~200 GHz up to THz frequencies. In this thesis, we primarily used the CHAMP$^+$ instrument (Kasemann et al. 2006, Güsten et al. 2008) in order to observe high-*J* CO lines (J_{up}= 6 up to 8). It is a PI instrument built by Max Planck Institute for Radioastronomy, Germany (PI: R. Güsten) with contribution from SRON-Groningen, the Netherlands. The instrument consists of two heterodyne receiver arrays, each with seven pixel detector elements for simultaneous operations in the 620–720 GHz and 780–950 GHz frequency ranges. The APEX beam sizes correspond to 8″ at 809 GHz and 9″ at 691 GHz. Its state-of-the-art technology combined with excellent atmospheric conditions at the site makes the instrument ideal to observe high-frequency molecular transitions.

---

[5] This thesis is based on data acquired with the Atacama Pathfinder Experiment (APEX). APEX is a collaboration between the Max-Planck-Institut für Radioastronomie, the European Southern Observatory, and the Onsala Space Observatory.

Figure 1.11 – *Left:* 12-m APEX telescope located at the Cerro Chajnantor plateau at 5100-m altitude. *Right:* 15-m JCMT located at Mauna Kea, Hawaii. Photo Credits: Umut Yıldız.

A detailed description of the instrument and observations of several sources in the current sample have been presented in van Kempen et al. (2009a,b,c), Yıldız et al. (2012, in prep (Chapter 4)). Maps of the ^{12}CO 6–5, 7–6 and ^{13}CO 6–5 lines over a few arcmin region were observed for all *Herschel* sources visible from Chajnantor, whereas ^{13}CO 8–7 and C^{18}O 6–5 lines were obtained for selected objects in staring mode. In addition, lower-J transitions were observed for southern sources using various receivers at APEX (van Kempen et al. 2006, 2009a,b,c). These new high-J CO observations along with molecular line surveys probe the velocity structure, physical conditions, and molecular abundances of dense gas around the protostars.

James Clerk Maxwell Telescope

The James Clerk Maxwell Telescope (JCMT[6]) is a 15-meter submillimeter telescope at an altitude of 4092 meters on Mauna Kea, Hawaii (Fig 1.11 *right*). Two instruments, HARP-B and RxA, are primarily used in order to observe low-J CO lines (e.g., 3–2 and 2–1) in this thesis. The HARP-B instrument (Dent et al. 2000, Smith et al. 2008, Buckle et al. 2009) is used to observe the 3–2 lines, which allows heterodyne spectroscopy with instantaneous mapping capability. The instrument consists of 16 SIS detectors with 4×4 pixel elements of 15″ each at 30″ separation. The tuning range is 325–375 GHz and it covers an area of 2′×2′ region in the sky. The beam size of each receptor is approximately 14″. RxA is a single-pixel double side band (DSB) receiver, operating between 211 and 276 GHz range. Our CO 2–1 lines were observed with RxA receiver with a beam size of ~23″. A fraction of the observations were obtained from the JCMT public archive[7] whereas the rest were obtained in dedicated campaigns.

1.4   WISH

---

[6] The JCMT is operated by The Joint Astronomy Centre on behalf of the Science and Technology Facilities Council of the United Kingdom, the Netherlands Organisation for Scientific Research, and the National Research Council of Canada.

[7] This research used the facilities of the Canadian Astronomy Data Centre operated by the National Research Council of Canada with the support of the Canadian Space Agency.

T he "Water In Star-forming regions with *Herschel* (WISH[8])" is a 425 hours guaranteed time key-program on *Herschel* Space Observatory in order to study the physical and chemical structure of star-forming regions by focussing on H_2O and other related species (van Dishoeck et al. 2011). The project involves more than 80 international scientists in 35 institutes from 10 countries. The program covers ~80 sources in seven sub-programs with different luminosities ranging from low- (0.8 $L_\odot$) to high-mass protostars (10^5 $L_\odot$); and in different evolutionary stages from pre-stellar cores to protoplanetary disks. In the WISH project, high spectral and spatial resolution spectroscopy is obtained by using both HIFI and PACS instruments.

Water is the primary target in the project, because it is one of the most abundant key molecules in star-forming regions so its formation in different environments needs to be understood. It is a cornerstone in the oxygen chemistry network, which is the basis for many other chemical reactions. Conversely, water is an excellent tracer for probing different physical conditions since its abundance variations are very large: in cold regions the water abundance is very low, only 10^{-9}–10^{-8} with respect to H_2, whereas in hot regions, most of the gas-phase oxygen is locked in water with an abundance of ~10^{-4}. Water is also found to be an excellent tracer of the dynamical processes in outflows, which contain large amounts of water (Kristensen et al. 2011, Vasta et al. 2012, Santangelo et al. 2012). More information about the project can be found in the review articles of van Dishoeck et al. (2011) and Kristensen & van Dishoeck (2011), and the results of the individual subprograms can be found in the dedicated website[8].

When quoting envelope or outflow abundances, it is of course important to compare this abundance with respect to something. At outflow positions far from the central source, *Spitzer* Space Telescope data provide direct constraints on the H_2 column density from observations of low-*J* rotational lines in the mid-infrared. Towards the central source position, H_2 is not detected because the extinction is too high even at MIR wavelengths (Maret et al. 2009). CO is a chemically stable molecule with many transitions at sub-mm and mm wavelengths. Therefore, observations of CO in many rotational transitions can provide the reference frame for the column densities of cold, warm, and hot gas, and thereby a reference frame against which to measure the H_2O abundance as well as that of other species, e.g., O_2.

This thesis is based on the data observed with HIFI in the low-mass subprogram. In total, the sample contains 29 low-mass Class 0 and Class I sources. The sample selection criteria with the coordinates and other basic information of the source list are presented in van Dishoeck et al. (2011) with updates in Kristensen et al. (2012). The low-mass sources are located in various nearby molecular clouds, e.g., the Perseus, Ophiuchus, Taurus, and Serpens molecular clouds. Fortunately, as it turns out, several CO and isotopolog transitions fall close to H_2O transitions making it possible to observe them in one setting and thereby maximizing telescope efficiency. These include: ^{13}CO 10–9 with H_2O 1_{11}–0_{00} (40 min); $C^{18}O$ 5–4 with $H_2^{18}O$ 1_{10}–1_{01} (60 min); $C^{18}O$ 9–8 with H_2O 2_{02}–1_{11} (20 min); and $C^{18}O$ 10–9 with H_2O 3_{12}–3_{03} (30 min or 5 hours). An example setup is shown in Fig. 1.12, $C^{18}O$ 9–8 (987.56 GHz) with H_2O 2_{02}–1_{11} (987.92 GHz). Two CO surveys are presented in this thesis (Chapters 3 and 5)

1.5   WISH live data show

W ISH HIFI data consist of either "Single Pointing" (DBS, PSw, FSw, LoadChop) or "Mapping" (OTF PSw, FSw) observations. The WISH observations were conducted between February 3, 2010 until February 25, 2012 by executing 821 AORs (Astronomical Observing Re-

---

[8] `http://www.strw.leidenuniv.nl/WISH/`
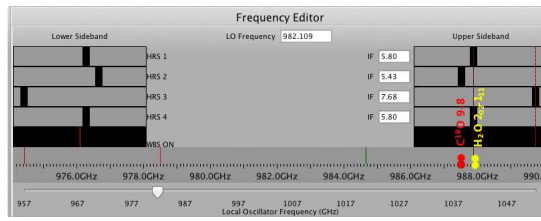
Figure 1.12 – WISH observations aim to cover as many lines as possible in one observing setup. The above example shows the setup for $C^{18}O$ 9–8 (987.56 GHz) with H_2O $2_{02}-1_{11}$ (987.92 GHz).

Figure 1.13 – A glimpse of "WISH Live Data Show" database that is available to the WISH team members.

quest). All the WISH proprietary data are collected in one computer at the Leiden Observatory. In order to provide easy and constant access to all WISH data by the team worldwide, a MySQL and Python powered database and HIFI data reduction pipeline has been constructed. This password protected database is called the "*WISH Live Data Show (LDS)*" (Fig. 1.13). Although the WISH project also contains PACS observations, PACS data are reduced by other team members and only collected in the LDS. The LDS data reduction pipeline primarily works for HIFI data, which interacts with the *Herschel* Science Archive (HSA), *Herschel* Interactive Processing Environment (HIPE), and GILDAS-CLASS softwares.

The database syncs with HSA for new observations every day. Then the pipeline downloads and reduces new HIFI data using the latest officially released HIFI pipeline, which therefore provides almost publication quality data 24 hours after the *Herschel* observations. The data are available in different formats, e.g., HIPE imported, CLASS, fits, and also quick image previews in png and eps format. We regularly check if HSA provides the data by using new pipelines, in that case all the observations are re-downloaded and re-reduced. In order to compare with old data reductions, nothing is deleted from the database, even data reduced with HIPE v.1.0 up to the latest version HIPE v.10.0 are available. Re-pipelining was done for all observations with the new calibration before publishing the HIFI first results papers in 2010 (HIPE v.1.x, v.2.x to HIPE v.3.0.1).

The steps in the pipeline are fully automatic, these include:

- Connecting to HSA *Observation Log* at 00:00 hrs
- Checking the new observations, if so, adding them to pipeline queue
- Connecting to HSA and importing data to HIPE
- Saving imported observation to disk
- Separating subbands of Level 2 data set

- Stitching the subbands
- Saving the stitched spectra as png and eps files
- Creating fits files for stitched and non-stitched spectra
- Converting fits files to GILDAS-CLASS format
- Creating webpages to display the output
- Updating the database if the pipeline is successful
- Saving all the output by adding the current date to filename in the "Log" folder

If re-pipelining, removing standing waves, or any other additional data manipulation is necessary, these steps are included after importing the data to HIPE. Re-pipelining starts from Level 0.5 data, which is mostly raw data but the data are processed such that backend (spectrometer) effects are removed and frequency calibrated. This database will become public after the WISH key program is finalized and it will be transferred to our legacy database LOMASS[9] (Leiden Observatory Single-dish Submm Spectral Database of Low-mass YSOs), which will archive thousands of spectra observed with many telescopes for many low-mass protostars.

1.6 This thesis

The primary focus of this thesis is the *formation of low-mass protostars*, specifically the earliest deeply embedded phase, when material from the collapsing envelope is still accreted onto the growing young star. A variety of state-of-the-art sub-/mm instruments are used for the observations in order to understand the physical and chemical nature of this phase, centered around the *Herschel* Space Observatory. Rotational transitions of molecules, specifically, low- and high-lying lines of CO and its isotopologs have been used to characterize the YSO structure and kinematics. The high frequency observations with *Herschel* allow much warmer gas to be probed than was possible previously. The following questions are addressed:

- How is CO excited in the different parts of the YSOs, and what are the locations and relative importance of shocks and UV heating? Can we quantify this '*feedback*' on the surroundings? How does this relate to what is seen in H_2O?
- Does the CO excitation and do the line characteristics change with evolution from the deeply embedded Class 0 YSOs to less deeply embedded Class I YSOs?
- What is the CO abundance structure throughout the envelope: where is CO frozen out and where does it evaporate? Is it processed to other molecules on the grains?
- What is the abundance of O_2 in protostellar environments? Why is it so anomalously low compared with CO?

These questions are addressed in the following chapters.

Chapter 2 — *Herschel*-HIFI observations of high-*J* lines (up to J_u=10) of ^{12}CO, ^{13}CO, and $C^{18}O$ are presented toward three deeply embedded low-mass protostars in the NGC 1333 star-forming region. The observations show several energetic components including shocked and quiescent gas. The results are: (***i***) ^{12}CO line widths increase from lower-*J* toward higher-*J* transitions. (***ii***) CO and its isotopologues trace different material. The ^{12}CO 10–9 lines are dominated by broad (*FWHM* 25–30 km s^{-1}) emission indicating a large-scale shock process (>1000 AU). Several CO and ^{13}CO line profiles reveal a medium-broad component (5–10 km s^{-1}), seen prominently in H_2O lines, indicative of small-scale shocks (<1000 AU). Narrow $C^{18}O$ lines (2–3 km s^{-1}) trace the quiescent envelope material. (***iii***) Higher-*J* isotopologue lines (e.g., $C^{18}O$ 9–8 and 10–9; E_{up}=237 and

---

[9] http://lomass.strw.leidenuniv.nl

289 K) probe high temperatures. However, analysis shows that for a power-law envelope at least 50% of the observed emission still comes from the colder <40 K parts of the envelope. Three different models using the `RATRAN` radiative transfer code are applied to the optically thin $C^{18}O$ lines to quantify the CO abundance. For the "*constant*" profile, the observed line intensities cannot all be reproduced simultaneously. For the "*anti-jump*" model, the outer abundance, X_0, was kept high for densities lower than the desorption density, n_{de}. It fits well the lower-J lines, but the higher-J lines are underproduced. In the "*drop*" model, the inner abundance, X_{in}, increases above T_{ev}. This model fits well all lines, however X_{in} is a factor of ~3-5 below X_0 for the best fit to the IRAS 2A data. This suggests that a significant fraction of the CO ice is transformed to other species on the grains.

Chapter 3 — This chapter builds on the results of Chapter 2 by presenting *Herschel*-HIFI observations of the same CO lines for a much larger sample of 26 deeply embedded low-mass Class 0 and Class I young stellar objects. This is the first large-scale spectrally resolved high-J CO survey ever conducted for these types of sources. Complementary lower-J CO maps were also observed using ground-based JCMT and APEX telescopes and convolved to matching beam sizes. The ^{12}CO 10–9 line is detected for all objects and can generally be decomposed into a narrow and broad component due to the quiescent envelope and entrained outflow material, respectively. The median excitation temperatures for ^{12}CO, ^{13}CO, and $C^{18}O$ derived from single-temperature fits to the J_{up}=2–10 integrated intensities are ~70 K, 48 K and 37 K, respectively, with no significant difference between Class 0 and Class I sources and no trend with M_{env} or L_{bol}. Thus, in contrast with the continuum SEDs, the spectral line energy distributions (SLEDs) do not show an evolution during the embedded stage. In contrast, the integrated line intensities of all CO isotopologs show a clear decrease with evolutionary stage as the envelope is dispersed.

Chapter 4 — Two well-known Class 0 low-mass protostars NGC 1333 IRAS 4A and IRAS 4B are mapped in the ^{12}CO 6–5 transition in order to characterize the warmer parts of the protostellar envelope using the new generation APEX-CHAMP$^+$ array receiver. This study allowed us to quantify the feedback of the protostars on their surroundings in terms of shocks, ultraviolet (UV) heating, photodissociation, and outflow dispersal. The map shows that the broad CO emission-line profiles trace entrained shocked gas along the outflow walls, which have an average temperature of ~100 K. At other positions surrounding the outflow and the protostar, the 6–5 line profiles are narrow indicating UV heating. The narrow ^{13}CO 6–5 data directly reveal this UV heated gas distribution for the first time. The amount of UV-photon-heated gas and outflowing gas are quantified from the combined ^{12}CO and ^{13}CO 6–5 maps and found to be comparable within a 20″ radius around IRAS 4A, which implies that UV photons can affect the gas as much as the outflows. Weak [C I] emission throughout the region indicates that there is a lack of CO dissociating photons. As for IRAS2A studied in Chapter 2, modeling of the $C^{18}O$ lines demonstrates the necessity of a "drop" abundance profile throughout the envelopes where the CO freezes out and is reloaded back into the gas phase through grain heating, thus providing quantitative evidence of the CO ice evaporation zone around the protostars. The inner abundances are less than the canonical value of $CO/H_2=2.7\times10^{-4}$, however, strengthening the conclusion that there is some processing of CO into other species on the grains.

Chapter 5 — Large-scale CO maps of 26 low-mass young stellar objects are obtained using APEX-CHAMP$^+$ (^{12}CO and ^{13}CO 6–5), together with JCMT-HARP-B (^{12}CO and ^{13}CO 3–2). The maps are high spatial and spectral resolution, particularly CO 6–5 maps have 9″ pixels thus resolving the morphology of the outflows. In this chapter, these maps are analyzed using the same

methods to determine the outflow parameters and the results are compared with higher-J CO lines obtained with *Herschel*. All sources in our sample show outflow activity via CO line wings. One of the key parameters, the outflow force, F_{CO}, is measured and correlations with other physical parameters are sought. F_{CO} versus L_{bol} plots show that Class 0 sources have more powerful outflows than the Class I sources, even if their luminosities are comparable. Overall, the various outflow parameters indicate reduced outflow activity with evolutionary stage, consistent with previous studies. F_{CO} is directly proportional with M_{env} and M_{CO}, indicating that higher outflow forces require higher envelope masses and involve higher outflow masses. Comparison with high-J CO lines probed by PACS, which trace currently shocked gas, shows that although the 6–5 and PACS transitions do not probe the same gas component, the two components are still linked. However, the link does not extend down to CO 3–2. The conclusion is that CO 6–5 depends on the shock characteristics (pre-shock density and velocity), whereas CO 3–2 is more sensitive to conditions in the surrounding environment (density).

Chapter 6 — *Herschel*-HIFI observations of molecular oxygen, O_2, at 487 GHz toward the deeply embedded low-mass Class 0 protostar, NGC 1333-IRAS 4A, are presented. The deep HIFI spectrum fails to detect O_2 at the velocity of the dense protostellar envelope, implying one of the deepest upper limits of O_2/H_2 at $\leq 6 \times 10^{-9}$ (3σ). However, a tentative (4.5σ) detection of O_2 is seen at the velocity of the surrounding NGC 1333 molecular cloud, shifted by 1 km s^{-1} relative to the protostar. Pure gas-phase models and gas-grain chemical models overproduce O_2 in the dense envelope, unless a long pre-collapse stage ($\sim 10^6$ years) is included, during which atomic and molecular oxygen are frozen-out onto the dust grains and fully converted into H_2O. These results imply that the gas and ice that enter protoplanetary disks are poor in O_2.

1.7 Future outlook

Further advances in our understanding of star formation will come from new technologies for high-frequency or highly efficient observations. Single dish millimeter telescopes will include instruments with many pixel detectors (e.g., 64-pixel heterodyne SuperCam at 345 GHz on the Sub-Millimeter Telescope). These array receivers will make it possible to produce large scale velocity maps of star-forming clouds that complement the big *Herschel* continuum surveys. This will aid in deciphering how dense cores form out of the larger filamentary structures seen in the Herschel images and how they eventually lead to the formation of individual stars or groups of stars.

On the other hand, the newly inaugurated Atacama Large Millimeter/ submillimeter Array (ALMA), the revolutionary interferometric observatory at an altitude of 5100 meters, opens up an entirely new era in the study of protostars, from low to high mass. Its 66 antennas with baselines ranging up to 16 km provide unprecedented sensitivity and angular resolution, down to 1 AU in the nearest star-forming regions. When working at full capacity, it will be well suited to unravel the physical mechanisms behind the formation of protostellar jets and outflows. Also, knowledge of binary star formation in the earliest deeply embedded phase is still lacking and the interactions of the outflows of binaries can only be disantangled with these high precision instruments. Thus, star formation research poses many interesting questions that can be answered in the coming years, highlighting its bright and exciting future.

Acknowledgements

Herschel-HIFI observations of high-J CO lines in the NGC 1333 low-mass star-forming region

U.A. Yıldız, E.F. van Dishoeck, L.E. Kristensen, R. Visser, J.K. Jørgensen, G.J. Herczeg, T.A. van Kempen, M.R. Hogerheijde, S.D. Doty, A.O. Benz, S. Bruderer, S.F. Wampfler, E. Deul, R. Bachiller, A. Baudry, M. Benedettini, E. Bergin, P. Bjerkeli, G.A. Blake, S. Bontemps, J. Braine, P. Caselli, J. Cernicharo, C. Codella, F. Daniel, A.M. di Giorgio, C. Dominik, P. Encrenaz, M. Fich, A. Fuente, T. Giannini, J.R. Goicoechea, Th. de Graauw, F. Helmich, F. Herpin, T. Jacq, D. Johnstone, B. Larsson, D. Lis, R. Liseau, F.-C. Liu, M. Marseille, C. McCoey, G. Melnick, D. Neufeld, B. Nisini, M. Olberg, B. Parise, J.C. Pearson, R. Plume, C. Risacher, J. Santiago-García, P. Saraceno, R. Shipman, M. Tafalla, A. G. G. M. Tielens, F. van der Tak, F. Wyrowski, P. Dieleman, W. Jellema, V. Ossenkopf, R. Schieder, J. Stutzki

Abstract

In this chapter, we study the *Herschel*-HIFI observations of high-*J* lines (up to J_u=10) of ^{12}CO, ^{13}CO and C^{18}O are presented toward three deeply embedded low-mass protostars, NGC 1333 IRAS 2A, IRAS 4A, and IRAS 4B, obtained as part of the *Water In Star-forming regions with Herschel* (WISH) key program. The spectrally-resolved HIFI data are complemented by ground-based observations of lower-*J* CO and isotopologue lines. The ^{12}CO 10–9 profiles are dominated by broad (FWHM 25–30 km s^{-1}) emission. Radiative transfer models are used to constrain the temperature of this shocked gas to 100–200 K. Several CO and ^{13}CO line profiles also reveal a medium-broad component (FWHM 5–10 km s^{-1}), seen prominently in H$_2$O lines. Column densities for both components are presented, providing a reference for determining abundances of other molecules in the same gas. The narrow C^{18}O 9–8 lines probe the warmer part of the quiescent envelope. Their intensities require a jump in the CO abundance at an evaporation temperature around 25 K, thus providing new direct evidence for a CO ice evaporation zone around low-mass protostars.

2.1   Introduction

The earliest protostellar phase just after cloud collapse – the so-called Class 0 phase – is best studied at mid-infrared and longer wavelengths (André et al. 2000). To understand the physical and chemical evolution of low-mass protostars, in particular the relative importance of radiative heating and shocks in their energy budget, observations are required that can separate these components. The advent of the Heterodyne Instrument for the Far-Infrared (HIFI) on *Herschel* opens up the possibility to obtain spectrally resolved data from higher-frequency lines that are sensitive to gas temperatures up to several hundred Kelvin.

Because of its high abundance and strong lines, CO is the primary molecule to probe the various components of protostellar systems (envelope, outflow, disk). The main advantage of CO compared with other molecules (including water) is that its chemistry is simple, with most carbon locked up in CO in dense clouds. Also, its evaporation temperature is low, around 20 K for pure CO ice (Collings et al. 2003, Öberg et al. 2005), so that its freeze-out zone is much smaller than that of water. Most ground-based observations of CO and its isotopologues have been limited to the lowest rotational lines originating from levels up to 35 K. ISO has detected strong far-infrared CO lines up to $J_\mathrm{u}=29$ from Class 0 sources (Giannini et al. 2001) but the emission is spatially unresolved in the large 80" beam. ISO also lacked the spectral resolution needed to separate the shocked and quiescent gas or to detect intrinsically-weaker ^{13}CO and $C^{18}O$ lines on top of the strong continuum.

The NGC 1333 region in Perseus (d = 235 pc; Hirota et al. 2008) contains several deeply embedded Class 0 sources within a ~1 pc region driving powerful outflows (e.g., Liseau et al. 1988, Hatchell & Fuller 2008). The protostars IRAS 4A and 4B, separated by ~31", and IRAS 2A are prominent submillimeter continuum sources (luminosities of 5.8, 3.8 and 20 $L_\odot$) with envelope masses of 4.5, 2.9 and 1.0 $M_\odot$, respectively (Sandell et al. 1991, Jørgensen et al. 2009). All three are among the brightest and best studied low-mass sources in terms of molecular lines, with several complex molecules detected (e.g., Blake et al. 1995, Bottinelli et al. 2007). Here HIFI data of CO and its isotopologues are presented for these three sources and used to quantify the different physical components. In an accompanying letter, Kristensen et al. (2010) present complementary HIFI observations of H_2O and analyze CO/H_2O abundance ratios.

2.2   Observations and results

The NGC 1333 data were obtained with HIFI (de Graauw et al. 2010) onboard the *Herschel* Space Observatory (Pilbratt et al. 2010), in the context of the WISH key program (van Dishoeck et al. 2011). Single pointings at the three source positions were carried out between 2010 March 3 and 15 during the *Herschel* HIFI priority science program (PSP). Spectral lines were observed in dual-beam switch (DBS) mode in HIFI bands

Table 2.1 – Overview of the observations of IRAS 2A, 4A, and 4B.

Mol.	Trans.	E_u/k_B (K)	Frequency (GHz)	Tel./Inst.	Beam size (a)	Ref.
CO	2–1	16.6	230.538	JCMT	22	1
	4–3	55.3	461.041	JCMT	11	2
	6–5	116.2	691.473	APEX	9	3
	10–9	304.2	1151.985	HIFI-5a	20	4
^{13}CO	10–9	290.8	1101.349	HIFI-4b	21	4
C^{18}O	1–0	5.3	109.782	Onsala	34	1
	2–1	15.8	219.560	JCMT	23	1
	3–2	31.6	329.331	JCMT	15	1
	5–4	79.0	548.831	HIFI-1a	42	4
	6–5	110.6	658.553	APEX	10	3
	9–8	237.0	987.560	HIFI-4a	23	4
	10–9	289.7	1097.162	HIFI-4b	21	4

Notes. (1) Jørgensen et al. (2002); (2) JCMT archive; (3) Yıldız et al. (2012); (4) this work

1a, 4a, 4b, and 5a with a chop reference position located 3' from the source positions. The observed positions (J2000) are: IRAS 2A: $3^h28^m55^s6$, $+31°14'37.''1$; IRAS 4A: $3^h29^m10^s5$, $+31°13'30.''9$; and IRAS 4B: $3^h29^m12^s0$, $+31°13'08.''1$ (Jørgensen et al. 2009).

Table 2.1 summarizes the lines observed with HIFI together with complementary lower-*J* lines obtained with ground-based telescopes. The *Herschel* data were taken using the wide band spectrometer (WBS) and high resolution spectrometer (HRS) backends. Owing to the higher noise ($\sqrt{2}$ more) in HRS than WBS, mainly WBS data are presented here. Only the narrow C^{18}O 5–4 lines use the HRS data. Integration times (on+off) are 10, 20, 30, 40, and 60 minutes for the ^{12}CO 10–9, C^{18}O 9–8, 10–9, ^{13}CO 10–9, and C^{18}O 5–4 lines respectively. The HIFI beam sizes correspond to ~20" (~4700 AU) at 1152 GHz and ~42" (~10000 AU) at 549 GHz. Except for the ^{12}CO 10–9 line, all isotopologue lines were observed together with H$_2$O lines.

The calibration uncertainty for the HIFI data is of the order of 20% and the pointing accuracy is around 2". The measured line intensities were converted to the main-beam brightness temperatures $T_{MB} = T_A^*/\eta_{MB}$ by using a beam efficiency $\eta_{MB} = 0.74$ for all HIFI lines. Data processing started from the standard HIFI pipeline in the *Herschel* interactive processing environment (HIPE[1]) ver. 3.0.1 (Ott 2010), where the V_{LSR} precision is of the order of a few m s^{-1}. Further reduction and analysis were done using the GILDAS-CLASS[2] software. The spectra from the H- and V-polarizations were averaged in order to obtain a better S/N. In some cases a discrepancy of 30% was found between the two polarizations, in which case only the H band spectra were used for analysis since their rms is lower.

---

[1] HIPE is a joint development by the Herschel Science Ground Segment Consortium, consisting of ESA, the NASA Herschel Science Center, and the HIFI, PACS and SPIRE consortia.
[2] http://www.iram.fr/IRAMFR/GILDAS/
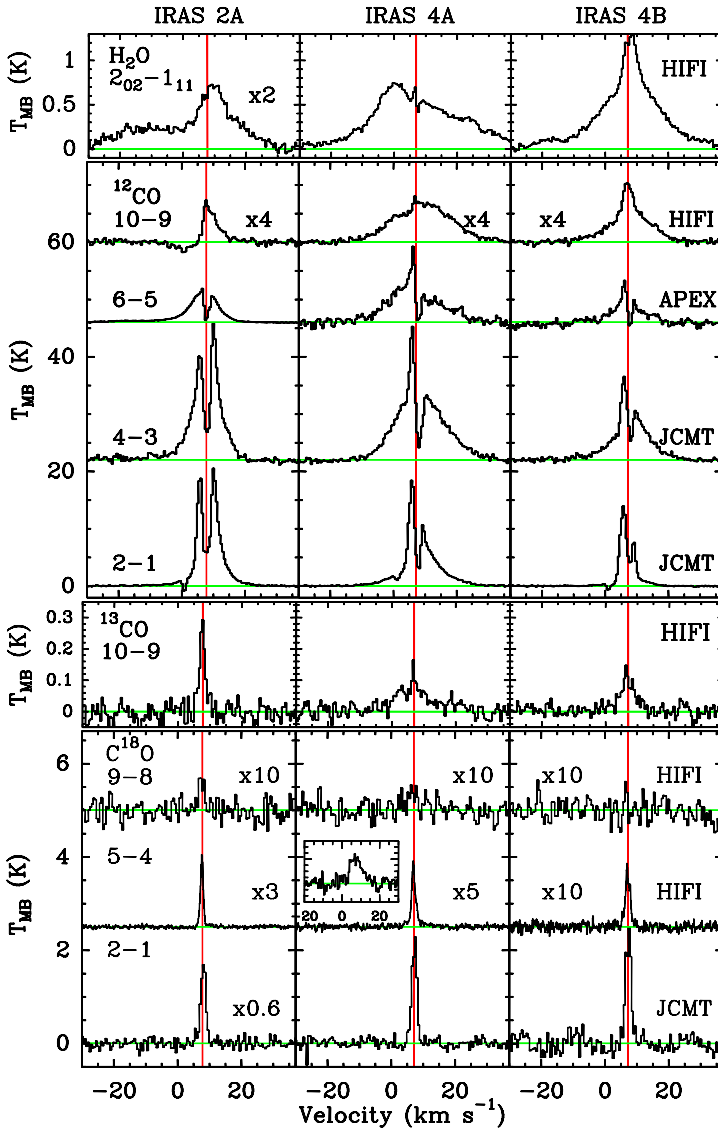
Figure 2.1 – Spectra at the central positions of IRAS 2A, 4A and 4B. *Top to bottom:* H_2O $2_{02}-1_{11}$ line from Kristensen et al. (2010) illustrating the medium and broad components, and spectra of ^{12}CO, ^{13}CO, and $C^{18}O$. The red lines correspond to the source velocities as obtained from the low-J $C^{18}O$ lines. The insert in the $C^{18}O$ 5–4 line for IRAS 4A illustrates the weak medium component with peak T_{MB} = 22 mK obtained after subtracting a Gaussian fit to the narrow line.

Table 2.2 – Observed line intensities.

Source	Mol.	Trans.	$\int T_{MB} dV$ (K km s^{-1})	T_{peak} (K)	rms[a] (K)
IRAS 2A	CO	2–1	127.5	20.5	0.08
		4–3	177.2	23.8	0.44
		6–5	57.0	5.9	0.11
		10–9	16.3	1.71	0.078
	^{13}CO	10–9	0.4	0.3	0.026
	C^{18}O	1–0	5.6	4.0	0.27
		2–1	5.83	2.3	0.15
		3–2	4.7	3.2	0.13
		5–4	0.62	0.46	0.004
		6–5	1.8	1.1	0.11
		9–8	0.2	0.07	0.018
		10–9	0.15	0.06	0.017
IRAS 4A	CO	2–1	117.2	18.4	0.07
		4–3	221.1	23.3	0.32
		6–5	121.9	13.2	0.59
		10–9	35.7	1.9	0.073
	^{13}CO	10–9	1.2	0.2	0.017
	C^{18}O	2–1	4.3	2.3	0.09
		5–4	0.5	0.26	0.005
		9–8	0.1	0.05	0.018
IRAS 4B	CO	2–1	54.8	13.9	0.07
		4–3	115.2	14.6	0.26
		6–5	43.3	7.3	0.36
		10–9	26.8	2.6	0.076
	^{13}CO	10–9	0.7	0.15	0.017
	C^{18}O	2–1	4.9	2.5	0.19
		5–4	0.23	0.12	0.005
		9–8	<0.07	-	0.019

Notes. [a]In 0.5 km s^{-1} bins.

Complementary ground-based spectral line observations of ^{12}CO 6–5 were obtained at the 12-m Atacama Pathfinder EXperiment Telescope (APEX), using the CHAMP$^+$ 2×7 pixel array receiver (Güsten et al. 2008). The lower-J spectral lines were obtained from the James Clerk Maxwell Telescope (JCMT) archive and from Jørgensen et al. (2002). Details will be presented elsewhere (Yıldız et al. 2012).

The observed line profiles are presented in Fig. 2.1 and the corresponding line intensities in Table 2.2. For the ^{12}CO 10–9 toward IRAS 2A, the emission from the blue line wing was chopped out due to emission at the reference position located in the blue part of the SVS 13 outflow. A Gaussian fitted to the red component of the line was used to obtain the integrated intensity.

Kristensen et al. (2010) identify three components in the H$_2$O line profiles centered close to the source velocities: a broad underlying emission profile (Gaussian with FWHM~25–30 km s^{-1}), a medium-broad emission profile (FWHM~5–10 km s^{-1}), and narrow self-
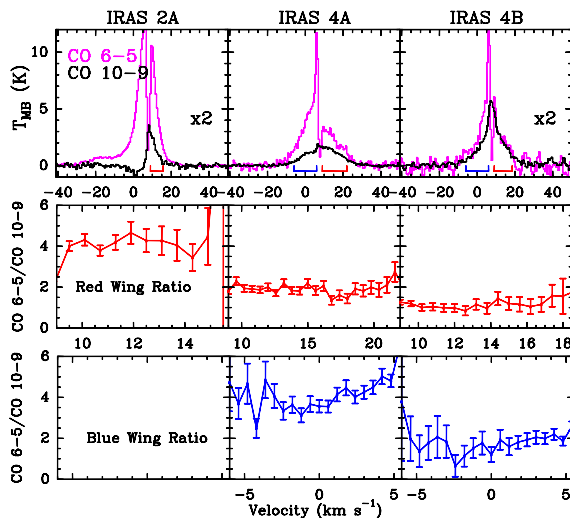
Figure 2.2 – Ratios of CO 6–5/CO 10–9. *Top*: CO line profiles. The CO 6–5 and 10–9 profiles have been multiplied by a factor of 2 for IRAS 2A and 4B. *Middle* and *bottom*: ratio of line wing intensity in the specified velocity range indicated in the top panel for the red and blue wings.

absorption lines (FWHM∼2–3 km s^{-1}); see the H_2O 2_{02}–1_{11} lines in Fig. 2.1. The same components are also seen in the CO line profiles, albeit less prominently than for H_2O. The broad component dominates the ^{12}CO 10–9 lines of IRAS 4A and 4B and is also apparent in the deep ^{12}CO 6–5 spectrum of IRAS 2A (Fig. 2.2). The medium component is best seen in the ^{13}CO 10–9 profiles of IRAS 4A and 4B and as the red wing of the ^{12}CO 10–9 profile for IRAS 2A. A blow-up of the very high S/N spectrum of $C^{18}O$ 5–4 for IRAS 4A (insert in Fig. 2.1) also reveals a weak $C^{18}O$ medium-broad profile. The narrow component is clearly observed in $C^{18}O$ emission and ^{12}CO low-J self-absorption. Kristensen et al. (2010) interpret the broad component as shocked gas along the outflow cavity walls, the medium component as smaller-scale shocks created by the outflow in the inner (<1000 AU) dense envelope, and the narrow component as the quiescent envelope, respectively.

2.3 Analysis and discussion

2.3.1 Broad and medium components: shocked gas

To quantify the physical properties of the broad outflow component, line ratios are determined for the wings of the line profiles. Figure 2.2 shows the CO 6–5/CO 10–9 ratio as a function of velocity. The APEX-CHAMP$^+$ CO 6–5 maps of IRAS 4A and 4B

Table 2.3 – Summary of column densities, $N(H_2)$ in cm^{-2} in the broad and medium components in 20″ beam.

Source	Broad Comp.	Medium Comp.
IRAS 2A	6×10^{19} [a]	2×10^{20} [b]
IRAS 4A	4×10^{20} [b]	6×10^{20} [c]
IRAS 4B	1×10^{20} [b]	2×10^{20} [c]

Notes. Obtained from [a] CO 6–5, [b] CO 10–9, [c] ^{13}CO 10–9 spectra.

from Yıldız et al. (2012) and IRAS 2A from van Kempen et al. (2009a) are resampled to a 20" beam so that both lines refer to the same beam. The ratios are compared with model non-LTE excitation line intensities calculated using the RADEX code (van der Tak et al. 2007, Fig. 2.4 in the Additional Materials 2.5.1). The density within a 20" diameter is taken to be $\geq 10^5$ cm^{-3} based on the modeling results of Jørgensen et al. (2002, see also Sect. 2.3.2 and Additional Materials 2.5.2). The detection of medium-broad CS 10–9 emission by Jørgensen et al. (2005b) toward IRAS 4A and 4B indicates densities of the order of a few 10^6 cm^{-3}. For the range of densities indicated in Fig. 2.4, the line ratios imply high temperatures: IRAS 2A, T_{kin} =70–130 K; IRAS 4A, T_{kin} =90–120 K; and IRAS 4B, T_{kin} =140–180 K.

The optical depth of the ^{12}CO emission is constrained by the ^{12}CO 10–9/^{13}CO 10–9 ratios. For IRAS 4B, the optical depth of the ^{12}CO line wings is found to drop with velocity, ranging from τ_{wing} ~12 near the center to ~0.4 at the highest velocities where ^{13}CO is detected. This justifies the assumption that the broad ^{12}CO 10–9 lines are optically thin. Total CO column densities in the broad component for these conditions are 4 and 1×10^{16} cm^{-2} for IRAS 4A and 4B, respectively. For IRAS 2A, the broad column density is calculated from the CO 6–5 spectrum as 6×10^{15} cm^{-2}. Using CO/H$_2$ = 10^{-4} gives the H$_2$ column densities listed in Table 2.3.

The medium component attributed to small-scale shocks in the inner envelope can be probed directly by the ^{13}CO 10–9 data for IRAS 4A and 4B. For IRAS 2A, the Gaussian fit to the red wing of the ^{12}CO 10–9 is used. By assuming a similar range of temperatures and densities as for the broad component, beam averaged ^{12}CO column densities of 2, 6, and 2×10^{16} cm^{-2} are found for IRAS 2A, 4A, and 4B respectively, if the lines are optically thin and using ^{12}C/^{13}C = 65. The very weak medium component found in the C^{18}O 5–4 profile for IRAS 4A agrees with this value if the emission arises from a compact (few ") source. Assuming CO/H$_2$=10^{-4} leads to the numbers in Table 2.3. The overall uncertainty in all column densities is a factor of 2 due to the range of physical conditions used to derive them and uncertainties in the adopted CO/H$_2$ ratio and calibration. The total amount of shocked gas is <1% of the total gas column density in the beam for each source (Jørgensen et al. 2002).
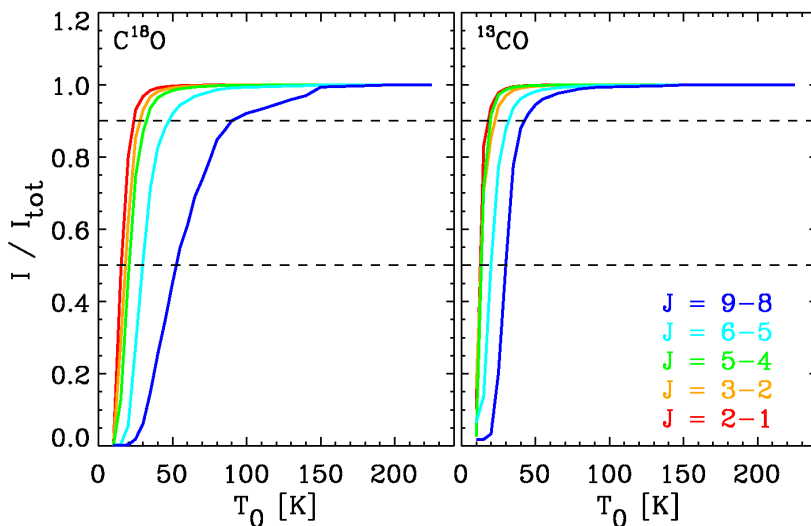
Figure 2.3 – Dependence of line intensities on temperature T_0 of $C^{18}O$ (left) and ^{13}CO (right) for an "anti-jump" model of the CO abundance in the IRAS 2A envelope. The line intensities are measured relative to a model where the CO abundance is undepleted at all radii. Each curve therefore represents the fraction of the line intensity for the given transition, which has its origin in gas at temperatures below T_0. The dashed lines indicate the levels corresponding to 50 and 90% respectively.

2.3.2   Narrow component: bulk warm envelope

The narrow width of the $C^{18}O$ emission clearly indicates an origin in the quiescent envelope. Naïvely, one would associate emission coming from a level with E_u/k_B=237 K (9–8) with the warm gas in the innermost part of the envelope. To test this hypothesis, a series of envelope models was run with varying CO abundance profiles. The models were constructed assuming a power-law density structure and then calculating the temperature structure by fitting both the far-infrared spectral energy distribution and the submillimeter spatial extent (Jørgensen et al. 2002). Figure 2.3 compares the fractional line intensities for the $C^{18}O$ and ^{13}CO transitions in a spherical envelope model for IRAS 2A as a function of temperature. In these models, the abundance in the outer envelope was kept high, X_0=2.7×10^{-4} with respect to H_2 (all available gas-phase carbon in CO), decreasing by a factor of 1000 at temperatures higher than a specific temperature, T_0 (a so-called 'anti-jump' model (see Schöier et al. 2004, for nomenclature). These models thereby give an estimate of the fraction of the line emission for a given transition (in the respective telescope beams) which has its origin at temperatures lower than T_0.

For $C^{18}O$, 90% of the emission in the transitions up to and including the 5–4 HIFI transition has its origin at temperatures lower than 25–30 K, meaning that these transitions are predominantly sensitive to the outer parts of the protostellar envelope. The 9–8 transition

is more sensitive to the warm parts of the envelope, but still 50% of the line flux appears to come from the outer envelope with temperatures less than 50 K. The ^{13}CO transitions become rapidly optically thick in the outer envelopes: even for the 9–8 transition, 90% of the line flux can be associated with the envelope material with temperatures lower than 40 K.

The $C^{18}O$ 9–8 line is clearly a much more sensitive probe of a CO ice evaporation zone than any other observed CO line. Jørgensen et al. (2005c) showed that the low-J $C^{18}O$ lines require a drop in the abundance at densities higher than 7×10^4 cm^{-3} due to freeze-out. However, they did not have strong proof for CO evaporation in the inner part from that dataset. Using the temperature and density structure for IRAS 2A as described above, we computed the $C^{18}O$ line intensities in the respective telescope beams following the method by Jørgensen et al. (2005c). In this 'anti-jump' model, the outer $C^{18}O$ abundance is kept fixed at $X_0 = 5.0 \times 10^{-7}$, whereas the inner abundance X_D and the freeze-out density n_{de} are free parameters. A χ^2 fit to only the $C^{18}O$ 1–0, 2–1 and 3–2 lines gives best-fit values of $X_D = 3 \times 10^{-8}$ and $n_{de} = 7 \times 10^4$ cm^{-3}, consistent with those of Jørgensen et al. (2005c). However, this model underproduces the higher-J lines by a factor of 3–4 (Fig. 2.6 in Additional Materials).

To solve this underproduction, the inner abundance has to be increased in a so-called 'drop-abundance' profile. The fit parameters are now the inner abundance X_{in} and the evaporation temperature T_{ev}, keeping X_D and n_{de} fixed at the above values. Figure 2.9 in Additional Materials shows the χ^2 plots to the $C^{18}O$ 6–5 and 9–8 lines. The evaporation temperature is not well constrained, but low temperatures of $T_{ev} \approx 25$ K are favored because they produce more $C^{18}O$ 5–4 emission. The best-fit $X_{in} = 1.5 \times 10^{-7}$ indicates a jump of a factor of 5 compared with X_D. Alternatively, T_{ev} can be kept fixed at 25 K and both X_{in} and X_D can be varied by fitting all five lines simultaneously. In this case, the same best-fit value for X_{in} is found but only an upper limit on X_D of $\sim 4 \times 10^{-8}$. Thus, for this physical model, $X_{in} > X_D$, implying that a jump in the abundance is needed for IRAS 2A.

2.4 Conclusions

Spectrally resolved *Herschel*-HIFI observations of high-J CO lines up to ^{12}CO 10–9 and $C^{18}O$ 9–8 have been performed toward three low-mass young stellar objects for the first time. These data provide strong constraints on the density and temperature in the various physical components, such as the quiescent envelope, extended outflowing gas, and small-scale shocks in the inner envelope. The derived column densities and temperatures are important for comparison with water and other molecules such as O_2, for which HIFI observations are planned. Furthermore, it is shown conclusively that in order to reproduce higher-J $C^{18}O$ lines within the context of the adopted physical model, a jump in the CO abundance due to evaporation is required in the inner envelope, something that was inferred, but not measured, from ground-based observations. Combination with even higher-J CO lines to be obtained with *Herschel*-PACS in the frame of the WISH key

program will allow further quantification of the different physical processes invoked to explain the origin of the high-J emission.

2.5 Additional materials

2.5.1 Radex model

Figure 2.4 shows the CO 6–5/10–9 line ratios for a slab model with a range of temperatures and densities.
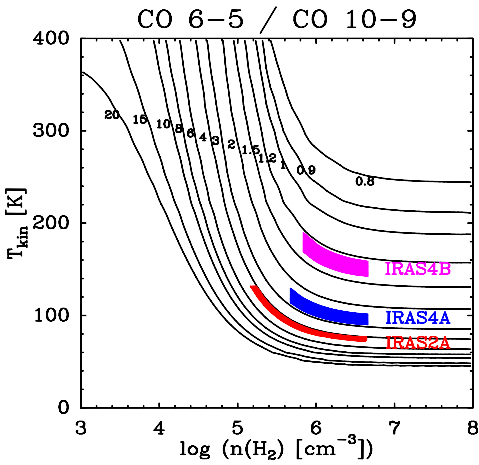
Figure 2.4 – Model line ratios of CO 6–5/10–9 for a slab model with a range of temperatures and densities. The adopted CO column density is 10^{17} cm^{-2} with a line width of 10 km s^{-1}, comparable to the inferred values. For these parameters the lines involved are optically thin. The colored lines give the range of densities within the 20″ beam for the three sources based on the models of Jørgensen et al. (2002).

2.5.2 Abundance profiles for IRAS 2A

Among the three sources, IRAS 2A has been selected for detailed CO abundance profile modeling because more data are available on this source, and because its physical and chemical structure has been well characterized through the high angular resolution submillimeter single dish and interferometric observations of Jørgensen et al. (2002, 2005a). The physical parameters are taken from the continuum modeling results of Jørgensen et al. (2002). In that paper, the 1D dust radiative transfer code DUSTY (Ivezić & Elitzur 1997) was used assuming a power law to describe the density gradient. The dust temperature as function of radius was calculated self-consistently through radiative transfer given a central source luminosity. Best-fit model parameters were obtained by comparison with the spectral energy distribution and the submillimeter continuum spatial extent. The resulting envelope structure parameters are used as input to the RATRAN radiative transfer modeling code (Hogerheijde & van der Tak 2000) to model the CO line intensities for a
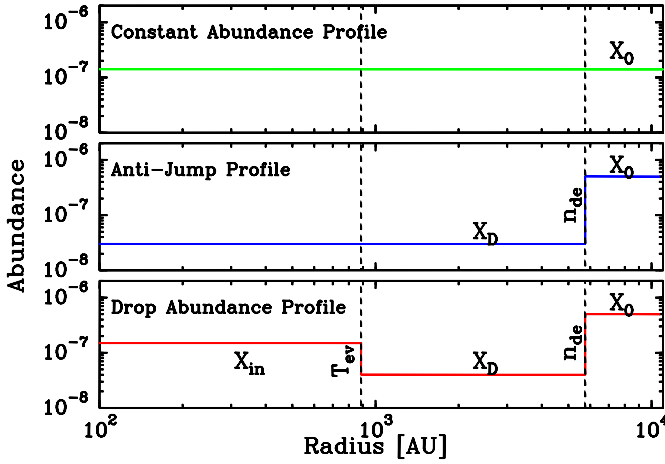
Figure 2.5 – Examples of constant, anti-jump, and drop abundance profiles for IRAS 2A for T_{ev}=25 K and n_{de}=7×10^4 cm^{-3}.

Table 2.4 – Summary of C^{18}O abundance profiles for IRAS 2A.

Profile	X_{in}	T_{ev} [K]	X_D	n_{de} [cm^{-3}]	X_0
Constant	-	-	-	-	1.4×10^{-7}
Anti-jump	-	-	3× 10^{-8}	7×10^4	5×10^{-7}
Drop	1.5×10^{-7}	25	~ 4×10^{-8}	7×10^4	5×10^{-7}

given CO abundance structure through the envelope. The model extends to 11000 AU from the protostar, where the density has dropped to 2×10^4 cm^{-3}. The CO-H$_2$ collisional rate coefficients of Yang et al. (2010) have been adopted.

The C^{18}O lines are used to determine the CO abundance structure because the lines of this isotopologue are largely optically thin and because they have well-defined Gaussian line shapes originating from the quiescent envelope without strong contaminations from outflows. Three types of abundance profiles are examined, namely 'constant', 'anti-jump' and 'drop' abundance profiles. Illustrative models are shown in Fig. 2.5 and the results from these models are summarized in Table 2.4.

2.5.2.1 Constant abundance model

The simplest approach is to adopt a *constant abundance* across the entire envelope. However, with this approach, and within the framework of the adopted source model, it is not possible to simultaneously reproduce all line intensities. This was already shown by Jørgensen et al. (2005c). For lower abundances it is possible to reproduce the lower-*J* lines, while higher abundances are required for higher-*J* lines. In Fig. 2.6, the C^{18}O spec-

tra of a constant-abundance profile are shown for an abundance of X_0=1.4×10^{-7}, together with the observed spectra of IRAS 2A. Based on these results, the constant-abundance profile is ruled out for all three sources.

2.5.2.2 Anti-jump abundance models

The *anti-jump model* is commonly adopted in models of pre-stellar cores without a central heating source (e.g., Bergin & Snell 2002, Tafalla et al. 2004). Following Jørgensen et al. (2005c), an anti-jump abundance profile was employed by varying the desorption density, n_{de}, and inner abundance X_{in}=X_D in order to find a fit to our observed lines. Here, the outer abundance X_0 was kept high at 5.0×10^{-7} corresponding to a ^{12}CO abundance of 2.4×10^{-4} for ^{16}O/^{18}O=550 as was found appropriate for the case of IRAS 2A by Jørgensen et al. (2005c). This value is consistent with the CO/H$_2$ abundance ratio determined by Lacy et al. (1994) for dense gas without CO freeze-out.

The best fit to the three lowest C^{18}O lines (1–0, 2–1 and 3–2) is consistent with that found by Jørgensen et al. (2005c), corresponding to n_{de}=7×10^4 cm^{-3} and X_D=3×10^{-8} (CO abundance of 1.7×10^{-5}). In the χ^2 fits, the calibration uncertainty of each line (ranging from 20 to 30%) is taken into account. These modeled spectra are overplotted on the observed spectra in Fig. 2.6 as the blue lines, and show that the anti-jump profile fits well the lower-J lines but very much underproduces the higher-J lines.

The value of X_0 was verified a posteriori by keeping n_{de} at two different values of 3.4×10^4 and 7×10^4. This is illustrated in Fig. 2.7 where the χ^2 contours show that for both values of n_{de}, the best-fit value of X_0 is ~5×10^{-7}, the value also found in Jørgensen et al. (2005c). The χ^2 contours have been calculated from the lower-J lines only, as these are paramount in constraining the value of X_0. Different χ^2 plots were made, where it was clear that higher-J lines only constrain X_D, as expected. The effect of n_{de} is illustrated in Fig. 2.8 for the two values given above.

2.5.2.3 Drop-abundance profile

In order to fit the higher-J lines, it is necessary to employ a *drop-abundance* structure in which the inner abundance X_{in} increases above the ice evaporation temperature T_{ev} (Jørgensen et al. 2005c). The abundances X_D and X_0 for $T < T_{ev}$ are kept the same as in the anti-jump model, but X_{in} is not necessarily the same as X_0. In order to find the best-fit parameters for the higher-J lines, the inner abundance X_{in} and the evaporation temperature T_{ev} were varied. The χ^2 plots (Fig. 2.9, left panel) show best-fit values for an inner abundance of X_{in} = 1.5×10^{-7} and an evaporation temperature of 25 K (consistent with the laboratory values), although the latter value is not strongly constrained. These parameters fit well the higher-J C^{18}O 6–5 and 9–8 lines (Fig. 2.6). The C^{18}O 5–4 line is underproduced in all models, likely because the larger HIFI beam picks up extended emission from additional dense material to the northeast of the source seen in BIMA
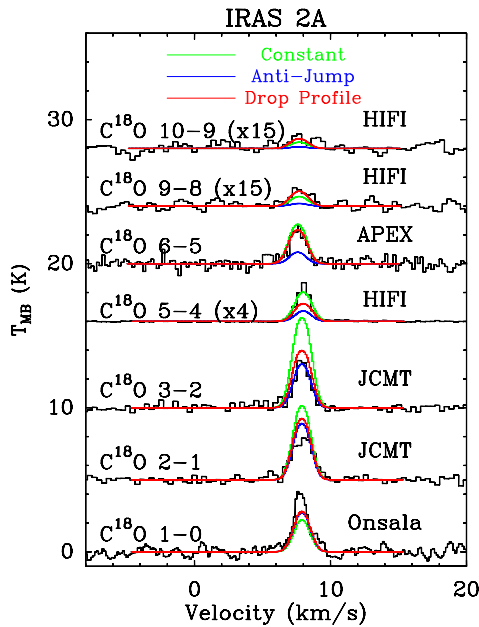
Figure 2.6 – Best fit constant (green), anti-jump (blue) and drop abundance (red) RATRAN models overplotted on the observed spectra. All spectra refer to single pointing observations. The calibration uncertainty for each spectrum is around 20–30% and is taken into account in the χ^2 fit. See Table 2.4 for parameters.
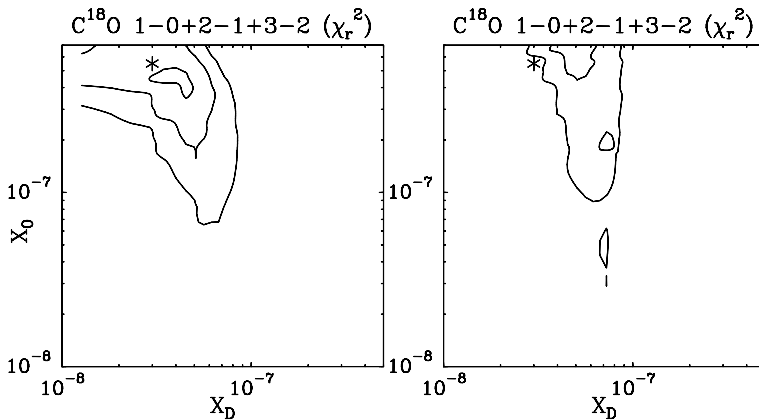
Figure 2.7 – The χ^2 plots for the anti-jump profiles where X_0 and X_D values are varied. *Right:* for $n_{de}=7\times10^4$ and *left:* for $n_{de}=3.4\times10^4$ cm^{-3}. The asterisk indicates the value for Jørgensen et al. (2005c) used here. Contours are plotted at the 2σ, 3σ, and 4σ confidence levels (*left*) and 3σ and 4σ confidence levels (*right*).

C^{18}O 1–0 (Volgenau et al. 2006) map.

Because the results do not depend strongly on T_{ev}, an alternative approach is to keep
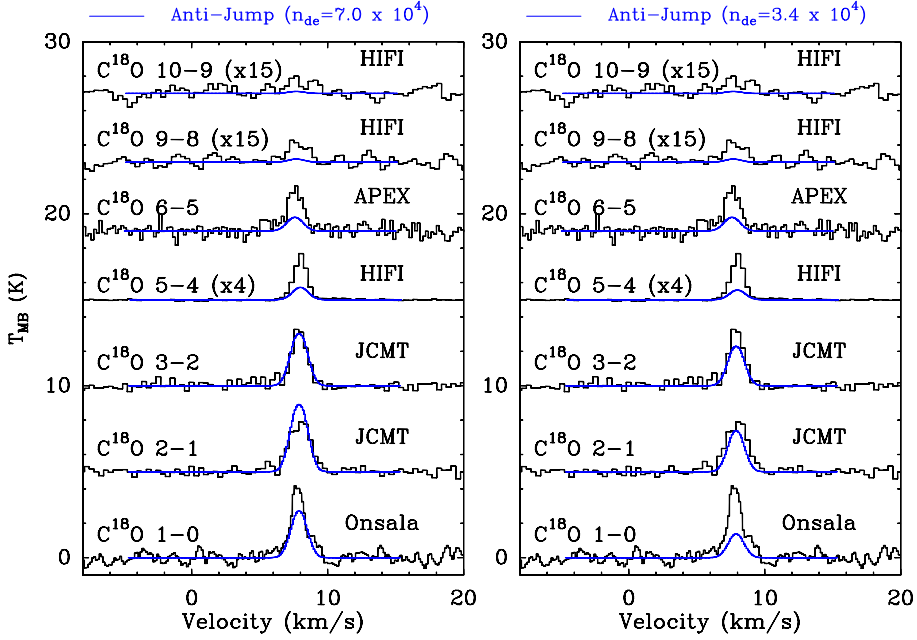
Figure 2.8 – The IRAS 2A spectra for the X_0 and X_D parameters corresponding to the values in Jørgensen et al. (2005c) for different n_{de} values of 3.4×10^4 and 7×10^4 .
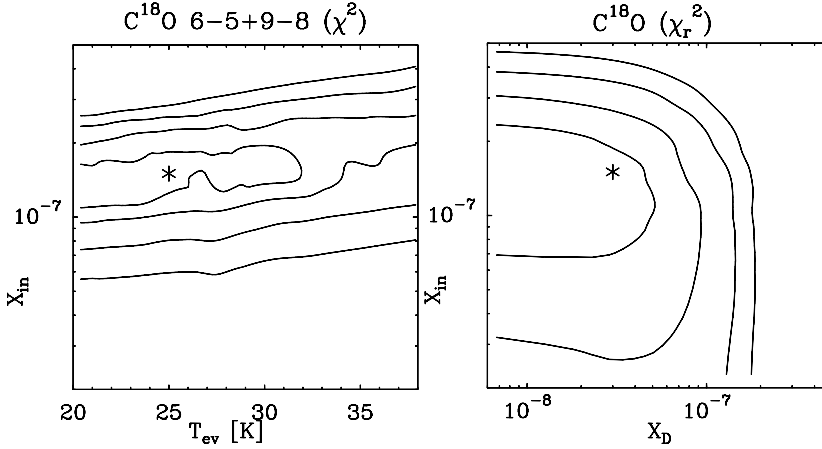
Figure 2.9 – Reduced χ^2 plots and best-fit parameters (indicated with *) for the anti-jump model fit to the lines of $C^{18}O$ 1–0, 2–1, 3–2, 6–5 and 9–8 (*right*) and for the drop abundance model fit to the higher-J lines of $C^{18}O$ 6–5 and 9–8 (*left*). Contours are plotted at the 1σ, 2σ, 3σ, and 4σ confidence levels.

the evaporation temperature fixed at 25 K and vary both X_{in} and X_D by fitting both low- and high-J lines simultaneously. In this case, only an upper limit on X_D of $\sim 4 \times 10^{-8}$ is

found (Fig. 2.9, right panel), whereas the inferred value of X_{in} is the same. This figure conclusively illustrates that $X_{in} > X_D$, i.e., that a jump in the abundance due to evaporation is needed.

The above conclusion is robust within the context of the adopted physical model. Alternatively, one could investigate different physical models such as those used by Chiang et al. (2008), which have a density enhancement in the inner envelope due to a magnetic shock wall. This density increase could partly mitigate the need for the abundance enhancement although it is unlikely that the density jump is large enough to fully compensate. Such models are outside the scope of this paper. An observational test of our model would be to image the N_2H^+ 1–0 line at high angular resolution: its emission should drop in the inner $\sim$900 AU ($\sim$4") where N_2H^+ would be destroyed by the enhanced gas-phase CO.

Acknowledgements

High-J CO survey of low-mass protostars observed with Herschel-HIFI

Umut A. Yıldız, Lars E. Kristensen, Ewine F. van Dishoeck,
Irene San José-García, Agata Karska, Daniel Harsono, Mario Tafalla,
Asuncion Fuente, Ruud Visser, Jes Jørgensen, Michiel Hogerheijde

Abstract

CONTEXT: In the deeply embedded stage of star formation, protostars start to heat and disperse their surrounding cloud cores. The evolution of these sources has traditionally been traced through dust continuum spectral energy distributions (SEDs) showing that the bolometric temperature becomes higher as the envelope is dissipated and the source transits from the Class 0 to the Class I stage.

AIMS: The aim is to constrain the physical characteristics (excitation, kinematics, column density) of the warm gas in low-mass protostellar envelopes using spectrally-resolved *Herschel* data of CO and compare those with the colder gas traced by lower excitation lines. By targeting a large sample of sources, the general evolution of these characteristics from the Class 0 to I stage can be studied.

METHODS: Herschel-HIFI observations of high-J lines of ^{12}CO ^{13}CO and $C^{18}O$ (up to $J_u = 10$, E_u up to 300 K) are presented toward 26 deeply embedded low-mass Class 0 and I young stellar objects, obtained as part of the *Water in Star-forming regions with Herschel* (WISH) key program. This s the first large spectrally resolved high-J CO survey conducted for these types of sources. Complementary lower-J CO maps were also observed using ground-based telescopes such as the JCMT and APEX and convolved to matching beam sizes.

RESULTS: The ^{12}CO 10–9 line is detected for all objects and can generally be decomposed into a narrow and broad component due to the quiescent envelope and entrained outflow material, respectively. The ^{12}CO excitation temperature increases with velocity from ~80 K up to ~180 K. The median excitation temperatures for ^{12}CO, ^{13}CO and $C^{18}O$ derived from single-temperature fits to the J_u=2–10 integrated intensities are ~70 K, 48 K and 37 K, respectively, with no significant difference between Class 0 and Class I sources and no trend with M_{env} or L_{bol}. Thus, in contrast with the continuum SEDs, the spectral line energy distributions (SLEDs) do not show an evolution during the embedded stage. In contrast, the integrated line intensities of all CO isotopologs show a clear decrease with evolutionary stage as the envelope is dispersed. Models of the collapse and evolution of protostellar envelopes reproduce well the $C^{18}O$ results, but underproduce the ^{13}CO and ^{12}CO excitation temperatures, due to lack of UV heating and outflow components in those models. The H_2O $1_{10} - 1_{01}$/CO 10–9 intensity ratio does not change significantly with velocity, in contrast with the H_2O/CO 3–2 ratio, indicating that CO 10–9 is the lowest transition for which the line wings probe the same warm shocked gas as H_2O. Modeling of the full suite of $C^{18}O$ lines indicates an abundance profile for Class 0 sources that is consistent with a freeze-out zone below 25 K and evaporation at higher temperatures, with but some fraction of the CO transformed into other species in this cold phase. In contrast, the observations for Class I sources are consistent with a constant high CO abundance profile.

CONCLUSIONS: The combination of high spectral resolution and availability of minor isotopolog lines is crucial for a proper analysis since each CO transition and isotopolog traces multiple physical components which can only be disentangled through their kinematics. Analysis of spectrally unresolved data such as provided by SPIRE and PACS must be done with caution.

3.1   Introduction

L ow-mass stars like our Sun form deep inside collapsing molecular clouds by accreting material onto a central dense source. As the source evolves, gas and dust move from the envelope to the disk and onto the star, resulting in a decrease of the envelope mass and a shift in the peak of the continuum spectral energy distribution to shorter wavelengths (e.g., Lada 1999, André et al. 2000, Young & Evans 2005). At the same time, jets and winds from the protostar entrain material and disperse the envelope. Spectral lines at submillimeter wavelengths trace this dense molecular gas and reveal both the kinematic signature of collapse (Gregersen et al. 1997, Myers et al. 2000, Kristensen et al. 2012) as well as the high velocity gas in the outflows (Arce et al. 2007).

The most commonly used probe is CO because it is the second most abundant molecule after H_2, has a simple energy level structure, and all main isotopolog lines are readily detectable (^{12}CO, ^{13}CO, $C^{18}O$, $C^{17}O$). Because of its small dipole moment, its rotational lines are easily excited and therefore provide an excellent estimate of the gas column density and the kinetic temperature. Although low excitation lines of CO have been observed in protostars for decades (e.g., Hayashi et al. 1994, Blake et al. 1995, Bontemps et al. 1996, Jørgensen et al. 2002, Fuller & Ladd 2002, Tachihara et al. 2002, Hatchell et al. 2005), no systematic studies have been undertaken so far of the higher excitation lines which probe the warm gas ($T > 100$ K) during protostellar evolution. Ground-based observations of other molecules exist as well and show in some (but not all) low-mass sources a variety of complex organic species commonly ascribed to 'hot cores' where ices evaporate molecules back into the gas phase (e.g., van Dishoeck & Blake 1998, Ceccarelli et al. 2007). Quantifying these hot core abundances has been complicated by the lack of a good reference of the H_2 column density in this warm ≥ 100 K gas.

With the launch of the *Herschel* Space Observatory (Pilbratt et al. 2010) equipped with new efficient detectors, observations of low-mass protostars in higher-J transitions of CO have become possible. In this paper, high-J refers to the lines $J_u \geq 6$ ($E_u > 100$ K) and low-J refers to $J_u \leq 5$ ($E_u < 100$ K). The Heterodyne Instrument for Far-Infrared (HIFI; de Graauw et al. 2010) on *Herschel* offers a unique opportunity to observe spectrally resolved high-J CO lines of various isotopologs with unprecendented sensitivity (see Yıldız et al. 2010, Plume et al. 2012, for early results). Even higher transitions of CO up to $J_u = 50$ are now routinely observed with the Photoconducting Array and Spectrometer (PACS) (Poglitsch et al. 2010) and the Spectral and Photometric Imaging Receiver (SPIRE) (Griffin et al. 2010) instruments on *Herschel*, but those data are spectrally unresolved, detect mostly ^{12}CO, and probe primarily a hot shocked gas component associated with the source (e.g., van Kempen et al. 2010b, Herczeg et al. 2012, Goicoechea et al. 2012, Karska et al. 2013, Manoj et al. 2013, Green et al. 2013; subm.). To study the bulk of the protostellar system and disentangle the various physical components, velocity resolved lines of isotopologs including optically thin $C^{18}O$ are needed.

In this paper, we use *Herschel*-HIFI single pointing observations of high-J CO and its isotopologs up to the 10–9 ($E_u/k = 300$ K) transition from low-mass protostars obtained in the

"Water in Star-forming regions with *Herschel*" (WISH) key program (van Dishoeck et al. 2011). The CO lines have been obtained as complement to the large set of lines from H_2O, OH and other related molecules in a sample of ~80 low to high-mass protostars at different evolutionary stages. This study focuses on low-mass protostellar sources ($L_{bol} < 100\ L_{\odot}$) ranging from the most deeply embedded Class 0 phase to the more evolved Class I stage. The *Herschel* CO data are complemented by ground-based lower-*J* transitions.

The warm gas probed by these high-*J* CO lines is much more diagnostic of the energetic processes that shape deeply embedded sources than the low-*J* lines observed so far. Continuum data from submillimeter to infrared wavelengths show that the temperature characterizing the peak wavelength of the SED (the so-called bolometric temperature T_{bol}; Myers & Ladd 1993) increases from about 25 K for the earliest Class 0 sources to about 200–300 K for the more evolved Class I sources, illustrating the increased dust temperatures as the source evolves. At the same time, the envelope gradually decreases with evolution from ~1 $M_{\odot}$ to <0.05 $M_{\odot}$ (Shirley et al. 2000, Young & Evans 2005). Our CO data probe gas over a similar range of temperatures and masses. Hence we pose the following questions regarding the evolution of the envelope and interaction with both the outflow and immediate environment: (*i*) Does the CO line intensity decrease with evolutionary stage from Class 0 to Class I in parallel with the dust? (*ii*) Does the CO excitation change with evolutionary stage, as does the dust temperature? (*iii*) How do the CO molecular line profiles (i.e., kinematics) evolve through 2–1 up to 10–9. For example, what fraction of emission contained in the envelope and outflow components? (*iv*) What is the relative importance of the different energetic processes in the YSO environment, e.g., passive heating of the envelope, outflows, photon heating, and how is this quantitatively reflected in the lines of the three CO isotopologs? (*v*) Can our data directly probe the elusive 'hot core' and provide a column density of quiescent warm ($T > 100$ K) gas as reference for chemical studies? How do those column densities evolve from Class 0 to Class I?

To address these questions, the full suite of lines and isotopologs is needed. The ^{12}CO line wings probe primarily the entrained outflow gas. The ^{13}CO lines trace the quiescent envelope but show excess emission that has been interpreted as being due to UV-heated gas along outflow cavity walls (Spaans et al. 1995, van Kempen et al. 2009b). The $C^{18}O$ lines probe the bulk of the collapsing envelope heated by the protostellar luminosity and can be used to constrain the CO abundance structure. These different diagnostic properties of the CO and isotopolog lines have been demonstrated through early *Herschel*-HIFI results of high-*J* CO and isotopologs up to 10–9 by Yıldız et al. (2010, 2012) for three low-mass protostars and by Fuente et al. (2012) for one intermediate protostar. Here we investigate whether the conclusions on column densities, temperatures of the warm gas and CO abundance structure derived for just a few sources hold more commonly in large number of sources covering different physical characteristics and evolutionary stages.

This paper presents *Herschel*-HIFI CO and isotopolog spectra for a sample of 26 low-mass protostars. The *Herschel* data are complemented by ground-based spectra to cover as many lines as possible from $J = 2-1$ up to $J = 10-9$, providing the most complete survey

Table 3.1 – Overview of the observed transitions.

Molecule	Trans. J_u-J_l	E_u [K]	A_{ul} [s^{-1}]	Freq. [GHz]
CO	2–1	16.6	6.910×10^{-7}	230.538000
	3–2	33.19	2.497×10^{-6}	345.795989
	4–3	55.3	6.126×10^{-6}	461.040768
	6–5	116.2	2.137×10^{-5}	691.473076
	7–6	154.9	3.422×10^{-5}	806.651806
	10–9	304.2	1.006×10^{-4}	1151.985452
^{13}CO	2–1	15.87	6.038×10^{-7}	220.398684
	3–2	31.7	2.181×10^{-6}	330.587965
	4–3	52.9	5.353×10^{-6}	440.765174
	6–5	111.05	1.868×10^{-5}	661.067277
	8–7	190.36	4.487×10^{-5}	881.272808
	10–9	290.8	8.797×10^{-5}	1101.349597
C^{18}O	2–1	15.81	6.011×10^{-7}	219.560354
	3–2	31.61	2.172×10^{-6}	329.330553
	5–4	79.0	1.062×10^{-5}	548.831010
	6–5	110.63	1.860×10^{-5}	658.553278
	9–8	237.03	6.380×10^{-5}	987.560382
	10–9	289.68	8.762×10^{-5}	1097.162875

Notes: The level energies, Einstein A coefficients, and line frequencies are from the LAMDA, JPL and CDMS databases (Schöier et al. 2005, Pickett et al. 2010, Müller et al. 2005).

of velocity resolved CO line profiles of these sources to date. We demonstrate that the combination of low- and high-J lines for the various CO isotopologs is needed to get the complete picture. The *Herschel* data presented here are also included in the paper by San José-García et al. (2013) comparing high-J CO from low- to high-mass YSOs.

The outline of the paper is as follows. In Section 3.2, the observations and the telescopes used to obtain the data are described. In Section 3.3, the *Herschel* and complementary lines are presented and a decomposition of the line profiles is made. In Section 3.4, the data for each of the CO isotopologs are analyzed, probing the different physical components. Rotational excitation diagrams are constructed, column densities and abundances are determined and kinetic temperatures in the entrained outflow gas are constrained. The evolution of these properties from the Class 0 to the Class I sources is studied and compared with evolutionary models. Section 3.7 summarizes the conclusions from this work.

3.2   Observations and complementary data

An overview of observed spectral lines with their upper level energies, Einstein A coefficients, and rest frequencies are presented in Table 3.1. The selection of the sources and their characteristics are described in van Dishoeck et al. (2011) and Kristensen et al.

(2012) together with the targeted coordinates. In total, 26 low-mass young stellar objects were observed in CO of which 15 are Class 0 and 11 Class I sources, with the boundary taken to be at $T_{\rm bol}$ = 70 K (Myers & Ladd 1993, Chen et al. 1995). In terms of envelope mass, the boundary between the two classes is roughly at 0.5 $M_\odot$ (Jørgensen et al. 2002). All Class I sources have been vetted to be truly embedded 'Stage I' sources cf. Robitaille et al. (2006) and not Class II edge-on disks or reddened background stars (van Kempen et al. 2009c,d). Throughout the paper, Class 0 sources are marked as red, and Class I sources are marked as blue in the figures. In addition to *Herschel*-HIFI spectra, data come from the 12-m sub-mm Atacama Pathfinder Experiment Telescope, APEX[1] at Llano de Chajnantor in Chile, and the 15-m James Clerk Maxwell Telescope, JCMT[2] at Mauna Kea, Hawaii. The overview of all the observations can be found in Table 3.9 (in the Additional Materials).

All data were acquired on the $T_{\rm A}^*$ antenna temperature scale, and were converted to main-beam brightness temperatures $T_{\rm MB} = T_{\rm A}^*/\eta_{\rm MB}$ by using the beam efficiencies ($\eta_{\rm MB}$) stated in each of the source Tables C.(1–26) in the Additional Materials.

Herschel: Spectral line observations of ^{12}CO 10–9, ^{13}CO 10–9, $C^{18}O$ 5–4, 9–8 and 10–9 were obtained with HIFI as part of the WISH guaranteed time key program on *Herschel*. Single pointing observations at the source positions were carried out between March 2010 and October 2011. An overview of the HIFI observations for each source is provided in Table 3.8 (in the Additional materials) with their corresponding *Herschel* Science Archive (HSA) obsids. The lines were observed in dual-beam switch (DBS) mode using a switch of 3′. The ^{12}CO 10–9 line was the only line targeted as a stand alone integration (10 min on + off, including overheads). The isotopolog CO transitions were observed in combination with the water lines: ^{13}CO 10–9 with H_2O 1_{11}–0_{00} (40 min); $C^{18}O$ 5–4 with $H_2^{18}O$ 1_{10}–1_{01} (60 min); $C^{18}O$ 9–8 with H_2O 2_{02}–1_{11} (20 min); and $C^{18}O$ 10–9 with H_2O 3_{12}–3_{03} (30 min or 5 hours). Only a subset of the H_2O lines were observed toward all Class I sources and therefore $C^{18}O$ 5–4 and part of the isotopolog CO 10–9 data are missing for these sources. For $C^{18}O$ 9–8, IRAS 2A, IRAS 4A, IRAS 4B, Elias 29, and GSS30 IRS1 were observed in very deep integrations for 5 hours in the open-time program OT1_rvisser_2 (PI: R. Visser). Also, the $C^{18}O$ 5–4 lines have very high S/N because of the long integration on the $H_2^{18}O$ line. Thus, the noise level varies per source and per line.

The *Herschel* data were taken using the wide-band spectrometer (WBS) and high-resolution spectrometer (HRS) backends. Owing to the higher noise ranging from a factor of 1.7 up to 4.7 of the HRS compared with the WBS, mainly WBS data are presented here except for the narrow $C^{18}O$ 5–4 lines where only the HRS data are used. The HIFI beam sizes are ~20″ (~4000 AU for a source at ~200 pc) at 1152 GHz and 42″ (~8400 AU) at 549 GHz.

---

[1] This publication is based on data acquired with the Atacama Pathfinder Experiment (APEX). APEX is a collaboration between the Max-Planck-Institut für Radioastronomie, the European Southern Observatory, and the Onsala Space Observatory.

[2] The JCMT is operated by The Joint Astronomy Centre on behalf of the Science and Technology Facilities Council of the United Kingdom, the Netherlands Organisation for Scientific Research, and the National Research Council of Canada.

The typical spectral resolution ranges from 0.68 km s^{-1} (band 1) to 0.3 km s^{-1} (band 5) in WBS, and 0.11 km s^{-1} (band 1) in HRS. Typical rms values range from 0.1 K for ^{12}CO 10-9 line to 9 mK for C^{18}O 10-9 in the longest integration times.

Data processing started from the standard HIFI pipeline in the *Herschel* Interactive Processing Environment (HIPE[3]) ver. 8.2.1 (Ott 2010), where the V_{LSR} precision is of the order of a few m s^{-1}. Further reduction and analysis were performed using the GILDAS-CLASS[4] software. The spectra from the H- and V-polarizations were averaged to obtain better S/N. In some cases a discrepancy of 30% or more was found between the two polarizations, in which case only the H band spectra were used for analysis. These sources are indicated in Tables A.(1–26) in the Appendix. Significant emission contamination from one of the reference position was found at the ^{12}CO 10–9 observation of IRAS 2A and IRAS 4A. In that case, only one reference position, which was clean, was used in order to reduce the data. On the other hand, even though the pointing accuracy is $\sim 2''$, the H- and V-polarizations have slightly shifted pointing directions (Band 1: $-6''.2$, $+2''.2$; Band 4: $-1''.3, -3''.3$; Band 5: $0''.0, +2''.8$), which may give rise to different line profiles in strong extended sources (Roelfsema et al. 2012). No corrections were made for these offsets. The HIFI beam efficiencies are 0.76, 0.74, and 0.64 for bands 1, 4, and 5, respectively (Roelfsema et al. 2012).

APEX: Maps of the ^{12}CO 6–5, 7–6 and ^{13}CO 6–5 lines over a few arcmin region were observed with the CHAMP$^+$ instrument (Kasemann et al. 2006, Güsten et al. 2008) at the APEX telescope for all sources visible from Chajnantor, whereas ^{13}CO 8–7 and C^{18}O 6–5 lines were obtained for selected objects in staring mode. The CHAMP$^+$ instrument consists of two heterodyne receiver arrays, each with seven pixel detector elements for simultaneous operations in the 620–720 GHz and 780–950 GHz frequency ranges. The APEX beam sizes correspond to $8''$ (~ 1600 AU for a source at 200 pc) at 809 GHz and $9''$ (~ 1800 AU) at 691 GHz. A detailed description of the instrument and observations of several sources in the current sample have been presented in van Kempen et al. (2009a,b,c), Yıldız et al. (2012) and the remaining maps will be given in Yıldız et al. (in prep.). Here only the data for the central source positions are considered. In addition, lower-J transitions were observed for southern sources using various receivers at APEX (van Kempen et al. 2006, 2009a,b,c).

JCMT: All sources visible from the JCMT were mapped by the HARP (Buckle et al. 2009) instrument over an area of $2' \times 2'$ in ^{12}CO, ^{13}CO and C^{18}O 3–2 transitions. HARP consists of 16 SIS detectors with 4×4 pixel elements of $15''$ each at $30''$ separation. Other 2–1 lines were observed with the single pixel RxA instrument at a beam size of $\sim 23''$ by Jørgensen et al. (2002). Part of the 2–1 observations were fetched from the JCMT public archive[5].

---

[3] HIPE is a joint development by the Herschel Science Ground Segment Consortium, consisting of ESA, the NASA Herschel Science Center, and the HIFI, PACS and SPIRE consortia.

[4] http://www.iram.fr/IRAMFR/GILDAS/

[5] This research used the facilities of the Canadian Astronomy Data Centre operated by the National Research Council of Canada with the support of the Canadian Space Agency.

Since the observations involve a number of different telescopes and frequencies, the beam sizes differ for each case. However, the maps obtained with the JCMT and APEX were resampled to a spectra with a common beam size. The native beam sizes for HIFI 10–9 and 9–8 and JCMT 2–1 transitions are 20″, 23″ and 22″, respectively. Thus, all line intensities were convolved to 20″ in order to compare the same spatial area in the analyses. The exception are a few CO 4–3 lines that are only available for a single pointing in an 11″ beam size which are indicated in the tables at the Appendix A. The 20″ beam corresponds to a diameter of 2500 AU for a source at 125 pc (closest distance), and 9000 AU for a source in 450 pc (furthest distance), so the observing beam encloses both the bulk of the dense envelope as well as outflow material. The data reduction and analysis for each source were finalized using the GILDAS-CLASS software. Calibration errors are estimated as ∼20% for the ground-based telescopes (Buckle et al. 2009, for JCMT), and ∼10% for the HIFI lines (Roelfsema et al. 2012).

The full APEX and JCMT maps are be presented in Yıldız et al. (in prep; Chapter 5) where the outflows are studied in more detail. The full set of lines for NGC 1333 IRAS 2A, IRAS 4A and IRAS 4B have also been presented in Yıldız et al. (2010, 2012) (except for the deeper $C^{18}O$ 10–9 data), but for completeness and comparison with the rest of the WISH sample, the data are included in this paper.

3.3 Results

3.3.1 CO line gallery

The ^{12}CO, ^{13}CO and $C^{18}O$ spectra from J=2–1 up to J=10–9 for each source are provided in the Appendix A. This appendix contains figures of all the observed spectra and tables with the extracted information. Summary spectra are presented in Fig. 3.1 for the CO 3–2, 10–9, ^{13}CO 10–9, $C^{18}O$ 5–4, 9–8, and 10–9 lines, respectively. Emission is detected in almost all transitions with our observing setup except some higher-J isotopolog lines discussed below. The high-J CO lines observed with *Herschel* are the first observations for these types of sources. Decomposition of line profiles is discussed in detail in San José-García et al. (2013) and is only briefly summarized below.

3.3.2 ^{12}CO lines

^{12}CO 10–9 emission is detected in all sources. Integrated and peak intensities are typically higher in the Class 0 sources compared with the Class I sources. Typical integrated intensities at the source positions range from 1 K km s^{-1} (in Oph IRS63) up to 82 K km s^{-1} (in Ser-SMM1), whereas peak intensities range from 0.6 K (in Oph IRS63) up to 9.3 K (in GSS30 IRS1). One striking result is that none of the ^{12}CO 10–9 observations show self-absorption (except for tiny dips in the Ser-SMM1 and GSS30 IRS1 spectra) whereas
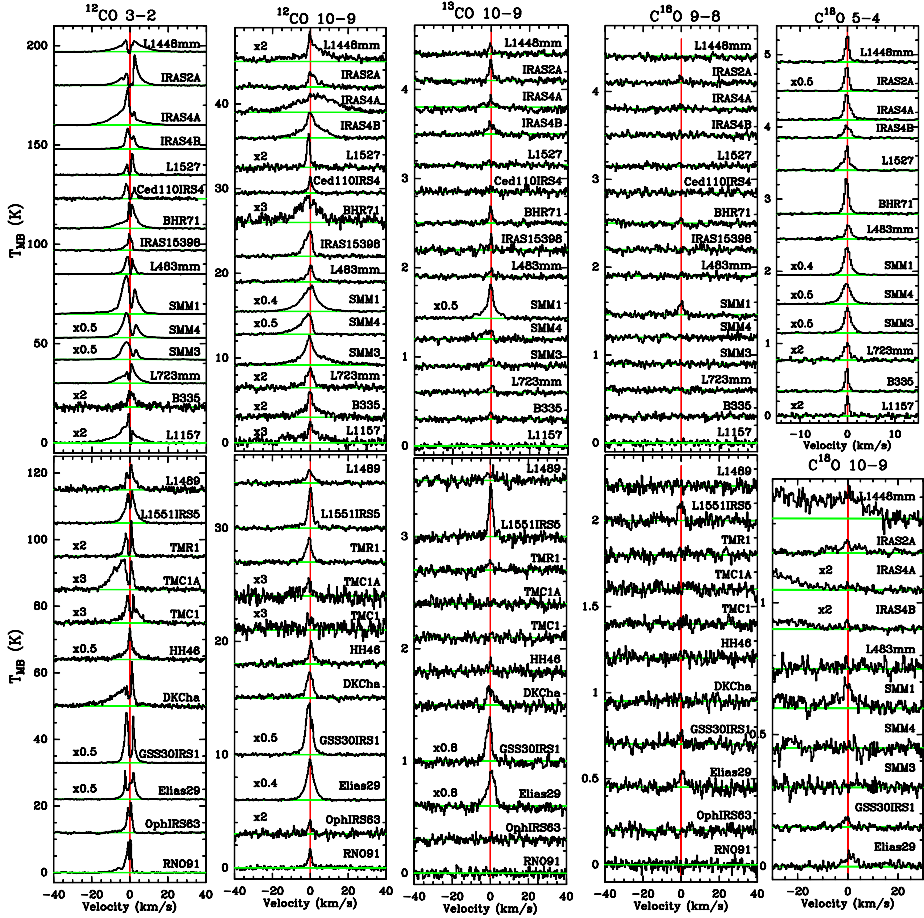
Figure 3.1 – On source CO spectra convolved to a ~20″ beam. From left to right: ^{12}CO 3–2, 10–9, ^{13}CO 10–9, $C^{18}O$ 9–8, 5–4 and 10–9, respectively. Only the CO 3–2 lines are observed with the JCMT, the rest of the data are from *Herschel*-HIFI. The spectra are plotted by shifting the source velocity (V_{LSR}) to 0 km s^{-1} (actual source velocities are given in Table 3.4). The lines are shifted vertically and the intensity scale of some sources is multiplied by a constant value for easy viewing. The top half of the figure shows the Class 0 sources whereas the bottom part displays the Class I sources. The right-most column displays the $C^{18}O$ 5–4 and $C^{18}O$ 10–9 lines for the Class 0 sources only. The latter lines are very close to the H_2O 3_{12}-3_{03} line resulting in an intensity rise on the blue side of the spectrum in some sources.
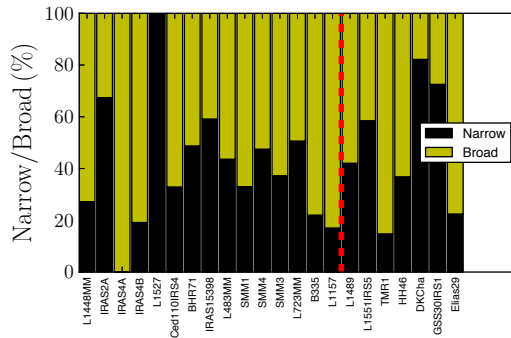
Figure 3.2 – Relative fraction of the integrated intensity of the narrow and broad components for each source. The ^{12}CO 10–9 profile decomposition is given in San José-García et al. (2013). Yellow regions indicate the broad component fraction and black the narrow component fractions. The red dashed line divides the Class 0 (left) and Class I (right) sources.

all of the CO 3–2 observations have strong self-absorption, which suggests optically thick line centers[6]. The absorption components are located at the source velocities as indicated by the peak of the low-*J* C^{18}O emission and are thus due to self-absorption from the outer envelope. Examining other available ^{12}CO transitions (lower than *J*=10–9) shows that the self-absorption diminishes with increasing *J* and disappears for all the sources except Ser-SMM1 and GSS30 IRS1 at around *J*=10–9 (see Figures A.(1–26) in Appendix).

For the ^{12}CO lines, more than two thirds of the sample can readily be decomposed into two Gaussian components with line widths of $\leq$7.5 km s^{-1} (narrow) and 11–25 km s^{-1} (broad; see San José-García et al. 2013, for details). The narrow component is due to the quiescent envelope whereas the broad component represents the swept-up outflow gas[7]. Fig. 3.2 summarizes the relative fraction of each of the components in terms of integrated intensities (also tabulated in Table 3.2). For four sources in the sample, i.e., TMC1A, TMC1, Oph IRS63, and RNO91, the profiles could not be decomposed due to low *S*/*N* in their spectra. The fraction of emission contained in the narrow component ranges from close to 0% (IRAS 4A) to nearly 100% (L1527; outflow in the plane of the sky), with a median fraction of 42%. This demonstrates that the contributions from these two components are comparable so care must be taken in interpreting spectrally unresolved data from *Herschel*-SPIRE and PACS, and, to some extent, near-IR transitions of the same molecules.

Figure 3.3 presents the averaged ^{12}CO 3–2, 10–9, and H$_2$O 1_{10}-1_{01} lines for the Class 0 and I sources in order to obtain a generic spectral structure for one type of source. To compare with the H$_2$O spectra, a similar averaging procedure was followed as in Kristensen et al. (2012), where ground state ortho-water composite spectra observed with

---

[6] The only exception is IRAS 15398 where the targeted position is off source, see Kristensen et al. (2012).

[7] The broad CO component is not necessarily the same physical component as seen in the broad H$_2$O profiles; this point will be further discussed in Sect. 3.5.3.

Table 3.2 – Relative fractions of integrated intensities calculated for broad and narrow components in ^{12}CO 10–9 lines.

Source	$\int T_{MB}dV$ (K km s^{-1})		%[a]	
	NC	BC	NC	BC
L1448MM	12.7	33.9	27	73
NGC1333-IRAS2A	6.4	3.1	67	33
NGC1333-IRAS4A	…	49.4	…	100
NGC1333-IRAS4B	5.6	23.6	19	81
L1527	4.2	…	100	…
Ced110IRS4	1.8	3.7	33	67
BHR71	7.8	8.2	49	51
IRAS15398	9.9	6.8	59	41
L483MM	4.7	6.3	44	56
Ser SMM1	26.2	53.1	33	67
Ser SMM4	31.7	35.0	47	53
Ser SMM3	9.3	15.7	37	63
L723MM	3.5	3.4	51	49
B335	2.6	9.2	22	78
L1157	1.4	6.8	17	83
L1489	2.5	3.4	42	58
L1551IRS5	8.5	6.0	59	41
TMR1	1.3	7.6	15	85
HH46	3.1	5.4	37	63
DK Cha	8.2	1.8	82	18
GSS30IRS1	31.2	11.8	73	27
Elias29	10.6	36.5	22	78
TMC1A	(1.4[b])	…	…	…
TMC1	(2.9[b])	…	…	…
Oph IRS63	(1.1[b])	…	…	…
RNO91	(5.2[b])	…	…	…

Notes: NC: Narrow Component, BC: Broad Component, [a]Relative percentages of the integrated intensities given in the 2nd and 3rd columns. [b]Due to low S/N in their spectra, profiles could not be decomposed, however, total integrated intensities are given.

Herschel-HIFI at 557 GHz were presented in a beam of 40″. In this comparison, the IRAS 15398 (Class 0), TMC1 and GSS30 IRS1 (Class I) spectra have been excluded from the averaging procedure. The CO 10–9 line of IRAS 15398 is taken at a position 15″ offset from the source position, the TMC1 spectrum was too noisy and the excitation of GSS30 IRS1 may not be representative of Class I sources (Kristensen et al. 2012). Therefore, 14 Class 0 and 9 Class I spectra are scaled to a common distance of 200 pc and averaged.

It is seen that the broad CO outflow component is much more prominent in the Class 0 than in the Class I sources (Figure 3.3). For the Class 0 sources, the 10–9 line is broader than the 3–2 lines. However, neither is as broad as the line wings seen in H_2O 557 GHz lines, for which the average H_2O spectra are taken from Kristensen et al. (2012). The comparison between CO and H_2O will be discussed further in Sect. 3.5.3.
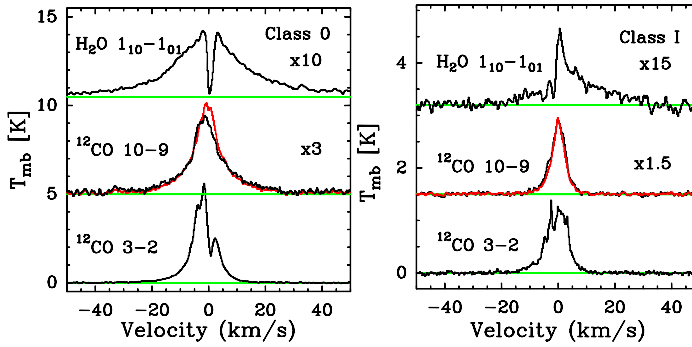
Figure 3.3 – Composite H_2O 1_{10}-1_{01}, CO 10–9 and CO 3–2 spectra of Class 0 and Class I sources averaged in order to compare the line profiles of two types of sources. All spectra are rescaled to a common distance of 200 pc, shifted to the central 0 km s^{-1} velocity, rebinned to a 0.3 km s^{-1} velocity resolution. The CO spectra refer to a 20″ beam, the H_2O spectra to a 40″ beam. The red spectra overlaid on top of the ^{12}CO 10–9 are obtained by normalizing all the spectra to a common peak temperature first and then averaging them.
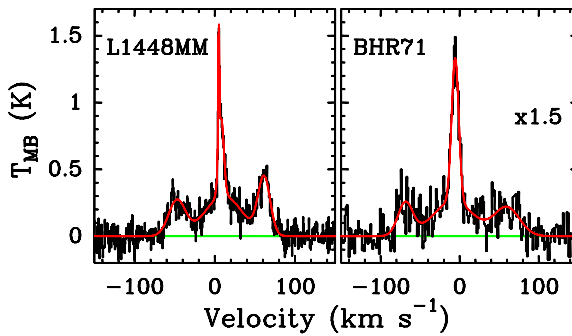
Figure 3.4 – ^{12}CO 10–9 spectra of L1448mm and BHR71, where bullet structures are shown. The green lines indicates the baseline and the red lines represent the Gaussian fits of the line profiles. Fit parameters are given in Table 3.3.

For a few sources, high velocity molecular emission features associated with shock material moving at velocities up to hundred km s^{-1} have been observed (Bachiller et al. 1990, Tafalla et al. 2010). For species like SiO, their abundance is increased due to shock-induced chemistry (Bachiller & Perez Gutierrez 1997, Bourke et al. 1997). These Extremely High Velocity (EHV) components (or 'bullet' emission) are also visible in the higher-*J* CO transitions, as well as in lower-*J* transitions, but the contrast in emission between bullet and broad outflow emission is greatly enhanced at higher frequencies. Bullets are visible specifically in CO 6–5 and 10–9 data toward L1448mm and BHR71 at ∼±60 km s^{-1} (see Fig. 3.4 for the bullets and Table 3.3 for the fit parameters). These bullets are also seen in H_2O observations of the same sources, as well as other objects (Kristensen et al. 2011, 2012).

Table 3.3 – Fit parameters obtained from the bullet sources.

Source	$\int T_{MB}dV$ [K km s^{-1}]	T_{peak} [K]	FWHM [km s^{-1}]	$\int T_{MB}dV$ [K km s^{-1}]	T_{peak} [K]	FWHM [km s^{-1}]
	EHV-B			Broad		
L1448MM	6.9	0.26	24.6	17.5	0.30	54.3
BHR71	4.2	0.16	25.2	10.8	0.18	55.6
	Narrow			EHV-R		
L1448MM	6.5	1.10	7.5	8.1	0.43	17.8
BHR71	4.2	0.71	10.0	3.9	0.14	27.1

3.3.3 ^{13}CO lines

^{13}CO emission is detected in all sources except for the 10–9 transition toward Oph IRS63, RNO91, TMC1A, and TMR1. The 10–9 integrated and peak intensities are higher in Class 0 sources compared with the Class I sources. Typical integrated intensities range from 0.1 K (L1527) up to 3.4 K km s^{-1} (Ser-SMM1). Peak intensities range from 0.1 K (L1448 MM, L1527) up to 0.4 K (Ser-SMM1). All 10–9 lines can be fitted by a single Gaussian except for Ser-SMM1 and IRAS 4A where two Gaussians are needed.

3.3.4 C^{18}O lines

C^{18}O emission is detected in all sources up to J=5–4. The 9–8 line is seen in several sources, mostly Class 0 objects (BHR71, IRAS 2A, IRAS 4A, IRAS 4B, Ser-SMM1, L1551 IRS5). The C^{18}O 10–9 line is detected after 5-hour integrations in IRAS 2A, IRAS 4A, IRAS 4B, Elias 29, GSS30 IRS1, and Ser-SMM1, with integrated intensities ranging from 0.05 (in IRAS 4A) up to 0.6 K km s^{-1} (Ser-SMM1). Peak intensities range from 0.02 K up to 0.07 K for the same sources. The rest of the high-J C^{18}O lines do not show a detection but have stringent upper limits. The high S/N and high spectral resolution C^{18}O 5–4 data reveal a weak, broad underlying component even in this minor isotopolog for several sources. The resulting decomposition into a narrow and broad Gaussian component is presented in San José-García et al. (2013).

The availability of transitions from 2–1 to 10–9 for many sources in optically thin C^{18}O lines also gives an opportunity to revisit source velocities, V_{LSR} that were previously obtained from the literature. Table 3.4 presents the results with nine sources showing a change in V_{LSR}, compared with values listed in van Dishoeck et al. (2011) ranging from 0.2 km s^{-1} (IRAS 4A) up to 1.0 km s^{-1} (L1551-IRS5).

Table 3.4 – Source parameters.

Source	d	$V_{\rm LSR}{}^a$	$L_{\rm bol}{}^b$	$T_{\rm bol}{}^b$	$M_{\rm env\ (10K)}{}^c$	$n_{\rm 1000AU}{}^{c,d}$	$n_{20''}{}^{c,e}$
	[pc]	[km s^{-1}]	[$L_\odot$]	[K]	[$M_\odot$]	[10^5 cm^{-3}]	[10^5 cm^{-3}]
L1448-MM	235	+5.2	9.0	46	3.9	39	11
NGC1333-IRAS2A	235	+7.7	35.7	50	5.1	17	4.0
NGC1333-IRAS4A	235	+7.0	9.1	33	5.6	67	15
NGC1333-IRAS4B	235	+7.1	4.4	28	3.0	57	17
L1527	140	+5.9	1.9	44	0.9	8.1	6.0
Ced110-IRS4	125	+4.2	0.8	56	0.2	3.9	2.8
BHR71	200	−4.4	14.8	44	2.7	18	5.4
IRAS15398	130	+5.1	1.6	52	0.5	16	11
L483mm	200	+5.2	10.2	49	4.4	5.1	2.8
Ser-SMM1	230	+8.5	30.4	39	16.1	41	14
Ser-SMM4	230	+8.0	1.9	26	2.1	54	23
Ser-SMM3	230	+7.6	5.1	38	3.2	11	5.5
L723	300	+11.2	3.6	39	1.3	8.0	2.2
B335	250	+8.4	3.3	36	1.2	15	4.3
L1157	325	+2.6	4.7	46	1.5	20	2.9
L1489	140	+7.2	3.8	200	0.2	1.9	1.2
L1551-IRS5	140	+6.2	22.1	94	2.3	12	6.4
TMR1	140	+6.3	3.8	133	0.2	2.1	1.2
TMC1A	140	+6.6	2.7	118	0.2	2.2	1.3
TMC1	140	+5.2	0.9	101	0.2	1.8	1.2
HH46-IRS	450	+5.2	27.9	104	4.4	12	1.1
DK Cha	178	+3.1	35.4	569	0.8	9.2	3.7
GSS30-IRS1	125	+3.5	13.9	142	0.6	1.7	1.1
Elias 29	125	+4.3	14.1	299	0.3	0.8	0.6
Oph-IRS63	125	+2.8	1.0	327	0.3	6.9	5.0
RNO91	125	+0.5	2.6	340	0.5	3.3	2.4

Notes: Sources above the horizontal line are Class 0, sources below are Class I. ^{a}Obtained from ground-based C^{18}O or C^{17}O observations. ^{b}Measured using *Herschel*-PACS data from the WISH and DIGIT key programmes (Karska et al. 2013, Green et al. 2013; subm.). ^{c}Determined from DUSTY modeling of the sources; see Kristensen et al. (2012). ^{d}Density at 1000 AU. ^{e}Density at a region of 20$''$ diameter.
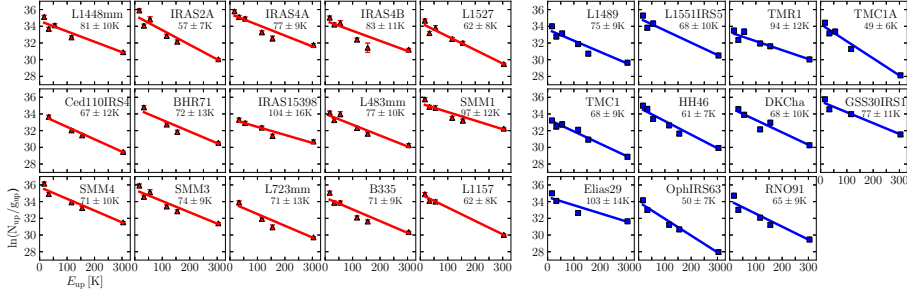
Figure 3.5 – Rotational diagrams for ^{12}CO lines using the integrated intensities. All data are convolved to a 20″ beam and each plot shows the best single temperature fit to the observed transitions (see also Table 3.5). *Left* panel (red): Class 0 sources; *right* panel (blue): Class I sources.
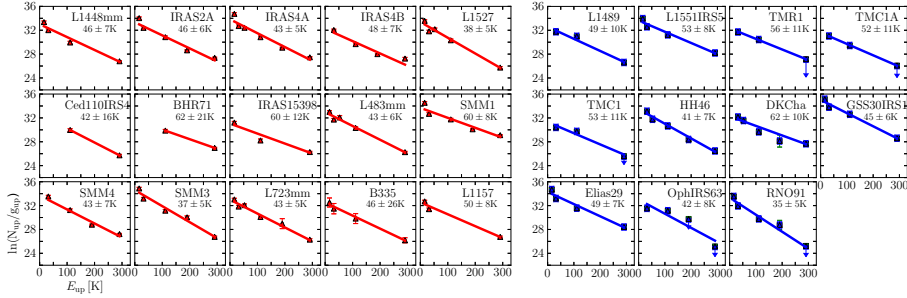
Figure 3.6 – Same as Fig. 3.5 but for ^{13}CO lines.
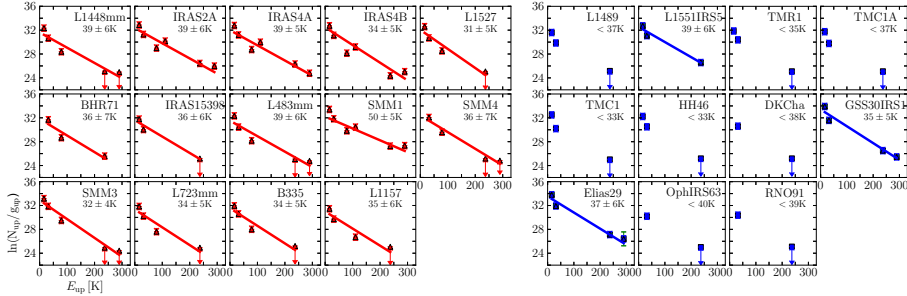
Figure 3.7 – Same as Fig. 3.5 but for C^{18}O lines.

3.4   Rotational diagrams

To understand the origin of the CO emission, rotational diagrams provide a useful starting point to constrain the temperature of the gas. In our sample, we have CO and isotopolog emission lines of all sources from J=2–1 up to 10–9 with upper level

energies from E_{up}=5 K to ~300 K. Rotational diagrams are constructed assuming that the lines can be characterized by a single excitation temperature T_{ex}, also called rotational temperature T_{rot}. Typically, the isotopolog ^{13}CO and C^{18}O lines are optically thin, as are the ^{12}CO line wings (van Kempen et al. 2009b, Yıldız et al. 2012), so no curvature should be induced in the excitation diagrams due to optical depth effects. However, the low-J ^{12}CO line profiles have strong self-absorption and their cores are optically thick, affecting the analysis (see Sect. 3.4.3). Because the C^{18}O 5–4 line has a beam size of 42″ and may thus contain unrelated cloud material, its uncertainty is artificially enhanced from 10% to 20% in order to reduce its weight in the fit calculations.

Using the level energies, Einstein A coefficients and line frequencies from Table 3.1 and the cited databases, rotational diagrams are constructed where the column density for each level is plotted against its level energy. This temperature T_{rot} is basically defined from the Boltzmann equation

$$\frac{N_{\mathrm{u}}}{N_{\mathrm{l}}} = \frac{g_{\mathrm{u}}}{g_{\mathrm{l}}}e^{(-\Delta E/kT_{\mathrm{rot}})}, \tag{3.1}$$

where N_{u} and N_{l} are the column densities in the upper and lower states, and g_{u} and g_{l} their statistical weights equal to $2J_{\mathrm{u}} + 1$ and $2J_{\mathrm{l}} + 1$, respectively. The CO column densities in individual levels are obtained from

$$\frac{N_{\mathrm{u}}}{g_{\mathrm{u}}} = \beta\frac{(\nu[\mathrm{GHz}])^2\,W[\mathrm{K\,km\,s^{-1}}]}{A_{\mathrm{ul}}[\mathrm{s^{-1}}]\,g_{\mathrm{u}}}, \tag{3.2}$$

where $\beta = 1937$ cm^{-2} and $W = \int T_{\mathrm{mb}}dV$ is the integrated intensity of the emission line.

The slope of the linear fit to the observations, $-(1/T_{\mathrm{rot}})$, gives the rotational temperature, whereas the y-intercept gives the total column density $ln(N_{\mathrm{total}}/Q(T_{\mathrm{rot}}))$ where $Q(T_{\mathrm{rot}})$ is the partition function referenced from CDMS for the temperature given by the fit.

The total integrated intensity W for each line is measured over the entire velocity range out to where line wings become equal to the 1σ noise. In L1448mm and BHR71, the bullet emission is not included in the intensity calculation. In IRAS 2A, the emission in the 10–9 line is corrected for emission at one of the reference positions, which results in a higher T_{rot} compared with Yıldız et al. (2012).

3.4.1 Rotational diagram results

In Figs. 3.5, 3.6 and 3.7, rotational diagrams are depicted for the ^{12}CO, ^{13}CO and C^{18}O lines, respectively. Extracted excitation temperatures and column densities are presented in Table 3.5; ^{12}CO column densities are not provided because they are affected by optical depth effects. In all sources, a single temperature component from J=2–1 up to 10–9 transitions provides a decent fit. Curvature is present for a number of sources which will be discussed in Sect. 3.4.3. The derived ^{12}CO rotational temperatures range from ~50 K to ~100 K. The median temperatures for both Class 0 and Class I sources are similar, T_{rot} = 71 K and 68 K, respectively.
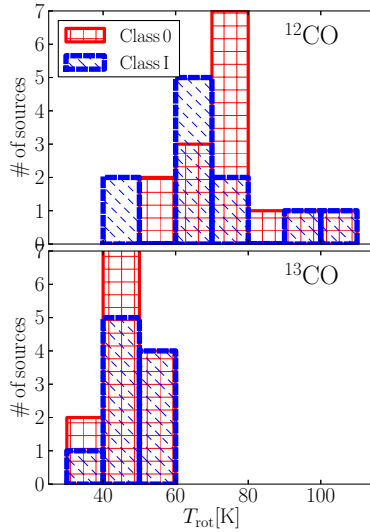
Figure 3.8 – Distribution of rotation temperatures ($T_{\rm rot}$) calculated from ^{12}CO and ^{13}CO line observations. The median temperatures are listed in Table 3.6.

For ^{13}CO, the temperatures range from $T_{\rm rot}$ ~35 K to ~60 K, with a median $T_{\rm rot}$=46 K and 49 K for Class 0 and Class I sources, respectively. For C^{18}O, the median temperature for Class 0 sources is $T_{\rm rot}$ = 36 K. For Class I sources, either lack of observational data or non-detections make it harder to obtain an accurate temperature. Nevertheless, upper limits are still given. The median $T_{\rm rot}$ for the sources with ≥3 data points is 37 K. A summary of the median rotational temperatures is given in Table 3.6. Fig. 3.8 presents the ^{12}CO and ^{13}CO temperatures in histogram mode for the Class 0 and I sources, with no statistically significant differences between them. Note that this analysis assumes that all lines have a similar filling factor in the ~20″ beam; if the higher-J lines would have a smaller filling factor than the lower-J lines the inferred rotational temperatures would be lower limits.

For the case of Serpens-SMM1, our inferred rotational temperatures of 97±12 and 60±8 K compare well with those of 103±15 and 76±6 K found by Goicoechea et al. (2012) from *Herschel*-SPIRE data for ^{12}CO and ^{13}CO, respectively. The SPIRE values were obtained from a fit to the J_u=4–14 levels, with the beam changing by a factor of ~3 from ~47″ to ~13″ across the ladder.

The ^{12}CO and ^{13}CO 2–1 lines included in Figs. 3.5 and 3.6 are observed in a similar ~20″ beam as the higher transitions, but they most likely include cold cloud emission as well. Removing those lines from the rotational diagrams increases the temperatures around 10-15 %. Similarly, the C^{18}O 5–4 line is observed in a 42″ beam and removing this line from the fit increases the temperatures around 5–10%, which is still within the error bars. In practice, we did not discard the C^{18}O 5–4 observations but increased their uncertainty to
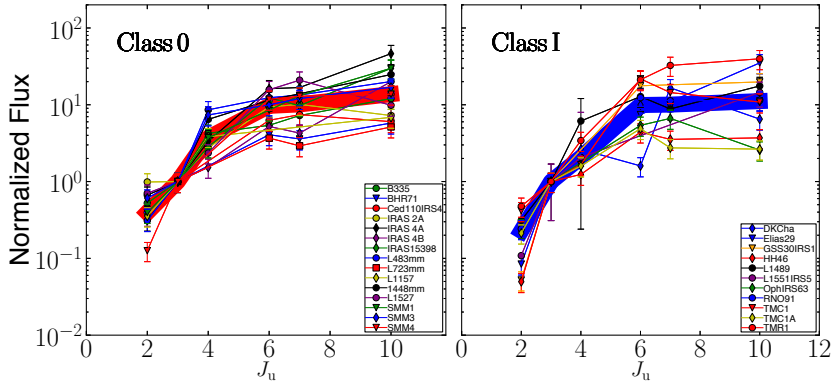
Figure 3.9 – ^{12}CO spectral line energy distribution (SLED) for the observed transitions. All of the fluxes are normalized to their own CO 3-2 flux for Class 0 (*left*) and Class I (*right*) sources separately. The beams are ~20" beam. The thick lines are the median values of each transitions.

Table 3.5 – Extracted rotational temperatures and column densities

Source	Rotational Temperature [K]			Column Density^a [10^{21} cm^{-2}]		Kinetic Temperature^b [K]	
	^{12}CO	^{13}CO	C^{18}O	^{13}CO	C^{18}O	Blue Wing	Red Wing
L1448-MM	81 ± 10	46 ± 7	39 ± 6	5.0 ± 0.7	4.4 ± 0.6	60–75	100–200
NGC1333-IRAS2A	57 ± 7	46 ± 6	39 ± 6	6.8 ± 0.9	9.2 ± 1.3	. . .	. . .
NGC1333-IRAS4A	77 ± 9	43 ± 5	39 ± 5	10.6 ± 1.3	6.5 ± 0.8	70–80	80–110
NGC1333-IRAS4B	83 ±11	48 ± 7	34 ± 5	2.4 ± 0.4	9.0 ± 1.4	110–170	110–280
L1527	62 ± 8	38 ± 5	31 ± 5	6.0 ± 0.8	5.5 ± 0.8	80–130	80–110
Ced110-IRS4	67 ±12	42 ± 16	. . .	3.0 ± 1.1	. . .	. . .	. . .
BHR71	72 ±13	62 ± 21	36 ± 7	1.7 ± 0.6	5.0 ± 1.0	75–105	70–140
IRAS15398	104 ±16	60 ± 12	36 ± 6	0.9 ± 0.2	4.0 ± 0.7	. . .	. . .
L483	77 ±10	43 ± 6	39 ± 6	4.5 ± 0.6	4.0 ± 0.6	105–300	100–240
Ser SMM1	97 ±12	60 ± 8	50 ± 5	12.7 ± 1.7	10.1 ± 1.1	90–120	100–230
Ser SMM4	71 ± 9	43 ± 7	36 ± 7	9.2 ± 1.6	8.8 ± 1.6	75–120	50–120
Ser SMM3	74 ± 9	37 ± 5	32 ± 4	19.8 ± 2.8	12.7 ± 1.8	75–175	80–260
L723	71 ±13	43 ± 5	34 ± 5	4.6 ± 0.6	2.8 ± 0.4	. . .	. . .
B335	71 ± 9	46 ± 6	34 ± 5	3.0 ± 1.7	3.6 ± 0.5	. . .	. . .
L1157	62 ± 8	50 ± 8	35 ± 6	3.4 ± 0.5	2.1 ± 0.3	75–130	85–120
L1489	75 ± 9	49 ± 10	<37	3.5 ± 0.7	<3.7	. . .	. . .
L1551-IRS5	68 ±10	53 ± 8	39 ± 6	10.7 ± 1.5	11.3 ± 1.8	70–130	70–130
TMR1	94 ±12	56 ± 11	<35	3.1 ± 0.6	< 4.9	. . .	. . .
TMC1A	49 ± 6	52 ± 11	<37	1.4 ± 0.3	<3.4	. . .	. . .
TMC1	68 ± 9	53 ± 11	<33	1.1 ± 0.2	<6.0	. . .	. . .
HH46-IRS	61 ±7	41 ± 7	<33	7.1 ± 1.1	<8.0	100–130	105–300
DK Cha	68 ±10	62 ± 10	<38	3.2 ± 0.5	<3.6	. . .	. . .
GSS30-IRS1	77 ± 11	45 ± 6	35 ± 5	37.0 ± 5.1	24.0 ± 3.7	160–300	130–240
Elias 29	103 ±14	49 ± 7	37 ± 6	19.1 ± 2.7	28.1 ± 4.4	340–400	340–400
Oph-IRS63	50 ± 7	42 ± 8	<40	4.6 ± 0.9	<2.4	. . .	. . .
RNO91	65 ± 9	35 ± 5	<39	5.2 ± 0.8	<2.9	. . .	. . .

Notes: Rotational temperatures and column densities calculated from ^{12}CO, ^{13}CO and C^{18}O observations. Kinetic temperatures calculated from blue and red line wings. ^{a}In H$_2$ column densities. Derived using a constant abundance ratio of CO/H$_2$=10^{-4}. ^{b}Obtained from CO 10–9/3–2 line intensity ratios.

Table 3.6 – Median rotational temperatures and colum densities of Class 0 and Class I sources calculated from ^{12}CO, ^{13}CO and C^{18}O.

	Rotational Temperature [K]			Column Density^a [10^{21} cm^{-2}]	
	^{12}CO	^{13}CO	C^{18}O	^{13}CO	C^{18}O
Class 0	71±13	46±6	36±7	4.6±0.6	5.2±0.9
Class I	68±9	49±10	. . .	4.6±0.9	. . .

Notes: Median's error is taken as global error value. ^{a}Derived using a constant abundance ratio of CO/H$_2$=10^{-4}.

give them less weight in the calculations.

Beam-averaged column densities of H$_2$ are given in Table 3.5. The ^{13}CO and C^{18}O column densities are converted to ^{12}CO column densities by using ^{12}C/^{13}C = 65 (based on Langer & Penzias 1990, Vladilo et al. 1993) and ^{16}O/^{18}O = 550 (Wilson & Rood 1994) and then using CO/H$_2$ = 10^{-4} to obtain the H$_2$ column density. The median H$_2$ column densities for Class 0 sources are 4.6×10^{21} cm^{-2} and 5.2×10^{21} cm^{-2} for ^{13}CO and C^{18}O data, respectively. For Class I sources the value is 4.6×10^{21} cm^{-2} for ^{13}CO, with the caveat that only few Class I sources have been measured in C^{18}O. The agreement between the two isotopologs indicates that the lines are not strongly affected by optical depths. Since this conversion uses a CO/H$_2$ abundance ratio close to the maximum, the inferred H$_2$ column densities should be regarded as minimum values. In particular, for Class 0 sources freeze-out and other chemical processes will lower the CO/H$_2$ abundance (see §3.6) (Jørgensen et al. 2002). Thus, the actual difference in column densities between the Class 0 and I stages is larger than is shown in Table 3.5.

3.4.2 CO ladders

Spectral Line Energy Distribution (SLED) plots are another way of representing the CO ladder where the integrated flux is plotted against upper level rotational quantum number, J_{up}. In Fig. 3.9, ^{12}CO line fluxes for the observed transitions are plotted. Since the CO 3–2 lines are available for all sources, all of the fluxes are normalized to their own CO 3–2 flux. The thick blue and red lines are the median values of all sources for each transition for each Class. It is readily seen that the Class 0 and I sources in our sample have similar excitation conditions, but that the Class I sources show a larger spread at high-J and have higher error bars due to the weaker absolute intensities. Thus, although the continuum SEDs show a significant evolution from Class 0 to Class I with T_{bol} increasing from <30 K to more than 500 K, this change is not reflected in the line SLEDs. This limits the usage of CO SLEDs as an evolutionary probe. One of the explanations for this lack of evolution is that T_{bol} depends on thermal emission from both the dust in the envelope and the extincted stellar flux, whereas the SLED only traces the temperature of the gas in the envelope, but has no stellar component.
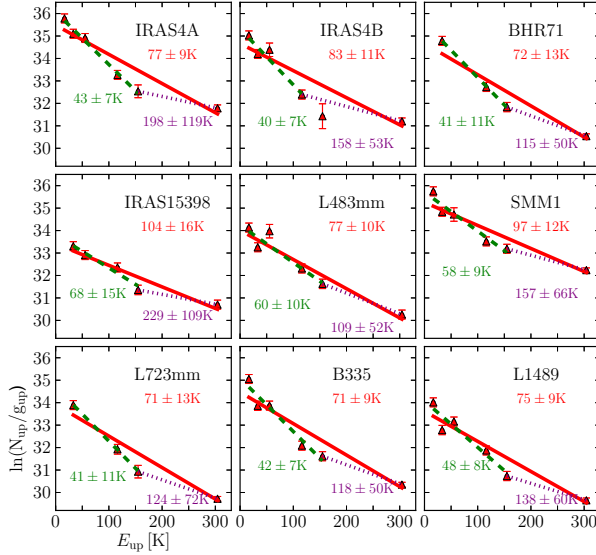
Figure 3.10 – Two temperature components fitted for selected sources to the ^{12}CO lines, from 2–1 to 7–6 (cold), from 7–6 to 10–9 (warm), and 2–1 to 10–9 (global).

3.4.3   Two temperature components?

Unresolved line observations of higher-*J* CO transitions (*J*=13 up to 50) by *Herschel*-PACS (Herczeg et al. 2012, Karska et al. 2013, Manoj et al. 2013) typically show two temperature components with ∼300 K and ∼900 K. Goicoechea et al. (2012) found three temperature components from combined SPIRE and PACS data, with the lower temperature of ∼100 K fitting lines up to J_u=14, similar to that found in our data. The question addressed here is if the higher 300 K component only appears for lines with $J_u > 10$ or whether it becomes visible in our data. One third of our sample shows a positive curvature in the ^{12}CO rotation diagrams (Fig. 3.5), specifically IRAS 4A, IRAS 4B, BHR71, IRAS 15398, L483mm, Ser-SMM1, L723mm, B335, and L1489 (see Fig. 3.10).

The curvature in ^{12}CO rotation diagrams is treated by dividing the ladder into two components, where the first fit is from 2–1 to 7–6 for the colder component and the second fit from 7–6 to 10–9 for the warmer component. The fit from 2–1 to 10–9 is named as global. The median T_{rot} is 43 K for the colder component and 138 K for the warmer component for these nine sources.

Close inspection of the SPIRE data by Goicoechea et al. (2012) shows a slight curvature for low-*J* in their cold component as well. The "two-component" decomposition is perhaps a generic feature for Class 0 low-mass protostars which implies that the CO 10–9 transition partly probes the warmer (∼300 K) component associated with the currently
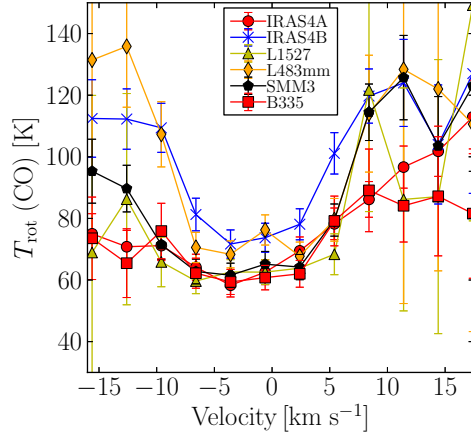
Figure 3.11 – Rotational temperatures calculated channel by channel for ^{12}CO. Each spectrum shifted to V_{LSR}=0 km s^{-1} and rebinned to 3 km s^{-1} velocity resolution.

shocked gas (Karska et al. 2013). A related explanation is that the narrow and broad components have different rotational temperatures, with the broad component being more prominent in Class 0 sources, which is consistent with the curvature primarily appearing in Class 0 sources.

3.4.4 Velocity resolved diagrams

To investigate whether the ^{12}CO narrow and broad components have different temperatures, Fig. 3.11 presents excitation temperatures calculated channel by channel for a few sources with high S/N. Each spectrum is shifted to V_{LSR}=0 km s^{-1} and rebinned to 3 km s^{-1} velocity resolution. It is obvious from Fig. 3.1 that the line wings are more prominent in the CO 10–9 transitions, specifically for Class 0 sources, as is reflected also in the increasing line widths with the increasing rotation level (see Figs. A.(1–26) in the Appendix; San José-García et al. 2013). Figure 3.11 shows that in the optically thin line wings, the excitation temperatures are a factor of 2 higher than in the line centers implying that the wings of the higher-J CO lines trace warmer material. Since the presence of self-absorption at line centers of the lower-J lines reduces their emission, the excitation temperatures at low velocities are further decreased if this absorption is properly corrected for.

Another way to illustrate the change with velocity is to look at the CO 10–9 and CO 3–2 spectra for each source as shown in Fig. 3.20 (in the Additional materials). Fig. 3.12 shows the blue and red line-wing ratios for the 14 sources with the highest S/N. For all sources, the line ratios increase with increasing velocity, consistent with Fig. 3.11.
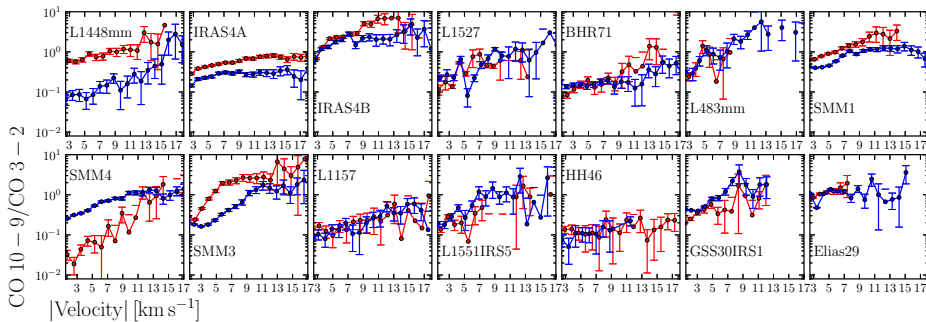
Figure 3.12 – Ratios of the CO 10–9/3–2 line wings for 14 protostars as function of velocity offset from the central emission. Spectra are shifted to V_{LSR}=0 km s^{-1}. The wings start at $\pm$2.5 km s^{-1} from V_{LSR} in order to prevent adding the central self-absorption feature in the CO 3–2 lines.

In summary, while a single rotational temperature provides a decent fit to the bulk of the CO and isotopolog data, both the ^{12}CO integrated intensity rotational diagrams and the velocity resolved diagrams indicate the presence of a second, warmer component for Class 0 sources. This warmer component is most likely associated with the broad line wings, as illustrated by the 10–9/3–2 line ratios.

3.4.5 Kinetic temperature

Having lines from low-to-high-*J* CO provides information about the physical conditions in the different parts of the envelope. The critical densities for the different transitions are n_{cr}=4.2$\times$10^5 cm^{-3}, 1.2$\times$10^5 cm^{-3}, and 2$\times$10^4 cm^{-3} for CO 10–9, 6–5 and 3–2 transitions at ∼50–100 K, using the CO collisional rate coefficients by Yang et al. (2010). For densities higher than n_{cr}, the emission is thermalized and therefore a clean temperature diagnostic, however, for lower densities the precise value of the density plays a role in the analysis. In the high density case ($n > n_{\mathrm{cr}}$), the kinetic temperature is equal to the rotation temperature. By using two different ^{12}CO lines, kinetic temperatures can be calculated if the density is known independently using the RADEX non-LTE excitation and radiative transfer program (van der Tak et al. 2007). The analysis below for CO 10–9/3–2 assumes that the emission originates from the same gas.

The resulting model line ratios are presented in Fig. 3.13 for a grid of temperatures and densities. Densities for each source are calculated from the envelope parameters determined by modeling of the submillimeter continuum emission and spectral energy distribution (Kristensen et al. 2012). A spherically symmetric envelope model with a power-law density structure is assumed (Jørgensen et al. 2002). The 20″ diameter beam covers a range of radii from ∼1250 AU (e.g., Ced110IRS4, Oph sources) up to 4500 AU (HH46) and the densities range from 5.8$\times$10^4 cm^{-3} (Elias 29) up to 2.3$\times$10^6 cm^{-3} (Ser-SMM4). The densities for all sources at the 10″ radius are given in Table 3.4. Note that these are
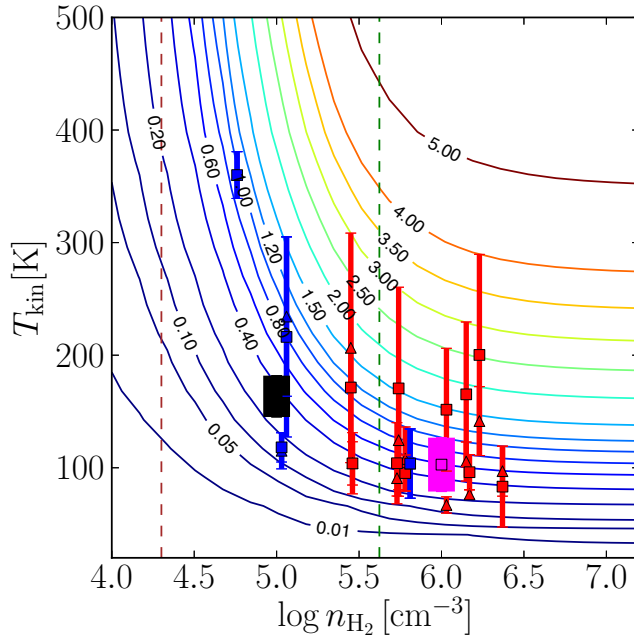
Figure 3.13 – Model CO 10–9/3–2 line intensity ratios as function of temperature and density, obtained for a CO column density of 10^{16} cm^{-2} with line-widths of 10 km s^{-1}, representative of the observed CO intensity and line width. Note that the bars are the ranges of lower and upper limits as seen from the observations in Fig. 3.12. Red markers are for Class 0 and blue markers are for Class I sources. Blue wing ratios are indicated with triangles and red wing ratios have square symbols. Thick magenta and black lines indicate the ratios from the composite spectra for Class 0 and Class I sources, respectively. Vertical dashed lines indicate the limits for n_{cr} for CO 3–2 (brown) and CO 10–9 (green). In the relevant density range, smaller ratios are indicative of higher kinetic temperatures.

lower limits since the densities increase inward of 10″. The envelope densities are used here as a proxy for the densities at the outflow walls where the entrainment occurs.

The majority of the Class 0 sources have densities that are similar or higher than the critical densities of the high-J CO lines, with the possible exceptions of Ced110-IRS4, L483mm, L723mm, and L1157. However, in Class I sources, the majority of the densities are lower than the critical densities with the exception of L1551 IRS5.

The inferred kinetic temperatures from the CO 10–9/3–2 blue and red line-wings, which change with velocity, are presented in Table 3.5 and range from 70 K to 250 K. The ratios for individual sources are included in Fig. 3.13 at the 10″ radius density of the sources. The thick red and blue bars indicate the average values of inferred temperature for composite Class 0 and Class I sources (Sect. 3.5.3). The kinetic temperatures are mainly above 100 K. However, if part of the CO 10–9 emission comes from the warmer component also probed in H$_2$O (see §5.3), these values should be regarded as upper limits.
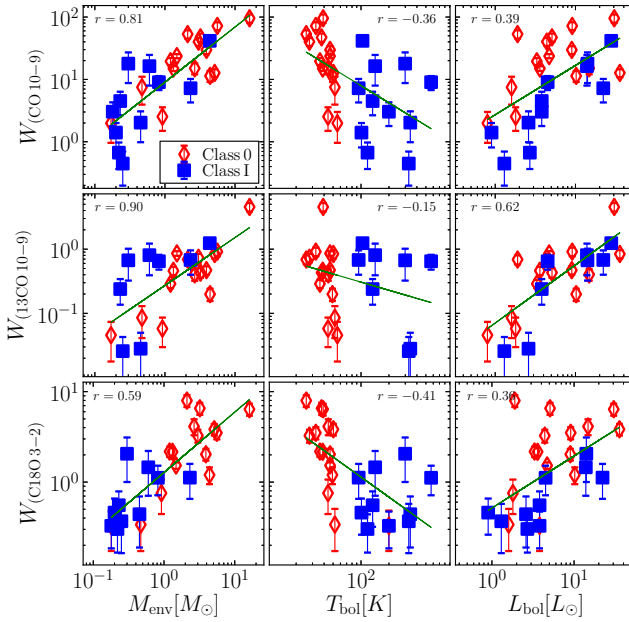
Figure 3.14 – From top to bottom, ^{12}CO 10–9, ^{13}CO 10–9, and C^{18}O 3–2 integrated intensity W normalized at 200 pc are plotted against various physical properties: envelope mass at 10 K radius, M_{env}; bolometric temperature, T_{bol}; and bolometric luminosity, L_{bol}. Green lines are the best fit to the data points and r values in each of the plots are Pearson correlation coefficient.

3.5 Correlations with physical properties

3.5.1 Integrated intensities

Figure 3.14 shows the integrated intensities W of the CO 10–9 lines plotted against L_{bol}, M_{env}, T_{bol}, and n(1000 AU). The intensities are scaled to a common distance of 200 pc. The bolometric luminosity, L_{bol} and bolometric temperature T_{bol} of the sources have been measured using data from infrared to millimeter wavelengths including new *Herschel* far-infrared fluxes, and are presented in Kristensen et al. (2012). These are commonly used evolutionary tracers in order to distinguish young stellar objects. The envelope mass, M_{env}, and envelope density at 1000 AU, n(1000 AU), are calculated from the DUSTY modeling by Kristensen et al. (2012).

In Fig. 3.14, the green lines are the best power-law fits to the entire data set. Clearly, the CO 10–9 lines are stronger for the Class 0 sources which have higher M_{env} and L_{bol} but lower T_{bol}, for all isotopologs. The same correlation is seen for other (lower-J) CO and isotopolog lines, such as CO 2–1, 3–2, 4–3, 6–5 and 7–6; examples for ^{13}CO 10–9 and C^{18}O 3–2 are included in Fig. 3.14. The Pearson correlation coefficients for ^{12}CO
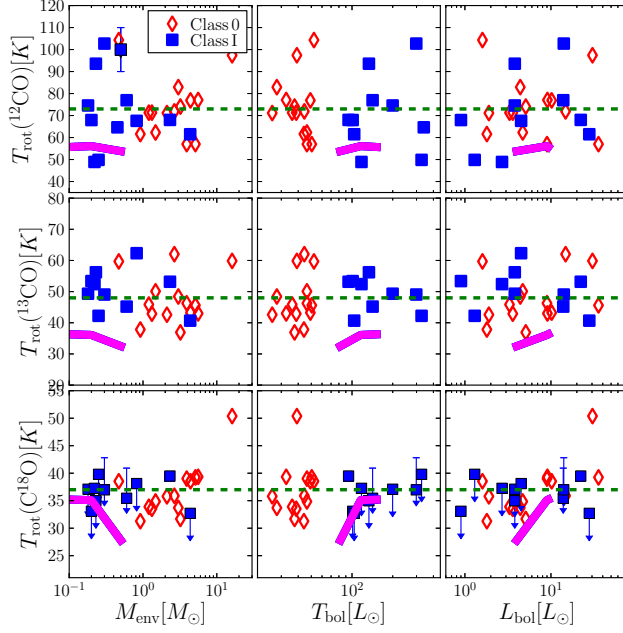
Figure 3.15 – Calculated rotational temperatures, T_{rot}, plotted M_{env}, T_{bol}, and L_{bol}, for ^{12}CO (*top*), ^{13}CO (*middle*), C^{18}O lines (*bottom*). The median excitation temperatures of ~70 K, 48 K and 37 K for ^{12}CO, ^{13}CO and C^{18}O, respectively, are indicated with the green dashed lines. Typical error bars for each of the T_{rot} values are shown in the upper left plot, represented in black. In the C^{18}O plots, blue arrows indicate the upper limits for a number of sources. These figures are compared with disk evolution models of Harsono et al. (subm., magenta solid lines) as explained in the text. The figures show that the excitation temperature does not change with the increasing luminosity, envelope mass or density, confirming that Class 0 and I sources have similar excitation conditions.

10–9 are r=0.39, 0.81, and –0.36 for L_{bol}, M_{env}, and T_{bol}, respectively. The coefficients, r, for M_{env} in ^{13}CO 10–9 and C^{18}O 3–2 are 0.90 and 0.59. Those correlations indicate that there is a strong correlation between the intensities and envelope mass, M_{env}. In the Pearson correlation, a strong correlation is defined as $|r| > 0.7$ to 1.0. Together with the high-J CO lines, the C^{18}O low-J lines are also good evolutionary tracers in terms of M_{env} and T_{bol}. Adding intermediate and high-mass WISH sources to extend the correlation to larger values of L_{bol} and M_{env} shows that these sources follow the same trend with similar slopes with a strong correlation (San José-García et al. 2013).

3.5.2 Excitation temperature and comparison with evolutionary models

Figure 3.15 presents the derived rotational temperatures for ^{12}CO, ^{13}CO and C^{18}O versus M_{env}, T_{bol}, and L_{bol}. In contrast with the integrated intensities, no systematic trend is seen

for any parameter. As noted in Sect. 3.4.2, this lack of change in excitation temperature with evolution is in stark contrast with the evolution of the continuum SED as reflected in the range of T_{bol}.

To investigate whether the lack of evolution in excitation temperature is consistent with our understanding of models of embedded protostars, a series of collapsing envelope and disk formation models with time has been developed by Harsono et al. (subm.), based on the formulation of Visser et al. (2009) and Visser & Dullemond (2010). Three different initial conditions are studied. The total mass of the envelope is taken as 1 $M_\odot$ initially in all cases, but different assumptions about the sound speed c_S and initial core angular momentum Ω result in different density structures as function of time. The three models cover the range of parameters expected for low-mass YSOs. The luminosity of the source changes with time from <1 to ~5–10 $L_\odot$. The dust temperature is computed at each time step using a full 2D radiative transfer model and the gas temperature is taken equal to the dust temperature.

Given the model physical structures, the CO excitation is then computed as a function of time (evolution) through full 2D non-LTE excitation plus radiative transfer calculations. The line fluxes are computed for i=45° inclination but do not depend strongly on the value of i. The resulting line intensities are convolved to a 20″ beam and CO rotational temperatures are computed using the 2–1 up to 10–9 lines. Details are provided in Harsono et al. (subm.). The resulting model excitation temperatures are plotted against model L_{bol}, T_{bol} and M_{env} values as a function of time, with envelope mass decreasing with time.

The first conclusion from this comparison is that the model rotational temperatures hardly show any evolution with time consistent with the observations, in spite of the envelope mass changing by two orders of magnitude. Although the density decreases to values below the critical densities, the temperature increases throughout the envelope so the rotational temperatures stay constant.

The second conclusion is that the model rotational temperatures are generally below the observed temperatures, especially for ^{12}CO and ^{13}CO. For ^{12}CO this could be due to the fact that outlow emission is not included in the models, which accounts typically for more than half of the line intensity and has a higher rotational temperature (see Sect. 3.4.4). For ^{13}CO, the model T_{rot} values are probably lower than the observed values because UV photon heating contributes along the outflow walls (see Visser et al. 2012, Yıldız et al. 2012, for quantitative discussion). The model $C^{18}O$ rotational temperatures are close to the observed values, illustrating that the envelope models are an accurate representation of the observations.

3.5.3   High-J CO vs. water

Do the average spectra of the Class 0 and Class I sources show any evolution and how does this compare with water? In Fig. 3.3, stacked and averaged ^{12}CO 3–2, 10–9, and H_2O 1_{10}-1_{01} spectra for the Class 0 and I sources have been presented. Consistent with the
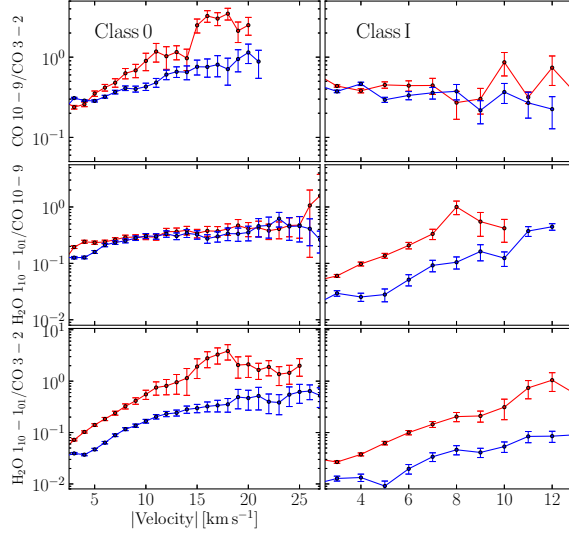
Figure 3.16 – Blue and red line wing ratios of CO 10–9/3–2 (*top panel*), H_2O 1_{10}-1_{01}/CO 10–9 (*middle panel*), and H_2O 1_{10}-1_{01}/CO 3–2 (*bottom panel*) for the composite Class 0 and Class I source spectra. The H_2O/CO 10–9 and H_2O/CO 3–2 ratios are a factor of two lower than shown in Fig. 3.3 due to the beam size difference of 20″ (CO 10–9 lines) to 40″ (H_2O 1_{10}-1_{01} lines).

discussion in Sect. 3.3.2 and San José-García et al. (2013), Class 0 sources have broader line widths than Class I sources, showing the importance of protostellar outflows in Class 0 sources. In general, Class I sources show weaker overall emission except for the bright sources GSS30 IRS1 and Elias 29, consistent with the trend in Fig. 3.14.

Fig. 3.16 shows the H_2O 1_{10}-1_{01}/CO 10–9, H_2O 1_{10}-1_{01}/CO 3–2, and CO 10–9/CO 3–2 line ratios. The CO 10–9/CO 3–2 line wings show increasing ratios from ~0.2 to ~1.0–3.0 for the averaged Class 0 spectrum, but a constant ratio of ~0.3 for the Class I sources. For average densities at a 10″ radius of ~10^6 cm^{-3} and ~10^5 cm^{-3} for Class 0 and Class I sources, respectively, the CO 10–9/CO 3–2 line ratios would imply temperatures of around 80–130 K for Class 0 and 140–180 K for Class I sources (also shown in Fig. 3.13 —thick purple and dark-blue lines), if the two lines probe the same physical component.

Franklin et al. (2008) examined the H_2O abundance as a function of velocity by using CO 1–0 as a reference frame. Here it is investigated how H_2O/CO line ratios change with increasing J by using CO 3–2 and 10–9 as reference frames. In Fig. 3.16, the CO 3–2 line has been convolved to a 40″ beam using the JCMT data (also done by Kristensen et al. 2012). For the 10–9 line, no map is available so the emission is taken to scale linearly with the beam size, as appropriate for outflow line wings assuming a 1D structure (Tafalla et al. 2010). Thus, the 10–9 intensities are a factor of two lower than those shown in, for

example, Fig. 3.3 where data in a 20″ beam were used. The line wing ratios are computed up to the velocity where the CO emission reaches down to ∼2σ noise limit, even though the H_2O line wings extend further.

Consistent with Kristensen et al. (2012), an increasing trend of H_2O/CO 3–2 line ratios with velocity is found for both Class 0 and Class I sources. However, the H_2O/CO 10–9 ratios show little variation with velocity for Class 0 sources, and the ratio is constant within the error bars. For the Class I sources an increasing trend in H_2O/CO 10–9 line ratios is still seen.

Because of the similarity of the CO 10–9 line wings with those of water, it is likely that they are tracing the same warm gas. This is in contrast with the 3–2 line, which probes the colder entrained gas. The conclusion that H_2O and high-*J* CO emission go together (but not low-*J* CO) is consistent with recent analyses (Santangelo et al. 2012, Vasta et al. 2012, Tafalla et al. 2013) of WISH data at outflow positions offset from the source. The CO 10–9 line seems to be the lowest-*J* transition whose line wings probe the warm shocked gas rather than the colder entrained outflow gas (see also Sect. 3.4.3); HIFI observations of higher-*J* lines up to *J*=16–15 should show an even closer correspondence between H_2O and CO (Kristensen et al., in prep.). That paper will also present H_2O/CO abundance ratios since deriving those from the data requires further modeling because the H_2O lines are subthermally excited and optically thick.

3.6 CO abundance and warm inner envelope

3.6.1 CO abundance profiles

The wealth of high quality $C^{18}O$ lines probing a wide range of temperatures allows the CO abundance structure throughout the quiescent envelope to be constrained. The procedure has been described in detail in Yıldız et al. (2010, 2012). Using the density and temperature structure of each envelope as derived by Kristensen et al. (2012, their Table C.1; see Sect. 3.4.5), the CO abundance profile can be inferred by comparison with the $C^{18}O$ data. The RATRAN (Hogerheijde & van der Tak 2000) radiative-transfer modeling code is used to compute line intensities for a given trial abundance structure.

Six sources with clear detections of $C^{18}O$ 9–8 and 10–9 have been modeled. The outer radius of the models is important for the lower-*J* lines and for Class 0 sources. It is taken to be the radius where either the density *n* drops to ∼1.0×10^4 cm^{-3}, or the temperature drops below 8–10 K, whichever is reached first. In some Class 0 sources (e.g., IRAS 4A, IRAS 4B), however, the density is still high even at temperatures of ∼8 K; here the temperature was taken to be constant of 8 K and the density was allowed to drop until ∼10^4 cm^{-3}. The turbulent velocity (Doppler-b parameter) is set to 0.8 km s^{-1}, which is representative of the observed $C^{18}O$ line widths for most sources (Jørgensen et al. 2002) except for Elias 29 where 1.5 km s^{-1} is adopted. The model emission is convolved with
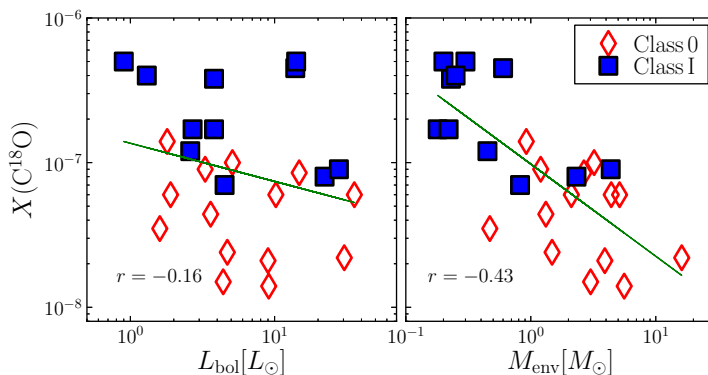
Figure 3.17 – Constant abundance profiles are fitted to the lower-J C^{18}O 3–2 are shown as function of L_{bol} and M_{env}. Green lines are the best fit to the data points and r values in each of the plots are Pearson correlation coefficient.

the beam in which the line has been observed.

First, constant abundance profiles are fitted to the lower-J C^{18}O 3–2, together with the 2–1 transitions, if available. In Fig. 3.17, these abundances are plotted as function of bolometric luminosities and envelope masses. Consistent with Jørgensen et al. (2002), Class 0 sources with higher envelope mass have lower average abundances in their envelopes than Class I sources, by more than an order of magnitude. This result is firm for lower-J transitions; however, in order to fit higher-J lines simultaneously, it is necessary to introduce a more complex 'drop' abundance profile with a freeze-out zone. The inner radius is determined by where the dust temperature falls below the CO evaporation temperature of 25 K. The outer radius is determined by where the density becomes too low for freeze-out to occur within the lifetime of the core.

Following Yıldız et al. (2010, 2012) for the NGC 1333 IRAS 2A, IRAS 4A and IRAS 4B protostars, such a drop-abundance profile provides a better fit to the C^{18}O data than a constant or 'anti-jump' abundance. The outer abundance X_0 is set to 5×10^{-7} below at a certain desorption density, n_{de}, corresponding to the maximum expected CO abundance of 2.7×10^{-4}. Best fit abundances for different sources are summarized in Table 3.7. As in our previous work and in Fuente et al. (2012) and Alonso-Albi et al. (2010), the CO abundance in the inner envelope is below the canonical value of 2.7×10^{-4} (Lacy et al. 1994) by a factor of a few for the Class 0 sources, probably due to processing of CO to other species on the grains during the cold phase.

Only two of the Class I sources (GSS30 IRS1 and Elias 29) have been observed in deep integrations of C^{18}O 10–9 and therefore they are the only Class I sources modeled in detail. These sources are located in the Ophiuchus molecular cloud, where two low-density foreground sheets contribute to the lowest-J 1–0 and 2–1 lines (e.g., Loren 1989, van Kempen et al. 2009d). To take this into account, a single slab foreground cloud is added in front of the protostars with 15 K temperature, 1.5×10^4 cm^{-3} H$_2$ density, and

Table 3.7 – Summary of $C^{18}O$ abundance profiles.

Source	Profile	X_{in}	T_{ev} [K]	X_D	n_{de} [cm^{-3}]	X_0
IRAS 2A[a]	Drop	1.5×10^{-7}	25	$\sim 4\times10^{-8}$	7×10^4	5×10^{-7}
IRAS 4A[b]	Drop	$\sim1\times10^{-7}$	25	5.5×10^{-9}	7.5×10^4	5×10^{-7}
IRAS 4B[b]	Jump	3×10^{-7}	25	1×10^{-8}	...	1×10^{-8}
Ser-SMM1	Drop	1.5×10^{-7}	25	1.0×10^{-8}	1.4×10^5	5×10^{-7}
Elias29	Constant	5×10^{-7}	...	5×10^{-7}	...	5×10^{-7}
GSS30IRS1	Jump	4×10^{-7}	25	2×10^{-8}	...	2×10^{-8}

Notes: X_{in} is the abundance of inner envelope, T_{ev} is the evaporation temperature, X_D drop zone abundance, n_{de} is the desorption density, and X_0 is the abundance of the outermost part of the envelope. Results from [a] Yıldız et al. (2010) [b] Yıldız et al. (2012)

10^{16} cm^{-2} CO column density. Best-fit models for the $C^{18}O$ 3–2, 9–8 and 10–9 lines toward GSS30 IRS1 and Elias 29 can then be well fit with a constant CO abundance close to the canonical value and do not require a freeze-out zone. Jørgensen et al. (2005c) argue that the size of the freeze-out zone evolves during protostellar evolution, i.e., for Class 0 sources the drop-zone should be much larger than for Class I sources. This is indeed consistent with the results found here.

3.6.2 Warm inner envelope

The higher-J $C^{18}O$ transitions such as 9–8 and 10–9 (E_u up to ~300 K) in principle trace directly the warmer gas in the inner envelope. Can we now use these data to put limits on the amount of warm >100 K gas, which could then be used as a reference for determining abundances of complex molecules?

In principle, one could argue that simply summing the observed column density of molecules in each level should provide the total warm column density, as done by Plume et al. (2012) for the case of Orion and in Table 3.5 based on the rotational diagrams. However, in the low-mass sources considered here freeze-out also plays a role and CO can be converted to other species on the grains. Thus, to convert to $N(H_2)$ in the warm gas, one needs to use the values of X_{in} that have been derived in Table 7. However, these values are derived in the context of a physical model of the source, so in principle one simply recovers the input model.

Besides the complication of the changing CO abundance with radius, there are two other effects that make a direct observational determination of the warm H_2 column densities far from simple. The first issue is the fact that not all emission in the 9–8 or 10–9 lines arises from gas at >100 K even though E_u=237–290 K. Figure 3.18 shows the cumulative $C^{18}O$ line intensities (solid curves) as functions of radius (or, equivalently, temperature) for four source models. I_{tot} are the intensities measured from the best-fit abundance models as tabulated in Table 3.7. Thus, the curves represent the fraction of line intensities
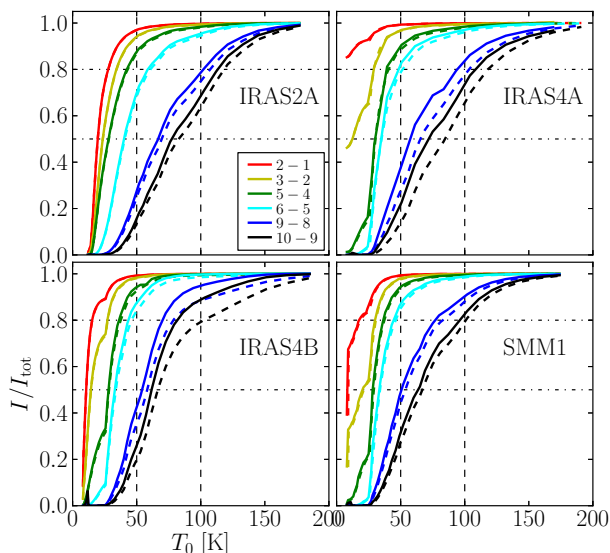
Figure 3.18 – Cumulative intensity I/I_{tot} for various $C^{18}O$ lines as function of envelope radius (as indicated by the temperature T_o) with the dust opacity included (solid curves), and dust opacity off (dashed curves). The dash-dotted lines indicates the fractions of 50 and 80%, respectively.

which have their origins in gas at temperatures below T_0 for the different transitions. As expected, about 90–95% of the $C^{18}O$ emission in the lower-J transitions up to $J_u \leq 3$ comes from gas at <40 K. However, even for the 9–8 transition, 30–50% comes from gas at less than 50 K whereas only ~10–20% originates at temperatures above 100 K. For the 10–9 transition, ~20–40% of the emission comes from >100 K. Thus, these are additional correction factors that would have to be applied to obtain the columns of gas >100 K.

A second potential issue is that the dust continuum at 1 THz may become optically thick so that warm $C^{18}O$ emission cannot escape. Figure 3.19 shows the dust opacity as function of radius throughout the envelope, obtained by multiplying the column densities with the κ_{dust}(1 THz) (Ossenkopf & Henning 1994, their Table 1, column 5) and integrating from the outer edge to each radius to find the optical depth (τ). It is seen that the dust is optically thin (τ <1) throughout the envelopes of those sources except for IRAS 4A, where it reaches to τ =1 at the innermost part of the envelope. To what extent is the fraction of high-J emission coming from >100 K affected by the dust? In Fig. 3.18 (dashed curves), the dust emission has been turned off in the `RATRAN` models. For the lower-J, lower-frequency transitions, almost no difference is found; however, for the higher-J transitions the cumulative intensities are somewhat higher (up to a factor of 2) when no dust is present.

In summary, there are various arguments why warm H_2 column densities cannot be inferred directly from the high-J $C^{18}O$ data. Moreover, all of these arguments use a simple
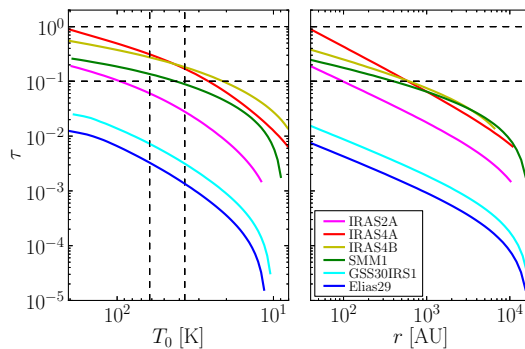
Figure 3.19 – Dust optical depth at 1 THz as function of envelope radius and temperature. Horizontal dashed lines indicate the $\tau=1$ and $\tau=0.1$ values whereas vertical dash-dotted lines are radii where the temperatures are between 40 K and 60 K.

spherically symmetric physical model of the source to quantify the effects. It is known that such models fail on the smaller scales (less than a few hundred AU) due to the presence of a (pseudo)disk and outflow cavities (e.g., Jørgensen et al. 2005b). Spatially resolved data are needed to pin down the structure of the inner envelopes and properly interpret the origin of the high-J $C^{18}O$ emission.

3.7 Conclusions

We have presented the first large-scale survey of spectrally resolved low- to high-J CO and isotopolog lines ($2 \leq J_{up} \leq 10$) in 26 low-mass young stellar objects by using data from *Herschel*-HIFI, APEX and JCMT telescopes. Velocity resolved data are key to obtain the complete picture of the protostellar envelope and the interaction of the protostar with the environment and follow the evolution from the Class 0 to Class I phase.

- The ^{12}CO line profiles can be decomposed into narrow and broad components, with the relative fractions varying from zero to nearly 100%, with a median of 42% of the $J=10$–9 emission in the narrow component. The average Class 0 profile shows a broader, more prominent wing than the average Class I profile.

- The 10–9 together with 3–2 intensities correlate strongly with total luminosity M_{env} and are inversely proportional with bolometric temperature T_{bol}, illustrating the dissipation of the envelope with evolution.

- Rotation diagrams are constructed for each source in order to derive rotational temperatures and column densities. Median temperatures of T_{rot} are 70 K, 48 K and 37 K, for the ^{12}CO, ^{13}CO and $C^{18}O$ transitions, respectively. The excitation temperatures and SLEDs are very similar for Class 0 and Class I sources in all three

isotopologs and do not show any trend with M_{env}, L_{bol} or T_{bol}, in contrast with the continuum SEDs.

- Models of the CO emission from collapsing envelopes reproduce the correlation of line intensity with M_{env} and the lack of evolution found in the observed excitation temperatures. They agree quantitatively for $C^{18}O$ but underproduce the ^{12}CO and ^{13}CO excitation temperatures, pointing to the combined effects of outflows and photon-heating in boosting these temperatures.

- The ^{12}CO 10–9/CO 3–2 intensity ratio as well as the overall rotational temperature increase with velocity for Class 0 sources. No such effect is found for the Class I sources, where the broad line wings are less prominent.

- Comparison of the ^{12}CO profiles with those of H_2O shows that the H_2O 1_{10}-1_{01}/CO 10–9 intensity ratio is nearly constant with velocity for Class 0 sources, contrary to the case for low-J CO lines. Combined with other findings, this suggests that the CO 10–9 line has contributions from the warmer ($\sim$300 K) shocked gas containing also water, rather than the colder ($\sim$100 K) entrained outflow gas traced by low-J CO lines.

- Analysis of the entire set of higher-J $C^{18}O$ lines within a given physical model shows further evidence for a freeze-out zone ('drop' abundance profile) in the envelopes of Class 0 sources with an inner CO abundance that is a factor of a few lower than the canonical CO abundance probably due to processing of CO on grains into more complex molecules. For Class I sources, no freeze-out zone is needed and the data are consistent with a constant high abundance value at a level that is an order of magnitude higher than the average abundance in the Class 0 phase.

- The warm (>100 K) H_2 column densities cannot be derived directly from $C^{18}O$ 9–8 or 10–9 lines because of contributions to the emission from colder gas in the envelope, dust extinction at high frequency, and more generally a lack of knowledge of the source structure on a few hundred AU scales.

Overall, our data show that the evolution from the Class 0 to the Class I phase is traced in the decrease of the line intensities reflecting envelope dissipation, a less prominent broad wing indicating a decrease in the outflow power, and an increase in the average CO abundance, reflecting a smaller freeze-out zone. The CO excitation temperature from J_u=2 to 10 shows little evolution between these two classes, however.

The next step in the study of CO in low mass protostars is clearly to obtain higher spectral and spatial resolution data with instruments like ALMA that recover the full range of spatial scales from <100 AU to >1000 AU in both low- and high−J CO and isotopolog lines.

Acknowledgements

3.8   Additional materials

Figure 3.20 – Zoom-in spectra of the line wings of ^{12}CO 3–2 (black) and ^{12}CO 10–9 (purple) overplotted for each source. The spectra are multiplied by a constant factor indicated in the figure in order to show the line wings in more detail. They have been rebinned to 0.6–1 km s^{-1}, to enhance signal-to-noise.

Table 3.8 – *Herschel* Obsids for related observations

Source	^{12}CO 10–9	^{13}CO 10–9	^{13}CO 8–7	C^{18}O 5–4	C^{18}O 9–8	C^{18}O 10–9
L1448-MM	1342203253	1342201803	. . .	1342203186	1342203182	1342201802
IRAS2A	1342191701	1342191657	1342225937	1342192206	1342191606	1342215968
IRAS4A	1342191721	1342191656	1342225938	1342192207	1342191605	1342249014
IRAS4B	1342191722	1342191655	1342225940	1342192208	1342191604	1342249851
L1527	1342203256	1342216335	. . .	1342203188	1342203156	. . .
Ced110IRS	1342201734	1342200765	. . .	. . .	1342201756	. . .
BHR71	1342201732	1342200764	. . .	1342200755	1342215915	. . .
IRAS 15398	1342214446	1342214414	. . .	. . .	1342203165	. . .
L483	1342217730	1342207374	. . .	1342207582	1342218213	1342207375
Ser SMM1	1342207701	1342207379	1342229782	1342194463	1342194994	1342207378
Ser SMM4	1342207700	1342207380	1342229782	1342194464	1342194993	1342207381
Ser SMM3	1342207699	1342207377	. . .	1342207580	1342207658	1342207376
L723-MM	1342210152	1342210168	. . .	1342219172	1342210041	. . .
B335	1342230175	1342219248	. . .	1342219182	1342219217	. . .
L1157	1342198346	1342200763	. . .	1342199077	1342197970	. . .
L1489	1342203254	1342203938	. . .	. . .	1342203158	. . .
L1551-IRS5	1342203258	1342203940	. . .	. . .	1342203153	. . .
TMR1	1342225917	1342203937	. . .	. . .	1342203157	. . .
TMC1A	1342225916	1342215969	. . .	. . .	1342203154	. . .
TMC1	1342203255	1342216336	. . .	. . .	1342203155	. . .
HH46	1342222281	1342194785	. . .	. . .	1342195041	. . .
DKCha	1342201733	1342201590	. . .	. . .	1342201755	. . .
GSS30 IRS1	1342214442	1342214413	. . .	. . .	1342203163	1342250604
Elias29	1342214443	1342214408	. . .	. . .	1342203162	1342249849
Oph IRS63	1342214441	1342214407	. . .	. . .	1342203164	. . .
RNO91	1342214440	1342214406	. . .	. . .	1342204512	. . .

Table 3.9 – Observed sources and lines.

Source	12CO						13CO						C18O					
	2–1	3–2	4–3	6–5	7–6	10–9	2–1	3–2	4–3	6–5	8–7	10–9	2–1	3–2	5–4	6–5	9–8	10–9
L1448-MM	JCMT	JCMT	JCMT	…[a]	…[a]	HIFI	JCMT	JCMT	…	APEX	…	HIFI	JCMT	JCMT	HIFI	…	HIFI	HIFI
NGC1333-IRAS2A	JCMT	JCMT	JCMT	APEX	APEX	HIFI	…	JCMT	JCMT	APEX	…	HIFI	JCMT	JCMT	HIFI	APEX	HIFI	HIFI
NGC1333-IRAS4A	JCMT	JCMT	JCMT	APEX	APEX	HIFI	JCMT	JCMT	JCMT	APEX	HIFI	HIFI	JCMT	JCMT	HIFI	APEX	HIFI	HIFI
NGC1333-IRAS4B	JCMT	JCMT	JCMT	APEX	APEX	HIFI	…	JCMT	…	APEX	HIFI	HIFI	JCMT	JCMT	HIFI	APEX	HIFI	HIFI
L1527	JCMT	JCMT	JCMT	APEX	APEX	HIFI	…	JCMT	JCMT	APEX	HIFI	HIFI	JCMT	JCMT	HIFI	…	HIFI	…
Ced110-IRS4	…	JCMT	…	APEX	APEX	HIFI	…	…	…	APEX	…	HIFI	…	…	…	…	HIFI	…
BHR71	…	APEX	…	APEX	APEX	HIFI	…	…	…	APEX	…	HIFI	…	APEX	HIFI	…	HIFI	…
IRAS15398	…	JCMT	JCMT	APEX	APEX	HIFI	…	JCMT	…	APEX	…	HIFI	JCMT	JCMT	…	…	HIFI	…
L483mm	JCMT	JCMT	JCMT	APEX	APEX	HIFI	JCMT	JCMT	JCMT	APEX	…	HIFI	JCMT	JCMT	HIFI	…	HIFI	HIFI
Ser-SMM1	JCMT	JCMT	JCMT	APEX	APEX	HIFI	JCMT	JCMT	…	APEX	HIFI	HIFI	JCMT	JCMT	HIFI	APEX	HIFI	HIFI
Ser-SMM4	JCMT	JCMT	JCMT	APEX	APEX	HIFI	…	JCMT	…	APEX	HIFI	HIFI	…	JCMT	HIFI	…	HIFI	HIFI
Ser-SMM3	JCMT	JCMT	JCMT	APEX	APEX	HIFI	JCMT	JCMT	…	APEX	APEX	HIFI	JCMT	JCMT	HIFI	…	HIFI	HIFI
L723	…	JCMT	…	APEX	APEX	HIFI	JCMT	JCMT	JCMT	APEX	APEX	HIFI	JCMT	JCMT	HIFI	…	HIFI	…
B335	JCMT	JCMT	JCMT	APEX	APEX	HIFI	JCMT	JCMT	…	APEX	…	HIFI	JCMT	JCMT	HIFI	…	HIFI	…
L1157	JCMT	JCMT	JCMT	JCMT	…	HIFI	JCMT	JCMT	…	JCMT	…	HIFI	JCMT	JCMT	HIFI	…	HIFI	…
L1489	JCMT	JCMT	JCMT	APEX	APEX	HIFI	…	JCMT	…	APEX	…	HIFI	JCMT	JCMT	…	…	HIFI	…
L1551-IRS5	JCMT	JCMT	JCMT	APEX	…	HIFI	JCMT	JCMT	…	APEX	…	HIFI	JCMT	JCMT	…	…	HIFI	…
TMR1	JCMT	JCMT	JCMT	APEX	APEX	HIFI	…	JCMT	…	APEX	…	HIFI	JCMT	JCMT	…	…	HIFI	…
TMC1A	JCMT	JCMT	JCMT	APEX	APEX	HIFI	…	JCMT	…	APEX	…	HIFI	JCMT	JCMT	…	…	HIFI	…
TMC1	JCMT	JCMT	JCMT	APEX	APEX	HIFI	…	JCMT	…	APEX	…	HIFI	JCMT	JCMT	…	…	HIFI	…
HH46-IRS	APEX	APEX	APEX	APEX	APEX	HIFI	…	APEX	APEX	APEX	APEX	HIFI	JCMT	APEX	…	APEX	HIFI	…
DK Cha	…	APEX	APEX	APEX	APEX	HIFI	…	…	APEX	APEX	APEX	HIFI	APEX	APEX	…	APEX	HIFI	…
GSS30-IRS1	JCMT	JCMT	…	APEX	…	HIFI	JCMT	JCMT	…	APEX	…	HIFI	JCMT	JCMT	…	…	HIFI	…
Elias 29	JCMT	JCMT	…	APEX	…	HIFI	JCMT	JCMT	…	APEX	…	HIFI	JCMT	JCMT	…	…	HIFI	…
Oph-IRS63	JCMT	JCMT	…	APEX	APEX	HIFI	…	JCMT	…	APEX	APEX	HIFI	JCMT	JCMT	…	…	HIFI	…
RNO91	JCMT	JCMT	…	APEX	APEX	HIFI	JCMT	JCMT	…	APEX	APEX	HIFI	JCMT	JCMT	…	…	HIFI	…

Notes: Sources above the horizontal line are Class 0, sources below are Class I. HIFI indicates *Herschel*-HIFI observations. [a]Gomez-Ruiz et al. in prep.

APEX-CHAMP⁺ high-J CO observations of low−mass young stellar objects:
III. NGC 1333 IRAS 4A/4B envelope, outflow, and ultraviolet heating

Umut A. Yıldız, Lars E. Kristensen, Ewine F. van Dishoeck,
Tim A. van Kempen, Arnoud Belloche, Rolf Güsten, Nienke van der Marel

Abstract

CONTEXT: The NGC 1333 IRAS 4A and IRAS 4B sources are among the most well-studied Stage 0 low-mass protostars, which drive prominent bipolar outflows. Spectrally resolved molecular emission lines provide crucial information about the physical and chemical structure of the circumstellar material as well as the dynamics of the different components. Most studies have so far concentrated on the colder parts ($T \leq 30$ K) of these regions.

AIMS: The aim is to characterize the warmer parts of the protostellar envelope using the new generation of submillimeter instruments. This will allow us to quantify the feedback of the protostars on their surroundings in terms of shocks, ultraviolet (UV) heating, photodissociation, and outflow dispersal.

METHODS: The dual frequency 2×7 pixel 650/850 GHz array receiver CHAMP$^+$ mounted on APEX was used to obtain a fully sampled, large-scale ~4′×4′ map at 9″ resolution of the IRAS 4A/4B region in the ^{12}CO J=6–5 line. Smaller maps were observed in the ^{13}CO 6–5 and [C I] J=2–1 lines. In addition, a fully sampled ^{12}CO J=3–2 map made with HARP-B on the JCMT is presented and deep isotopolog observations are obtained at selected outflow positions to constrain the optical depth. Complementary *Herschel*-HIFI and ground-based lines of CO and its isotopologs, from J=1–0 up to 10–9 ($E_u/k \approx 300$ K), are collected at the source positions and used to construct velocity-resolved CO ladders and rotational diagrams. Radiative-transfer models of the dust and lines are used to determine the temperatures and masses of the outflowing and photon-heated gas and infer the CO abundance structure.

RESULTS: Broad CO emission-line profiles trace entrained shocked gas along the outflow walls, which have an average temperature of ~100 K. At other positions surrounding the outflow and the protostar, the 6–5 line profiles are narrow indicating UV excitation. The narrow ^{13}CO 6-5 data directly reveal the UV heated gas distribution for the first time. The amount of UV-photon-heated gas and outflowing gas are quantified from the combined ^{12}CO and ^{13}CO 6–5 maps and found to be comparable within a 20″ radius around IRAS 4A, which implies that UV photons can affect the gas as much as the outflows. Weak [C I] emission throughout the region indicates that there is a lack of CO dissociating photons. Our modeling of the C^{18}O lines demonstrates the necessity of a "drop" abundance profile throughout the envelopes where the CO freezes out and is reloaded back into the gas phase through grain heating, thus providing quantitative evidence of the CO ice evaporation zone around the protostars. The inner abundances are less than the canonical value of CO/H$_2$=2.7×10^{-4}, however, implying that there is some processing of CO into other species on the grains. The implications of our results for the analysis of spectrally unresolved *Herschel* data are discussed.

4.1 Introduction

In the very early stages of star formation, newly forming protostars are mainly characterized by their large envelopes ($\sim 10^4$ AU in diameter) and bipolar outflows (Lada 1987, Greene et al. 1994). As gas and dust from the collapsing core accrete onto the central source, the protostar drives out material along both poles at supersonic speeds to distances of up to a parsec or more. These outflows have a significant impact on their surroundings, by creating shock waves that increase the temperature and change the chemical composition (Snell et al. 1980, Bachiller & Tafalla 1999, Arce et al. 2007). By sweeping up material, they carry off envelope mass and limit the growth of the protostar. They also create a cavity through which ultraviolet photons from the protostar can escape and impact the cloud (Spaans et al. 1995). Quantifying these active 'feedback' processes and distinguishing them from the passive heating of the inner envelope by the protostellar luminosity is important to achieving a complete understanding of the physics and chemistry during protostellar evolution.

Most studies of low-mass protostars to date have used low-excitation lines of CO and isotopologs ($J_{\mathrm{u}} \leq 3$) combined with dust continuum mapping to characterize the cold gas in envelopes and outflows (e.g., Blake et al. 1995, Bontemps et al. 1996, Shirley et al. 2002, Robitaille et al. 2006). A wealth of other molecules has also been observed at mm wavelengths, but their use as temperature probes is complicated by their steep abundance gradients through the envelope driven by release of ice mantles (e.g., van Dishoeck & Blake 1998, Ceccarelli et al. 2007, Bottinelli et al. 2007). Moreover, molecules with large dipole moments such as CH_3OH are often highly subthermally excited unless densities are very high (e.g. Bachiller et al. 1995, Johnstone et al. 2003). With the opening up of high-frequency observations from the ground and in space, higher excitation lines of CO can now be routinely observed so that their diagnostic potential as temperature and column density probes can now be fully exploited.

Tracing warm gas with CO up to J=7–6 from the ground requires optimal atmospheric conditions, as well as state-of-art detectors. The combination is offered by the CHAMP$^+$ 650/850 GHz 2×7 pixel array receiver (Kasemann et al. 2006), which is currently mounted at the Atacama Pathfinder EXperiment (APEX) Telescope at 5100 m altitude on Cerro Chajnantor (e.g. Güsten et al. 2008). Moreover, the spectroscopic instruments on the *Herschel Space Observatory* have the sensitivity to observe CO lines up to J=44–43 unhindered by the Earth's atmosphere, even for low-mass young stellar objects (e.g., van Kempen et al. 2010a,b, Lefloch et al. 2010, Yıldız et al. 2010). Together, these data allow us to address questions such as (i) is CO excited by shocks or UV heating? (ii) How much warm gas is present in the inner regions of the protostellar envelopes and from which location does it originate? What is the mass of the swept-up gas and how warm is it? (iii) What is the CO abundance structure throughout the envelope: where is CO frozen out and where is it processed?

Over the past several years, our group has conducted a survey of APEX-CHAMP$^+$ mapping of high$-J$ lines of CO and isotopologs of embedded low-mass Stage 0 and 1 (cf.

nomenclature by Robitaille et al. 2006) young stellar objects (YSOs) (van Kempen et al. 2009a,b,c, Paper I and II in this series). These data complement our earlier surveys at lower frequency of CO and other molecules with the James Clerk Maxwell Telescope (JCMT), IRAM 30m, APEX, and Onsala telescopes (e.g., Jørgensen et al. 2002, 2004, van Kempen et al. 2009c). More recently, the same sources are being observed with the *Herschel* Space Observatory in the context of the 'Water in star-forming regions with Herschel' (WISH) key program (van Dishoeck et al. 2011). The ^{12}CO J=6–5 (E_u/k=115 K) line is particularly useful in tracing the outflows through broad line-wings, complementing recent mapping in the ^{12}CO J=3–2 line with the HARP-B array on the JCMT (e.g., Curtis et al. 2010b). The availability of lines up to CO J=7–6 gives much tighter constraints on the excitation temperature of the gas, which together with the higher angular resolution of the high frequency data should result in a more accurate determination of outflow properties such as the force and momentum.

In addition to broad line-wings, van Kempen et al. (2009b) also found *narrow* extended ^{12}CO 6–5 emission along the cavity walls. Combined with narrow ^{13}CO 6–5 emission, this was interpreted as evidence of UV photon-heated gas, following the earlier work of Spaans et al. (1995). The mini-survey by van Kempen et al. (2009c) found this narrow extended emission to be ubiquitous in low-mass protostars. Further evidence of UV photon heating was provided by far-infrared CO lines with J_u=10 to 20 observed with *Herschel*-PACS (van Kempen et al. 2010b, Visser et al. 2012). However, *Herschel* has only limited mapping capabilities; PACS lacks velocity resolution and HIFI has a quite large beam (20"– 40"). Thus, the large-scale velocity-resolved maps at < 10" resolution offered by APEX-CHAMP$^+$ form an important complement to the *Herschel* data. In this paper, we present fully sampled high-J CHAMP$^+$ maps of one of the largest and most prominent low-mass outflow regions, NGC 1333 IRAS 4.

NGC 1333 IRAS 4A and IRAS 4B (hereafter only IRAS 4A and IRAS 4B) are two low-mass protostars in the southeast corner of the NGC 1333 region (see Walawender et al. 2008, for review). They have attracted significant attention owing to their strong continuum emission, powerful outflows, and rich chemistry (André & Montmerle 1994, Blake et al. 1995, Bottinelli et al. 2007). They were first identified as water maser spots by Ho & Barrett (1980) and later confirmed as protostellar candidates by IRAS observations (Jennings et al. 1987) and resolved individually in JCMT-SCUBA submm continuum maps (Sandell et al. 1991, Sandell & Knee 2001, Di Francesco et al. 2008). Using mm interferometry, it was subsequently found that both protostars are in proto-multiple systems (Lay et al. 1995, Looney et al. 2000). The projected separation between IRAS 4A and IRAS 4B is 31" (~7500 AU). The companion to IRAS 4B is clearly detected at a separation of 11", whereas that of IRAS 4A has a separation of only 2" (Jørgensen et al. 2007). The distance to the NGC 1333 nebula remains unclear (see Curtis et al. 2010a, for more thorough discussions). In this paper, we adopt the distance of 235±18 pc based on VLBI parallax measurements of water masers in SVS 13 in the same cluster (Hirota et al. 2008).

We present an APEX-CHAMP$^+$ ^{12}CO 6–5 map over a 4'×4' area at 9" resolution, together with ^{13}CO 6–5 and [C I] J=2–1 maps over a smaller region (1' × 1'). Moreover, ^{13}CO 8–7

and $C^{18}O$ 6–5 lines are obtained at the central source positions. These data are analyzed together with the higher-J *Herschel*-HIFI observations of CO and isotopologs published by Yıldız et al. (2010), as well as lower-J JCMT, IRAM 30m, and Onsala archival data so that spectrally resolved information on nearly the entire CO ladder up to 10–9 (E_u/k=300 K) is obtained for all three isotopologs. The spectrally resolved data allow the temperatures in different components to be determined, and thus provide an important complement to spectrally unresolved *Herschel* PACS and SPIRE data of the CO ladder of these sources. In addition, a new JCMT HARP-B map of ^{12}CO 3–2 was obtained over the same area, as well as deep ^{13}CO spectra at selected outflow positions to constrain the optical depth. The APEX-CHAMP$^+$ and JCMT maps over a large area can test the interpretation of the different velocity components seen in HIFI data, which has so far been based on only single position data.

The outline of the paper is as follows. In Section 4.2, the observations and the telescopes where the data have been obtained are described. In Section 4.3, the inventory of complementary lines and maps are presented. In Section 4.4, the data are analyzed to constrain the temperature and mass of the molecular outflows. In Section 4.5, the envelope abundance structure of these protostars is discussed. In Section 4.6, the amount of shocked gas is compared quantitatively to that of photon-heated gas. In Section 4.7, the conclusions of this work are summarized.

4.2   Observations

Table 4.1 gives a brief overview of the IRAS 4A and 4B sources. Spectral line data were obtained primarily from the 12-m sub-mm Atacama Pathfinder Experiment Telescope, APEX[1] (Güsten et al. 2008) at Llano de Chajnantor in Chile. In addition, we present new and archival results from the 15-m James Clerk Maxwell Telescope, JCMT[2] at Mauna Kea, Hawaii; the 3.5-m *Herschel* Space Observatory[3] (Pilbratt et al. 2010) and IRAM 30m telescope. Finally, we use published data from the Onsala 20-m and 14-m Five College Radio Astronomy Observatory, FCRAO telescopes.

APEX: The main focus of this paper is the high-J CO 6–5 and [C I] 2–1 maps of IRAS 4A and 4B, obtained with APEX-CHAMP$^+$ in November 2008 and August 2009. The protostellar envelopes and their complete outflowing regions were mapped in CO 6–5 emission using the on-the-fly mapping mode acquiring more than 100 000 spectra in 1.5 hours covering a Nyquist sampled 240″×240″ region. The instrument consists of two heterodyne

---

[1] This publication is based on data acquired with the Atacama Pathfinder Experiment (APEX). APEX is a collaboration between the Max-Planck-Institut für Radioastronomie, the European Southern Observatory, and the Onsala Space Observatory.

[2] The JCMT is operated by The Joint Astronomy Centre on behalf of the Science and Technology Facilities Council of the United Kingdom, the Netherlands Organisation for Scientific Research, and the National Research Council of Canada.

[3] Herschel is an ESA space observatory with science instruments provided by European-led Principal Investigator consortia and with important participation from NASA.

Table 4.1 – Source properties

Source	RA(J2000)	Dec(J2000)	Distance[a]	L_{bol}[b]	V_{LSR}[c]
	[$^{\text{h m s}}$]	[$^{\circ}$ ′ ″]	[pc]	[$L_{\odot}$]	[km s^{-1}]
IRAS 4A	03 29 10.5	+31 13 30.9	235	9.1	+7.0
IRAS 4B	03 29 12.0	+31 13 08.1	235	4.4	+7.1

Notes: [a] Adopted from Hirota et al. (2008). [b] Karska et al. (subm.) [c] Obtained from C^{18}O and C^{17}O lines (this work).

receiver arrays, each with seven pixel detector elements for simultaneous operations in the 620–720 GHz and 780–950 GHz frequency ranges (Kasemann et al. 2006, Güsten et al. 2008). The following two lines were observed simultaneously: ^{12}CO 6–5 and [C I] 2–1 (large map); ^{13}CO 6–5 and [C I] 2–1 (smaller map); C^{18}O 6–5 and ^{13}CO 8–7 (staring at source positions); and ^{12}CO 6–5 and ^{12}CO 7–6 (staring at source positions).

The APEX beam sizes correspond to 8″ (~1900 AU at a distance of 235 pc) at 809 GHz and 9″ (~2100 AU) at 691 GHz. The observations were completed under excellent weather conditions (precipitable water vapor, PWV ~0.5 mm) with typical system temperatures of 1900 K for CHAMP$^+$-I (SSB, 691 GHz), and 5600 K for CHAMP$^+$-II (SSB, 809 GHz). The relatively high system temperatures are due to the high atmospheric pathlength at the low elevation of the sources of ~25°. For CHAMP$^+$-II, there is also a significant contribution from the receiver temperature. The observations were done using position-switching toward an emission-free reference position in settings ^{12}CO 6–5 + [C I] 2–1 or CO 7–6, and ^{13}CO 6–5 + [C I] 2–1. However, in the setting C^{18}O 6–5 and ^{13}CO 8–7, a beam-switching of +/–90″ was used in staring mode in order to increase the S/N on the central pixel (van Dishoeck et al. 2009). The CHAMP$^+$ array uses the Fast Fourier Transform Spectrometer (FFTS) backend (Klein et al. 2006) for all seven pixels with a resolution of 0.12 MHz (0.045 km s^{-1} at 800 GHz).

JCMT: A CO 3–2 fully sampled map was obtained from the JCMT with the HARP-B instrument in March 2010. HARP-B consists of 16 SIS detectors with 4×4 pixel elements of 15″ each at 30″ separation. The opacity at the time of observations was excellent ($\tau_{225\text{GHz}}$ <0.04) and the on-the-fly method was used to fully cover the entire outflow. Apart from the maps, line data of CO and its isotopologs (e.g., 2–1 and 3–2 lines) were obtained from the JCMT and its public archive[4]. In Tables 4.2 and 4.3, the offset values of the archival data from the protostellar source coordinates are provided. In addition, we observed four distinct outflow knots of IRAS 4A in deep ^{12}CO and ^{13}CO 2–1 integrations to constrain the optical depth (see Table 4.2 for coordinates). The B1 and R1 positions are the blue and red-shifted outflow knots closest to IRAS 4A, and B2 and R2 are the two prominent dense outflow knots furthest from the source position.

Herschel: Spectral lines of ^{12}CO 10–9, ^{13}CO 10–9, C^{18}O 5–4, 9–8, and 10–9 were ob-

---

[4] This research used the facilities of the Canadian Astronomy Data Centre operated by the National Research Council of Canada with the support of the Canadian Space Agency.

served with the *Herschel* Space Observatory using the Heterodyne Instrument for Far-Infrared (HIFI); (de Graauw et al. 2010). All observations were done in dual-beam-switch (DBS) mode with a chop reference position located 3′ from the source positions. Except for the $C^{18}O$ 10–9 spectra, these data were presented in Yıldız et al. (2010) and observational details can be found there.

IRAM-30m: The lower-J ^{13}CO 1–0 and $C^{17}O$ 2–1 transitions were observed with the IRAM 30-m telescope [5] by Jørgensen et al. (2002) and Pagani et al. (in prep).

Onsala: The lowest-J $C^{17}O$ and $C^{18}O$ 1–0 transitions were observed with the Onsala 20-m radiotelescope by Jørgensen et al. (2002), and the spectra are used here.

FCRAO: ^{12}CO 1–0 spectrum of IRAS 4A is extracted from COMPLETE survey map (Arce et al. 2010) observed with FCRAO.

Tables 4.2 and 4.3 summarizes the list of observed lines for each instrument. Information about the corresponding rest frequencies and upper-level energies of the transitions are included, together with the beam sizes and efficiencies of the instruments. The data were acquired on the T_{A}^{*} antenna temperature scale, and were converted to main-beam brightness temperatures $T_{MB} = T_{A}^{*}/\eta_{MB}$ using the stated beam efficiencies (η_{MB}). The $CHAMP^{+}$ beam efficiencies were taken from the $CHAMP^{+}$ website[6] and forward efficiencies are 0.95 in all observations. The JCMT beam efficiencies were taken from the JCMT Efficiencies Database[7], and the *Herschel*-HIFI efficiencies were assumed to be 0.76 in all bands except band 5, where it is 0.64 (Roelfsema et al. 2012). The Onsala efficiencies were taken from Jørgensen et al. (2002). Calibration errors were estimated to be ∼20% for the ground-based telescopes, and ∼10% for the HIFI lines. For the data reduction and analysis, the "Continuum and Line Analysis Single Dish Software", CLASS program which is part of the GILDAS software[8], is used. The routines in GILDAS convolved the irregularly gridded on-the-fly data with a Gaussian kernel of a size of one third of the beam, yielding a Nyquist-sampled map.

---

[5] Based on observations carried out with the IRAM 30m Telescope. IRAM is supported by INSU/CNRS (France), MPG (Germany) and IGN (Spain).

[6] http:www.mpifr.de/div/submmtech/heterodyne/champplus/champ_efficiencies.15-10-09.html

[7] http://www.jach.hawaii.edu/JCMT/spectral_line/Standards/eff_web.html

[8] http:www.iram.fr/IRAMFR/GILDAS

Table 4.2 – Overview of the observations of IRAS 4A

Source	Mol.	Trans. J_u-J_l	E_u [K]	Freq. [GHz]	Telescope	Beam size ["]	Efficiency η	Map	Offset[a] [$\Delta\alpha$ ", $\Delta\delta$ "]	Obs. Date	References
IRAS 4A	CO	1–0	5.5	115.271202	FCRAO	46	0.45	yes	(0.0,0.0)	01/01/2000	(1)
		2–1	16.6	230.538000	JCMT-RxA	22	0.69	no	(0.0,0.3)	21/10/1995	(2)
		3–2	33.2	345.795989	JCMT-HARP-B	15	0.63	yes	(0.0,0.0)	18/03/2010	(3)
		4–3	55.3	461.040768	JCMT	11	0.38	no	(0.0,0.2)	23/12/1994	(2)
		6–5	116.2	691.473076	APEX-CHAMP$^+$	9	0.48	yes	(0.0,0.0)	11/11/2008	(3)
		7–6	154.9	806.651806	APEX-CHAMP$^+$	8	0.45	yes	(1.5,1.3)	10/11/2008	(3)
		10–9	304.2	1151.985452	*Herschel*-HIFI	20	0.66	no	(0.0,0.0)	05/03/2010	(4)
	^{13}CO	1–0	5.3	110.201354	IRAM 30m	23	0.77	yes	(0.0,0.0)	21/07/2010	(5)
		2–1	15.87	220.398684	JCMT-RxA	23	0.74	no	(0.0,0.1)	11/11/2001	(2)
		3–2	31.7	330.587965	JCMT-B3	15	0.60	no	(0.0,0.1)	16/09/2009	(2)
		4–3	52.9	440.765174	JCMT	11	0.38	no	(0.2,0.8)	25/03/2003	(2)
		6–5	111.05	661.067277	APEX-CHAMP$^+$	9	0.52	yes	(0.0,0.0)	24/08/2009	(3)
		8–7	190.36	881.272808	APEX-CHAMP$^+$	7	0.42	no	(0.0,0.0)	26/08/2009	(3)
		10–9	290.8	1101.349597	*Herschel*-HIFI	21	0.76	no	(0.0,0.0)	04/03/2010	(4)
	C^{17}O	1–0	5.39	112.358777	Onsala	33	0.43	no	(0.0,0.0)	13/11/2001	(6)
		2–1	16.18	224.713533	IRAM 30m	17	0.43	no	(0.0,0.0)	13/11/2001	(6)
		3–2	32.35	337.061513	JCMT-B3	15	0.60	no	(1.5,1.2)	25/08/2001	(2)
	C^{18}O	1–0	5.27	109.782173	Onsala	34	0.43	no	(0.0,0.0)	11/03/2002	(6)
		2–1	15.81	219.560354	JCMT-RxA	23	0.69	no	(0.0,0.6)	03/12/1993	(2)
		3–2	31.61	329.330553	JCMT-B3	15	0.60	no	(0.2,1.2)	26/08/2001	(2)
		5–4	79.0	548.831010	*Herschel*-HIFI	42	0.76	no	(0.0,0.0)	15/03/2010	(4)
		6–5	110.63	658.553278	APEX-CHAMP$^+$	10	0.48	no	(0.0,0.0)	26/08/2009	(3)
		9–8	237.0	987.560382	*Herschel*-HIFI	23	0.76	no	(0.0,0.0)	03/03/2010	(4)
		10–9	289.7	1097.162875	*Herschel*-HIFI	21	0.76	no	(0.0,0.0)	31/07/2010	(4)
	[C I]	2–1	62.3	809.341970	APEX-CHAMP$^+$	8	0.43	yes	(0.0,0.0)	24/08/2009	(3)
I4A B1[b]	CO	3–2	33.2	345.795989	JCMT-HARP-B	15	0.63	yes	(−12.0,−12.0)	18/03/2010	(3)
	CO	6–5	116.2	691.473076	APEX-CHAMP$^+$	9	0.48	yes	(−12.0,−12.0)	11/11/2008	(3)
I4A B2[b]	CO	2–1	16.6	230.538000	JCMT-RxA	22	0.69	no	(−34.5,−61.9)	02/07/2009	(3)
		3–2	33.2	345.795989	JCMT-HARP-B	15	0.63	yes	(−34.5,−61.9)	18/03/2010	(3)
		6–5	116.2	691.473076	APEX-CHAMP$^+$	9	0.48	yes	(−34.5,−61.9)	11/11/2008	(3)
	^{13}CO	2–1	15.9	220.398684	JCMT-RxA	22	0.69	no	(−34.5,−61.9)	02/07/2009	(3)
I4A R1[c]	CO	3–2	33.2	345.795989	JCMT-HARP-B	15	0.63	yes	(12.0,12.0)	18/03/2010	(3)
	CO	6–5	116.2	691.473076	APEX-CHAMP$^+$	9	0.48	yes	(12.0,12.0)	11/11/2008	(3)
I4A R2[c]	CO	2–1	16.6	230.538000	JCMT-RxA	22	0.69	no	(52.5,68.1)	02/07/2009	(3)
		3–2	33.2	345.795989	JCMT-HARP-B	15	0.63	yes	(52.5,68.1)	18/03/2010	(3)
		6–5	116.2	691.473076	APEX-CHAMP$^+$	9	0.48	yes	(52.5,68.1)	11/11/2008	(3)
	^{13}CO	2–1	15.9	220.398684	JCMT-RxA	22	0.69	no	(52.5,68.1)	02/07/2009	(3)

Notes: [a] Offset from the IRAS 4A source coordinates given in Table 4.1. [b] I4A-BX are the blueshifted outflow positions, and [c] I4A-RX are the redshifted outflow positions. These regions are also depicted in Fig. 4.3. (1) Ridge et al. (2006); (2) Archive; (3) this work; (4) Yıldız et al. (2010); (5) Jørgensen et al. (2002); (6) Pagani et al. in prep.

**Table 4.3** – Overview of the observations of IRAS 4B

Source	Mol.	Trans. J_u-J_l	E_u [K]	Freq. [GHz]	Telescope	Beam size ["]	Efficiency η	Map	Offset[a] [$\Delta\alpha$ ", $\Delta\delta$ "]	Obs. Date	References
IRAS 4B	CO	2–1	16.6	230.538000	JCMT-RxA	22	0.69	no	(0.0,0.0)	21/10/1995	(2)
		3–2	33.2	345.795989	JCMT-HARP-B	15	0.60	yes	(0.0,0.0)	18/03/2010	(3)
		4–3	55.3	461.040768	JCMT	11	0.38	no	(0.0,0.2)	22/01/2010	(2)
		6–5	116.2	691.473076	APEX-CHAMP⁺	9	0.48	yes	(0.0,0.0)	11/11/2008	(3)
		7–6	154.9	806.651806	APEX-CHAMP⁺	8	0.45	no	(0.0,0.0)	10/11/2008	(3)
		10–9	304.2	1151.985452	*Herschel*-HIFI	20	0.66	no	(0.0,0.0)	06/03/2010	(4)
	^{13}CO	1–0	5.3	110.201354	IRAM 30m	23	0.77	yes	(0.0,0.0)	21/07/2010	(5)
		3–2	31.7	330.587965	JCMT-B3	15	0.60	no	(0.0,0.0)	25/08/2001	(2)
		6–5	111.1	661.067276	APEX-CHAMP⁺	10	0.52	yes	(0.0,0.0)	24/08/2009	(3)
		8–7	190.4	881.272808	APEX-CHAMP⁺	7	0.42	no	(0.0,0.0)	30/08/2009	(3)
		10–9	290.8	1101.349597	*Herschel*-HIFI	21	0.76	no	(0.0,0.0)	04/03/2010	(4)
	C^{17}O	1–0	5.39	112.358777	IRAM 30m	33	0.43	no	(0.0,0.0)	13/11/2001	(6)
		2–1	16.18	224.713533	Onsala	17	0.43	no	(0.0,0.0)	13/11/2001	(6)
		3–2	32.35	337.060513	JCMT-B3	15	0.60	no	(0.0,0.0)	25/08/2001	(2)
	C^{18}O	1–0	5.27	109.782173	Onsala	34	0.43	no	(0.0,0.0)	11/03/2002	(6)
		2–1	15.81	219.560354	JCMT-RxA	23	0.69	no	(0.0,0.6)	08/02/1992	(2)
		3–2	31.61	329.330552	JCMT-B3	15	0.60	no	(0.2,1.2)	29/08/2001	(2)
		5–4	79.0	548.831006	*Herschel*-HIFI	42	0.76	no	(0.0,0.0)	15/03/2010	(4)
		6–5	110.63	658.553278	APEX-CHAMP⁺	10	0.48	no	(0.0,0.0)	30/08/2009	(3)
		9–8	237.0	987.560382	*Herschel*-HIFI	23	0.76	no	(0.0,0.0)	03/03/2010	(4)
		10–9	289.7	1097.162875	*Herschel*-HIFI	21	0.76	no	(0.0,0.0)	31/07/2010	(4)
	[C I]	2–1	62.3	809.341970	APEX-CHAMP⁺	8	0.42	yes	(0.0,0.0)	24/08/2009	(3)

Notes: [a] Offset from the IRAS 4B source coordinates given in Table 4.1. (2) Archive; (3) this work; (4) Yıldız et al. (2010); (5) Jørgensen et al. (2002); (6) Pagani et al. in prep.
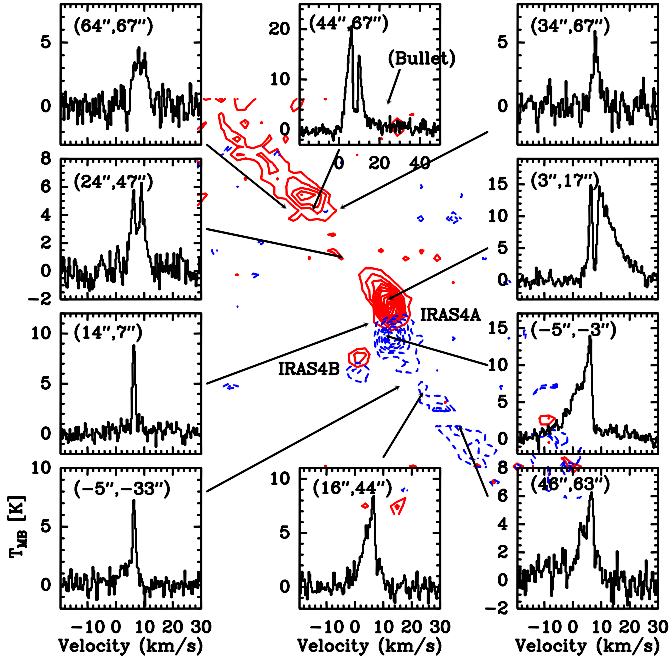
Figure 4.1 – Gallery of ^{12}CO 6–5 spectra from ten different locations. Spectra of the IRAS 4A and 4B central positions are shown in Fig. 4.2. The arrows indicate the exact locations of the corresponding spectra with respect to the outflow lobes and each spectrum is given with the offset from IRAS 4A. Note the mix of narrow (<2 km s^{-1}) and medium (10–15 km s^{-1}) profiles together with the broad lines (25–30 km s^{-1}) at the outflowing positions close to the center of IRAS 4A. We also note that the velocity scale of the (44″,67″) panel is different to emphasize the weak "bullet" emission (see text). The vertical scale is for T_{mb}. The contours are ^{12}CO 6–5 emission where the levels start from 3σ (15 K km s^{-1}) with an increasing step size of 2σ (10 K km s^{-1}). The blue and red velocity ranges are selected from -20 to 2.7 and from 10.5 km s^{-1} to 30 km s^{-1}, respectively.

4.3 Results

4.3.1 The CO line gallery

Figure 4.1 illustrates the quality of the APEX spectra as well as the variation in line profiles across the map. Several different velocity components can be identified, which can be most clearly seen at the central source positions. Figure 4.2 presents the gallery of CO lines at IRAS 4A and 4B using the APEX, JCMT, *Herschel*, IRAM 30m, Onsala and FCRAO telescopes. Available spectra of ^{12}CO, ^{13}CO, C^{18}O, C^{17}O, and [C I] ranging from 1–0 up to 10–9 are shown. Integrated intensities and peak temperatures are summarized in Table 4.4, which includes the rms of each spectrum after resampling all spectra to the same velocity resolution of 0.5 km s^{-1}. The S/N and dynamic range of the spectra is generally excellent with peak temperatures ranging from 30 mK to >20 K
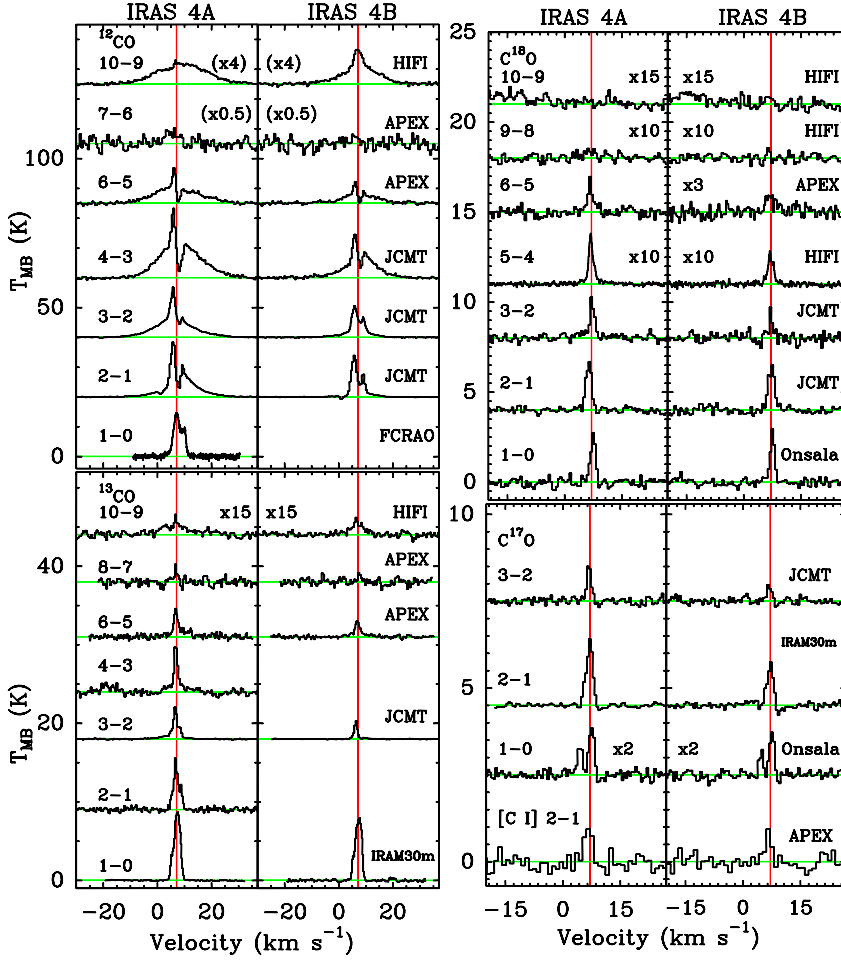
Figure 4.2 – Single spectra obtained from the central positions of IRAS 4A and 4B presented on a T_{MB} scale. From bottom to top, *Left:* ^{13}CO 1–0, ^{13}CO 2–1, ^{13}CO 3–2, ^{13}CO 4–3, ^{13}CO 6–5, ^{13}CO 8–7, ^{13}CO 10–9; ^{12}CO 1–0, ^{12}CO 2–1, ^{12}CO 3–2, ^{12}CO 4–3, ^{12}CO 6–5, ^{12}CO 7–6, ^{12}CO 10–9; *Right:* [C I] 2–1, $C^{17}O$ 1–0, $C^{17}O$ 2–1, $C^{17}O$ 3–2; $C^{18}O$ 1–0, $C^{18}O$ 2–1, $C^{18}O$ 3–2, $C^{18}O$ 5–4, $C^{18}O$ 6–5, $C^{18}O$ 9–8, $C^{18}O$ 10–9. The spectra have been shifted vertically for viewing purposes and refer to the observing beams presented in Tables 4.2 and 4.3. The red vertical line corresponds to the source velocity, V_{LSR} as measured from the $C^{18}O$ and $C^{17}O$ lines.

Table 4.4 – Observed line intensities for IRAS 4A and 4B in all observed transitions.

Source	Mol.	Transition	$\int T_{MB}dV^a$ [K km s^{-1}]	T_{peak} [K]	Blue ($\int T_{MB}dV$)^b [K km s^{-1}]	Red ($\int T_{MB}dV$)^c [K km s^{-1}]	rms^d [K]
IRAS 4A	CO	1–0	60.1	13.0	1.1	26.1	0.45
		2–1	117.1	18.4	12.9	37.8	0.11
		3–2	128.0	16.8	34.4	30.6	0.07
		4–3	220.0	23.4	47.4	86.8	0.29
		6–5	110.5	11.9	31.8	37.4	0.33
		7–6	55.0	10.0	…	…	4.39
		10–9	40.7	1.9	9.9	17.6	0.07
	^{13}CO	1–0	26.2	8.5	…	…	0.03
		2–1	16.0	6.5	…	…	0.23
		3–2	11.4	4.0	1.2	0.2	0.04
		4–3	15.2	5.7	…	…	0.36
		6–5	11.4	3.6	0.7	1.7	0.21
		8–7	2.4	2.2	…	…	0.39
		10–9	1.1	0.2	…	…	0.02
	C^{17}O	1–0	1.8	0.7	…	…	0.05
		2–1	3.8	1.9	…	…	0.04
		3–2	1.6	1.0	…	…	0.09
	C^{18}O	1–0	4.3	2.7	…	…	0.18
		2–1	4.9	2.7	…	…	0.13
		3–2	4.2	2.3	…	…	0.17
		5–4	0.6	0.4	…	…	0.006
		6–5	3.3	2.0	…	…	0.21
		9–8	0.16	0.05	…	…	0.02
		10–9	<0.05^e	…	…	…	0.02
	[C I]	2–1	2.3	1.0	…	…	0.21^f
I4A-B1	CO	3–2	92.8	14.0	64.8	10.1	0.37
		6–5	96.6	13.7	81.6	4.5	0.32
I4A-B2	CO	2–1	49.5	7.1	32.8	7.6	0.04
	^{13}CO	2–1	11.6	3.7	…	…	0.03
I4A-B2	CO	3–2	71.2	12.3	12.8	40.5	0.42
		6–5	109.1	10.8	16.4	79.2	0.86
I4A-R2	CO	2–1	41.1	8.8	13.7	20.3	0.04
	^{13}CO	2–1	13.3	4.6	…	…	0.03
IRAS 4B	CO	2–1	54.7	13.9	1.0	4.6	0.07
		3–2	57.0	10.5	6.6	6.7	0.05
		4–3	114.4	14.6	20.4	35.4	0.29
		6–5	52.3	5.9	10.7	16.5	0.34
		7–6	<39.0^e	…	…	…	4.51
		10–9	29.7	2.9	5.9	8.7	0.08
	^{13}CO	1–0	23.9	7.9	…	…	0.09
		3–2	5.9	2.3	…	…	0.03
		6–5	6.8	2.0	0.4	0.8	0.16
		8–7	2.7	2.3	…	…	0.39
		10–9	0.6	0.15	…	…	0.02
	C^{17}O	1–0	1.3	0.6	…	…	0.05
		2–1	2.3	1.3	…	…	0.06
		3–2	0.5	0.4	…	…	0.07
	C^{18}O	1–0	4.4	2.9	…	…	0.18
		2–1	5.3	2.5	…	…	0.16
		3–2	1.9	1.7	…	…	0.23
		5–4	0.3	0.2	…	…	0.007
		6–5	0.9	0.4	…	…	0.07
		9–8	<0.06^e	…	…	…	0.02
		10–9	<0.06^e	…	…	…	0.02
	[C I]	2–1	1.8	0.9	…	…	0.17^f

Notes: ^{a}Velocity range used for integration: –20 km s^{-1} to 30 km s^{-1}. ^{b}Blue emission is calculated by selecting a velocity range of –20 to 2.7 km s^{-1}. ^{c}Red emission is calculated by selecting a velocity range of 10.5 to 30 km s^{-1}. ^{d}In 0.5 km s^{-1} bins. ^{e}Upper limits are 3σ. ^{f}In 1.0 km s^{-1} bins.

compared with the rms values from 0.006 to 0.4 K. Note in particular the very high S/N obtained at the C^{18}O 5–4 line with *Herschel* (~6 mK in 0.5 km s^{-1} bins). Even C^{18}O is detected up to J=10–9 in IRAS 4B, albeit only tentatively (1.5 σ) in the 10–9 line itself. Together with the IRAS 2A data of Yıldız et al. (2010), this is the first time that the complete CO ladder up to 10–9 is presented for low-mass protostars, not just for ^{12}CO but also for its isotopologs, and with spectrally resolved data.

As discussed in Kristensen et al. (2010) based on H_2O spectra, the central line profiles can be decomposed into three components. A *narrow* profile with a FWHM of 2–3 km s^{-1} can mainly be found in the optically thin $C^{18}O$ and $C^{17}O$ isotologue lines at the source velocity. This profile traces the quiescent envelope material. Many ^{12}CO and ^{13}CO line profiles contain a *medium* component with a FWHM of 5–10 km s^{-1}, which is indicative of small-scale shocks in the inner dense protostellar envelope (<1000 AU). The latter assignment is based largely on interferometry maps of this component toward IRAS 2A (Jørgensen et al. 2007). The ^{12}CO lines are mainly dominated by the *broad* component that has a FWHM of 25–30 km s^{-1} on >1000 AU scales representative of the swept-up outflow gas (Fig. 4.2).

4.3.2 Maps

The observations presented here are large-scale 240″ × 240″ maps in ^{12}CO 6–5 and ^{12}CO 3–2 covering the entire IRAS 4A/B region, together with smaller scale 80″ × 80″ maps of ^{13}CO 6–5 and [C I] 2–1 around the protostellar sources.

4.3.2.1 ^{12}CO 6–5 map

The large ^{12}CO 6–5 map over an area of 240″×240″ (∼56 500 × 56 500 AU) includes all the physical components of both protostars. Figure 4.3 (left) shows a ^{12}CO 6–5 contour map of the blue and red outflow lobes, whereas Fig. 4.3 (right) includes the map of individual spectra overplotted on a contour map. This spectral map has been resampled to 10″×10″ pixels for visual convenience, although the contours are calculated for a Nyquist sampling rate of 4.″5 × 4.″5 pixel size. All spectra are binned to a 0.3 km s^{-1} velocity resolution. The red and blue outflow contours are obtained by integrating the blue and red wings of each spectrum separately. The selected ranges are –20 to 2.7 km s^{-1} for the blue and 10.5 to 30 km s^{-1} for the red emission. These ranges are free of cloud and envelope emission and are determined by averaging spectra from outflow-free regions.

The ^{12}CO 6–5 map shows a well-collimated outflow to the NE and SW directions centered at IRAS 4A with two knots like a mirror image on each side. Close to the protostar itself, the outflow appears to be directed in a pure N-S direction, with the position angle on the sky rotating through about 45° at a 10″ (2350 AU) distance. This N-S direction was seen in the interferometer data of Jørgensen et al. (2007) and Choi et al. (2011), and the high angular resolution of APEX-CHAMP$^+$ now allows this component to be revealed also in single dish data. Its morphology could be indicative of a rotating/wandering jet emanating from either IRAS 4A or two flows from each of the binary components of IRAS4A. The outflow from IRAS 4B is much more spatially compact moving in the N-S direction. Overall, the CO 6–5 CHAMP$^+$ maps are similar to the CO 3–2 map shown in Fig. 4.20 and in Blake et al. (1995). However, owing to the ∼2 times larger beam, the N-S extension around IRAS 4A is not obvious in the 3–2 map and the knots are less 'sharp'. In addition, the compact IRAS 4B outflow is clearly revealed in single-dish data here for
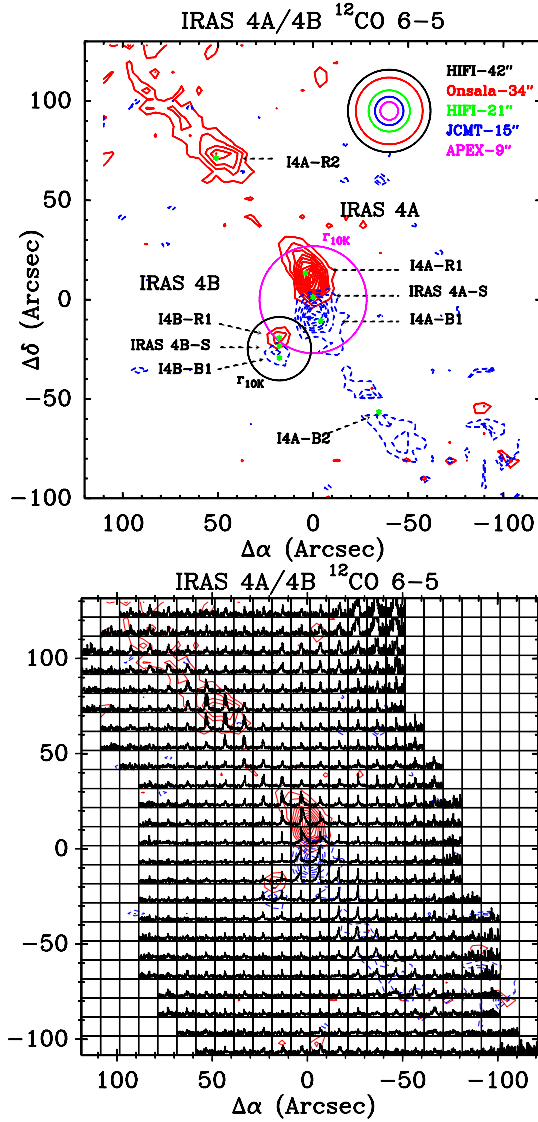
Figure 4.3 – (*Right:*) The ^{12}CO 6–5 spectral map of IRAS 4A and 4B over the 240″×240″ mapping area. Individual spectra are shown on the T_{MB} scale from –2 K to 12 K and velocity scale from –20 km s^{-1} to 30 km s^{-1}. The outflows of IRAS 4A and 4B are overplotted over the entire spectral map. The map is centered on IRAS 4A. The contour levels start from 3σ (15 K km s^{-1}) with an increasing step size of 2σ (10 K km s^{-1}). (*Left:*) Envelopes of IRAS 4A and 4B at the 10 K radius are shown together with the beam-sizes compared. See Fig. 1 caption and Sect. 3.2.1 for the details and the positions at which deep spectra are obtained.
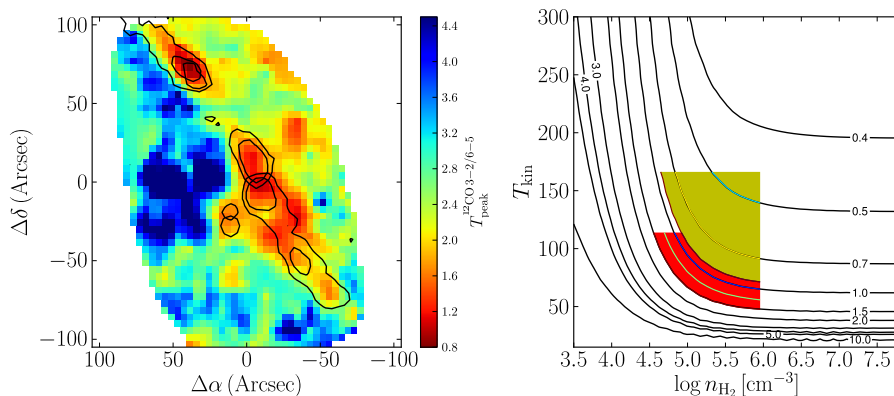
Figure 4.4 – *Left:* Map of peak intensity ratios of the ^{12}CO 3–2 /6–5 lines. *Right:* Model of the CO 3–2 / CO 6–5 line intensity ratio as function of temperature and density. The red region represents the observed range for IRAS 4A, and the yellow range for IRAS 4B. The CO column density is taken to be 10^{17} cm^{-2} with a line width of 10 km s^{-1}, these conditions are chosen because they are representative of the observed CO 6–5 flux and line width. The colored lines give the range of densities within the 20$''$ beam for the two sources based on the models of Kristensen et al. (2012). In the relevant density range, smaller ratios are indicative of higher temperatures.

the first time. In the north-western part of the map, the southern tip of the SVS 13 flow is seen (HH 7–11; Curtis et al. 2010b).

4.3.2.2 ^{12}CO 3–2 map

The large and fully sampled ^{12}CO 3–2 JCMT HARP-B map covers the same area as the ^{12}CO 6–5 map. In Fig. 4.20, we show the CO 3–2 contour and spectral maps presenting blue and red outflow lobes. Here, the spectral map is resampled to 15$''$×15$''$ pixels and the contours are calculated at the Nyquist sampling rate of 7.5"× 7.5"pixel size. The same velocity ranges as in the CO 6–5 map are used to calculate the blue and red outflow emission. Overall, the 3–2 map is very similar to those presented by Blake et al. (1995) and Curtis et al. (2010b).

The line ratio map of CO 3–2/CO 6–5 is presented in Fig. 4.4. The CO 6–5 map is convolved to the same beam as CO 3–2 and the peak antenna temperatures have been used to avoid having differences in line widths dominate the ratios. The distribution of the line ratios is flat at 0.8–1.0 around the center and outflow knots, with values of up to 2.5 in the surrounding regions. As discussed further in Sect. 4.4.2.1, this implies higher temperatures towards the center and outflow knots than in the envelope at some distance away from the outflow.

Figure 4.5 shows maps of the maximum spectral velocities V_{max} obtained from the full width at zero intensity (FWZI) at each position for both the 6–5 and 3–2 maps. A 1.5σ
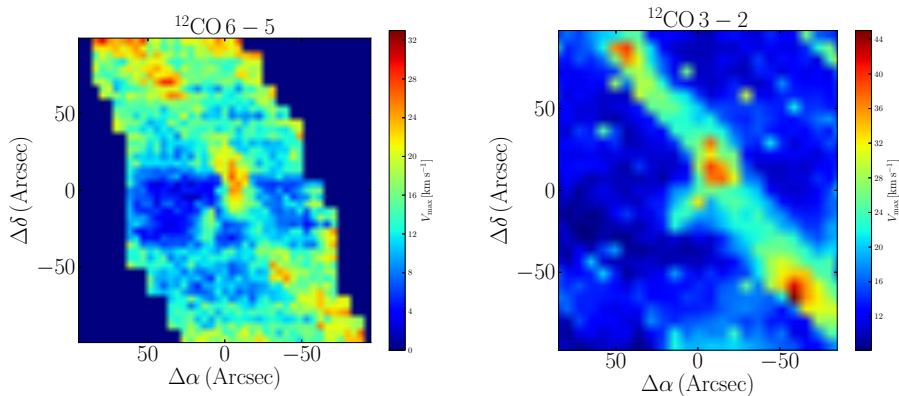
Figure 4.5 – Maps of V_{max} obtained from full width at zero intensity (FWZI) at each position in both CO 6–5 (*left*) and CO 3–2 (*right*) maps.

cutoff is applied to determine the FWZIs in both maps. Owing to the lower rms of the data, CO 3–2 can trace higher velocities than CO 6–5. Overall, the profiles indicate narrow lines throughout the envelope with broad shocked profiles along the outflows (see also Fig. 4.1). Similar results were found by van Kempen et al. (2009b) for the HH 46 protostar and outflow. The highest velocities of V_{max} = 25–30 km s^{-1} are found at the source positions (where both red and blue wings contribute) and the positions of the outflow knots.

Specifically, the IRAS 4A-R2 outflow knot has an extremely high velocity component (EHV or "bullet") at $V \sim 20$–35 km s^{-1} as seen clearly in the 3–2 map (Fig. 4.21 in the Auxillary Figures). In the CO 6–5 map, the "bullet" emission is only weakly detected ($\sim$5σ, Fig. 4.1) and is ignored in the rest of this paper.

4.3.2.3 ^{13}CO 6–5 map

The ^{13}CO 6–5 isotopolog emission was mapped over a smaller $80'' \times 80''$ region presented in Fig. 4.6. This map only covers the immediate environment of the protostellar envelopes of both protostars and the outflow of IRAS 4B. Figure 4.6 (left) shows the map of total integrated intensity, whereas Fig. 4.6 (right) shows the spectral map with the outflow contours obtained using the same velocity range as in the CO 6–5 map. The ^{13}CO 6–5 lines are not simple narrow Gaussians, but clearly show the medium outflow component centered on the protostars. The medium component has a FWHM of $\Delta v = 8$–10 km s^{-1}, while the narrow component has again $\Delta v = 1.5$-2 km s^{-1}.
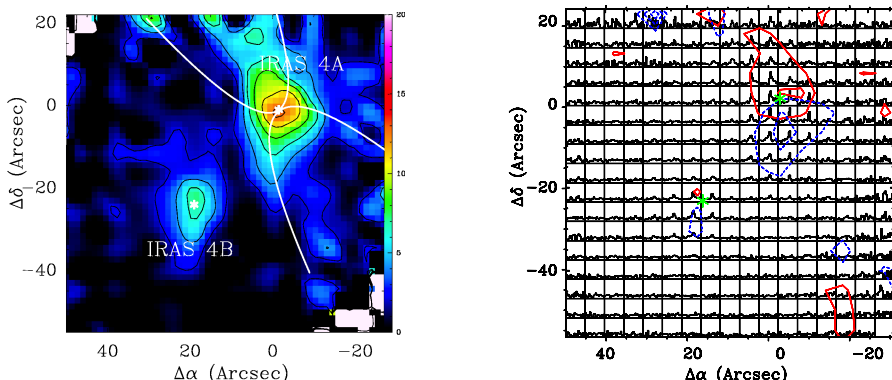
Figure 4.6 – ^{13}CO 6–5 maps of IRAS 4A (0,0) and IRAS 4B (22.5,-22.8). *Left*: Integrated intensity map of IRAS 4A and 4B in a 80″×80″ area. The white elliptical biconical shape delineate the outflow cones as discussed in Sect. 4.6. *Right*: Blue and redshifted outflows seen in the ^{13}CO 6-5 line profiles overplotted on a spectral map of the same region. Individual spectra are shown on a T_{MB} scale from −1 K to 4 K and the velocity scale runs from −5 km s^{-1} to 15 km s^{-1}. The contour levels for both figures are 3σ, 6σ, 9σ, ... where σ=0.6 K.

4.3.2.4 [C I] 2–1 map

Figure 4.22 (in the Auxillary Figures) shows the weak detection of atomic carbon emission in and around the envelope and the outflow cavities, with the ^{12}CO 6–5 red and blue contours overlaid (see also Fig. 4.3 right panel). This figure is a combination of three different observations, with one map covering only the central region (obtained in parallel with the ^{13}CO 6–5 map). Thus, the noise level is higher at the edges of the figure. The spectra have been resampled to 1 km s^{-1} velocity resolution in order to significantly reduce the noise; nevertheless, the [C I] line is barely detected with a peak temperature of at most 1 K. The weak emission indicates that CO is not substantially dissociated throughout the region, i.e., the UV field cannot contain many photons with wavelengths <1100 Å (van Dishoeck & Black 1988), as also concluded in van Kempen et al. (2009a). The low S/N of the [C I] data precludes detection of any broad outflow component. In HH 46, we note that stronger [C I] emission is found at the bow shock position, but this line is still narrow (ΔV ~1 km s^{-1}; van Kempen et al. 2009b).

4.3.3 Morphology

By examining the morphology of the outflows from the CO 3–2 and 6–5 maps, it is possible to quantify the width and length of the outflows. The CO 6–5 map is used to calculate these quantities because it has a higher spatial resolution by a factor of two. The length of the outflow, R_{CO}, is defined as the total outflow extension assuming the outflows are fully covered in the map. By taking into account the distance to the source, the projected R_{CO} is measured as 105″ (~25 000 AU) and 150″ (~35 000 AU) for IRAS 4A for its blue and

red outflow lobes, respectively. The difference in extent could be a result of the denser gas deflecting or blocking the blue outflow lobe (Choi et al. 2011). For IRAS 4B, the extents are 12″ (~1 900 AU) and 9″ (~750 AU), respectively, but these should be regarded as upper limits since the IRAS 4B outflow is not resolved. The width of the IRAS 4A outflow is ~20"(~4 700 AU), after deconvolution with the beam size. These values do not include corrections for inclination.

The "collimation factor", R_{coll}, for quantifying the outflow bipolarity is basically defined as the ratio of the major to minor axes of the outflow. This quantity has been used to distinguish Stage 0 objects from the more evolved Stage I objects, in which the outflow angle has been widened (Bachiller & Tafalla 1999, Arce & Sargent 2006). The R_{coll} for IRAS 4A is found to be 5.3±0.5 for the blue outflow lobe and 7.5±0.5 for the red outflow lobe. For IRAS 4B, no collimation factor can be determined since the outflow is unresolved. Nevertheless, the much smaller extent of the IRAS 4B outflow raises the question of whether IRAS 4B is much younger than IRAS 4A or whether this is simply an effect of inclination. The inclination of an outflow, which is defined as the angle between the outflow direction and the line of sight (Cabrit & Bertout 1990), can in principle be estimated from the morphology in the contour maps.

The IRAS 4 system is part of a clustered star-forming region so that the formation timescales for any of the YSOs in this region are expected to be similar. In addition, the bolometric luminosities of IRAS 4A and 4B are comparable. For IRAS 4B, the *Herschel*-PACS observations of Herczeg et al. (2012) detect only line emission from the blue outflow lobe, with the red outflow lobe being hidden by >1000 mag of extinction. These data support a close to face-on orientation where the blue lobe punches out of the cloud with little extinction and the red lobe is buried deep inside the cloud. The high resolution millimeter interferometer data of Jørgensen et al. (2007) as well as our data, however, do not show any overlap between the IRAS 4B blue and red outflow lobes, which would imply that they are not completely, but close to face-on with an inclination close to the line of sight of ~15–30°. This range is consistent with that of 10–35° suggested for IRAS 4B based on VLBI H_2O water maser observations (Desmurs et al. 2009). The large extent of the collimated outflow of IRAS 4A with, at the same time, high line-of-sight velocities suggests an inclination of ~45–60° to the line of sight. It is unlikely to be as high as the values of 80–85° claimed for L1527 (i=85°) and L483 (80°; Tobin et al. 2008). Karska et al. (in prep.) find much lower velocities (~6–10 km s^{-1}) in their CO 6–5 maps for these sources than in IRAS 4A/4B (~20–30 km s^{-1}).

Under the assumption that the intrinsic lengths of the flows are similar, Fig. 4.7 presents the various options for the relative orientation of the two outflows viewed from different angles, all three of which can lead to the observed projected situation seen in Fig. 4.7a. In the first scenario, the envelopes are very close to each other and interact accordingly (Fig. 4.7b). In the second scenario, the envelopes may be sufficiently separated in distance such that they do not interact with each other. In this case, IRAS 4A is either in front of IRAS 4B (Fig. 4.7c) or IRAS 4B is in front of IRAS 4A (4.7d).

The dynamical age of the outflows can be determined by $t_{\mathrm{dyn}} = R_{\mathrm{CO}}/\overline{V}_{\mathrm{max}}$, where $\overline{V}_{\mathrm{max}}$ is
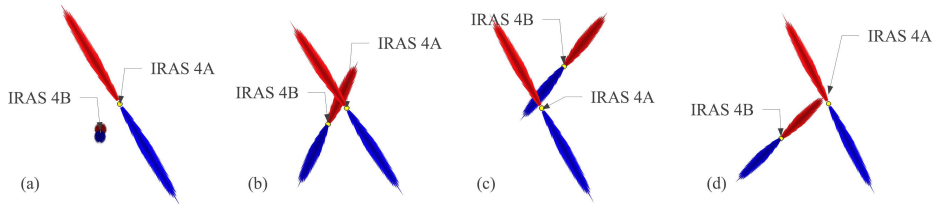
Figure 4.7 – Four different projection scenarios of the IRAS 4A and 4B outflows are presented, assuming that the two outflows have similar physical extents. These scenarios are treated by keeping the position of IRAS 4A fixed and rotating the plane of the sky through ~60° for better comprehension the difference of IRAS 4B in (b)-(d). (*a*) shows the geometry projected on the plane of the sky; (*b*) the protostars are at the same distance and very close to each other so that their envelopes overlap; (*c*) IRAS 4A is in front of IRAS 4B; and (*d*) IRAS 4B is in front of IRAS 4A. In the latter two scenarios, the envelopes may be sufficiently distant from each other and may not overlap.

the average total velocity extent measured relative to the source velocity (Cabrit & Bertout 1992). The values of $\overline{V}_{\mathrm{max}}$ for IRAS 4A and IRAS 4B are found to be ~20 and ~15 km s^{-1}, respectively, which are representative of the outflow tips (Fig. 4.5). Using these velocities, the t_{dyn} is 5900 yr. and 9200 yr. for IRAS 4A for the blue and red outflow lobes, respectively. Knee & Sandell (2000) found 8900 yr. (blue) and 16 000 yr. (red) for the IRAS 4A outflow lobes, whereas Lefloch et al. (1998) found 11 000 yr. for both of the outflow lobes in IRAS 4A from an SiO 2–1 map. All of these analyses assume a steady flow, whereas the knots clearly have larger widths than the rest of the flow (Fig. 4.5), which is indicative of episodic accretion and outflow. The constant flow assumption is indeed the main uncertainty in the determination of dynamical ages, although our approach of taking the maximum velocity combined with the maximum extent should give more reliable estimates than 'global' methods (Downes & Cabrit 2007).

4.4 Analysis: Outflow

4.4.1 Rotational temperatures and CO ladder

The most direct quantity that can be derived from the CO lines at the source position are the rotational temperatures (Fig. 4.8). It is important to note that all lines are most accurately reproduced by a single temperature, indicating that they probe the same gas up to J=10–9. Values of 69±7 K and 83±10 K are found for ^{12}CO, whereas those for ^{13}CO and C^{18}O are up to a factor of two lower (see Table 4.5). Since the ^{12}CO integrated intensities are dominated by the line wings, this may indicate that the outflowing gas is somewhat warmer than the bulk of the envelope dominating the isotopolog emission. On the other hand, the higher optical depths of the ^{12}CO lines can also result in higher rotational temperatures. A quantitative analysis of the implied kinetic temperatures is given in Sect. 4.4.2.1.
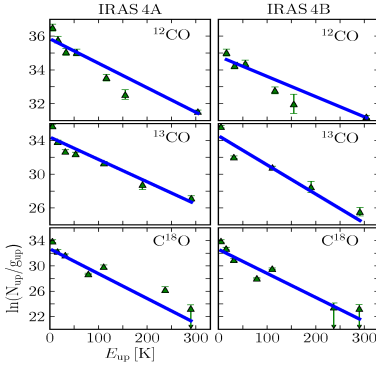
Figure 4.8 – Rotation diagrams measured for the CO and isotopolog lines at the source positions of IRAS 4A and 4B. The column density of each observation in each rotational level divided by the statistical weight is plotted against the excitation energy of the level. The fitted line shows the Boltzmann distribution of the rotational populations. Derived values of the rotation temperatures are presented in Table 4.5.

Table 4.5 – Rotational temperatures (in K) for the NGC 1333 sources.

Source	^{12}CO	^{13}CO	C^{18}O
IRAS 2A[a]	61±8	. . .	34±4
IRAS 4A	69±7	38±4	25±4
IRAS 4B	83±10	29±3	26±4

Notes: [a] IRAS 2A rotational temperatures are calculated for comparison using data from Yıldız et al. (2010).
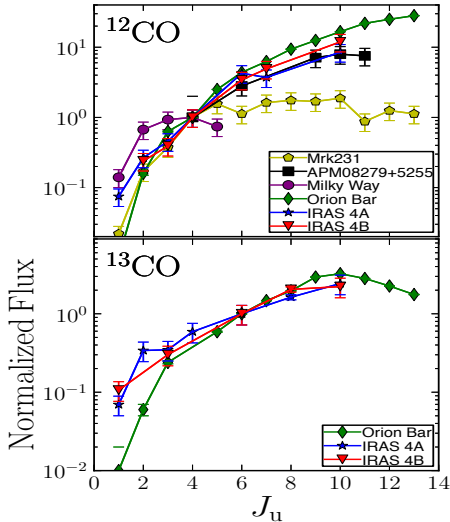
Figure 4.9 – CO line fluxes for the observed transitions. The ^{12}CO and ^{13}CO lines are normalized relative to the J=4–3 and J=6–5 lines, respectively. Observations of the Milky Way (Wright et al. 1991), the dense Orion Bar PDR (Habart et al. 2010), the ultraluminous galaxy Mrk231 (van der Werf et al. 2010), and the high redshift quasar APM08279+5255 (Weiss et al. 2007a) are compared. In IRAS 4A and 4B, the available maps are convolved to 20″ in order to compare similar spatial regions.

Another way of representing the CO ladder is provided in Fig. 4.9, where ^{12}CO and ^{13}CO line fluxes are normalized relative to the J=4–3 and J=6–5 lines, respectively. These

figures have been used in large-scale Milky Way and extragalactic studies to characterize the CO excitation (e.g. Weiss et al. 2007b). Other astronomical sources are overplotted for comparison, including the weighted average spectrum of diffuse gas in the Milky Way measured by COBE-FIRAS from Wright et al. (1991), the dense Orion Bar PDR from *Herschel*-SPIRE spectra from Habart et al. (2010), SPIRE spectra of the ultraluminous infrared galaxy Mrk231 from van der Werf et al. (2010), and broad absorption-line quasar observations of APM08279+5255 from ground-based data of Weiss et al. (2007a). For IRAS 4A and 4B, the ^{12}CO and ^{13}CO maps are convolved to 20″, where available, in order to compare similar spatial regions. It can seen that the low-mass YSOs studied here have very similar CO excitations up to $J_u = 10$ to the Orion Bar PDR and even to ultraluminous galaxies; in contrast, the excitation of CO of the diffuse Milky Way and Mkr 231 appears to turn over at lower J. Our conclusion that the ^{13}CO high-J lines trace UV heated gas (§6) is consistent with its similar excitation to the Orion Bar.

4.4.2 Observed outflow parameters

The CO emission traces the envelope gas swept up by the outflow over its entire lifetime, thus provides a picture of the overall outflow activity. The outflow properties can be derived by converting the CO line observations to physical parameters. Specifically, kinetic temperatures, column densities, outflow masses, outflow forces, and kinetic luminosities can be derived from the molecular lines. In the following sections, the derivation of these parameters is discussed.

4.4.2.1 Kinetic temperature

The gas kinetic temperature is obtained from CO line ratios. Figure 4.10 presents the observed line wing ratios of CO 3–2/6–5 at the source positions of IRAS 4A and 4B, as well as the four outflow knots identified in Fig. 4.3. The CO 6-5 map is resampled to a 15″ beam so that the lines are compared for the same beam. The ratios are then analyzed using the RADEX non-LTE excitation and radiative transfer program (van der Tak et al. 2007), as shown in Fig. 4.4 (right). The density within the beam is taken from the modeling results of Kristensen et al. (2012) based on spherically symmetric envelope models assuming a power-law density structure (see Jørgensen et al. 2002, Sect. 4.5). The analysis assumes that the lines are close to being optically thin, which is justified in Section 4.4.2.2. For the CO 6–5 transition, the critical density is $n_{cr}=1\times10^5$ cm^{-3}, whereas for CO 3–2, $n_{cr}=2\times10^4$ cm^{-3} based on the collisional rate coefficients of Yang et al. (2010). For densities higher than n_{cr}, the levels are close to being thermalized and are thus a clean temperature diagnostic; for lower densities, the precise value of the density plays a role in the analysis.

From the adopted envelope model, the density inside ~1750 AU (7.5″) is >10^6 cm^{-3} for both sources, i.e., well above the critical densities. The inferred temperatures from the CO 3–2/6–5 line wings are T_{kin} ~60–90 and ~90–150 K at the source centers of IRAS 4A
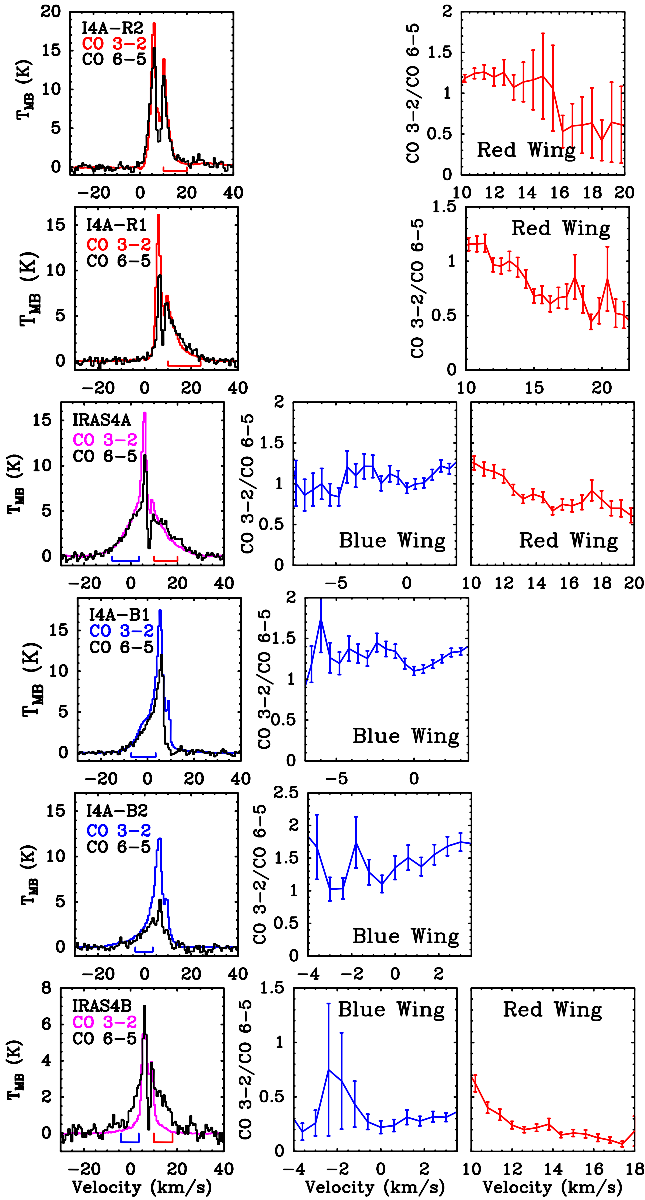
Figure 4.10 – Ratio of the T_{MB} temperatures of ^{12}CO 3–2/^{12}CO 6–5. From top to bottom; left hand column shows IRAS 4A red outflow knots I4A-R2, I4A-R1, central source, blue outflow knots I4A-B1, I4A-B2 and IRAS 4B central source positions. Coordinates of these positions are given in Table 4.2. The spectra are binned to 0.6 km s^{-1}. The blue and red masks under the spectra in the left column show the range is used for the ratio calculations. Right hand column shows the ratios of these transitions.
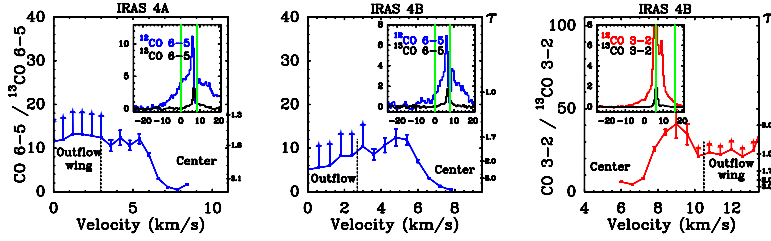
Figure 4.11 – Ratio of T_{MB} ^{12}CO 6–5/^{13}CO 6–5 at the IRAS 4A and IRAS 4B source positions and ^{12}CO 3–2/^{13}CO 3–2 at the IRAS 4B in left, middle, and right figures, respectively. The insets display the corresponding spectra and the green lines show the limits of the velocities over which these ratios are taken. The resulting optical depths of ^{12}CO as a function of velocity are shown on the right-hand axes. The spectra are binned to 0.6 km s^{-1}.

and 4B. These values are somewhat lower than, but consistent with, the temperatures of 90–120 K and 140–180 K found in Yıldız et al. (2010) using the CO 6-5/10-9 line ratios. For the outflow positions B1 and R1, the density is $\sim$3$\times$10^5 cm^{-3}, which results in temperatures of 100–150 K. The B2 and R2 positions are beyond the range of the envelope model, however assuming typical cloud densities of $\sim$10$^{4-5}$ cm^{-3}, the ratios indicate a higher temperature range of 140–200 K. Note that the line ratios in Fig. 4.10 are remarkably constant with velocity, showing little or no evidence of a temperature change with velocity.

4.4.2.2 Optical depths

The optical depth τ is obtained from the line ratio of two different isotopologs of the same transition. In Fig. 4.11, spectra of ^{12}CO 6–5 and ^{13}CO 6–5 for IRAS 4A and 4B and ^{12}CO 3–2 and of ^{13}CO 3–2 at the IRAS 4B source centers are shown. For presentation purposes, only the wing with the highest S/N ratio is shown, but the same trend holds for the other wing. Figure 4.12 includes the spectra and the line wing ratios of two dense outflow knots in ^{12}CO 2–1 and ^{13}CO 2–1 at the positions labeled I4A-R2 (northern red outflow knot) and I4A-B2 (southern blue outflow knot). Line ratios are measured only for the line wings excluding the central narrow emission or self-absorption. The optical depths are then derived assuming that the two species have the same excitation temperature and that the ^{13}CO lines are optically thin. The abundance ratio of ^{12}CO/^{13}CO is taken as 65 (Langer & Penzias 1990). The resulting optical depths of ^{12}CO as a function of velocity are shown on the right-hand axes of Figs. 4.11 and 4.12. High optical depths >2 are found at velocities that are very close to the central emission implying that the central velocities are optically thick and become optically thinner away from the center at the line wings of the outflowing gas.
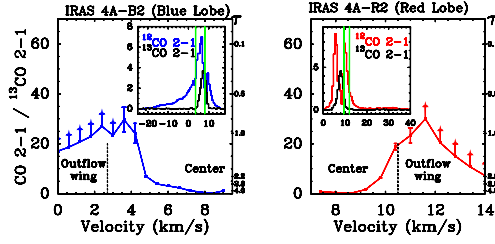
Figure 4.12 – Ratio of T_{MB} ^{12}CO 2–1/^{13}CO 2–1 at the I4A-B2 (left) and I4A-R2 (right) outflow positions. The insets display the corresponding spectra and the green lines show the limits of the velocities over which these ratios are taken. The resulting optical depths of ^{12}CO as a function of velocity are shown on the right-hand axes. The spectra are binned to 0.6 km s^{-1}.

4.4.2.3 Outflow mass

The gas mass in a particular region can be calculated from the product of the column densities at each position and the surface area

$$M_{\text{outflow}} = \mu_{H_2}\, m_H \times \sum_i (N_{H_2,i} \times A) \qquad (4.1)$$

where the factor μ_{H_2}=2.8 includes the contribution of helium (Kauffmann et al. 2008), m_H is the mass of the hydrogen atom, A is the surface area in one pixel (4″5×4″5), $\sum_i N_{H_2,i}$ is the pixel averaged H_2 column density over the selected velocity range, and the sum is over all pixels. To calculate the mass of the outflowing material, the CO 3–2 and 6–5 maps are resampled to a Nyquist sampling rate and calculated separately for each 15″ and 9″ pixel, respectively. As found in Sect. 4.4.2.2, the bulk of the emission in the line wings has a low optical depth. The CO column density is then obtained from

$$\frac{N_u}{g_u} = \beta \frac{(\nu[\text{GHz}])^2\, W[\text{K km s}^{-1}]}{A_{ul}[\text{s}^{-1}]\, g_u}, \qquad (4.2)$$

where $\beta = 1937$ cm^{-2}, g_u=2J+1, and $W = \int T_{mb}dV$ is the integrated intensity over the line wing. This intensity is calculated separately for the blue and red line wings with the velocity ranges defined in Sect. 4.3.2.3. The total CO column density, N_t, can then be found by

$$N_t = N_u Q_T \frac{1}{g_u\, e^{-E_u/kT_{ex}}}, \qquad (4.3)$$

where Q_T is the partition function corresponding to a specific excitation temperature, T_{ex}. The assumed T_{ex} is 75 K based on Sect. 4.4.2.1, but using T_{ex}=100 K results in only ~10% less mass. The column density N_{H_2} is obtained assuming an ^{12}CO/H_2 abundance ratio of 10^{-4}, which is lower than the canonical value of 2.7×10^{-4} (Lacy et al. 1994). The precise value of the CO abundance in the outflow is uncertain because some of the CO may be frozen out onto dust grains. The total H_2 column densities in the outflows

derived from the CO 6–5 data are 1.0×10^{22} cm^{-2} and 1.8×10^{22} cm^{-2} for IRAS 4A, and 1.0×10^{21} cm^{-2} and 9×10^{20} cm^{-2} for IRAS 4B, summed over the entire blue and red outflow lobes, respectively (see Table 4.6).

The masses of the outflowing material in the IRAS 4A blue and red lobes are then 6.1×10^{-3} and 1.0×10^{-2} M$_\odot$, and for IRAS 4B, 6.0×10^{-4} and 5.3×10^{-4} M$_\odot$, respectively. The masses have also been calculated from the CO 3–2 map, and the resulting values are ~2 times larger, which is partly because this line traces the colder gas of an assumed T_{ex}=50 K. Curtis et al. (2010b) used the JCMT CO 3–2 map of the entire Perseus molecular cloud to calculate the masses of the outflows from many sources in the region. They obtained around a factor of two higher mass for the total outflow in IRAS 4A (7.1×10^{-2} vs. our measurement of 3.0×10^{-2} M$_\odot$ from the 3–2 data) and around a factor of three higher value for the IRAS 4B outflow (1.1×10^{-2} vs. our measurement 1.8×10^{-3} M$_\odot$). These differences are well within the expected uncertainties, i.e., caused by choosing slightly different velocity ranges.

4.4.3 Outflow energetics

Theories of the origin of jets and winds and models of the 'feedback' of young stars on their surroundings require constraints on the characteristic force and energetics of the flow to infer the underlying physical processes. Specifically, the outflow force, kinetic luminosity, and mass ouflow rate can be measured from our data. The outflow force is defined as

$$F_{CO} = \frac{1}{R_{CO}} \mu_{H_2} \, m_H \times \sum_i (N_{H_2,i} \times A \times \Delta V^2_{max,i}). \qquad (4.4)$$

To date, this parameter has been determined by using lower-J lines for several young stellar objects (Cabrit & Bertout 1992, Bontemps et al. 1996, Hogerheijde et al. 1998, van Kempen et al. 2009b). The kinetic luminosity can be obtained from

$$L_{kin} = \frac{1}{2R_{CO}} \mu_{H_2} \, m_H \times \sum_i (N_{H_2,i} \times A \times \Delta V^3_{max,i}) \qquad (4.5)$$

and the mass outflow rate

$$\dot{M} = \frac{M_{outflow}}{t_{dyn}}. \qquad (4.6)$$

The outflow parameters derived from the observations are presented in Table 4.6. No correction factors were applied (cf. Cabrit & Bertout 1990).

Table 4.6 – Outflow properties of the red and blue outflow lobes of IRAS 4A and IRAS 4B.

Source	Trans.	Lobe	$V_{max}{}^a$ [km s^{-1}]	$R_{CO}{}^a$ [AU]	$t_{dyn}{}^{a,b}$ [yr]	N_{H_2} [cm^{-2}]	$M_{outflow}{}^c$ [M$_\odot$]	$\dot{M}^{a,e}$ [M$_\odot$ yr^{-1}]	$F_{CO}{}^{a,f}$ [M$_\odot$ yr^{-1}km s^{-1}]	$L_{kin}{}^{a,g}$ [L$_\odot$]
IRAS 4A	CO 3–2	Blue	22	2.8×10^4	5.9×10^3	8.6×10^{21}	1.3×10^{-2}	2.1×10^{-6}	5.0×10^{-5}	2.9×10^{-4}
		Red	18	3.9×10^4	1.0×10^4	1.2×10^{22}	1.8×10^{-2}	1.7×10^{-6}	3.9×10^{-5}	2.0×10^{-4}
	CO 6–5	Blue	20	2.5×10^4	5.9×10^3	1.0×10^{22}	6.1×10^{-3}	1.0×10^{-6}	3.1×10^{-5}	2.2×10^{-4}
		Red	18	3.5×10^4	9.2×10^3	1.8×10^{22}	1.0×10^{-2}	1.1×10^{-6}	3.7×10^{-5}	2.5×10^{-4}
IRAS 4B	CO 3–2	Blue	18	3.5×10^3	...	4.6×10^{20}	6.7×10^{-4}	...	1.9×10^{-5}	1.1×10^{-4}
		Red	15	4.7×10^3	...	7.5×10^{20}	1.1×10^{-3}	...	2.0×10^{-5}	9.7×10^{-5}
	CO 6–5	Blue	20	1.9×10^3	...	1.0×10^{21}	6.0×10^{-4}	...	3.4×10^{-5}	2.5×10^{-4}
		Red	12	7.5×10^2	...	9.1×10^{20}	5.3×10^{-4}	...	7.7×10^{-5}	4.5×10^{-4}

Notes: [a] Uncorrected for inclination. [b] Dynamical timescale. [c] Constant temperature of 75 K assumed for the CO 6–5 calculations, and 50 K assumed for the CO 3–2 calculations. Uncorrected for inclination as explained in Sect. 4.4.2.3. [e] Mass outflow rate, [f] outflow force, and [g] kinetic luminosity.

Table 4.7 – Spherical envelope models derived from dust-continuum radiative-transfer calculations of Kristensen et al. (2012).

Source	Y^a	p^b	$\tau_{100}{}^c$	$r_{in}{}^d$ [AU]	$r_{out}{}^e$ [AU]	$r_{10K}{}^f$ [AU]	$n_{r_{in}}{}^g$ [cm^{-3}]	$n_{r_{out}}{}^h$ [cm^{-3}]	$n_{10K}{}^i$ [cm^{-3}]	$N_{H_2,10K}{}^j$ [cm^{-2}]	$M_{10K}{}^k$ [M$_\odot$]
IRAS 4A	1000	1.8	7.7	33.5	3.3×10^4	6.4×10^3	3.1×10^9	1.2×10^4	2.4×10^5	1.9×10^{24}	5.1
IRAS 4B	800	1.4	4.3	15.0	1.2×10^4	3.8×10^3	2.0×10^9	1.8×10^5	8.7×10^5	1.0×10^{24}	3.0

Notes: [a] r_{in}/r_{out}. [b] Power law index. [c] Opacity at 100 μm. [d] Inner radius of the envelope. [e] Outer radius of the envelope, reaching out to 8 K. [f] 10 K radius. [g] Number density at r_{in}. [h] Number density at r_{out}. [i] Number density at 10 K radius. [j] H$_2$ column density. [k] Total mass of the envelope in 10 K radius.

4.5 Analysis: Envelope properties and CO abundance

4.5.1 Envelope model

To quantify the density and temperature structure of each envelope, the continuum emission is modeled using the 1D spherically symmetric dust radiative transfer code DUSTY (Ivezić & Elitzur 1997). The method closely follows that of Schöier et al. (2002) and Jørgensen et al. (2002, 2005b), and is discussed further in Kristensen et al. (2012). The inner boundary of the envelope is set to be where the dust temperature has dropped to 250 K (= r_{in}). The density structure of the envelope is assumed to follow a power law with an index p, i.e., $n \propto r^{-p}$, where p is a free parameter. The other free parameters are the size of the envelope, $Y = r_{out}/r_{in}$ and the opacity at 100 μm, τ_{100}. A grid of DUSTY models was run and compared to the SEDs obtained from the literature and radial emission profiles at 450 μm and 850 μm (Di Francesco et al. 2008). The best-fit solutions were obtained using a χ^2 method and are listed in Table 4.7, where the derived physical parameters of the envelopes are also listed.

A complication for the IRAS 4A/4B system is that they are so close to each other that their envelopes could overlap. Figs. 4.3 and 4.13 compare the envelopes at the 10 K radius and the observed beam sizes. The model envelopes start to overlap almost immediately from the central protostars if the two sources are at the same distance. In this case, the summed density of the two envelopes does not drop below 1.5×10^6 cm^{-3} (Fig. 4.13, *left*). Another scenario discussed in Sect. 4.3.2.3 is that the two sources are sufficiently well-separated in distance such that they do not interact and therefore have separate envelopes (Fig. 4.7c and 4.7d). The density and temperature profiles as a function of radius for such a scenario are shown in Fig. 4.13 (*right*). Since the overlap area is small even in the case that the sources are at exactly the same distance, the subsequent analysis is done adopting this latter scenario.

The resulting envelope structure is used as input to the RATRAN line radiative-transfer modeling code (Hogerheijde & van der Tak 2000). In Table 4.7, the inferred values from DUSTY that are used in RATRAN are given. In IRAS 4A, the outer radius is taken to be the radius where the density n drops to 1.2×10^4 cm^{-3}, and the temperature is considered to be constant after it reaches 8 K. The total masses of the envelopes are 5.1 M$_\odot$ (out to a radius of 6.4×10^3 AU) and 3.0 M$_\odot$ (3.8×10^3 AU) at the 10 K radius and 37.0 M$_\odot$ (3.3×10^4 AU) and 18.0 M$_\odot$ (1.2×10^4 AU) at the 8 K radius for IRAS 4A and 4B, respectively. The turbulent velocity is set to 0.8 km s^{-1}, which is representative of the observed C^{18}O line widths. However, the narrow component of the ^{13}CO lines is better reproduced with turbulent velocities of 0.5 km s^{-1} and 0.6 km s^{-1} for IRAS 4A and 4B, respectively. The model emission is convolved with the beam in which the line has been observed.
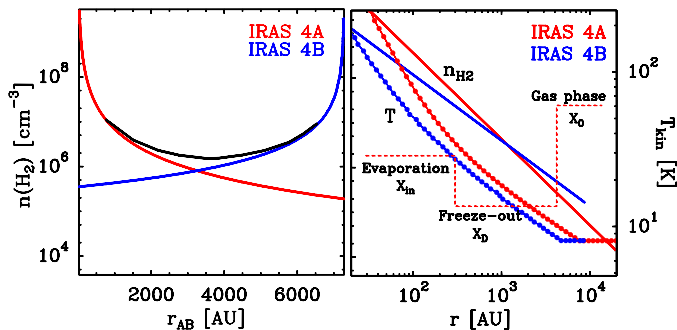
Figure 4.13 – Power-law density profiles discussed for two scenarios in Section 4.3. In the left panel, the IRAS 4A position is taken as the reference and r_{AB} indicates the 4A-4B distance. In the right-hand panel, the individual envelope profiles are shown. This panel includes a typical drop-abundance profile, with an outer abundance X_0, a freeze-out abundance X_D, and an inner abundance X_{in}. In an anti-jump profile, the evaporation jump in the inner envelope is lacking.

4.5.2 CO abundance profile

Yıldız et al. (2010) present *Herschel*-HIFI single pointing observations of CO and isotopologs up to 10–9 (E_u/k=300 K) for NGC 1333 IRAS 4A, 4B, and 2A. They used the $C^{18}O$ and $C^{17}O$ isotopolog data from 1–0 up to 9–8 to infer the abundance structure of CO through the envelope of the IRAS 2A protostellar envelope. For that source, the inclusion of the higher-J lines demonstrates that CO must evaporate back into the gas phase in the inner envelope. In contrast, the low-J lines primarily trace the freeze-out in the outer envelope (Jørgensen et al. 2002, 2005b). The maximum possible abundance of CO with respect to H_2 is 2.7×10^{-4} as measured in warm dense gas. Interestingly, the inner abundance in the warm gas was found to be less for IRAS 2A by a factor of a few. One goal of this study is to investigate whether this conclusion holds more commonly, in particular for the CO abundance profiles in IRAS 4A and 4B.

The CO abundance profile models were constructed for both IRAS 4A and 4B in the isotopolog lines of $C^{18}O$ and $C^{17}O$ using the methods outlined above. The lines are optically thin and have narrow line-widths characteristic of the quiescent surrounding envelope. The CO-H_2 collision parameters from Yang et al. (2010) were used. The calibration errors were taken into account in the modeling. Following the recipe of Yıldız et al. (2010) for IRAS 2A, "constant", "anti-jump", "drop", and "jump" abundance profiles were investigated (see Fig. 4.13, right). The abundance ratio of $C^{18}O/C^{17}O$ was taken as 3.65 (Wilson & Rood 1994).

4.5.2.1 Constant abundance profile

As a first iteration, a constant abundance was used to model the $C^{18}O$ and $C^{17}O$ lines, but it was impossible to reproduce all line intensities with this profile. In IRAS 4A, higher-J
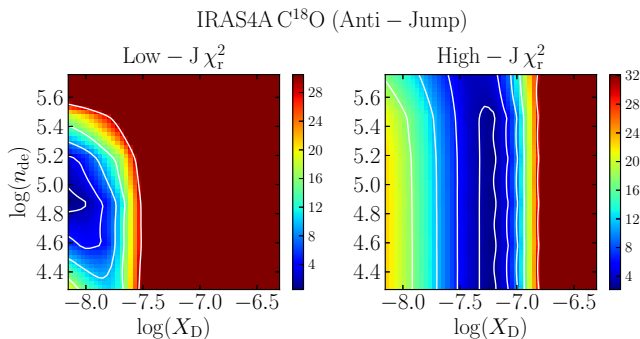
Figure 4.14 – Reduced χ^2 plots for the anti-jump abundance profile in IRAS 4A for the $C^{18}O$ lines in which the freeze-out abundance X_D and depletion density n_{de} are varied. The left panel take the low-J lines $C^{18}O$ 1–0, 2–1, 3–2 into account, whereas the right panels use the high-J $C^{18}O$ 5–4, 6–5, 9–8, and 10–9 lines. The contours are plotted for the 1σ, 2σ, 3σ, 4σ, and 5σ confidence levels.

$C^{18}O$ lines converge well around an abundance of $X\sim6\times10^{-8}$, although was necessary to consider lower abundances to produce lower-J lines, around $X\sim1$–2×10^{-8}. In IRAS 4B, higher-J lines were accurately described for $\sim1\times10^{-7}$ and lower-J lines again with 1–2×10^{-8}. Here, low-J refers to the $J \leq 3$ lines and high-J to the $J \geq 5$ lines.

4.5.2.2 Anti-jump abundance profile

For IRAS 4A, an anti-jump profile was run for the $C^{18}O$ and $C^{17}O$ lines. In an anti-jump profile, the evaporation jump in the inner envelope is omitted, that is the inner abundance, $X_{in}=X_D$, and the depletion density, n_{de}, are varied while the outer abundance remains high at $X_0=5\times10^{-7}$ corresponding to a ^{12}CO abundance of 2.7×10^{-4} for $^{16}O/^{18}O=550$ (see Yıldız et al. 2010, for the motivation behind keeping X_0 at this value). Reduced-χ^2 plots are shown in Fig. 4.14 where lower and higher-J lines are shown separately in order to illustrate their different constraints. Lower-J lines indicate an n_{de} of 7.5×10^4 cm^{-3} and X_D of 1×10^{-8}. The higher-J lines do not constrain n_{de} but an upper limit of 2.5×10^5 cm^{-3} and a well-determined X_D value of 5×10^{-8} are obtained. Since the density at the outer edge of the IRAS 4B envelope does not drop below 1.8×10^5 cm^{-3}, applying an anti-jump profile was impossible. CO remains frozen-out throughout the outer parts of the envelope.

4.5.2.3 Drop and jump abundance profile

To fit all observed lines, a "drop" abundance profile is needed in which the inner abundance X_{in} increases above the ice evaporation temperature, T_{ev} (Jørgensen et al. 2005c), as found for the IRAS 2A envelope (Yıldız et al. 2010). The n_{de} and X_D parameters inferred from the anti-jump profile from the low-J lines are used to determine the evaporation temperature and inner abundance (X_{in}). As for IRAS 2A, the reduced χ^2 plots
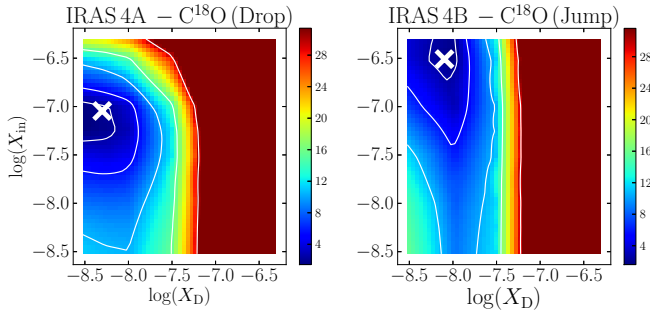
Figure 4.15 – Reduced χ^2 plots for the drop and jump abundance profile for the C^{18}O lines in IRAS 4A and 4B, respectively. The freeze-out abundance X_D and inner abundance X_{in} were varied. All lines were taken into account except J=1–0 and 5–4 owing to the comparatively larger beam sizes. The contours are plotted at 1σ, 2σ, 3σ, and 4σ confidence levels and white crosses show the best-fit values.
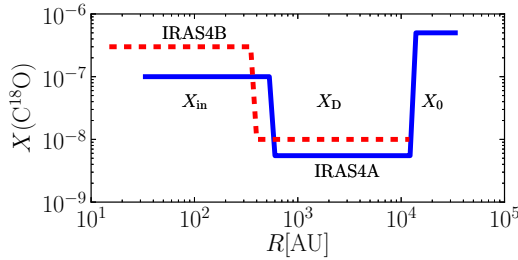

Figure 4.16 – Schematic diagram showing the best-fit abundance profiles for IRAS 4A (blue, solid lines) and IRAS 4B (red, dashed lines).

(not shown) indicate that the evaporation temperature is not well-determined, thus a laboratory lower limit of ~25 K is taken. Figure 4.15 *left* shows the χ^2 plots in which the inner abundance X_{in} and X_D are varied. The models are run for a desorption density of 7.5×10^4 cm^{-3} in IRAS 4A. Best-fit values for the lower- and higher-J lines are X_{in} ~1×10^{-7} and X_D=5.5×10^{-8}. For IRAS 4B, a jump abundance profile was applied in which the CO abundance stays low in the outer part (see Sect. 4.5.2.2). With this model, again, X_{in} and X_D values are varied (Fig. 4.15 *right*). The best fit gives X_{in} ~3×10^{-7} and X_D=1×10^{-8}.

Best-fit values obtained with the above-mentioned models are summarized in Table 4.8 and a simple cartoon is shown in Fig. 4.16. Modeled lines are overplotted on the observed C^{18}O lines in Fig. 4.17 convolving each line to the beam in which they were observed. In the models, the C^{18}O 1-0 and 5-4 lines are underproduced because their much larger beam sizes pick up emission from the extended surroundings not included in the model.

Table 4.8 includes the IRAS 2A results from Yıldız et al. (2010), who found that X_{in} is a factor of about 3-5 lower than X_0 in IRAS 2A and a factor of 5 lower in IRAS 4A. Fuente et al. (2012) found a similar factor for the envelope of the intermediate mass pro-
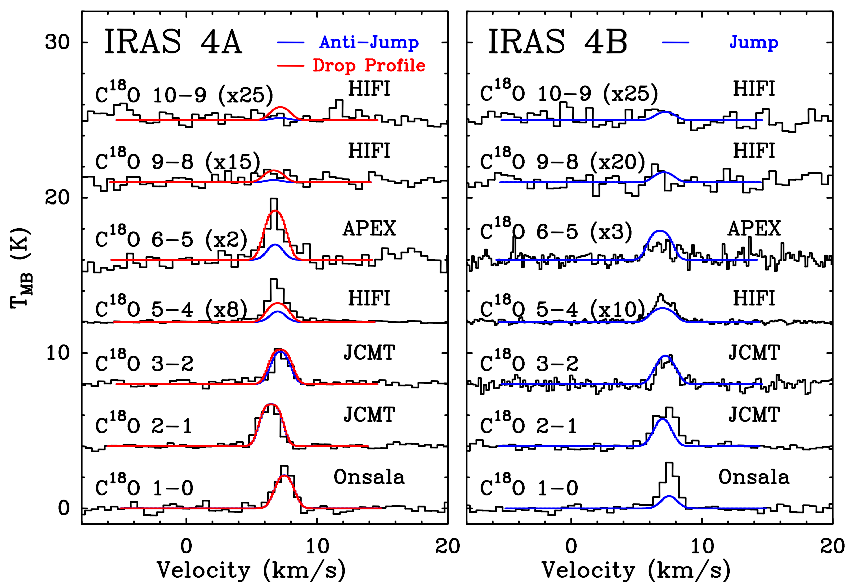
Figure 4.17 – *Left:* Line profiles obtained with the best-fit anti-jump (blue) and drop abundance (red) envelope models overplotted on the observed $C^{18}O$ lines in IRAS 4A. *Right:* Similar best-fit jump abundance profile for IRAS 4B. See Table 4.8 for best-fit parameters.

Table 4.8 – Summary of $C^{18}O$ abundance profiles for IRAS 4A and 4B.

Profile	X_{in}	T_{ev} [K]	X_D	n_{de} [cm^{-3}]	X_0
IRAS 4A					
Constant	...	...	...	...	1–5×10^{-8}
Anti-jump	...	...	1.0× 10^{-8}	7.5×10^4	5×10^{-7}
Drop	~1×10^{-7}	25	5.5×10^{-9}	7.5×10^4	5×10^{-7}
IRAS 4B					
Constant	...	...	...	...	1-6×10^{-8}
Jump	3×10^{-7}	25	1.0× 10^{-8}	...	1×10^{-8}
IRAS 2A[a]					
Constant	...	...	...	...	1.4×10^{-7}
Anti-jump	...	...	3× 10^{-8}	7×10^4	5×10^{-7}
Drop	1.5×10^{-7}	25	~ 4×10^{-8}	7×10^4	5×10^{-7}

Notes: [a] Results from Yıldız et al. (2010).

tostar NGC 7129 IRS. Thus, the conclusion of Yıldız et al. (2010) for IRAS 2A that $X_{in} < X_0$ holds more generally and is not linked to a specific source. This, in turn, may imply that a fraction of the CO is processed into other molecules in the cold phase when the CO resides on the grains. The lack of strong centrally-peaked [C I] emission in the [C I] map indicates that CO is not significantly (photo)dissociated in the inner envelope.
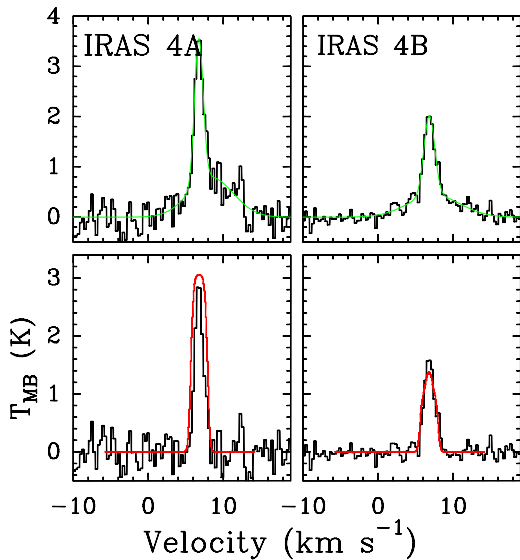
Figure 4.18 – *Top panels:* ^{13}CO 6–5 spectra of IRAS 4A and 4B at the source positions. The green line is the fit to the narrow plus broad components. *Bottom panels:* The same lines after subtracting the broad component. The red line indicates the ^{13}CO envelope model emission using the CO drop abundance profile derived from the C^{18}O data. The figure indicates that a substantial fraction of the on-source emission comes from the passively-heated envelope. For IRAS 4A, however, there is also significant extended emission that is not due to the envelope (see Fig. 4.19).

4.6   Analysis: UV-heated gas

In addition to shocks, UV photons can also heat the gas. Qualitatively, the presence of UV-heated gas is demonstrated by the detection of extended narrow ^{12}CO and ^{13}CO 6–5 emission in our spectrally resolved data (Hogerheijde et al. 1998, van Kempen et al. 2009b, van Dishoeck et al. 2009). This emission is observed to surround the outflow walls (Sect. 4.3.2.1) suggests a scenario in which UV photons escape through the outflow cavities and either impact directly the envelope or are scattered into the envelope on scales of a few thousand AU (Spaans et al. 1995). Our map also displays narrow ^{12}CO 6–5 emission on larger scales as well as in and around the bow-shock regions (Fig. 4.1). At all of these locations, the UV photons are most likely produced by the bow- and jet-shocks themselves, with the UV photons directly impacting the cavity walls and quiescent envelope. At velocities of 80 km s^{-1} or more, these shocks produce photons with high enough energies that they can even photodissociate CO (Neufeld & Dalgarno 1989).

Quantitatively, the tightest constraints on the UV-heated gas come from the narrow component of the ^{13}CO emission. However, at the source positions, the passively-heated envelope also contributes to the intensity. To model this component, the best-fit C^{18}O abundance profile of each source was taken and its abundance multiplied by the ^{13}C/^{18}O abundance ratio of 8.5. Figure 4.18 presents the resulting RATRAN ^{13}CO 6–5 line profiles at the central positions. The observed spectra for IRAS 4A and 4B are overplotted where the (weak) broad component was removed by fitting two Gaussians to the spectra. The model spectra obtained with this profile were found to fit the ^{13}CO 6–5 narrow emission profiles very well, implying that the contribution from the envelope is indeed significant.
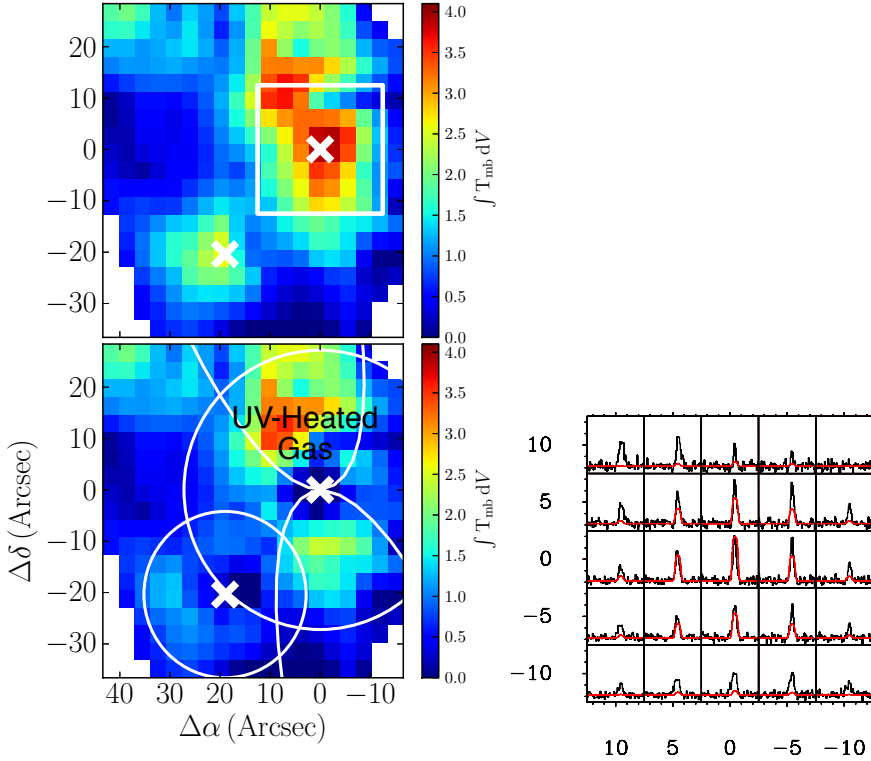
Figure 4.19 – *Top:* Central region of the ^{13}CO 6–5 map covering IRAS 4A. The broad component has been removed from the entire map. The red lines indicate the envelope model emission. *Middle:* Integrated intensity map of the narrow ^{13}CO 6–5 emission, obtained by removing the broad component. The white square box indicates the region covered in the top figure. This map shows both the envelope and UV-heated gas. *Bottom:* ^{13}CO map obtained after subtracting the model ^{13}CO 6–5 envelope emission convolved to the APEX beam from the above map. White circles show the limits of the 10 K radius envelope and white cones show the direction of the outflows. This map represents the UV-heated gas only.

In Fig. 4.19, the same method was applied to the entire ^{13}CO 6–5 map to probe the extent of the envelope emission. In the *middle* panel, the observed integrated intensity map of only the narrow component is plotted. In the *bottom* panel, the ^{13}CO map from the envelope model is convolved with the APEX beam and subsequently subtracted from the corresponding observed spectra. For both sources, the envelope model reproduces ^{13}CO 6–5 emission at the central position. For IRAS 4B, no significant emission remains at off-source positions. For IRAS 4A, however, narrow and extended emission is clearly visible beyond the envelope. Figure 4.19 *top* panel overplots the model envelope profiles on top of the observed profiles, showing that only the central positions are well-reproduced by this model. The excess emission has a width of only a few km s^{-1} such that it is unrelated to the outflow. Heating by UV photons is the only other plausible explanation. This

Table 4.9 – Comparison of photon-heated and outflow masses over the area mapped by ^{13}CO 6–5.

Source	$M_{\text{total}}{}^a$ Envelope	$M_{\text{cones}}{}^b$ Envelope	$M_{\text{outflow}}{}^c$ ^{12}CO 6–5	$M_{\text{UV}}{}^d$ ^{13}CO 6–5
IRAS 4A	5.0	1.5	3.7×10^{-3}	1.7×10^{-2}
IRAS 4B	3.1	0.9	1.0×10^{-3}	...

Notes: All masses are given in $M_\odot$ and the area taken in the calculations is shown in Fig. 4.19. ^{a} Total mass of the spherical envelope inferred from the continuum radiative-transfer modeling using DUSTY. ^{b} Envelope mass in both of the outflow cones assuming that each cone contains ~15% of the total envelope mass out to the mapped radius. ^{c} Outflow mass calculated from the ^{12}CO 6–5 outflow wings over the mapped ^{13}CO area. ^{d} UV photon-heated gas mass calculated from the narrow ^{13}CO 6–5 spectra over the mapped area after subtracting the modeled envelope emission.

interpretation is strengthened by the excess emission occuring precisely along the cavity walls, as shown in the *bottom* panel. The ^{13}CO 6–5 transition requires a temperature of $T\approx50$ K to be excited, which is consistent with the model predictions of Visser et al. (2012) showing a plateau around this temperature on scales of a few 1000 AU from the protostar. Hence, these observations constitute the first direct observational evidence for the presence of UV-heated cavity walls.

To compare the amount of gas heated by UV photons and gas swept up by the outflows, the masses in each of these components were calculated using the CO 6–5 and ^{13}CO 6-5 data (narrow component only) over the same region. The mass of the UV-heated gas was calculated assuming that $T_{\text{ex}}=75$ K and CO/H$_2=10^{-4}$. Since the ^{13}CO 6–5 map is smaller than that of CO 6–5, the outflow masses could not simply be taken from Table 5, but were recomputed over the smaller area covered by the ^{13}CO data. Both numbers were compared to the total gas mass in this area, obtained from the spherical model envelope based on the DUSTY results (see Sect. 4.5). To compare the same area as covered by the outflows, only the mass in an elliptical biconical shape was considered, with each cone occupying ~15% volume of the entire envelope out to the 10 K radius that would be present if the area had not been evacuated (see Fig. 4.6). The 10 K limit is still within the borders of the ^{13}CO map (Fig. 4.3). The UV photon-heated gas mass was derived from the ^{13}CO 6–5 narrow emission-line map after the envelope emission had been subtracted (*bottom* panel of Fig. 4.19). The inferred masses — total, UV-heated, and outflow — are summarized in Table 4.9.

Interestingly, for IRAS 4A, the mass of UV-photon-heated gas is somewhat higher than that of the outflowing gas, demonstrating that UV photons can have at least an equally large impact on their surroundings as the outflows. Although the uncertainties in the derived values are a factor of 2-3 (largely owing to uncertainties in CO/H$_2$), both masses are, however, only a few percent of the total quiescent envelope mass in the same area. For IRAS 4B, UV photons are apparently unable to escape the immediate protostellar environment (see also discussion in Herczeg et al. 2012). In addition, the near pole-on geometry in this case makes the detection of extended emission along the outflow cavity

more difficult.

4.7   Conclusions

T̶he two nearby Stage 0 low-mass YSOs, NGC1333 IRAS 4A and IRAS 4B, have been mapped in ^{12}CO 6–5 using APEX-CHAMP$^+$, with the resultant map covering the large-scale molecular outflow from IRAS 4A. ^{12}CO 6–5 emission is detected everywhere in the map. Velocity-resolved line profiles appear mainly in two categories: broad lines with $\Delta v >10$ km s^{-1} and narrow lines with $\Delta v <2$ km s^{-1}. The broad lines originate in the molecular outflow, whereas the narrow lines are interpreted as coming from UV heating of the gas. This interpretation is supported by the location of the narrow profiles, which "encapsulate" the broad outflow lines.

Comparing the CO 6–5 map with a CO 3–2 map obtained at the JCMT allows for a determination of the kinetic temperature of the outflow gas as a function of position through the outflow. The temperature peaks at the outflow knots and exceeds 100 K. The temperature is found to be constant with velocity, and there is no indication of higher temperatures being reached at higher velocities. Our high S/N multi-line data of ^{12}CO and isotopologs have allowed us to derive excitation temperatures, line widths, and optical depths, and thus the outflow properties, more accurately than before.

Smaller ^{13}CO 6–5 maps centered on the source positions have also been obtained with APEX-CHAMP$^+$. The ^{13}CO 6–5 emission is detected within a 20" radius of each source, and the line profiles are narrower than observed for the outflowing gas. The narrow ^{13}CO emission traces gas with a temperature of ~50 K at these densities, with the gas being heated by the UV photons. The mass of the outflowing gas is measured from the ^{12}CO data, whereas the mass of the UV-heated gas is measured from the narrow ^{13}CO spectra after subtracting the spherical envelope and outflow contributions. For IRAS 4A, the mass of the UV-heated gas is at least comparable to the mass of the outflow. This result shows that close to the source position on scales of a few thousand AU, UV heating is just as important as shock heating in terms of exciting CO to the J=6 level. Outflow- and envelope-subtracted ^{13}CO 6–5 maps clearly reveal the first direct observational images of these UV-heated cavity walls.

Single-pointing C^{18}O data have been obtained at the JCMT, APEX-CHAMP$^+$ and most recently with *Herschel*-HIFI, the latter observing lines up to J=10–9. The data have been used to constrain the CO abundance throughout the envelopes of the two sources. To reproduce the high-J C^{18}O emission, a "drop" in the abundance profile is required. This "drop" corresponds to the zone where CO is frozen out onto dust grains, thus provides quantitative evidence of the physical characteristics of this zone. The CO abundance rises in the inner part where $T > 25$ K, but not to its expected canonical value of 2.7×10^{-4} (Lacy et al. 1994), indicating that some further processing of the molecule is taking place.

The combination of low-J CO lines (up to J=3–2) and higher-J CO lines such as J=6–5

opens up a new window for quantifying the warm ($T \sim 100$ K) gas surrounding protostars and along their outflows. These spectrally resolved data form an important complement to spectrally unresolved data of the same lines such as being acquired for similar sources with *Herschel*-SPIRE. From our data, it is clear that the ^{12}CO lines covered by SPIRE are dominated by the entrained outflow gas with an excitation temperature of ~ 100 K. For ^{13}CO, lines centered on the protostar are dominated by emission from the warm envelope, which is passively heated by the protostellar luminosity. Off source on scales of a few thousand AU, however, UV-photon heated gas along the cavity walls dominates the emission. The UV-heated component becomes visible in ^{12}CO lines higher than 10–9, but it is likely that for Stage 0 sources this component will be overwhelmed by shocks for all lines in spectrally unresolved data (Visser et al. 2012). Thus, the ^{12}CO and ^{13}CO data provide complementary information on the physical processes in the protostellar environment: ^{12}CO traces swept-up outflow (lower-J) and currently shocked (higher-J) gas, whereas ^{13}CO traces warm envelope and photon-heated gas. Our results imply that spectrally unresolved ^{12}CO/^{13}CO line ratios have only a limited meaning.

Understanding the excitation of chemically simple molecules such as CO is a prerequisite for interpreting other molecules, in particular H_2O data from *Herschel*-HIFI. Furthermore, understanding the distribution of warm CO on large spatial scales (> 1000 AU) is necessary for interpreting future high spatial resolution data from ALMA.

4.8   Auxillary figures

We present the CO 3–2 map obtained from JCMT, which is discussed in Sect. 4.3.2.2, and the CHAMP$^+$ map of [C I] 2–1, which is discussed in Sect. 4.3.2.4.
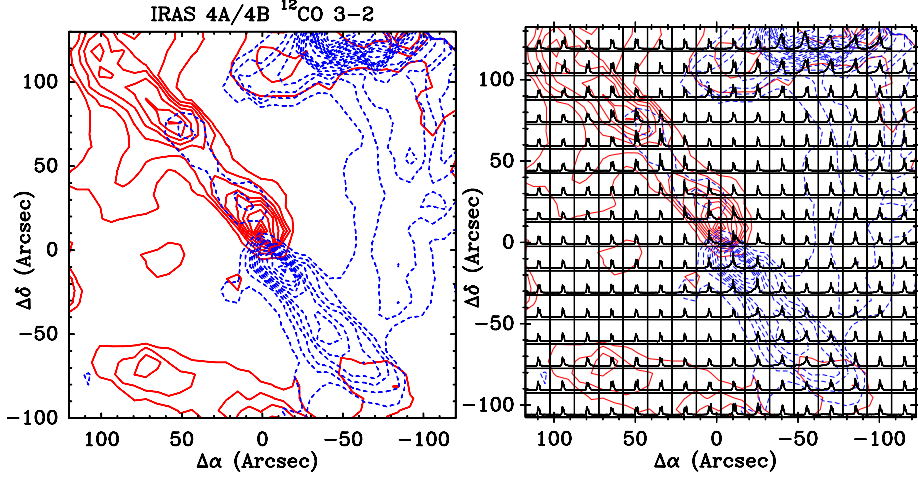

Figure 4.20 – ^{12}CO 3–2 spectral map of IRAS 4A and 4B over the 240″×240″ mapping area. Individual spectra are shown on the T_{MB} scale from –2 K to 16 K and velocity scale from –20 km s^{-1} to 30 km s^{-1}. The maps are centered on IRAS 4A. The contour levels start from 20σ (10 K km s^{-1}) with an increasing step size of 5 K km s^{-1}.
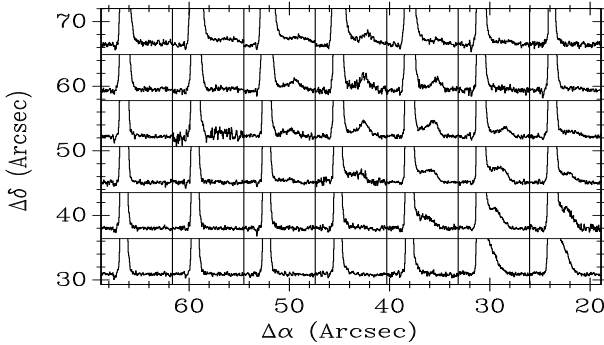
Figure 4.21 – Zoomed image of ^{12}CO 3–2 spectra at the IRAS 4A-R2 outflow knot position. Bullet emission at +35 km s^{-1} is visible in the upper left part of the IRAS 4A outflow. Individual spectra are shown on the T_{MB} scale from –0.7 to 2.5 K and velocity scale from –10 km s^{-1} to 45 km s^{-1}. The coordinates are relative to IRAS 4A.

Acknowledgements
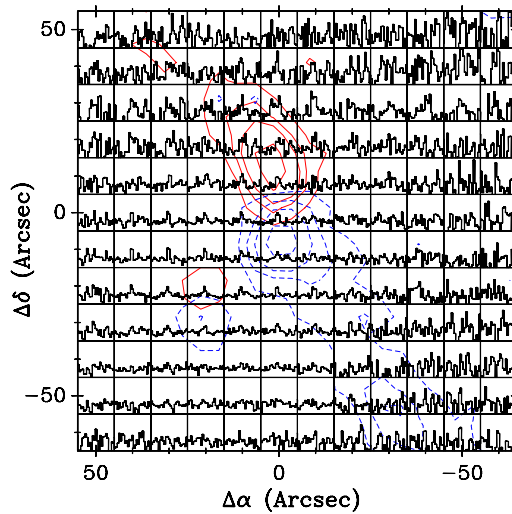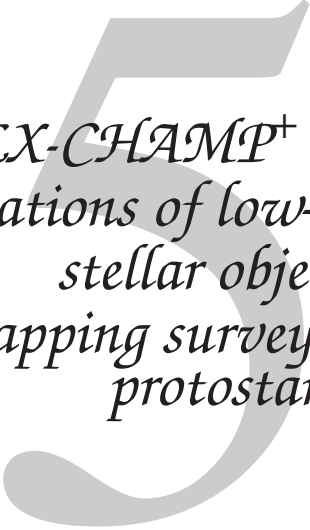
Figure 4.22 – [C I] 2–1 spectral map (rebinned to 10″x10″ with a 1 km s^{-1} velocity resolution) is overlaid on a ^{12}CO 6–5 outflow contour map. In the [C I] 2–1 map, individual spectra are shown on a T_{MB} scale of from –1 K to 3 K and the velocity scale runs from –5 K km s^{-1} to 20 K km s^{-1}. The map is centered on the IRAS 4A position.

APEX-CHAMP⁺ high-J CO observations of low–mass young stellar objects: IV. Mapping survey of low-mass protostars

Umut A. Yıldız, Ewine F. van Dishoeck, Lars E. Kristensen, Tim A. van Kempen,
Michiel R. Hogerheijde, Agata Karska, Friedrich Wyrowski, Nienke van der Marel,
Arnaud Belloche, Rolf Güsten

In preparation

Abstract

CONTEXT: During the embedded stage of star formation, the envelope mass and bipolar outflow characteristics undergo significant evolution. The outflow is the dominant feedback agent, and its evolution reflects the accretion processes of the forming star.

AIMS: Our aim is to quantify the outflow force for a large sample of sources in a consistent manner to determine the evolution of outflow activity integrated over the lifetime of the protostar. The outflow activity is then compared with other energetic parameters of the system to search for correlations and evolutionary trends.

METHODS: Large-scale maps of 26 young stellar objects which are part of the *Herschel* WISH key program are obtained using the CHAMP$^+$ instrument on the Atacama Pathfinder EXperiment (^{12}CO and ^{13}CO 6–5; $E_{up} \sim 100$ K), together with the HARP-B instrument on the James Clerk Maxwell Telescope (^{12}CO and ^{13}CO 3–2; $E_{up} \sim 30$ K). The maps have high spatial resolution, particularly the CO 6–5 maps taken with a 9″ beam, resolving the morphology of the outflows. These maps are analyzed using the same methods to determine outflow parameters and the results are compared with higher-J CO lines obtained with *Herschel*.

RESULTS: All sources in our sample show outflow activity via CO line wings. One of the key parameters, the outflow force, F_{CO}, is measured and correlations with other physical parameters are sought. F_{CO} versus L_{bol} plots show that Class 0 sources have more powerful outflows than the Class I sources, even if their luminosities are comparable. Overall, the various outflow parameters indicate reduced outflow activity with evolutionary stage, consistent with previous studies. F_{CO} is directly proportional to M_{env} and $M_{outflow}$, indicating that higher outflow forces require higher envelope masses and involve higher outflow masses. Comparison of the CO 6–5 results with H_2O lines observed with HIFI and high-J CO lines probed by PACS, both tracing currently shocked gas, shows that the two components are still linked, even though the transitions do not probe the same gas component. The link does not extend down to CO 3–2. The conclusion is that CO 6–5 depends on the shock characteristics (pre-shock density and velocity), whereas CO 3–2 is more sensitive to conditions in the surrounding environment (density).

5.1   Introduction

During the early phases of star-formation, material surrounding the newly forming star accretes onto the forming protostar. At the same time, it launches winds or jets at supersonic speeds from the star-disk system, which sweep up surrounding envelope material in large bipolar outflows. The material is accelerated and pushed to distances of several tens of thousands of AU, and these outflows play a pivotal role in the physics and chemistry of the star-forming cores (Snell et al. 1980, Goldsmith et al. 1984, Lada 1987, Greene et al. 1994, Bachiller & Tafalla 1999, Arce & Sargent 2006, Tafalla et al. 2013). The youngest protostars have highly collimated outflows driven by jets, whereas at later stages wide-angle winds drive less collimated outflows. However, there is still not a general consensus to explain the launching mechanisms and nature of these outflows (Arce et al. 2007).

The goal of this chapter is to investigate how the outflow activity varies with evolution and how this compares with other measures of the accretion processes. The outflows show the integrated activity over the entire lifetime of the protostar, which could be the result of multiple accretion and ejection events. It is important to distinguish this probe from the current accretion rate, as reflected for example in the luminosity of the source, in order to understand the accretion history. The well-known "luminosity problem" in low-mass star-formation indicates that protostars are underluminous compared to theoretical models (Kenyon et al. 1990, Evans et al. 2009, Enoch et al. 2009, Dunham et al. 2013). One of the possible resolutions to this problem is that of "episodic accretion", in which the star builds up through short bursts of rapid accretion over long periods of time rather than continuous steady-state accretion. An accurate and consistent quantification of outflow properties such as the outflow force and mass is key to investigate this problem.

CO outflows have been observed in the last few decades in many sources, but those observations were mainly done via lower-J CO rotational transitions ($J_{\rm u} \leq 3$) which probe colder swept-up or entrained gas ($T \sim 50$–100 K) (e.g., Bachiller et al. 1990, Blake et al. 1995, Bontemps et al. 1996, Tafalla et al. 2000, Curtis et al. 2010b, and many others). One of the key parameters that is used for the evolutionary studies of star formation is the "outflow force", which is known as the strength of an outflow and defined similar to the centripetal force. These studies conclude that the outflow force correlates well with bolometric luminosity, $L_{\rm bol}$, a correlation which holds over several orders of magnitude. Furthermore, the outflow force from Class 0 sources is stronger than for Class I sources, indicating an evolutionary trend. The correlations, however, often show some degree of scatter, typically more than an order of magnitude in $F_{\rm CO}$ for any value of $L_{\rm bol}$. Some of the uncertainties in these studies include the opacity in the line wings, the adopted inclination angle and cloud contamination at low outflow velocities. Comparison with other outflow tracers such as water now being observed with the *Herschel* Space Observatory is further complicated by the fact that the various studies use different analysis methods to derive outflow parameters from low-J CO maps.

Tracing warmer gas ($T \gtrsim 100$ K) in the envelope or in the surroundings requires obser-

vations of higher-J transitions of CO, e.g., $J_u \geq 5$, for which ground-based telescopes demand excellent weather conditions on dry observing sites. The CHAMP$^+$ instrument, mounted on the Atacama Pathfinder EXperiment (APEX) at an altitude of 5100 meters on Cerro Chajnantor (Güsten et al. 2008), has a 650/850 GHz 2×7 pixel array receiver (Kasemann et al. 2006), which is ideally suited to observe higher-J CO transitions and efficiently map extended sources. Broad line wings of CO 6–5 (E_u/k=115 K) suffer less from opacity effects than CO 3–2 (E_u/k=33 K) (van Kempen et al. 2009a, Yıldız et al. 2012). Moreover, the ambient cloud contribution is smaller for these higher-J transitions, except close to the source position, where the protostellar envelope may still contribute. Even higher-J CO lines up to J_u=50 are now routinely observed with the *Herschel* (Pilbratt et al. 2010) and provide information on the shocked gas in the *Herschel* beam (Herczeg et al. 2012, Manoj et al. 2013, Goicoechea et al. 2012, Benedettini et al. 2012, Nisini et al. 2013, Karska et al. 2013).

In this chapter, we present an APEX-CHAMP$^+$ survey of 26 low-mass young stellar objects (YSOs), which were mapped in CO $J = 6$–5 and isotopologues in order to trace their outflow activity, following van Kempen et al. (2009a,b) and Yıldız et al. (2012), papers I, II and III in this series. These data complement our earlier surveys at lower frequency of CO and other molecules with the James Clerk Maxwell Telescope (JCMT) and APEX (e.g., Jørgensen et al. 2002, 2004, van Kempen et al. 2009c). The same sources are covered in the *Herschel* key project, "Water in star-forming regions with Herschel" (WISH; van Dishoeck et al. 2011). Many of the sources are also included in the "Dust, Ice and Gas in Time" program (DIGIT; PI: N. Evans; Green et al. 2013; subm.).

The YSOs in our sample cover both the deeply embedded Class 0 stage as well as the less embedded Class I stage (André et al. 2000, Robitaille et al. 2006). The full data set covering many sources allows us to address important characteristics of YSOs through the evolution from Class 0 to Class I in a more accurate manner. These characteristics can be inferred from their different morphologies, outflow forces, envelope masses, etc. and eventually be compared with evolutionary models.

The study presented here is complementary to that of Yıldız et al. (2013; subm.), where only the source position was studied in CO transitions from $J = 1$–0 to 10–9 ($E_{up} \sim 300$ K), and trends with evolution were examined. The results obtained from the ^{12}CO maps are complemented by ^{13}CO 6–5 data of the same sources, with the narrower ^{13}CO 6–5 lines found to be a good tracer of the UV photon-heated gas (Spaans et al. 1995, van Kempen et al. 2009b, Yıldız et al. 2012). However, this analysis if beyond the scope of this chapter, and the ^{13}CO maps are only presented in Figs. 5.15 and 5.16 in the Additional Materials.

The outline of the chapter is as follows. In Section 5.2, the observations and the telescopes where the data have been obtained are described. In Section 5.3, physical parameters obtained from molecular outflows are given. In Section 5.4, these results are discussed, and conclusions from this work are presented in Sect. 5.5.
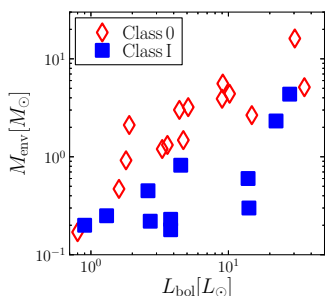
Figure 5.1 – Bolometric luminosity, L_{bol}, versus envelope mass, M_{env}, for the surveyed sources. Red triangles and blue squares indicate Class 0 and Class I sources, respectively.

5.2 Sample and observations

5.2.1 Sample

The sample selection criteria with the coordinates and other basic information of the source list are presented in van Dishoeck et al. (2011) with updates in Kristensen et al. (2012), and is the same as the sample presented in Yıldız et al. (2013; subm.). It consists of 15 Class 0 and 11 Class I embedded protostellar sources located in the Perseus, Ophiuchus, Taurus, and Serpens molecular clouds. The average distance is 200 pc, with a maximum distance of 450 pc.

Figure 5.1 presents the envelope mass (M_{env}) as a function of bolometric luminosity (L_{bol}) for all sources. The envelope mass is obtained from dust modelling, which is measured either at the $T_{dust}=10$ K radius or at the $n=10^4 cm^{-3}$ radius, depending on which is smaller (Kristensen et al. 2012). Class 0 sources and Class I sources are well separated in the diagram, with the Class 0 sources having higher envelope masses. The parameters are taken from Kristensen et al. (2012) based on fits of the spectral energy distributions (SEDs) including new *Herschel*-PACS fluxes, as well as the spatial extent of the envelopes observed at submillimeter wavelengths. This type of correlation diagram has been put forward by Saraceno et al. (1996) and subsequently used as an evolutionary diagram for embedded YSOs with lower envelope masses representing later stages (e.g., Bontemps et al. 1996, Hogerheijde et al. 1998, Hatchell et al. 2007). In our sample, envelope masses range from 0.04 $M_\odot$ (Elias 29) to 16 $M_\odot$ (SMM1) and the luminosities range from 0.8 $L_\odot$ (Ced110IRS1) to 35.7 $L_\odot$ (IRAS 2A). The large range of masses and luminosities makes the sample well suited for statistical studies and trends with various source parameters. The range of luminosities studied is similar to that of Bontemps et al. (1996), ~0.5 to 15 $L_\odot$, but our sample is more weighted toward higher luminosities.

5.2.2   Observations

Molecular line observations of CO in the J=6–5 transitions were done with the 12-m submillimeter Atacama Pathfinder EXperiment, APEX[1] (Güsten et al. 2008) at Llano de Chajnantor in Chile, whereas the J=3–2 transition was primarily observed at the 15-m James Clerk Maxwell Telescope, JCMT[2] at Mauna Kea, Hawaii.

APEX: ^{12}CO and ^{13}CO 6–5 maps of the survey were obtained with the CHAMP$^+$ instrument on APEX between June 2007 and September 2012. The CHAMP$^+$ instrument consists of two heterodyne receiver arrays, each with seven pixel detector elements for simultaneous operations in the 620–720 GHz and 780–950 GHz frequency ranges (Kasemann et al. 2006, Güsten et al. 2008). The observational procedures are explained in detail in van Kempen et al. (2009a,b,c) and Yıldız et al. (2012). Simultaneous observations were done with the following settings of the lower and higher frequency bands: ^{12}CO 6–5 with ^{12}CO 7–6; ^{13}CO 6–5 with [C I] 2–1. ^{12}CO maps cover the entire outflow extent with a few exceptions (L1527 and L1551-IRS5), whereas ^{13}CO maps cover only a ~100″×100″ region around the central source position. L1157 is part of the WISH survey, but because it is not accessible from APEX (dec = +68°), no CO 6–5 data are presented.

The APEX beam size is ~9″ (~1800 AU for a source at 200 pc) at 691 GHz. The observations were done using position-switching toward an emission-free reference position. The CHAMP$^+$ instrument uses the Fast Fourier Transform Spectrometer (FFTS) backend (Klein et al. 2006) for all seven pixels with a resolution of 0.12 MHz (0.052 km s^{-1} at 691 GHz). Typical *rms* for the CO 6–5 and ^{13}CO 6–5 observations are ~0.2 K in 0.2 km s^{-1} channels. Apart from the high-J CO observations, some of the 3–2 line observations were also conducted with APEX for a few southern sources, e.g., DK Cha, Ced 110 IRS4, and HH 46 (van Kempen et al. 2009c).

JCMT: Fully sampled on-the-fly maps of ^{12}CO and ^{13}CO 3–2 were obtained using the HARP-B instrument mounted on the JCMT. HARP-B consists of 16 SIS detectors with 4×4 pixel elements of 15″ each at 30″ separation. Most of the maps were obtained through our own dedicated proposals, with a subset obtained from the JCMT public archive[3].

The data were acquired on the T_{A}^* antenna temperature scale and were converted to main-beam brightness temperatures $T_{\mathrm{MB}} = T_{\mathrm{A}}^*/\eta_{\mathrm{MB}}$ using the beam efficiencies (η_{MB}). The CHAMP$^+$ beam efficiencies were taken from the CHAMP$^+$ website[4] and forward ef-

---

[1] This publication is based on data acquired with the Atacama Pathfinder Experiment (APEX). APEX is a collaboration between the Max-Planck-Institut für Radioastronomie, the European Southern Observatory, and the Onsala Space Observatory.

[2] The JCMT is operated by The Joint Astronomy Centre on behalf of the Science and Technology Facilities Council of the United Kingdom, the Netherlands Organisation for Scientific Research, and the National Research Council of Canada.

[3] This research used the facilities of the Canadian Astronomy Data Centre operated by the National Research Council of Canada with the support of the Canadian Space Agency.

[4] http:www.mpifr.de/div/submmtech/heterodyne/champplus/champ_efficiencies.15-10-09.html

ficiencies are 0.95 in all observations. The various beam efficiencies are all stated in Yıldız et al. (2013; subm.) and are typically ~ 0.5 (see also the thesis Appendix). The JCMT beam efficiencies were taken from the JCMT Efficiencies Database[5], and 0.63 is used for all HARP-B observations. Calibration errors are estimated to be $\sim$20% for both telescopes. Typical *rms* noise levels of the 3–2 data are from 0.05 K to 0.1 K in 0.2 km s^{-1} channels.

For the data reduction and analysis, the "Continuum and Line Analysis Single Dish Software", CLASS program, which is part of the GILDAS software[6], is used. In particular, linear baselines were subtracted from all spectra. ^{12}CO and ^{13}CO 6–5 and 3–2 line profiles of the central source positions of all the sources in the sample are presented in Yıldız et al. (2013; subm.).

5.2.3 ^{12}CO maps

All spectra are binned to a 0.5 km s^{-1} velocity resolution for analyzing the outflows. The intensities of the blue and red outflow lobes are calculated by integrating the blue and red emission in each of the spectra separately, where the integration limits are carefully selected for each source by using their CO 6–5 lines (see Fig. 5.10). First, in order to find the inner velocity limit (V_{in}), a spatial region not part of the outflow is selected. The spectra in this region are averaged to determine the narrow line emission coming from the envelope and surrounding cloud and V_{in} is estimated. Second, the outer velocity limits (V_{out}) are determined from a representative high S/N spectrum inside each of the blue and red outflow lobes. The outer velocity limits are selected as the velocity where the emission in the spectrum goes down to the 1σ limit. Finally, the blue- and red-shifted integrated intensity is measured by integrating over these velocity limits across the entire map.

The resulting maps of all sources are presented in Figs. 5.2 and 5.3, where blue and red contours show the blue- and red-shifted outflow lobes, respectively. A few maps only cover the central $\sim 2'\times2'$, specifically the four Class 0 sources IRAS 2A, L723mm, L1527, and the two Class I sources Elias 29 and L1551IRS5. Source-by-source outflow and intensity maps obtained from the 6–5 and 3–2 data are presented in Figs. 5.11–5.14 in the Additional Materials.

5.2.4 ^{13}CO maps

The ^{13}CO 6–5 and 3–2 transitions were mapped around the central $\sim 1'\times1'$, corresponding to typically 10^4 AU $\times$ 10^4 AU. The total integrated intensity is measured for all the sources, where the limits correspond to the velocities at which the emission reaches down to 1σ. ^{13}CO maps can be used to quantify the UV-heated gas around the outflow cavity

---

[5] http://www.jach.hawaii.edu/JCMT/spectral_line/Standards/eff_web.html
[6] http:www.iram.fr/IRAMFR/GILDAS
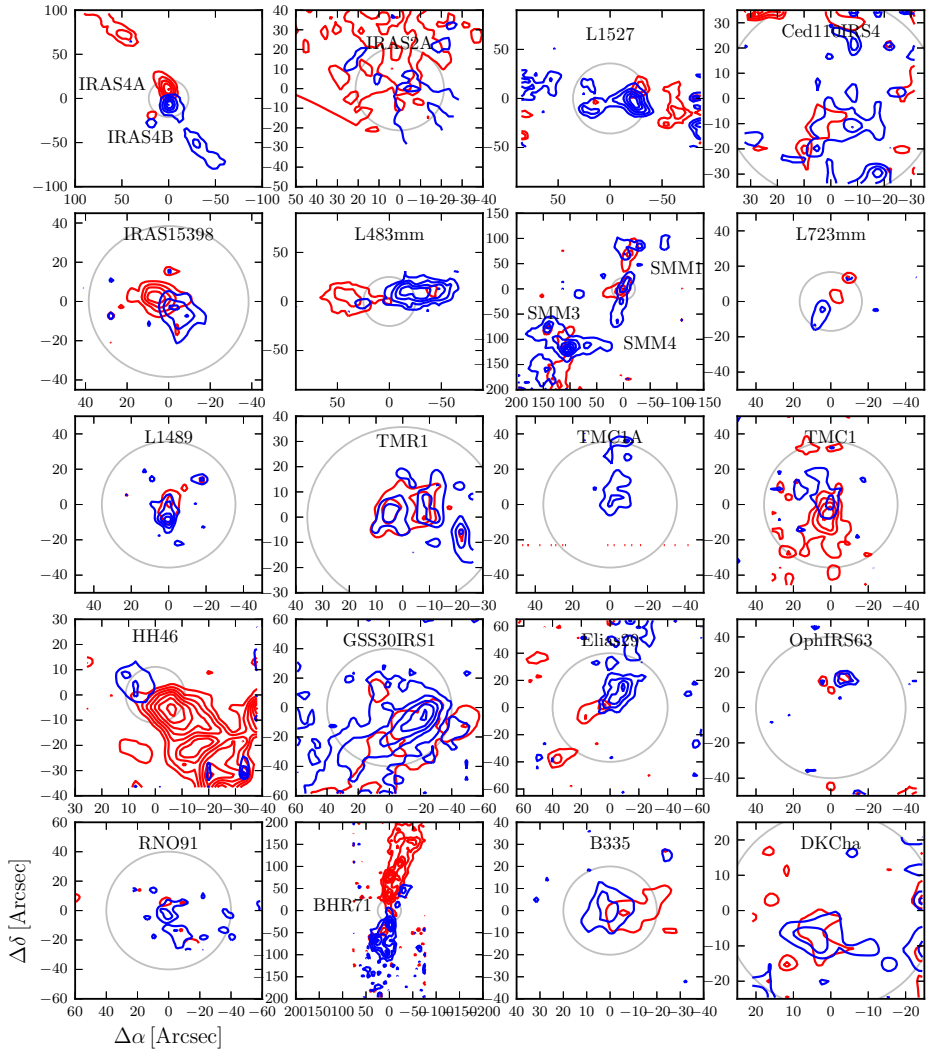
Figure 5.2 – Overview of the outflows traced by the ^{12}CO 6–5 observations with the APEX-CHAMP⁺ instrument. Contour levels are given in Table 5.5 and the source is located at (0,0) in each map, with the exception of the maps of NGC1333-IRAS4A and 4B, and Ser-SMM1, SMM3 and SMM4, which are located in the same maps, respectively. The circle in each plot corresponds to a region of 5000 AU radius at the distance of each source.
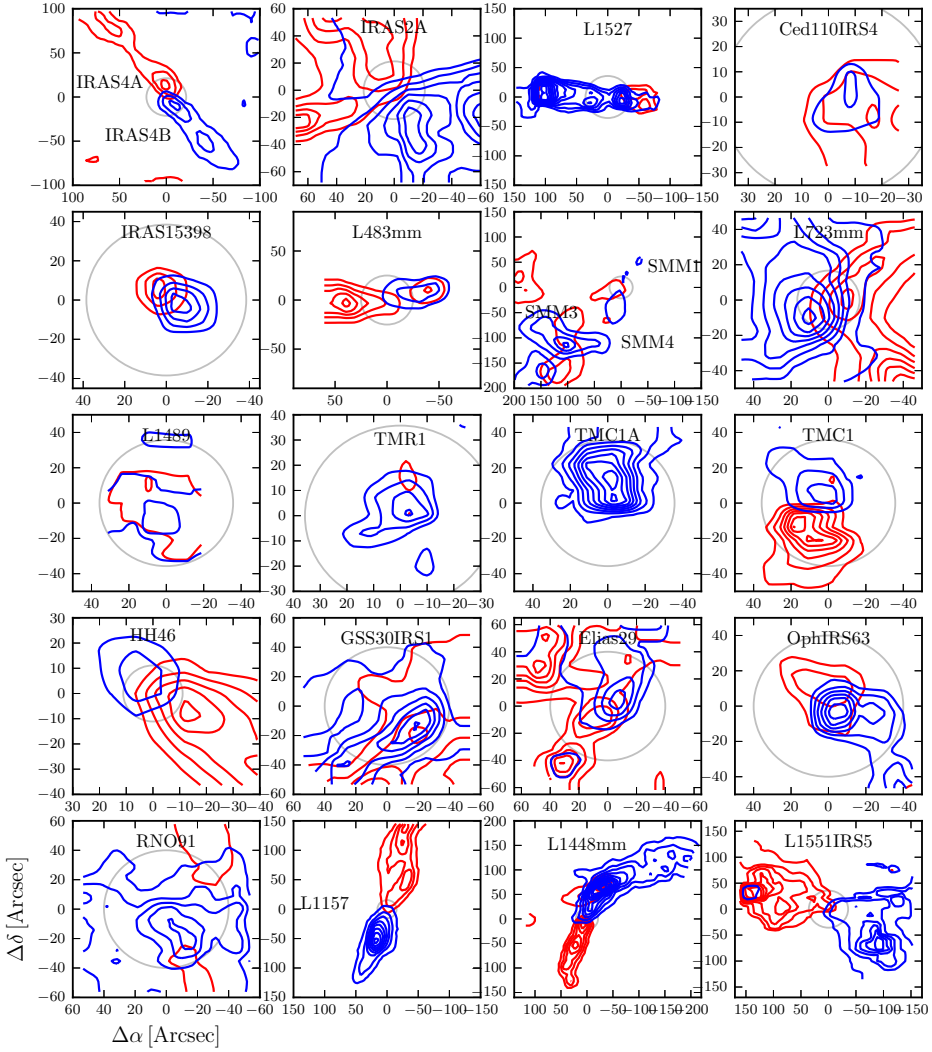
Figure 5.3 – Overview of the entire set of outflows traced by the ^{12}CO 3–2 observations with the JCMT and APEX. Contour levels are given in Table 5.5 and the source is located at (0,0) in each map, with the exception of the maps of NGC1333-IRAS4A and 4B, and Ser-SMM1, SMM3 and SMM4, which are located in the same maps, respectively. The circle in each plot corresponds to a region of 5000 AU radius at the distance of each source.

walls as demonstrated by Yıldız et al. (2012). All maps are presented in Figs. 5.15 and 5.16 in the Additional materials.

5.3 Results

5.3.1 Outflow morphology

All sources show strong outflow activity in both CO transitions, $J = 3$–2 and 6–5, as evident from both the maps and spectra (Figs. 5.2, 5.3, and Figs. 5.10–5.14). The advantage of the CO 6–5 maps is that they have higher spatial resolution by a factor of two than the CO 3–2 maps. On the other hand, the CO 3–2 maps have the advantage of higher S/N than the CO 6–5 maps by typically a factor of 4 in antenna temperature.

Most sources show a clear blue-red bipolar structure. In a few cases only one lobe is observed. Particular examples are TMC1A, which shows no red-shifted outflow lobe, and HH 46, which has only a very small blue-shifted outflow lobe. One explanation is that these sources are at the edge of the cloud and that there is no cloud material to run into (van Kempen et al. 2009b). For L723mm, IRAS 2A and BHR71, two outflows are driven by two independent protostars (Lee et al. 2002, Parise et al. 2006) and both outflows are detected in our CO 3–2 maps. In CO 6–5, only one outflow shows up toward L723, whereas both outflows are seen towards IRAS2A and BHR71.

Visual inspection shows that the Class 0 outflows are more collimated than their Class I counterparts as expected (e.g., Arce et al. 2007). The length of the outflows can be quantified for most of the sources. R_{CO} is defined as the total outflow extent assuming that the outflows are fully covered in the map. R_{CO} is measured separately for the blue and red outflow lobes as the projected size, with sometimes significantly different values. In some sources, e.g., Ced110 IRS4, Elias 29, and DK Cha, the blue and red outflow lobes overlap, likely because the outflow is observed nearly pole on. In those cases, R_{CO} could not be properly estimated and the estimated value is a lower limit.

5.3.2 Outflow parameters

In the following, different outflow parameters, including mass, force and luminosity, are measured. These parameters have previously been determined from lower-J lines for several young stellar objects (e.g., Cabrit & Bertout 1992, Bontemps et al. 1996, Hogerheijde et al. 1998, Hatchell et al. 2007) and more recently from CO 6–5 by van Kempen et al. (2009b) and Yıldız et al. (2012) for a small subset of the sources presented here. All parameters are listed in Tables 5.1–5.3.

Table 5.1 – Outflow properties of the red and blue outflow lobes of YSOs.

Source	Trans.	Inclination [°]	Lobe	$V_{max}{}^a$ [km s^{-1}]	$R_{CO}{}^a$ [AU]	$t_{dyn}{}^{a,b}$ [10^3 yr]	$M_{outflow}{}^{c,d}$ [M$_\odot$]	$\dot{M}^{d,e}$ [M$_\odot$ yr^{-1}]	$F_{CO}{}^{d,f}$ [M$_\odot$ yr^{-1}km s^{-1}]	$L_{kin}{}^{d,g}$ [L$_\odot$]
IRAS2A	CO 3–2	70	Blue	23	3.3×10^4	6.7	2.4×10^{-1}	3.6×10^{-5}	8.3×10^{-4}	1.6×10^0
			Red	15	3.3×10^4	10.2	7.7×10^{-1}	7.6×10^{-5}	1.2×10^{-3}	1.5×10^0
IRAS4A	CO 6–5	50	Blue	23	2.5×10^4	5.1	5.6×10^{-2}	1.1×10^{-5}	2.6×10^{-4}	4.8×10^{-1}
			Red	23	3.5×10^4	7.3	3.7×10^{-1}	5.1×10^{-5}	1.2×10^{-3}	2.2×10^0
	CO 3–2	50	Blue	23	2.5×10^4	5.1	3.4×10^{-2}	6.6×10^{-6}	1.5×10^{-4}	2.9×10^{-1}
			Red	23	3.5×10^4	7.3	2.5×10^{-1}	3.5×10^{-5}	7.9×10^{-4}	1.5×10^0
IRAS4B	CO 6–5	10	Blue	18	3.5×10^3	0.9	2.2×10^{-3}	2.4×10^{-6}	4.3×10^{-5}	6.3×10^{-2}
			Red	16	2.4×10^3	0.7	8.4×10^{-3}	1.2×10^{-5}	1.9×10^{-4}	2.4×10^{-1}
	CO 3–2	10	Blue	23	3.5×10^3	0.7	4.0×10^{-4}	5.5×10^{-7}	1.3×10^{-5}	2.4×10^{-2}
			Red	15	2.4×10^3	0.8	4.2×10^{-3}	5.6×10^{-6}	8.3×10^{-5}	1.0×10^{-1}
L1527	CO 6–5	70	Blue	9	1.5×10^4	8.5	3.0×10^{-2}	3.5×10^{-6}	3.0×10^{-5}	2.1×10^{-2}
			Red	7	1.1×10^4	7.5	8.7×10^{-2}	1.2×10^{-5}	8.2×10^{-5}	4.8×10^{-2}
	CO 3–2	70	Blue	7	3.2×10^4	20.6	6.8×10^{-2}	3.3×10^{-6}	2.4×10^{-5}	1.5×10^{-2}
			Red	11	1.1×10^4	4.8	4.5×10^{-2}	9.4×10^{-6}	1.1×10^{-4}	9.6×10^{-2}
Ced110IRS4	CO 6–5	30	Blue	10	3.8×10^3	1.7	2.8×10^{-4}	1.6×10^{-7}	1.7×10^{-6}	1.4×10^{-3}
			Red	11	3.8×10^3	1.6	1.4×10^{-3}	8.7×10^{-7}	9.4×10^{-6}	8.3×10^{-3}
BHR71	CO 6–5	70	Blue	16	4.4×10^4	13.4	6.0×10^{-1}	4.5×10^{-5}	6.9×10^{-4}	8.8×10^{-1}
			Red	16	4.0×10^4	11.5	3.2×10^{-1}	2.7×10^{-5}	4.5×10^{-4}	6.1×10^{-1}
IRAS15398	CO 6–5	50	Blue	12	2.6×10^3	1.1	7.3×10^{-4}	6.9×10^{-7}	7.9×10^{-6}	7.4×10^{-3}
			Red	11	2.6×10^3	1.1	4.4×10^{-3}	3.9×10^{-6}	4.2×10^{-5}	3.8×10^{-2}
	CO 3–2	50	Blue	13	3.2×10^3	1.2	7.9×10^{-4}	6.5×10^{-7}	8.2×10^{-6}	8.5×10^{-3}
			Red	12	2.0×10^3	0.8	1.3×10^{-3}	1.7×10^{-6}	2.0×10^{-5}	2.0×10^{-2}
L483mm	CO 6–5	70	Blue	9	1.2×10^4	6.7	4.0×10^{-2}	6.0×10^{-6}	5.1×10^{-5}	3.6×10^{-2}
			Red	7	1.0×10^4	7.0	1.3×10^{-1}	1.8×10^{-5}	1.2×10^{-4}	6.9×10^{-2}
	CO 3–2	70	Blue	13	1.4×10^4	5.2	4.3×10^{-3}	8.2×10^{-7}	1.0×10^{-5}	1.1×10^{-2}
			Red	13	1.0×10^4	3.7	6.5×10^{-2}	1.7×10^{-5}	2.2×10^{-4}	2.4×10^{-1}

Notes: [a]Velocities and extent are not corrected for inclination. [b]Dynamical timescale. [c]Constant temperatures of 100 K and 75 K are assumed for the CO 6–5 and CO 3–2 calculations. [d]Corrected for inclination as explained in Sect. 5.3.2.2. [e]Mass outflow rate [f]Outflow force [g]Kinetic luminosity.

Table 5.2 – Outflow properties of the red and blue outflow lobes of YSOs.

Source	Trans.	Inclination [°]	Lobe	$V_{max}{}^a$ [km s^{-1}]	$R_{CO}{}^a$ [AU]	$t_{dyn}{}^{a,b}$ [10^3 yr]	$M_{outflow}{}^{c,d}$ [M$_\odot$]	$\dot{M}^{d,e}$ [M$_\odot$ yr^{-1}]	$F_{CO}{}^{d,f}$ [M$_\odot$ yr^{-1}km s^{-1}]	$L_{kin}{}^{d,g}$ [L$_\odot$]
SMM1	CO 6–5	50	Blue	17	3.4×10^4	9.6	8.6×10^{-2}	8.9×10^{-6}	1.5×10^{-4}	2.1×10^{-1}
			Red	21	1.8×10^4	4.2	1.5×10^{-1}	3.5×10^{-5}	7.1×10^{-4}	1.2×10^0
	CO 3–2	50	Blue	19	3.4×10^4	8.6	1.1×10^{-1}	1.3×10^{-5}	2.4×10^{-4}	3.8×10^{-1}
			Red	21	1.8×10^4	4.2	1.6×10^{-1}	3.7×10^{-5}	7.5×10^{-4}	1.3×10^0
SMM4	CO 6–5	30	Blue	19	3.4×10^4	8.8	1.7×10^{-1}	2.0×10^{-5}	3.6×10^{-4}	5.5×10^{-1}
			Red	12	3.4×10^4	13.6	3.0×10^{-1}	2.2×10^{-5}	2.6×10^{-4}	2.6×10^{-1}
	CO 3–2	30	Blue	19	3.4×10^4	8.6	2.4×10^{-1}	2.8×10^{-5}	5.3×10^{-4}	8.2×10^{-1}
			Red	12	3.4×10^4	14.2	5.5×10^{-1}	3.9×10^{-5}	4.5×10^{-4}	4.2×10^{-1}
SMM3	CO 6–5	50	Blue	20	4.6×10^3	1.1	3.3×10^{-2}	3.0×10^{-5}	6.1×10^{-4}	1.0×10^0
			Red	12	4.6×10^3	1.8	5.5×10^{-2}	3.1×10^{-5}	3.9×10^{-4}	3.9×10^{-1}
	CO 3–2	50	Blue	21	4.6×10^3	1.0	4.0×10^{-2}	3.9×10^{-5}	8.1×10^{-4}	1.4×10^0
			Red	12	4.6×10^3	1.9	8.9×10^{-2}	4.7×10^{-5}	5.4×10^{-4}	5.1×10^{-1}
B335	CO 6–5	70	Blue	12	6.2×10^3	2.4	5.4×10^{-3}	2.2×10^{-6}	2.8×10^{-5}	2.8×10^{-2}
			Red	7	7.5×10^3	5.4	6.6×10^{-2}	1.2×10^{-5}	8.1×10^{-5}	4.4×10^{-2}
L723mm	CO 6–5	50	Blue	13	1.2×10^4	4.4	2.8×10^{-2}	6.5×10^{-6}	8.4×10^{-5}	9.0×10^{-2}
			Red	11	1.2×10^4	5.3	9.4×10^{-2}	1.8×10^{-5}	1.9×10^{-4}	1.7×10^{-1}
	CO 3–2	50	Blue	19	2.1×10^4	5.4	7.6×10^{-2}	1.4×10^{-5}	2.7×10^{-4}	4.1×10^{-1}
			Red	16	1.8×10^4	5.4	2.6×10^{-1}	4.8×10^{-5}	7.6×10^{-4}	9.8×10^{-1}
L1157	CO 3–2	70	Blue	10	4.4×10^4	20.0	2.4×10^{-1}	1.2×10^{-5}	1.3×10^{-4}	1.1×10^{-1}
			Red	15	5.2×10^4	16.0	9.7×10^{-1}	6.1×10^{-5}	9.4×10^{-4}	1.2×10^0
L1489	CO 6–5	50	Blue	12	2.1×10^3	0.9	3.7×10^{-4}	4.3×10^{-7}	4.9×10^{-6}	4.6×10^{-3}
			Red	7	2.1×10^3	1.5	3.7×10^{-3}	2.5×10^{-6}	1.7×10^{-5}	9.5×10^{-3}
	CO 3–2	50	Blue	15	2.1×10^3	0.7	1.2×10^{-3}	1.8×10^{-6}	2.7×10^{-5}	3.2×10^{-2}
			Red	10	2.1×10^3	1.0	9.8×10^{-3}	9.6×10^{-6}	9.4×10^{-5}	7.6×10^{-2}
L1551IRS5	CO 3–2	70	Blue	13	1.7×10^4	6.3	2.2×10^{-2}	3.5×10^{-6}	4.5×10^{-5}	4.6×10^{-2}
			Red	11	1.7×10^4	7.4	9.6×10^{-2}	1.3×10^{-5}	1.4×10^{-4}	1.2×10^{-1}

Notes: ^{a}Velocities and extent are not corrected for inclination. ^{b}Dynamical timescale. ^{c}Constant temperatures of 100 K and 75 K are assumed for the CO 6–5 and CO 3–2 calculations. ^{d}Corrected for inclination as explained in Sect. 5.3.2.2. ^{e}Mass outflow rate ^{f}Outflow force ^{g}Kinetic luminosity.

Table 5.3 – Outflow properties of the red and blue outflow lobes of the YSOs.

Source	Trans.	Inclination [°]	Lobe	V_{max}^a [km s^{-1}]	R_{CO}^a [AU]	$t_{dyn}^{a,b}$ [10^3 yr]	$M_{outflow}^c$ [M$_\odot$]	$\dot{M}^{a,e}$ [M$_\odot$ yr^{-1}]	$F_{CO}^{a,f}$ [M$_\odot$ yr^{-1} km s^{-1}]	$L_{kin}^{a,g}$ [L$_\odot$]
TMR1	CO 6–5	50	Blue	10	4.9×10^3	2.4	8.5×10^{-4}	3.5×10^{-7}	3.3×10^{-6}	2.6×10^{-3}
			Red	6	4.9×10^3	4.1	4.4×10^{-3}	1.1×10^{-6}	6.2×10^{-6}	2.9×10^{-3}
	CO 3–2	50	Blue	11	1.4×10^4	6.1	2.0×10^{-3}	3.3×10^{-7}	3.6×10^{-6}	3.2×10^{-3}
			Red	4	3.5×10^3	4.5	7.8×10^{-3}	1.7×10^{-6}	6.5×10^{-6}	2.0×10^{-3}
TMC1A	CO 3–2	50	Blue	19	5.6×10^3	1.4	3.2×10^{-3}	2.3×10^{-6}	4.5×10^{-5}	7.0×10^{-2}
			Red	7	1.7×10^3	1.1	2.7×10^{-3}	2.6×10^{-6}	1.9×10^{-5}	1.1×10^{-2}
TMC1	CO 6–5	50	Blue	12	2.8×10^3	1.2	6.1×10^{-4}	5.3×10^{-7}	6.1×10^{-6}	5.7×10^{-3}
			Red	15	2.8×10^3	0.9	5.5×10^{-3}	6.2×10^{-6}	9.2×10^{-5}	1.1×10^{-1}
	CO 3–2	50	Blue	16	3.5×10^3	1.1	8.2×10^{-4}	7.7×10^{-7}	1.2×10^{-5}	1.6×10^{-2}
			Red	17	2.1×10^3	0.6	5.2×10^{-3}	8.8×10^{-6}	1.5×10^{-4}	2.1×10^{-1}
HH46	CO 6–5	50	Blue	12	6.8×10^3	2.8	1.8×10^{-2}	6.6×10^{-6}	7.6×10^{-5}	7.2×10^{-2}
			Red	20	2.7×10^4	6.5	1.3×10^{-1}	2.0×10^{-5}	3.9×10^{-4}	6.4×10^{-1}
	CO 3–2	50	Blue	17	2.7×10^4	7.6	6.9×10^{-2}	9.0×10^{-6}	1.5×10^{-4}	2.1×10^{-1}
			Red	6	6.8×10^3	5.8	4.1×10^{-1}	7.0×10^{-5}	3.8×10^{-4}	1.7×10^{-1}
DKCha	CO 6–5	10	Blue	9	1.8×10^3	0.9	1.8×10^{-4}	2.0×10^{-7}	1.8×10^{-6}	1.4×10^{-3}
			Red	9	1.8×10^3	0.9	2.4×10^{-4}	2.5×10^{-7}	2.2×10^{-6}	1.6×10^{-3}
GSS30IRS1	CO 6–5	30	Blue	19	1.5×10^4	3.8	1.0×10^{-2}	2.6×10^{-6}	4.8×10^{-5}	7.3×10^{-2}
			Red	17	1.5×10^4	4.3	5.9×10^{-2}	1.4×10^{-5}	2.2×10^{-4}	3.0×10^{-1}
	CO 3–2	30	Blue	14	1.5×10^4	5.1	8.4×10^{-3}	1.7×10^{-6}	2.3×10^{-5}	2.7×10^{-2}
			Red	17	1.5×10^4	4.3	5.1×10^{-2}	1.2×10^{-5}	1.9×10^{-4}	2.6×10^{-1}
Elias29	CO 6–5	30	Blue	11	5.0×10^3	2.2	1.9×10^{-3}	8.6×10^{-7}	9.3×10^{-6}	8.3×10^{-3}
			Red	12	3.1×10^3	1.3	4.9×10^{-3}	3.9×10^{-6}	4.6×10^{-5}	4.4×10^{-2}
	CO 3–2	30	Blue	13	3.1×10^3	1.2	5.3×10^{-3}	4.6×10^{-6}	5.9×10^{-5}	6.1×10^{-2}
			Red	13	1.9×10^3	0.7	2.6×10^{-2}	3.7×10^{-5}	4.6×10^{-4}	4.8×10^{-1}
OphIRS63	CO 6–5	50	Blue	8	2.5×10^3	1.5	5.2×10^{-4}	3.5×10^{-7}	2.8×10^{-6}	1.8×10^{-3}
			Red	7	2.5×10^3	1.6	5.3×10^{-3}	3.2×10^{-6}	2.3×10^{-5}	1.4×10^{-2}
	CO 3–2	50	Blue	13	1.0×10^4	3.6	6.4×10^{-4}	1.8×10^{-7}	2.4×10^{-6}	2.6×10^{-3}
			Red	6	7.5×10^3	5.7	1.4×10^{-2}	2.5×10^{-6}	1.5×10^{-5}	7.7×10^{-3}

Notes: [a]Velocities and extent are not corrected for inclination. [b]Dynamical timescale. [c]Constant temperatures of 100 K and 75 K are assumed for the CO 6–5 and CO 3–2 calculations. Corrected for inclination as explained in Sect. 5.3.2.2. [e]Mass outflow rate [f]Outflow force [g]Kinetic luminosity.

5.3.2.1 Outflow mass

One of the most basic outflow parameters is the mass. The inferred mass only depends on three assumptions: the line opacity, the distribution of level populations, and the CO abundance with respect to H$_2$. In the following we assume that the line wings are optically thin, as has been demonstrated observationally for CO 6–5 for a few sources with massive outflows (e.g., NGC1333-IRAS4A, Yıldız et al. 2012). CO 3–2 emission is also assumed optically thin in the following, although that assumption may not be fully valid (see discussion below). The level populations are assumed to follow a Boltzmann distribution with a single temperature, $T_{\rm ex}$. Finally, the abundance ratio is taken as [H$_2$/^{12}CO]=1.2×10^4.

The upper level column density per statistical weight in a single pixel (4″5×4″5 for CO 6–5, 7″5×7″5 for CO 3–2) is calculated as

$$\frac{N_{\rm u}}{g_{\rm u}} = \frac{\beta \nu^2 \int T_{\rm mb} dV}{A_{\rm ul}\, g_{\rm u}} \ . \tag{5.1}$$

The constant β is $8\pi k/hc^3$=1937 cm^{-2} (GHz^2 K km)$^{-1}$. The remaining parameters are for the specific transition, where ν is the frequency, $A_{\rm ul}$ is the Einstein A coefficent and $g_{\rm u}$=2J+1.

The total CO column density in a pixel, $N_{\rm total}$, is

$$N_{\rm total} = \frac{N_{\rm u}}{g_{\rm u}} Q(T) e^{E_{\rm u}/kT_{\rm ex}} \ ; \tag{5.2}$$

$Q(T)$ is the partition function corresponding to a specific excitation temperature, $T_{\rm ex}$, which is assumed as 75 K and 100 K for CO 3–2 and CO 6–5 observations, respectively (van Kempen et al. 2009b, Yıldız et al. 2012).

The mass is calculated as

$$M_{\rm outflow} = \mu_{\rm H_2}\, m_{\rm H}\, A \left[\frac{\rm H_2}{^{12}\rm CO} \right] \sum_j N_{{\rm total},j} \tag{5.3}$$

where the factor $\mu_{\rm H_2}$=2.8 includes the contribution of helium (Kauffmann et al. 2008) and $m_{\rm H}$ is the mass of the hydrogen atom. A is the surface area of one pixel j. The sum is over all outflow pixels. The effect of the assumed excitation temperature results in only ~10% smaller mass at 100 K compared to 75 K.

5.3.2.2 Outflow velocity

The maximum outflow velocity, $V_{\rm max}$ is defined as $\|V_{\rm outflow}\text{-}V_{\rm LSR}\|$, the total velocity extent measured relative to the source velocity. $V_{\rm max}$ is estimated by selecting a representative spectrum from the blue and red outflow lobes separately, and its $FWZI$ (full-width at zero-intensity) is selected as the global value for $V_{\rm max}$ (Cabrit & Bertout 1992). Here, the

Table 5.4 – Inclination correction factors.

$i(°)$	10	30	50	70
c_i	1.2	2.8	4.4	7.1

Notes: Line of sight inclinations, where i=0° indicates pole-on (Downes & Cabrit 2007, van der Marel et al. 2013; subm.).

zero-intensity level refers to the 1σ *rms* level in 0.5 km s^{-1} channels and the *FWZI* is measured from where the line profile first crosses this cutoff.

Two issues arise when determining V_{max}: V_{max} is a function of the *rms* noise level and generally decreases with increasing *rms*. For noisy data, V_{max} may be underestimated compared to its true value. Second, if the outflow lobes are inclined, V_{max} suffers from projection effects. Both effects will increase the value of V_{max} if properly taken into account. As for the noise level, van der Marel et al. (2013; subm.) show that the effect on the outflow force may amount to a factor of a few at most and we ignore this issue in the following.

The second issue with determining V_{max} is the value of the inclination of the outflow lobes, which is difficult to estimate. The inclination is defined as the angle between the outflow direction and the line of sight (Cabrit & Bertout 1990, i=0° is pole on) and is determined based on the morphology in our high spatial resolution maps. Our estimates are listed in Tables 5.1– 5.3, and are consistent with the literature where available (Cabrit & Bertout 1992, Gueth et al. 1996, Bourke et al. 1997, Hogerheijde et al. 1997, Micono et al. 1998, Brown & Chandler 1999, Lommen et al. 2008, Tobin et al. 2008, van Kempen et al. 2010b).

Small radial velocities are expected for an outflow which lies in the plane of the sky. Therefore a correction factor for inclination, c_i is applied in the calculations. In Table 5.4, the correction factors from Downes & Cabrit (2007) are tabulated. The correction factors have been applied to the outflow rate, force and luminosity as listed in Tables 5.1–5.3.

5.3.2.3   Outflow force

One of the key outflow parameters is the outflow force, F_{CO}. The best method for computing the outflow force is still debated and the results suffer from ill-constrained observational parameters, such as inclination, i. van der Marel et al. (2013; subm.) compare seven different methods proposed in the literature to calculate outflow forces. The "separation method" (see below) in their paper is found to be the preferred method, which is less affected by the observational biases. The method can also be applied to low spatial resolution observations or incomplete maps. Uncertainties are estimated to be a factor of a few.

In the following, the outflow force is calculated separately for the blue- and red-shifted
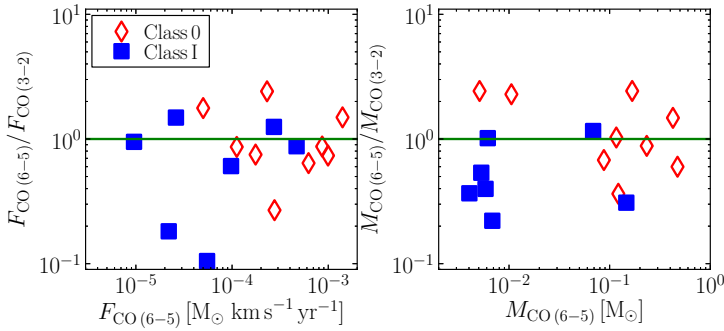
Figure 5.4 – Outflow forces (*left*) and outflow masses (*right*), calculated from CO 6–5 and 3–2 emission are compared for Class 0 and I sources. Green lines are for a ratio of 1.

lobes. The mass is calculated for each channel separately and multiplied by the central velocity of that particular channel. They are then summed and the sum is over all pixels j in the map with outflow emission. This method is formulated as:

$$F_{CO} = c_i \frac{V_{max} \sum_j \left[\int M(V')V'dV' \right]_j}{R_{CO}}, \tag{5.4}$$

where c_i is the inclination correction, and R_{CO} is the projected size of one of the outflow lobes. These values are computed separately from the CO 3–2 and 6–5 maps of the same source (see Tables 5.1–5.3).

The difference in outflow force between the red and blue outflow lobes ranges from ~1 up to a factor of 10. For sources with a low outflow force this is a result of differences in the inferred outflow mass per lobe, which, in these specific cases, is primarily a result of low S/N. In these cases, the overall uncertainty on the outflow force is high, up to a factor of ten. In other cases, such as HH46 as mentioned above, there is a real asymmetry between the different lobes which is caused by a difference in the surrounding environment. In the following, only the sum of the outflow force as measured from each outflow lobe will be used.

Figure 5.4 shows how the outflow forces and outflow masses calculated from CO 3–2 and 6–5 differ. For strong outflows, there is a factor of a few difference in the two calculations. Interestingly, for both parameters, the values from CO 6–5 are higher in the Class 0 sources but lower in the Class I sources than those from CO 3–2. One possible explanation is that the bright outflows from Class 0 sources suffer more from opacity effects in the 3–2 transition and so the mass is underestimated. Class I sources, on the other hand, generally suffer from low S/N in the 6–5 transition leading to an apparent lower mass. Figure 5.5 displays F_{CO} for Class 0 and Class I sources separately. Generally, Class 0 sources have higher outflow forces and are thus more powerful than their Class I counterparts (Bontemps et al. 1996).
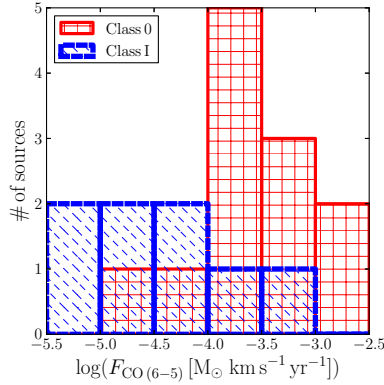
Figure 5.5 – Histograms of calculated total outflow force F_{CO} is shown for Class 0 (red) and Class I (blue) sources.

5.3.3 Other outflow parameters

Other outflow parameters that characterize the outflow activity are the dynamical age, t_{dyn}, outflow mass rate, $\dot{M}_{outflow}$, and kinetic luminosity, L_{kin}.

The dynamical age is determined as

$$t_{dyn} = \frac{R_{CO}}{V_{max}} \ .$$

(5.5)

This age is usually also a lower limit on the age of the protostar (Curtis et al. 2010b). The outflow mass loss rate is computed according to

$$\dot{M}_{outflow} = \frac{M_{outflow}}{t_{dyn}} \ .$$

(5.6)

The kinetic luminosity is given by

$$L_{kin} = \frac{1}{2}F_{CO}V_{max} \ .$$

(5.7)

Outflow parameters derived from the above equations with inclination corrections are presented in Tables 5.1–5.3. Based on the CO 6–5 observations, the strongest outflow emanates from IRAS4A, with the highest value of both outflow force and kinetic luminosity. Other strong outflows include L1448mm, L1157, and BHR71. The results show that outflows have total swept-up masses between ~1 $M_\odot$ (BHR71) to 4×10^{-4} $M_\odot$ (DK Cha), with average mass loss rates between 5×10^{-7} to 7×10^{-5} $M_\odot yr^{-1}$, and outflow forces of 4×10^{-6} to 1×10^{-3} $M_\odot yr^{-1}$ km s^{-1}.
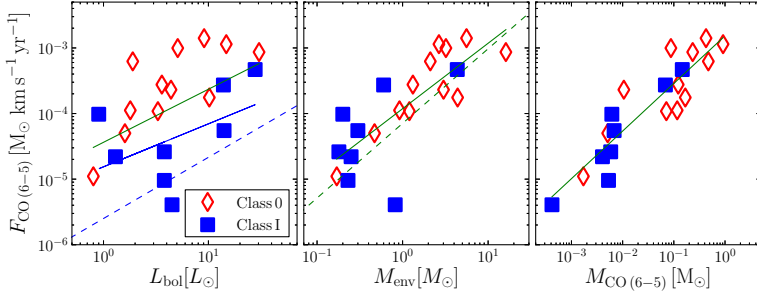
Figure 5.6 – Correlations of F_{CO} with L_{bol}, M_{env}, and $M_{outflow}$, where F_{CO} is determined from the CO 6–5 data. Red and blue symbols indicate Class 0 and Class I sources, respectively. The green solid line is the fit to all values and the blue solid line is the fit to the Class I sources only. Blue and green dashed lines are the best fits from Bontemps et al. (1996).
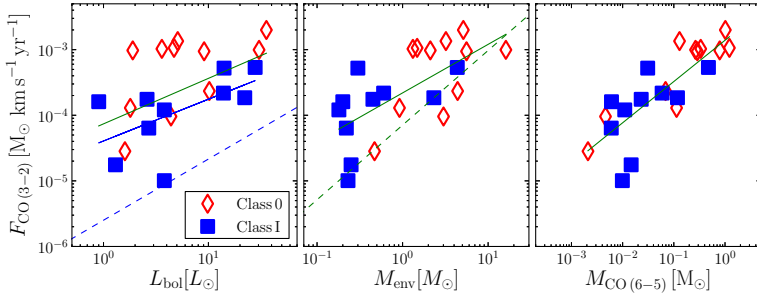
Figure 5.7 – Correlations between F_{CO} as measured from CO 3–2 and bolometric luminosity, envelope mass and outflow mass as determined from CO 6–5.

5.3.4 Correlations

Most previous studies of the outflow force were done using either CO 2–1 or 3–2 (e.g., Cabrit & Bertout 1992, Bontemps et al. 1996, Hogerheijde et al. 1998, Hatchell et al. 2007, van Kempen et al. 2009c). These low-J lines inevitably suffer from opacity effects, but without targeted, deep surveys of, e.g., ^{13}CO, it is difficult to quantify how much the CO column density is underestimated. Furthermore, cloud or envelope emission may contribute to the emission at the lowest outflow velocities at which the bulk of the mass is flowing. With these CO 6–5 observations, some of the above-mentioned issues can be avoided, or their effects can be lessened. In particular, CO 6–5 emission is typically optically thin in the line wings (van Kempen et al. 2009b, Yıldız et al. 2012). Furthermore, the contribution from the surrounding cloud and envelope is much less than for the case of CO 3–2 (Fig. 5.10). Thus, it is important to revisit the correlations of outflow force with bolometric luminosity and envelope mass using these new measurements.

In Fig. 5.6, F_{CO} is plotted against L_{bol}, M_{env}, and $M_{outflow}$, where the F_{CO} and $M_{outflow}$

values are taken from the CO 6–5 data. The best fit between F_{CO} and L_{bol} is shown with the green line corresponding to

$$\log(F_{CO}) = -(5.02 \pm 0.1) + (0.95 \pm 0.27)\log(L_{bol}) . \tag{5.8}$$

Outflows from Class 0 and Class I sources are well-separated; Class 0 sources show more powerful outflows compared to Class I sources of similar luminosity. The Pearson correlation coefficients are r=0.37, 0.42, and 0.68 for all sources, Class 0, and Class I sources, respectively, corresponding to confidences of $\sim 2.3, 2.0$ and 2.7σ, respectively.

The best fit between F_{CO} and M_{env} is described as

$$\log(F_{CO}) = -(4.37 \pm 0.1) + (1.14 \pm 0.15)\log(M_{env}) \tag{5.9}$$

and Pearson correlation coefficients are r=0.49, 0.39, and 0.66 ($\sim 3.1, 1.9$ and 2.6σ) for all sources, Class 0, and Class I, respectively. Since early stage Class 0 sources have more envelope mass their outflow force is much higher than for the Class I sources. Only the first correlation appears significant.

Finally, as expected, a strong correlation is found between F_{CO} and $M_{outflow}$ with a Pearson correlation coefficient of r=0.75 for all sources ($\sim 4.7\sigma$). The best fit is described as

$$\log(F_{CO}) = -(2.85 \pm 0.1) + (0.77 \pm 0.34)\log(M_{CO}) . \tag{5.10}$$

Previously, Bontemps et al. (1996) surveyed 45 sources using CO 2–1 observations with small-scale maps. In Fig. 5.6, the blue and green dashed lines of F_{CO} vs. L_{bol} and M_{env} show the fit results from their Figs. 5 and 6 (Bontemps et al. 1996). Since their number of Class I sources is higher than Class 0 sources, the fit was only done for Class I sources in F_{CO} vs. L_{bol}. In Fig. 5.6, the blue solid line shows the fit for only Class I sources and the correlation is described by,

$$\log(F_{CO}) = -(5.52 \pm 0.1) + (0.87 \pm 0.39)\log(L_{bol}) . \tag{5.11}$$

In the F_{CO} vs. M_{env} plot, the fits are shown as green lines for the entire sample. Even though Bontemps et al. (1996) sample is weighted toward lower luminosities, our F_{CO} measurements from CO 6–5 data follow their relation for Class I sources obtained from 2–1 data, but with a shift to higher values of F_{CO}.

Examining the same outflow parameters measured using the CO 3–2 transition, and their correlation with the same outflow parameters, a different picture arises (Fig. 5.7). For the sources in our sample, the correlations follow the same trend but they are all weaker. In particular, the correlations with L_{bol} is at the ~1.5σ level, whereas the correlation with M_{env} is 2.1σ. Although the measured values of, e.g., F_{CO}, fill out the same parameter space as when the measurements are done with CO 6–5, the scatter is larger. The scatter remains of the order of one order of magnitude, which is similar to the scatter reported in the literature (e.g., Bontemps et al. 1996), but because of the limited source sample (20 sources with F_{CO} measurements) it is difficult to compare these 3–2 measurements with what is presented in the literature.
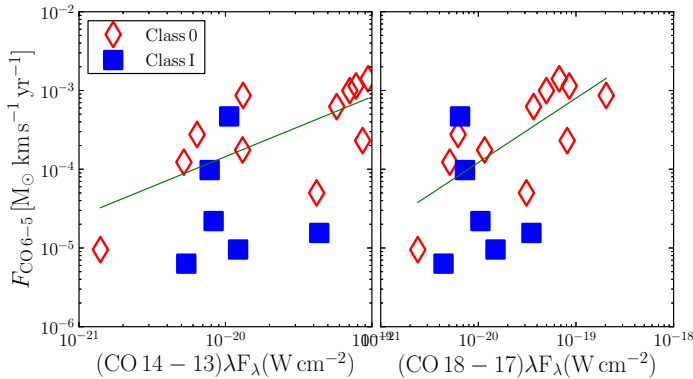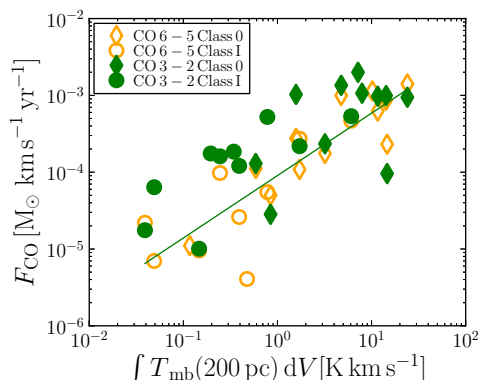
Figure 5.8 – Correlation between F_{CO} and the CO 14–13 and 18–17 fluxes obtained from *Herschel*-PACS.

5.4 Discussion

Our results show that the outflow parameters inferred from the CO 6–5 data show the same trends with L_{bol} and evolutionary stage as found previously in the literature, but with stronger correlations than for the 3–2 data. Even though the same telescope and methods are used for all sources and the spatial resolution is high, there remains a scatter of at least an order of magnitude in the correlation between F_{CO} and L_{bol}. This could point to the importance of "episodic accretion" as a resolution to the "luminosity problem" (Evans et al. 2009, Dunham et al. 2010, 2013). Some Class 0 sources are very luminous, which is likely due to a current rapid burst in accretion which happens every 10^3-10^4 years (Dunham et al. 2010). However, their location in the high state is not constant and would drop in the course of time, on timescales as fast as 10^2 years (Johnstone et al. 2013). The envelope mass, on the other hand, is independent of the current luminosity, and the stronger correlation with M_{env} may simply reflect that more mass is swept up.

Since the outflow force gives the integrated activity over the entire lifetime of YSO, it is also interesting to compare this parameter with the currently shocked gas probed by the *Herschel*-PACS high-J CO observations ($J_u > 14$). In Fig. 5.8, F_{CO} is plotted versus CO 14–13 and CO 18–17 fluxes ($E_{up} \sim 580$ and 940 K) obtained from Karska et al. (2013), Goicoechea et al. (2012), Herczeg et al. (2012) and van Kempen et al. (2010a). There is a weak correlation between the CO 18–17 flux and F_{CO} ($r = 0.69 \sim 2.6\sigma$; Fig. 5.8). This correlation illustrates that although CO 18–17 likely traces a different outflow component than CO 6–5 (Santangelo et al. 2012, Nisini et al. 2013, Tafalla et al. 2013), a component closer to the shock front, the underlying driving mechanism is the same. Furthermore, CO 18–17 emission is often extended along the outflow direction (Karska et al. 2013) and clearly traces, spatially, a component related to that traced by CO 6–5. Although the excitation of CO 18–17 requires higher densities and temperatures ($n_{crit} \sim 10^6$

Figure 5.9 – Correlation between F_{CO} measured from the CO 6–5 and CO 3–2 data and the integrated intensity of the ground-state H_2O $1_{10}-1_{01}$ transition at 557 GHz. The integrated intensities are scaled to a common distance of 200 pc (Kristensen et al. 2012). The correlation is strong, 3.8σ.

cm^{-3}; $E_{up} \sim 940$ K) than CO 6–5 ($n_{crit} \sim 10^5$ cm^{-3}; $E_{up} \sim 120$ K), CO 6–5 likely follows in the wake of the shocks traced by the higher-J lines and therefore the excitation of both lines ultimately depend on the actual shock conditions. Testing this scenario requires velocity-resolved line profiles of high-J lines such as CO 16–15 (Kristensen et al. in prep.).

Another indication that the outflow force as measured from CO 6–5 is more closely linked to the currently shocked gas than 3–2 comes from comparing H_2O and F_{CO}. Water is one of the best shock tracers, as evidenced most recently by several *Herschel* observations (van Kempen et al. 2010b, Lefloch et al. 2010, Nisini et al. 2010, Vasta et al. 2012, Tafalla et al. 2013). Kristensen et al. (2012) compared the integrated intensity of the H_2O $1_{10}-1_{01}$ transition at 557 GHz with the outflow forces presented in the literature. These observed line intensities are scaled by the square of the source distance to a common distance of d_{avg}=200 pc. The outflow forces were calculated using a variety of methods and data sets, and provided an inhomogeneous sample. No correlation of H_2O integrated intensity with F_{CO} was found. Revisiting this comparison with the newly measured outflow forces reveals a weak correlation with the force measured from CO 3–2 data (2.5σ) and a strong correlation with the force measured from the CO 6–5 data (3.8σ) (Fig. 5.9) (see also Bjerkeli et al. 2012). Thus, F_{CO} as deduced from 6–5 can be used as a measure of the outflow force of the shocked gas, rather than just the entrained, swept-up gas.

5.5   Conclusions

In this chapter, we present large-scale maps of 26 YSOs obtained with the APEX-CHAMP$^+$ instrument (^{12}CO and ^{13}CO 6–5), together with the JCMT-HARP-B instrument (^{12}CO and ^{13}CO 3–2). Our sample consists of deeply embedded Class 0 sources as well as less deeply embedded Class I sources. With these high spatial and spectral resolution maps, we have studied the outflow activity of these two different evolutionary stages

of YSOs in a consistent manner. All embedded sources show large scale outflow activity that can be traced by the CO line wings, however their activity is reduced in the course of evolution to the later evolutionary stages as indicated by several outflow parameters.

One of the key outflow parameters, the outflow force, F_{CO} is quantified and correlations with other physical parameters are sought. In agreement with previous studies, Class 0 sources have higher outflow forces than Class I sources. F_{CO} is directly proportional to M_{env} and $M_{outflow}$, showing that higher outflow forces are associated with higher envelope mass or outflow mass, as present in Class 0 sources. Comparing the outflow force as measured from CO 6–5 data to H_2O observed with *Herschel*-HIFI and high-J CO observed with *Herschel*-PACS reveals a correlation, suggesting that the outflow force from 6–5 is at least weakly related to current shock activity. This is in contrast with the outflow force measured from CO 3–2, where there is little or no correlation with water and these high-J fluxes.

Acknowledgements

5.6 Additional materials

Table 5.5 – Integration limits and contour levels.

| Source | Blue Lobe[a] | | | Red Lobe[a] | | | CO 6–5 | | CO 3–2 | |
	V_{max} [km s^{-1}]	$V_{out,blue}$ [km s^{-1}]	$V_{in,blue}$ [km s^{-1}]	V_{max} [km s^{-1}]	$V_{in,red}$ [km s^{-1}]	$V_{out,red}$ [km s^{-1}]	Lowest Cntr[b] [K km s^{-1}]	Step Size[b] [K km s^{-1}]	Lowest Cntr[b] [K km s^{-1}]	Step Size[b] [K km s^{-1}]
L1448mm[c]	35.0	−32.0	3.0	37.0	8.0	45.0	…	…	10	10
IRAS2A[c]	23.0	−17.0	6.0	25.0	11.0	36.0	15	20	15	15
IRAS4A	23.1	−15.9	4.0	22.8	9.1	30.0	20	20	20	20
IRAS4B	18.1	−10.9	4.0	15.8	9.1	23.0	20	20	20	20
L1527	8.5	−2.6	4.5	7.1	7.4	13.0	7	4	5	3
Ced110IRS4	7.2	−3.0	3.5	5.8	5.5	10.0	8	5	5	3
BHR71	15.5	−19.9	−6.0	16.4	−3.9	12.0	20	20	…	…
IRAS15398	11.5	−6.4	2.5	10.9	6.6	16.0	5	5	3	3
L483MM	8.5	−3.3	4.0	6.8	6.7	12.0	8	8	5	8
SMM1	17.0	−8.5	6.0	20.5	10.5	29.0	15	20	30	25
SMM4	18.5	−10.5	6.0	12.0	10.5	20.0	15	20	30	25
SMM3	20.1	−12.5	6.0	12.4	10.5	20.0	15	20	30	25
L723MM	13.0	−1.8	9.0	10.8	12.2	22.0	15	10	5	5
B335	12.3	−3.9	6.5	6.6	9.1	15.0	…	…	…	…
L1157[c]	10.4	−7.8	1.5	15.4	3.7	18.0	…	…	10	20
L1489	11.5	−4.3	5.0	6.8	8.7	14.0	3	2	5	10
L1551IRS5[c]	12.7	−6.5	4.5	10.8	7.5	17.0	…	…	10	10
TMR1	9.5	−3.2	4.0	5.7	6.8	12.0	3	3	2	2
TMC1A	15.0	−8.4	4.0	5.4	8.6	12.0	5	5	2	5
TMC1	11.5	−6.3	4.0	14.8	6.7	20.0	4	5	3	3
HH46	11.5	−6.3	4.0	19.8	6.2	25.0	15	8	10	10
DKCha	9.3	−6.2	1.5	8.9	4.3	12.0	5	5	5	5
GSS30IRS1	18.5	−15.0	1.5	16.5	6.0	20.0	20	30	15	15
Elias29	10.8	−6.5	2.5	11.7	6.5	16.0	15	10	7.5	5.0
OphIRS63	8.0	−5.2	1.0	7.2	3.8	10.0	4	1.5	2	1
RNO91	7.5	−7.0	−1.0	5.5	2.0	6.0	3	3	3	3

Notes: [a]Velocity integration limits as shown in Fig. 5.10. [b]Contour levels are given in absolute intensities. [c]Obtained from ^{12}CO 3–2.
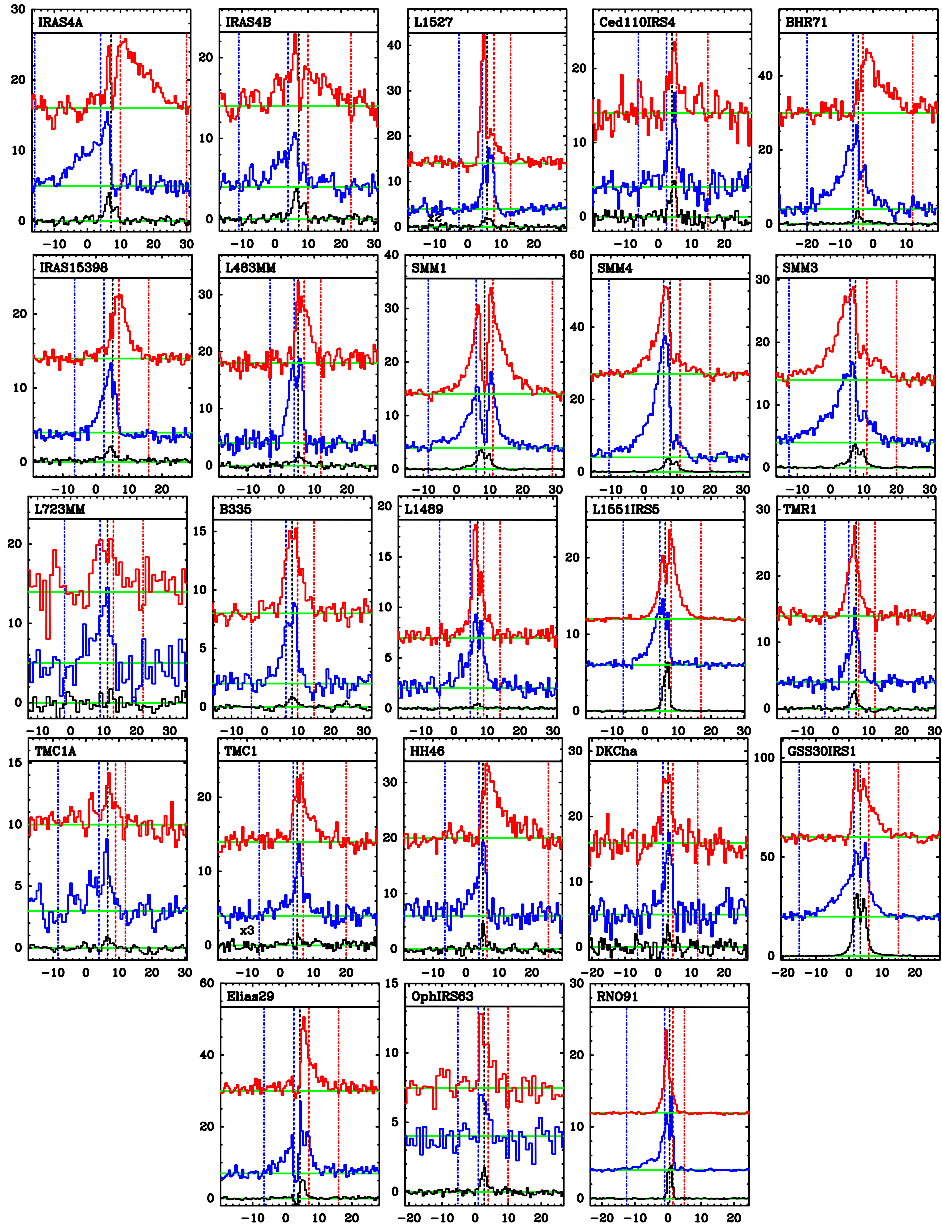
Figure 5.10 – CO 6–5 spectra with selected integration limits indicated. Each panel presents these limits for each source. The black spectrum at the *bottom* is taken from a clean position representative for the envelope emission. The blue spectrum at the *middle* is the representative spectrum from the blue outflow lobe, and red spectrum at the *top* is the representative spectrum from the red outflow lobe. Each panel shows four vertical lines showing the limits, these are $V_{out,blue}$ *(dot-dash blue line)*, $V_{in,blue}$ *(dashed blue line)*, $V_{in,red}$ *(dashed red line)*, and $V_{out,red}$ *(dot-dash red line)*.
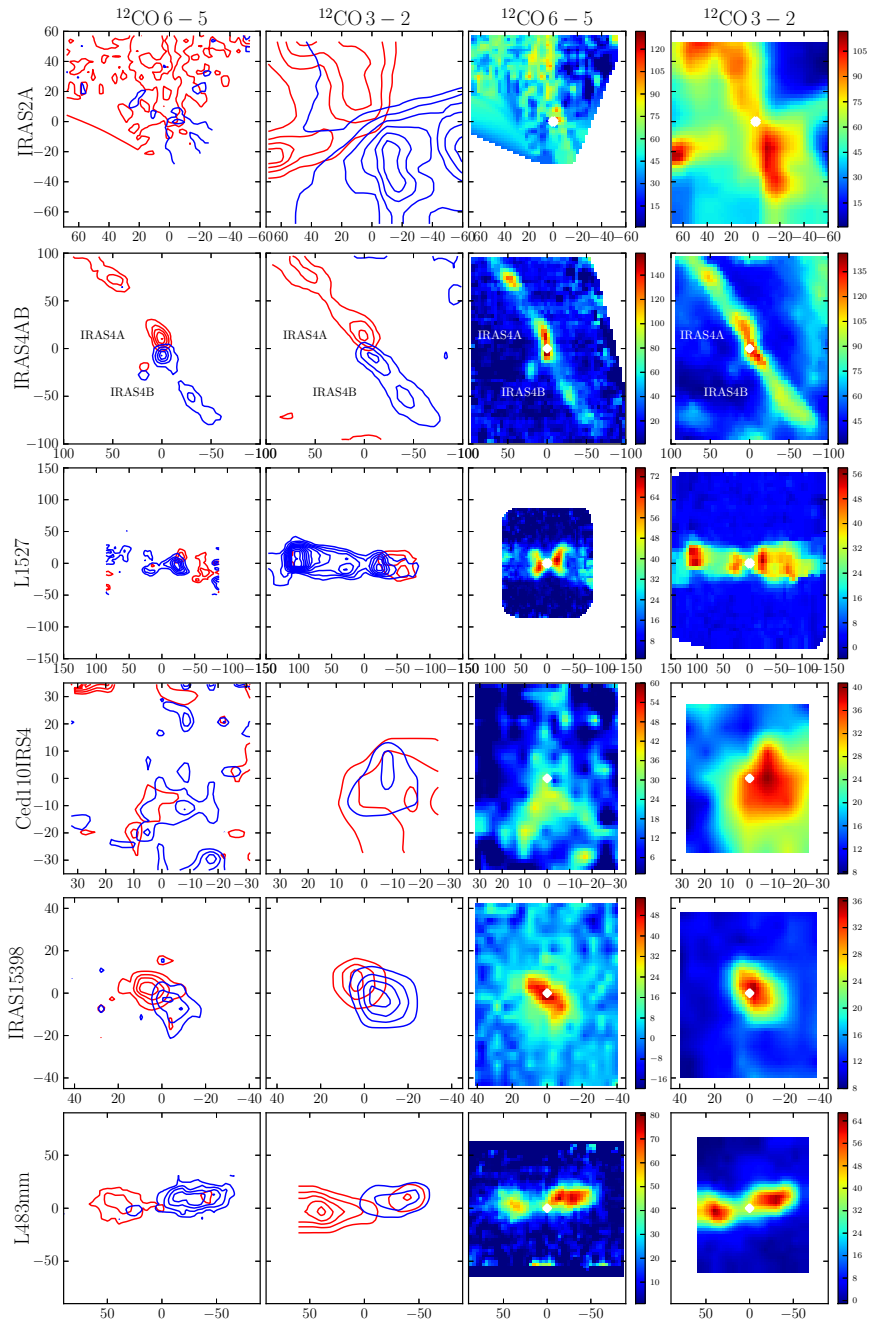
Figure 5.11 – Each row contains contour and integrated intensity maps of sources in ^{12}CO 6–5 and 3–2. The contour levels and integration limits are given in Table 5.5 and integration limits shown in Fig. 5.10.
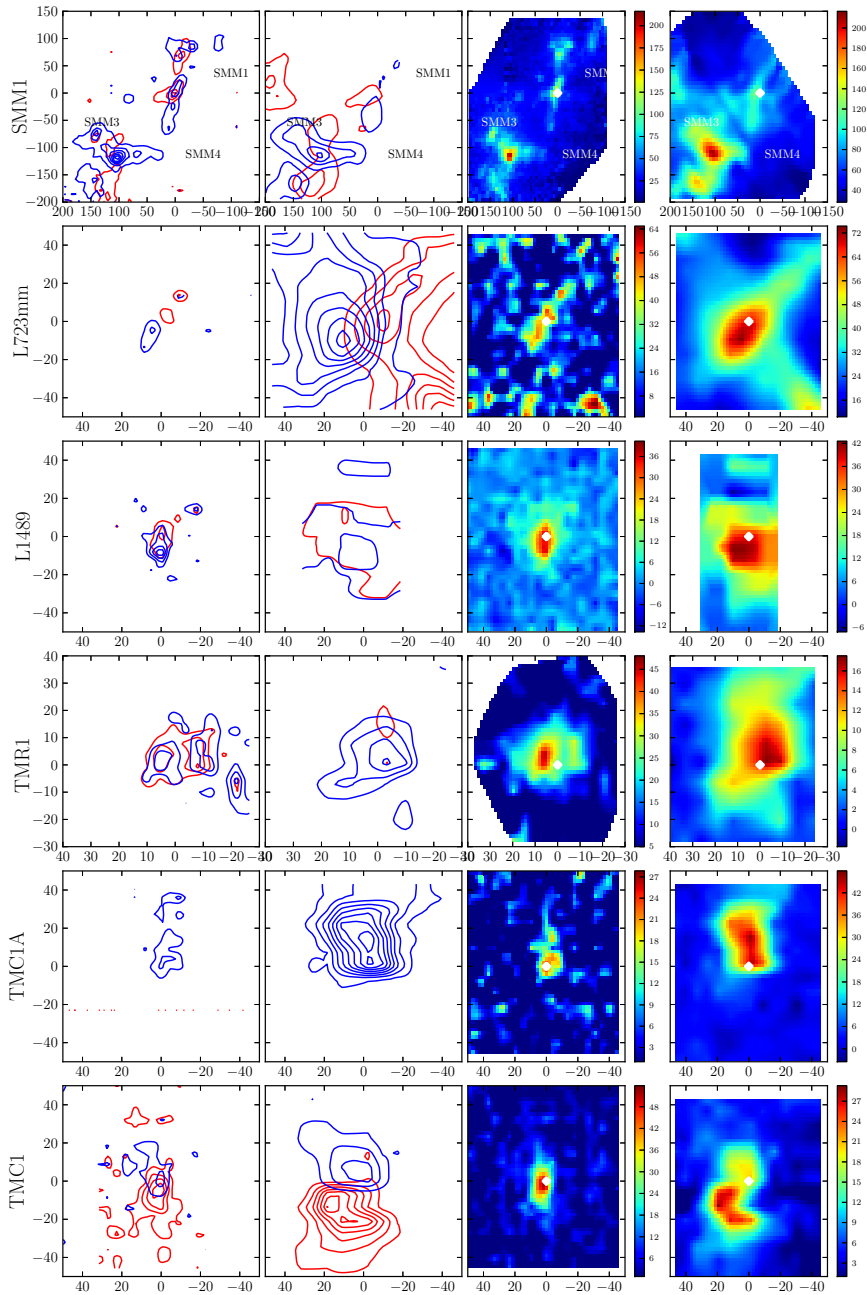
Figure 5.12 – Caption is same as Fig. 5.11.
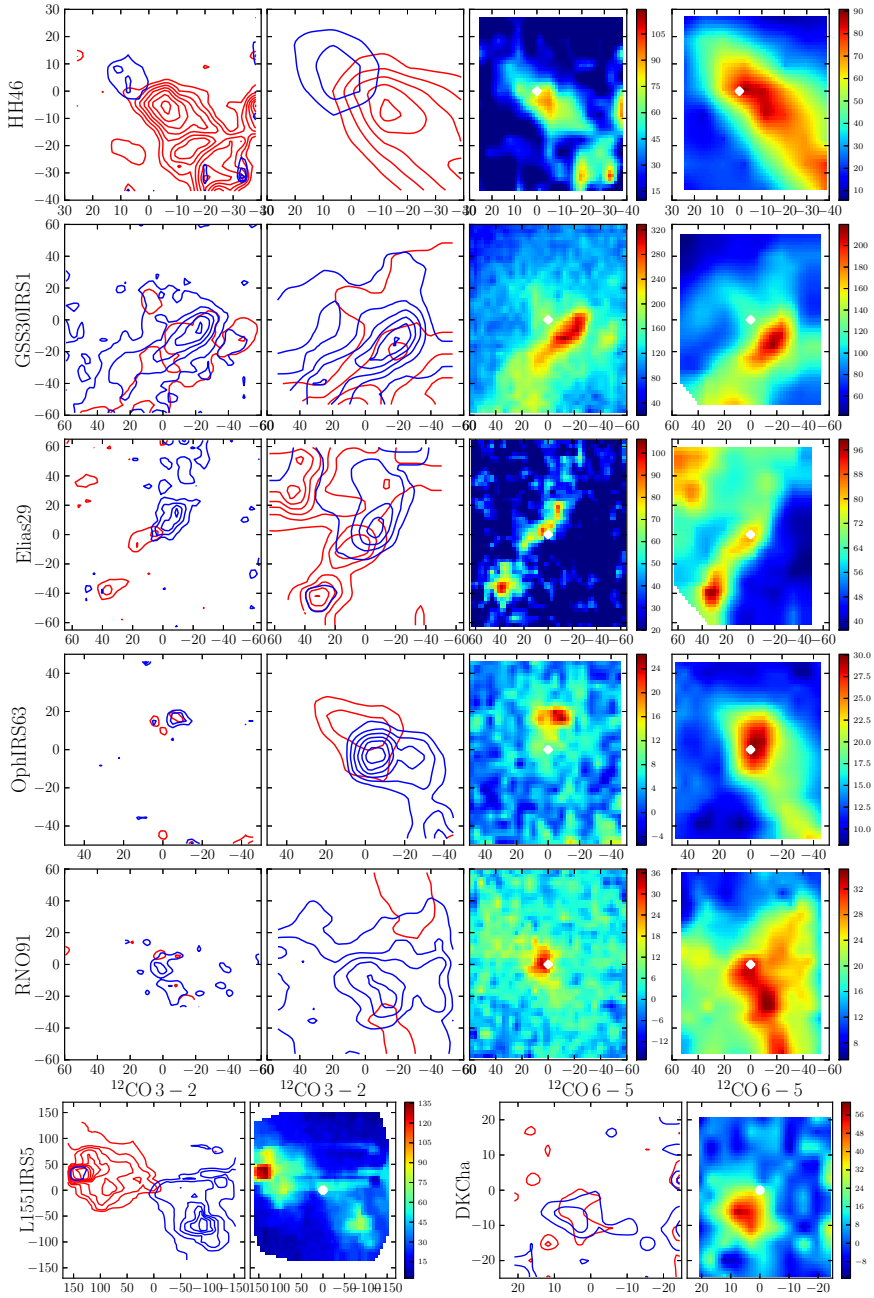
Figure 5.13 – Caption is same as Fig. 5.11.
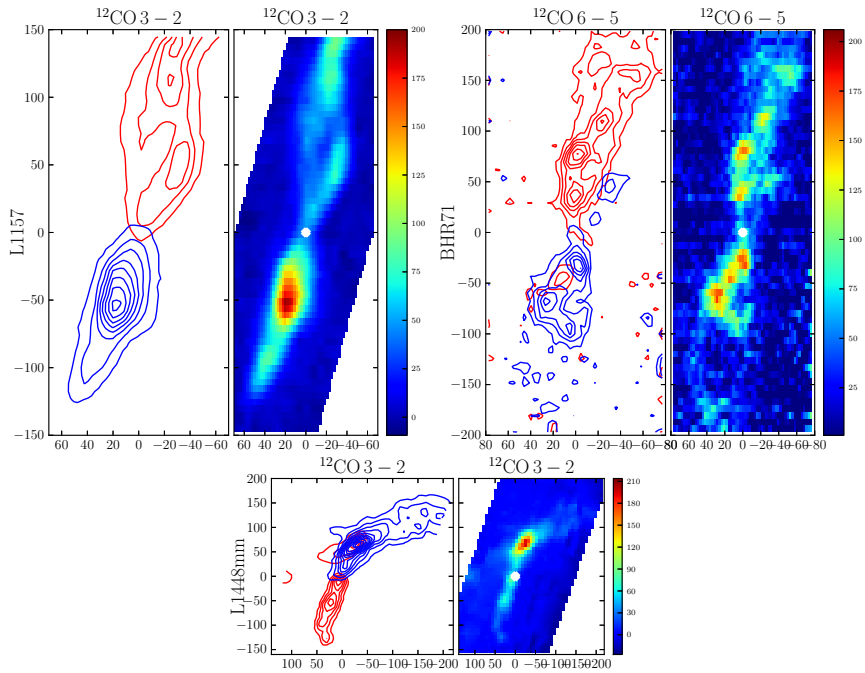
Figure 5.14 – Caption is same as Fig. 5.11.
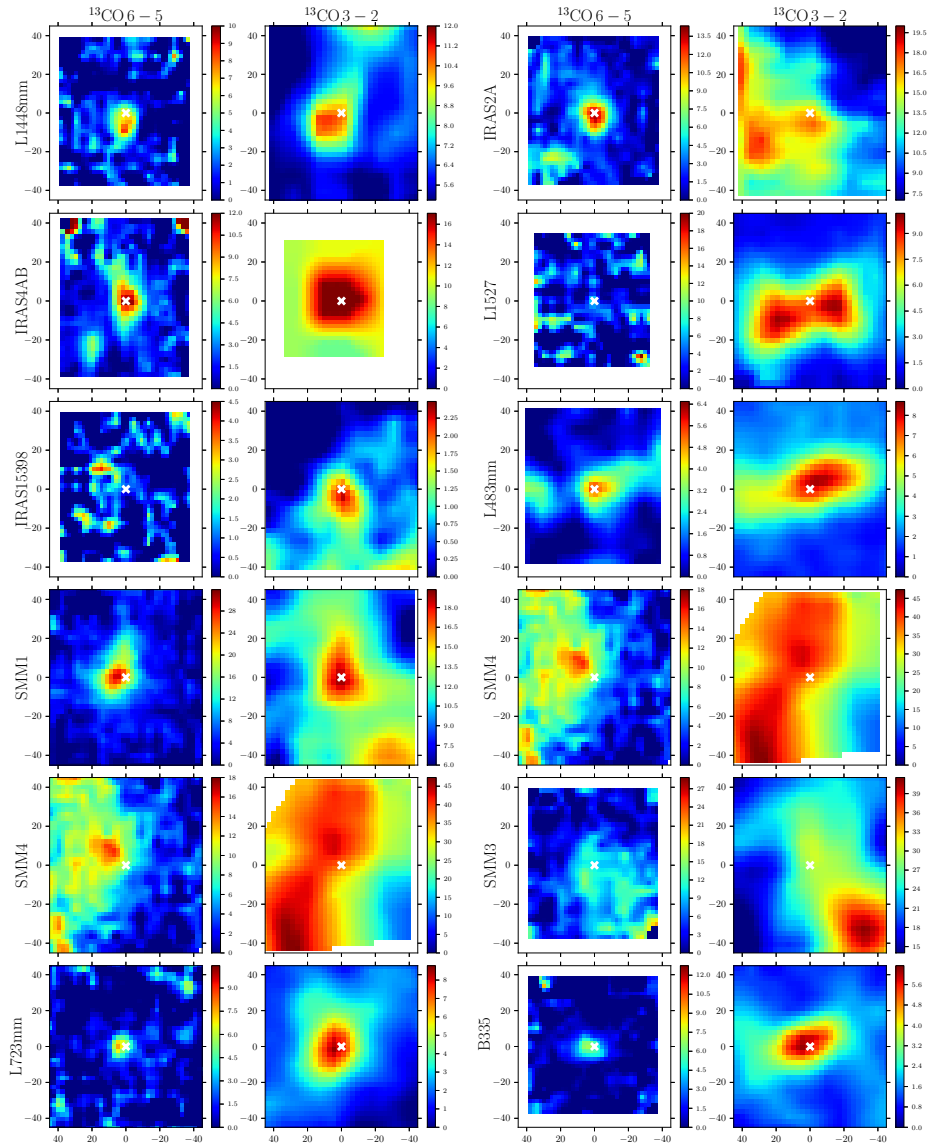
Figure 5.15 – Integrated intensity maps of sources are presented in ^{13}CO 6–5 and 3–2. Integration limits are described in Sect. 5.2.4.
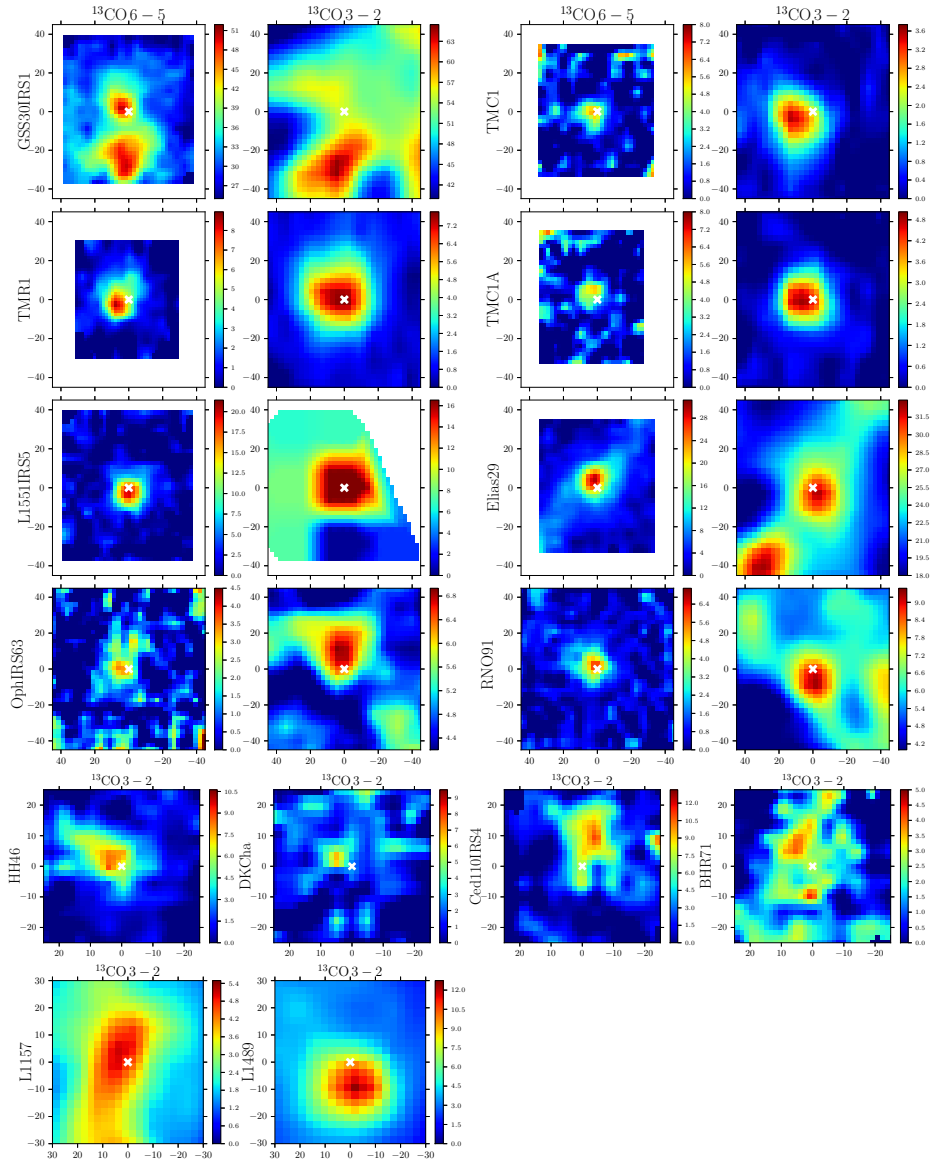
Figure 5.16 – Caption is same as Fig. 5.15.

6
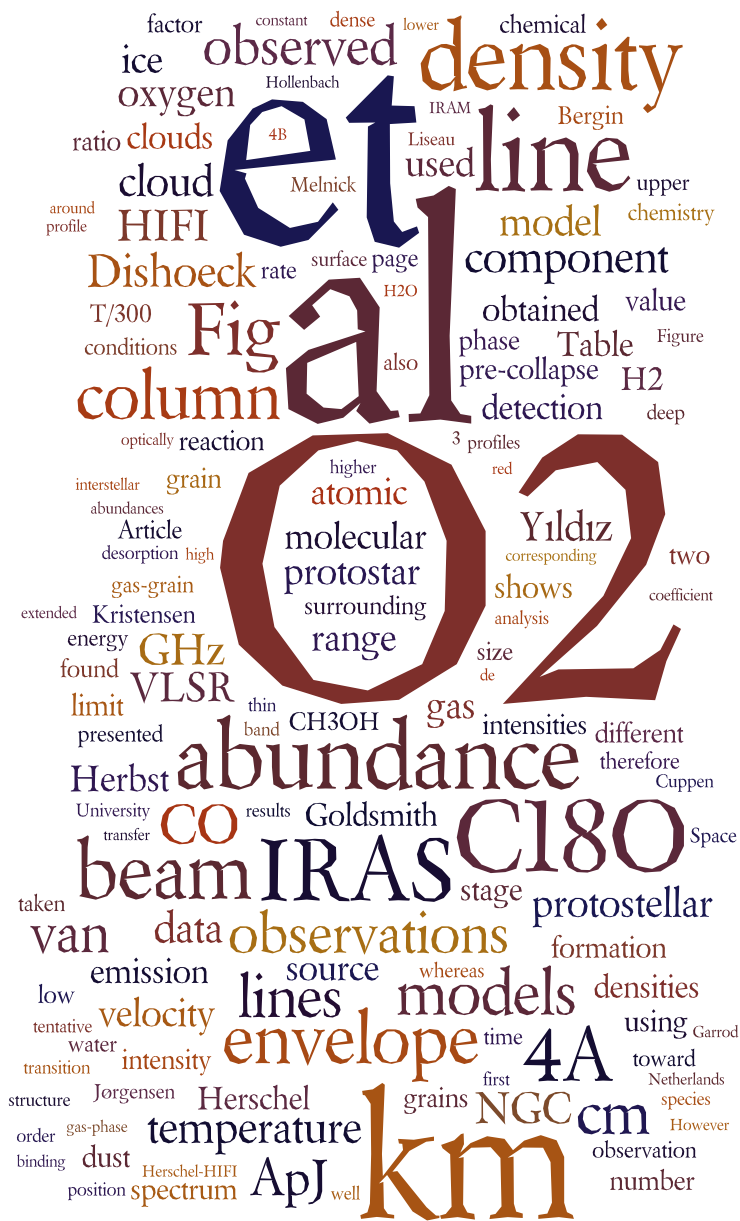
Deep observations of O_2 toward a low-mass protostar with Herschel

Umut A. Yıldız, Kinsuk Acharyya, Paul F. Goldsmith, Ewine F. van Dishoeck,
Gary Melnick, René Liseau, Jo-Hsin Chen, Laurent Pagani, Edwin Bergin,
Paola Caselli, Eric Herbst, Ruud Visser, Dariusz C. Lis, Maryvonne Gerin

Abstract

CONTEXT: According to traditional gas-phase chemical models, O$_2$ should be abundant in molecular clouds, but until recently, attempts to detect interstellar O$_2$ line emission with ground- and space-based observatories have failed.

AIMS: Following the multi-line detection of O$_2$ with low abundances in the Orion and ρ Oph A molecular clouds with *Herschel*, it is important to investigate other environments, and we here quantify the O$_2$ abundance near a solar-mass protostar.

METHODS: Observations of molecular oxygen, O$_2$, at 487 GHz toward a deeply embedded low-mass Class 0 protostar, NGC 1333 IRAS 4A, are presented, using the Heterodyne Instrument for the Far Infrared (HIFI) on the *Herschel* Space Observatory. Complementary data of the chemically related NO and CO molecules are obtained as well. The high spectral resolution data are analysed using radiative transfer models to infer column densities and abundances, and are tested directly against full gas-grain chemical models.

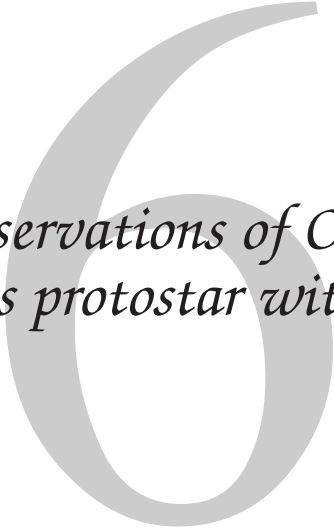*RESULTS:* The deep HIFI spectrum fails to show O$_2$ at the velocity of the dense protostellar envelope, implying one of the deepest upper limits of O$_2$/H$_2$ at $\leq 6 \times 10^{-9}$ (3σ). The O$_2$/CO abundance ratio is less than 0.005. However, a tentative (4.5σ) detection of O$_2$ is seen at the velocity of the surrounding NGC 1333 molecular cloud, shifted by 1 km s^{-1} relative to the protostar. Pure gas-phase models and gas-grain chemical models overproduce O$_2$ in the dense envelope, unless a long pre-collapse stage ($\sim 10^6$ years) is included, during which atomic and molecular oxygen are frozen-out onto the dust grains and fully converted into H$_2$O. The same model also reproduces the chemically related NO molecule if hydrogenation of NO on the grains to more complex molecules such as NH$_2$OH, found in recent laboratory experiments, is included. The tentative detection of O$_2$ in the surrounding cloud is consistent with a low density PDR model with an enhancement of the incident radiation field by a factor of ~ 500.

CONCLUSIONS: The low O$_2$ abundance in the collapsing envelope around a low-mass protostar suggests that the gas and ice entering protoplanetary disks is very poor in O$_2$.

6.1 Introduction

E ven though molecular oxygen (O_2) has a simple chemical structure, it remains diffi-
cult to detect in the interstellar medium after many years of searches (Goldsmith et al.
2011, and references therein). Oxygen is the third most abundant element in the Universe,
after hydrogen and helium, which makes it very important in terms of understanding the
formation and evolution of the chemistry in astronomical sources.

Pure gas-phase chemistry models suggest a steady-state abundance of $X(O_2) \approx 7 \times 10^{-5}$
relative to H_2 (e.g., Table 9 of Woodall et al. 2007), however observations show that the
abundance is several orders of magnitude lower than these model predictions. Early (un-
successful) ground-based searches of O_2 were done through the $^{16}O^{18}O$ isotopologue
(Goldsmith et al. 1985, Pagani et al. 1993), for which some of the lines fall in a trans-
parent part of the atmosphere. Due to the oxygen content of the Earth's atmosphere, it is
however best to observe O_2 from space. Two previous space missions, the *Submillimeter
Wave Astronomy Satellite* (*SWAS;* Melnick et al. 2000) and the *Odin Satellite* (Nordh et al.
2003) were aimed to detect and study interstellar molecular oxygen through specific tran-
sitions. *SWAS* failed to obtain a definitive detection of O_2 at 487 GHz toward nearby
clouds (Goldsmith et al. 2000), whereas *Odin* observations of O_2 at 119 GHz gave upper
limits of $\leq 10^{-7}$ (Pagani et al. 2003), except for the ρ Ophiuchi A cloud ($X(O_2) \sim 5 \times 10^{-8}$;
Larsson et al. 2007).

The *Herschel* Space Observatory provides much higher spatial resolution and sensitiv-
ity than previous missions and therefore allows very deep searches for O_2. Recently,
Herschel-HIFI provided firm multi-line detections of O_2 in the Orion and ρ Oph A molec-
ular clouds (Goldsmith et al. 2011, Liseau et al. 2012). The abundance was found to range
from $X(O_2) \simeq 10^{-6}$ (in Orion) to $X(O_2) \simeq 5 \times 10^{-8}$ (in ρ Oph A). The interpretation of the low
abundance is that oxygen atoms are frozen out onto grains and transformed into water ice
that coats interstellar dust, leaving little atomic O in the gas to produce O_2 (Bergin et al.
2000). So far, O_2 has only been found in clouds where (external) starlight has heated the
dust and prevents atomic O from sticking onto the grains and being processed into H_2O
as predicted by theory (Hollenbach et al. 2009) or where O_2 is enhanced in postshock gas
(Goldsmith et al. 2011). Not every warm cloud has O_2, however. Melnick et al. (2012)
report a low upper limit on gaseous O_2 toward the dense Orion Bar photon-dominated
region (PDR).

Although the detection of O_2 in some molecular clouds is significant, these data tell little
about the presence of O_2 in regions where solar systems may form. It is therefore impor-
tant to also make deep searches for O_2 near solar-mass protostars to understand the origin
of molecular oxygen in protoplanetary disks and eventually (exo-)planetary atmospheres.
Even though the bulk of the O_2 in the Earth's atmosphere arises from life, the amount of
O_2 that could be delivered by cometesimal impacts needs to be quantified. In the present
paper, a nearby low-mass deeply embedded protostar is targeted, which has one of the
largest line of sight hydrogen column densities of $N(H_2) \sim 10^{24}$ cm^{-2} as derived from dust
modeling (Jørgensen et al. 2002, Kristensen et al. 2012). Since the *Herschel* beam size
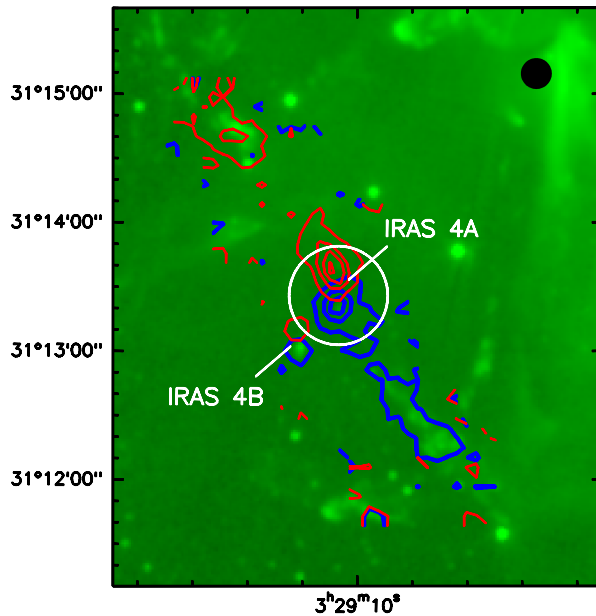
Figure 6.1 – *Spitzer*/IRAC1 (Gutermuth et al. 2008) and CO 6–5 contours (Yıldız et al. 2012) are overlaid to illustrate the NGC 1333 IRAS 4A and 4B protostars. The white circle in the center represents the observed HIFI beam of 44″ centred on IRAS 4A, illustrating that it partially overlaps with the outer part of the IRAS 4B envelope. The contours indicate the outflows, with levels starting from 3σ (15 K km s^{-1}) with an increasing step size of 6σ (30 K km s^{-1}). Blue and red velocity ranges are selected from -20 to 2.7 and from 10.5 to 30 km s^{-1}, respectively. The black dot on upper right corner shows the beam size of the CO 6–5 data.

at 487 GHz is a factor of ∼6 smaller than that of *SWAS*, much deeper information can be obtained for these compact sources. Protostars also differ from dense clouds or PDRs by the fact that a significant fraction of the dust is heated internally by the protostellar luminosity to temperatures above those needed to sublimate O and O$_2$.

NGC 1333 IRAS 4A is located in the southeast part of the NGC 1333 region, together with IRAS 4B (henceforth IRAS 4A and IRAS 4B). A distance of 235±18 pc is adopted based on VLBI parallax measurements of water masers in the nearby source SVS 13 (Hirota et al. 2008). Both objects are classified as deeply-embedded Class 0 low-mass protostars (André & Montmerle 1994) and are well-studied in different molecular lines such as CO, SiO, H$_2$O and CH$_3$OH (e.g., Blake et al. 1995, Lefloch et al. 1998, Bottinelli et al. 2007, Kristensen et al. 2010, Yıldız et al. 2012). Figure 6.1 shows a CO J=6–5 contour map obtained with APEX (Yıldız et al. 2012) overlaid on a *Spitzer*/IRAC1 (3.6 μm) image (Gutermuth et al. 2008). Both IRAS 4A and IRAS 4B have high-velocity outflows seen at different inclinations. The projected separation between the source centers of IRAS 4A and RAS 4B is 31″ (∼7300 AU). The source IRAS4A was chosen for the deep O$_2$ search because of its chemical richness and high total column density. In contrast with

many high-mass protostars, it has the advantage that even deep spectra do not show line confusion.

On a larger scale, early millimeter observations of CO and ^{13}CO J=1–0 by Loren (1976) and Liseau et al. (1988) found two (possibly colliding) clouds in the NGC 1333 region, with velocities separated by up to 2 km s^{-1}. Černis (1990) used extinction mapping in the NGC 1333 region to confirm the existence of two different clouds. The IRAS 4A protostellar envelope is centred at the lower velocity around V_{LSR}=7.0 km s^{-1}, whereas the lower (column) density cloud appears around V_{LSR}=8.0 km s^{-1}. The high spectral resolution of our data allows O_2 to be probed in both clouds. Optically thin isotopologue data of $C^{18}O$ 1–0 up to 5–4 are used to characterize the conditions in the two components. Note that these velocities do not overlap with those of the red outflow lobe, which start at V_{LSR}=+10.5 km s^{-1}.

We present here the first deep observations of the O_2 3_3–1_2 487 GHz line towards a deeply embedded low mass Class 0 protostar observed with *Herschel*-HIFI. Under a wide range of conditions, the O_2 line at 487 GHz is the strongest line, therefore this line is selected for long integration times. The data are complemented by ground-based observations of CO isotopologues and NO using the IRAM 30m and JCMT telescopes. The CO data are used to characterize the kinematics and conditions in the clouds as well as the column of gas where CO is not frozen out. Since the O_2 ice has a very similar binding energy as the CO ice, either in pure or mixed form (Collings et al. 2004, Acharyya et al. 2007), CO provides a good reference for O_2. NO is chosen because it is a related species that could help to constrain the chemistry of O_2. In the gas, O_2 can be produced from atomic O through the reaction (Herbst & Klemperer 1973, Black & Smith 1984)

$$O + OH \rightarrow O_2 + H \qquad\qquad (6.1)$$

with rate constants measured by (Carty et al. 2006). The nitrogen equivalent of Eq. (6.1) produces NO through

$$N + OH \rightarrow NO + H. \qquad\qquad (6.2)$$

The outline of the paper is as follows. Section 6.2 describes the observations and the telescopes where the data were obtained. Results from the observations are presented in Section 6.3. The deep HIFI spectrum reveals a non-detection of O_2 at the velocity of the central protostellar source. However, a tentative (4.5σ) detection is found originating from the surrounding NGC 1333 cloud at V_{LSR}=8 km s^{-1}. In Section 6.3.4, radiative transfer models are used to determine the gas-phase abundance profiles of CO, O_2 and NO in the protostellar envelope, whereas full gas-grain modeling is conducted to interpret the non-detection in Section 6.4. In Section 6.5, the implications for the possible detection in the 8 km s^{-1} component are discussed and in Section 6.6, the conclusions from this work are summarized.

Table 6.1 – Overview of the observed lines.

Molecule	Transition J_{u}-J_{l}	$E_{\mathrm{u}}/k_{\mathrm{B}}$ [K]	A_{ul} [s^{-1}]	Frequency [GHz]	Telescope/ Instrument
O$_2$	3_3–1_2	26.4	8.657×10^{-9}	487.2492640	*Herschel*-HIFI
C^{18}O	1–0	5.3	6.266×10^{-8}	109.7821734	IRAM 30m-EMIR
C^{18}O	3–2	31.6	2.172×10^{-6}	329.3305525	JCMT-HARP-B
C^{18}O	5–4	79.0	1.062×10^{-5}	548.8310055	*Herschel*-HIFI
NO (1)	3_1–2_1	19.3	1.387×10^{-6}	250.8169540	JCMT-RxA
NO (2)	3_1–2_1	19.3	1.553×10^{-6}	250.8155940	JCMT-RxA
NO (3)	3_1–2_1	19.3	1.849×10^{-6}	250.7964360	JCMT-RxA
NO (4)	3_1–2_1	19.3	4.437×10^{-7}	250.7531400	JCMT-RxA

6.2   Observations

The molecular lines observed towards the IRAS 4A protostar ($3^{\mathrm{h}}29^{\mathrm{m}}10\overset{\mathrm{s}}{.}5$, $+31°13'30\overset{''}{.}9$ (J2000); Jørgensen et al. 2009) are presented in Table 6.1 with the corresponding frequencies, upper level energies ($E_{\mathrm{u}}/k_{\mathrm{B}}$), and Einstein A coefficients. The O$_2$ data were obtained with the Heterodyne Instrument for the Far-Infrared (HIFI; de Graauw et al. 2010) onboard the *Herschel* Space Observatory (Pilbratt et al. 2010), in the context of the 'Herschel Oxygen Project' (HOP) open-time key program, which aims to search for O$_2$ in a range of star-forming regions and dense clouds (Goldsmith et al. 2011). Single pointing observations at the source position were carried out on operation day OD 445 on August 1 and 2, 2010 with *Herschel* obsids of 1342202025-...-1342202032. The data were taken in dual-beam switch (DBS) mode in HIFI band 1a with a chop reference position located 3′ from the source position. Eight observations were conducted with an integration time of 3477 seconds each, and eight different local-oscillator (LO) tunings were used in order to allow deconvolution of the signal from the other side band. The LO tunings are shifted by 118 MHz up to 249 MHz. Inspection of the data shows no contamination from the reference position in any of the observations nor from the other side-band. The total integration time is thus 7.7 hours (27816 seconds) for the on+off source integration.

The central frequency of the O$_2$ 3_3–1_2 line is 487.249264 GHz with an upper level energy of E_{u}=26.4 K and an Einstein A coefficient of 8.657×10^{-9} s^{-1} (Drouin et al. 2010). In HIFI, two spectrometers are in operation, the "Wide Band Spectrometer" (WBS) and the "High Resolution Specrometer" (HRS) with resolutions of 0.31 km s^{-1} and 0.073 km s^{-1} at 487 GHz, respectively. Owing to the higher noise ranging from a factor of 1.7 up to 4.7 of the HRS compared with the WBS, only WBS observations were used for the analysis. There is a slight difference between the pointings of the H and V polarizations in HIFI, but this difference of ΔH_{V} (–6$\overset{''}{.}$2, +2$\overset{''}{.}$2; Roelfsema et al. 2012) for Band 1 is small enough to be neglected relative to the beam size of 44″ (FWHM). Spectra from both polarizations were carefully checked for differences in intensities of other detected lines but none were found. Therefore the two polarizations are averaged to improve the S/N.
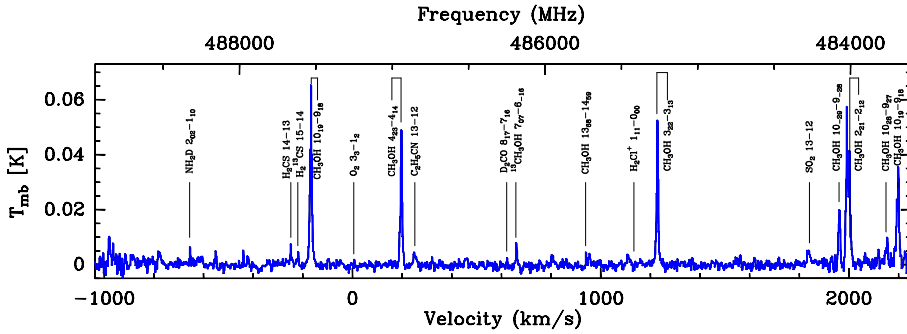
Figure 6.2 – Full spectrum taken with HIFI, with the H- and V-polarization spectra averaged. The frequency range is 488.94 GHz to 483.59 GHz from left to right. The entire bandwidth is 5.35 GHz. The O_2 line is centred near V_{LSR}=7.0 km s^{-1}. A blow-up of the spectrum is presented in Fig. A.1.

Data processing started from the standard HIFI pipeline in the *Herschel* Interactive Processing Environment (HIPE[1]) ver. 8.2.1 (Ott 2010), where the V_{LSR} precision is of the order of a few m s^{-1}. The lines suffer from significant standing waves in each of the observations. Therefore a special task `FitHifiFringe` in HIPE was used to remove standing waves. The fitting routine was applied to each observation one by one and it successfully removed a large part of the standing waves. Further processing and analysis was done using the GILDAS-`CLASS`[2] software. A first order polynomial was applied to all observations, which were subsequently averaged together. The standard antenna temperature scale T_A^* is corrected to main beam temperature T_{MB} by applying the efficiency of 0.76 for HIFI band 1a (Roelfsema et al. 2012, Fig. 6.2).

To understand and constrain the excitation and chemistry of O_2, complementary transitions in NO and $C^{18}O$ are observed. Nitrogen monoxide (NO) was observed with the James Clerk Maxwell Telescope (JCMT[3]) by using Receiver A with a beam size of 20″ as part of the M10BN05 observing program. The total integration time for this observation is 91 minutes. $C^{18}O$ 1–0 is observed with the IRAM 30m telescope[4] over an area of 1′×1′ with a 22″ beam. A $C^{18}O$ 3–2 HARP-B map over 2′×2′ is obtained with the JCMT with a 15″ beam (also in Yıldız et al. 2012). Both maps are convolved to a beam of 44″ in order to directly compare with the O_2 spectra in the same beam. Note that this convolution to a 44″ beam is critical to reveal both the 7.0 and 8.0 km s^{-1} velocity components. The 15″ beam spectra presented in Yıldız et al. (2012) show primarily the 7.0 km s^{-1} component.

---

[1] HIPE is a joint development by the Herschel Science Ground Segment Consortium, consisting of ESA, the NASA Herschel Science Center, and the HIFI, PACS and SPIRE consortia.

[2] http://www.iram.fr/IRAMFR/GILDAS/

[3] The JCMT is operated by the Joint Astronomy Centre on behalf of the Science and Technology Facilities Council of the United Kingdom, the Netherlands Organisation for Scientific Research, and the National Research Council of Canada.

[4] Based on observations carried out with the IRAM 30m Telescope. IRAM is supported by INSU/CNRS (France), MPG (Germany) and IGN (Spain).

Table 6.2 – Summary of the observed line intensities in a 44″ beam.

Molecule	Transition	$\int T_{MB}dV$ [K km s^{-1}]	T_{peak} [K]	FWHM [km s^{-1}]	$\int T_{MB}dV$ [K km s^{-1}]	T_{peak} [K]	FWHM [km s^{-1}]	*rms* [mK]
		7.0 km s^{-1} component[a]			8.0 km s^{-1} component[b]			
O$_2$	3_3–1_2	< 0.0027[c]	…	…	0.0069	0.0046	1.3	1.3[d]
C^{18}O	1-0	1.30	1.38	0.9	2.25	2.35	0.9	26[e]
C^{18}O	3-2	1.32	1.36	0.9	1.67	1.74	0.9	99[e]
C^{18}O	5-4	0.39	0.36	1.0	0.13	0.13	1.0	10[e]
NO (3)	3_1–2_1	0.12[f]	0.10[f]	2.9	…	…	…	46[e]

Notes: [a]V_{LSR}=7.0 km s^{-1} component. [b]V_{LSR}=8.0 km s^{-1} component. [c]3σ upper limit. [d]In 0.35 km s^{-1} bins. [e]In 0.3 km s^{-1} bins. [f]Intensities are scaled to 44″ beam by multiplying by a factor 0.6.

The C^{18}O 5–4 line was obtained with *Herschel*-HIFI within the "Water in Star-forming regions with *Herschel*" (WISH) guaranteed-time key program (van Dishoeck et al. 2011) in a beam size of 40″ and reported in Yıldız et al. (2012). Beam efficiencies are 0.77, 0.63, and 0.76 for the 1–0, 3–2, and 5–4 lines, respectively. The calibration uncertainty for HIFI band 1a is 15%, whereas it is 20% for the IRAM 30m and JCMT lines.

The HIFI beam size at 487 GHz of ~44″ corresponds to a 5170 AU radius for IRAS 4A at 235 pc (Fig. 6.1, white circle). It therefore overlaps slightly with the dense envelope around IRAS4B (see also Fig. 4.13; Yıldız et al. 2012) but this is neglected in the analysis. The NO data were taken as a single pointing observation, therefore the beam size is ~20″, about half of the diameter covered with the O$_2$ observation. In Fig. 6.13, the C^{18}O 3–2 map is convolved to different beam sizes and corresponding intensities are measured. It is seen that the intensity decreases by a factor of 0.6 with the increasing beam size (20″ to 40″), illustrating that the IRAS 4A envelope is not a point source. Assuming that the same distribution holds for the NO emission, this same factor of 0.6 is used to scale the NO intensity to a 44″ beam.

6.3   Results

In Fig. 6.2, the full *Herschel*-HIFI WBS spectrum is presented. Although the bandwidth of the WBS data is 4 GHz, the entire spectrum covers 5.35 GHz as a result of combining eight different observations where the LO frequencies were slightly shifted in each of the settings. The *rms* of this spectrum is 1.3 mK in 0.35 km s^{-1} bin, therefore many faint lines are detected near the main targeted O$_2$ 3_3–1_2 line. These lines include some methanol (CH$_3$OH) lines, together with e.g., SO$_2$, NH$_2$D, and D$_2$CO lines. These lines are shown in Fig. 6.12 (in the Additional materials) in detail, and are tabulated with the observed information in Table 6.6 (in the Additional materials).
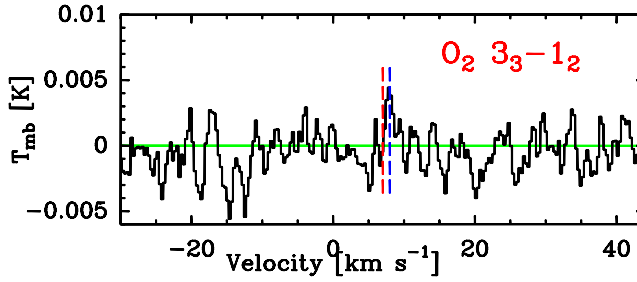
Figure 6.3 – Spectrum of Fig. 6.2 magnified around the O_2 3_3–1_2 line. The red dashed line indicates the LSR velocity of the IRAS 4A envelope at 7.0 km s^{-1}and the blue dashed line shows the velocity at 8.0 km s^{-1}.
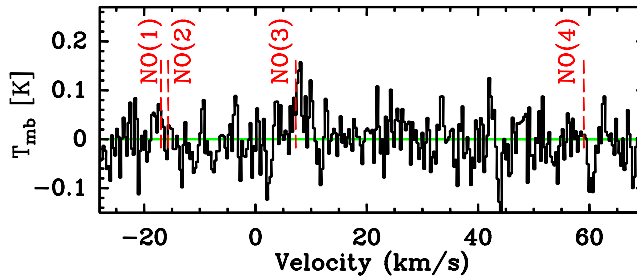
Figure 6.4 – Spectrum of the NO 3_1–2_1 transition showing the location of four hyperfine (HF) components.The spectrum is centred on the NO(3) (HF) component.

6.3.1 O_2

A blow-up of the HIFI spectrum centred around the O_2 487 GHz position is presented in Fig. 6.3. The source velocity of IRAS 4A is V_{LSR}=7.0 km s^{-1} as determined from many $C^{18}O$ lines (Yıldız et al. 2012), and is indicated by the red dashed line in the figure. This spectrum of 7.7 hours integration time staring at the IRAS 4A source position is still not sufficient for a firm detection of the O_2 line at 487 GHz at the source velocity. However, a tentative detection at V_{LSR}=8.0 km s^{-1} is seen and will be discussed in more detail in Sect. 6.5.

6.3.2 NO

In Fig. 6.4, the JCMT spectrum covering the hyperfine components of the NO 3_1–2_1 transition is presented. For this specific transition, the expected ratios of the line intensities in the optically thin limit are NO (1) : NO (2) : NO (3) : NO (4) = 75:126:200:24. The JCMT observations have an *rms* of 40 mK in 0.3 km s^{-1} bin and 3σ emission is detected only at the intrinsically strongest hyperfine transition, NO (3), with an integrated intensity
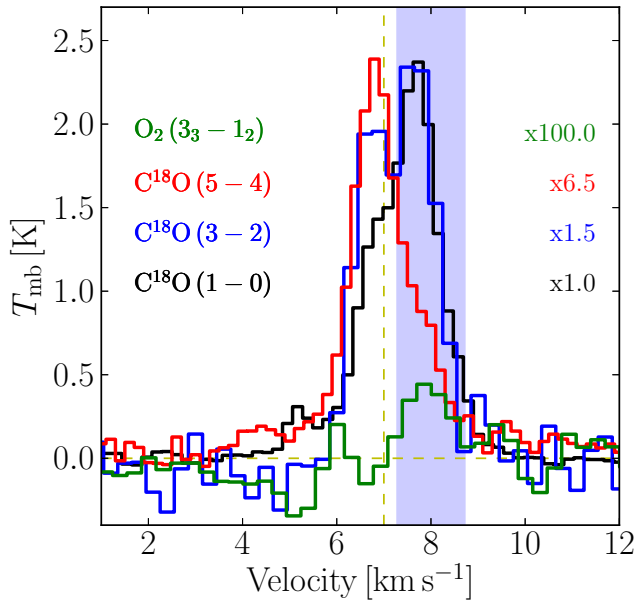
Figure 6.5 – O_2 3_3–1_2 spectrum overplotted with the $C^{18}O$ 1–0, 3–2, and 5–4 lines in a 44" beam. The $C^{18}O$ spectra are scaled to the same peak intensity. Note the shift in velocity from 8.0 to 7.0 km s^{-1} with increasing J.

of 0.2 K km s^{-1} centred at V_{LSR}=7.0 km s^{-1}. As discussed in § 6.2, this intensity is scaled by a factor of 0.6 to obtain the value in a 44" beam. Because the data are taken in a 20" beam, they are less sensitive to the extended 8.0 km s^{-1} component.

6.3.3 C^{18}O

Figure 6.5 shows the C^{18}O 1–0, 3–2, and 5–4 lines overplotted on the O_2 line. The peak of the C^{18}O emission shifts from V_{LSR}=8.0 km s^{-1} to 7.0 km s^{-1} as J increases. The C^{18}O 1–0 line is expected to come primarily from the surrounding cloud at 8.0 km s^{-1} due to the low energy of the transition (E_{up}= 5.3 K). On the other hand, the 5–4 line has higher energy (E_{up}= 79 K), therefore traces the warmer parts of the protostellar envelope at 7.0 km s^{-1}. As a sanity check, the ^{13}CO 1–0, 3–2, and 6–5 transitions from Yıldız et al. (2012) were also inspected and their profiles are consistent with those of the C^{18}O lines, however they are not included here due to their high opacities. The integrated intensities $\int T_{mb}dV$ for each of the 7.0 km s^{-1} and 8.0 km s^{-1} components are given in Table 6.2.
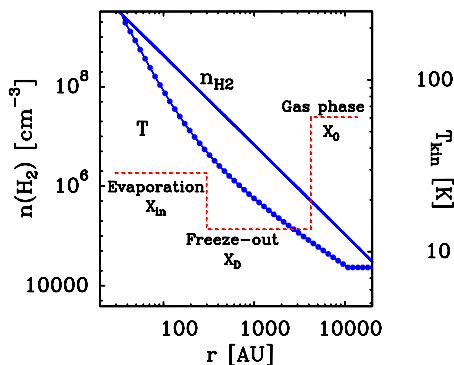
Figure 6.6 – Variation of number density and temperature of the NGC 1333 IRAS 4A envelope as function of radial distance, taken from the model of Kristensen et al. (2012). Overplotted red dashed line shows the limits of drop abundance profile obtained by the C^{18}O modeling.

6.3.4 Column densities and abundances

6.3.4.1 Constant excitation temperature results

A first simple estimate of the O$_2$ abundance limit in the IRAS 4A protostellar envelope (V_{LSR}=7.0 km s^{-1} component) is obtained by computing column densities within the 44″ beam. The collisional rate coefficients for the O$_2$ 3$_3$–1$_2$ line give a critical density of n_{cr}=1×10^3 cm^{-3} for low temperatures (Lique 2010, Goldsmith et al. 2011). The density at the 5000 AU radius corresponding to this beam is found to be 4×10^5 cm^{-3} based on the modeling results of Kristensen et al. (2012, see also Fig. 6.6 and below). This value is well above the critical density, implying that the O$_2$ excitation is thermalized. The width of the O$_2$ 3$_3$–1$_2$ line is taken to be similar to that of C^{18}O, ΔV≈1.0 km s^{-1}. The O$_2$ line is assumed to be optically thin and a temperature of 30 K is used. The 3σ O$_2$ column density limit at V_{LSR}=7.0 km s^{-1} is then N(O$_2$)=1.2×10^{15} cm^{-2}.

The total H$_2$ column density of the 7.0 km s^{-1} component in the 44″ beam is computed from the model of Kristensen et al. (2012) through

$$N_{X,\text{beam}} = \frac{\int \int n_X(z,b)\text{d}zG(b)2\pi b\text{d}b}{\int G(b)2\pi b\text{d}b}, \tag{6.3}$$

where b is the impact parameter, and $G(b)$ is the beam response function. The resulting value is N(H$_2$)=2.1×10^{23} cm^{-2}, which is an order of magnitude lower than the pencil-beam H$_2$ column density of 1.9×10^{24} cm^{-2}. Using the 44″-averaged H$_2$ column density implies an abundance limit X(O$_2$)$\leq$ 5.7×10^{-9}. This observation therefore provides the deepest limit on the O$_2$ abundance observed to date. It is ~4 orders of magnitude lower than the chemical model predictions of X(O$_2$) ~7×10^{-5}.

Another option is to compare the O$_2$ column density directly with that of C^{18}O. These lines trace the part of the envelope where CO and, by inference, O$_2$ are not frozen out because of their similar binding energies (Collings et al. 2004, Acharyya et al. 2007). Using the C^{18}O lines therefore provides an alternative constraint on the models. The integrated

Table 6.3 – Summary of column densities in a 44″ beam. See text for the conditions used for the calculations.

Molecule	Column Density [cm⁻²]		Abundance w.r.t. H_2	
	$N(7 \text{ km s}^{-1})^a$	$N(8 \text{ km s}^{-1})^b$	$X(7 \text{ km s}^{-1})^c$	$X(8 \text{ km s}^{-1})^d$
O_2	$<1.2\times10^{15\,e}$	$(2.8-4.3)\times10^{15}$	$<5.7\times10^{-9}$	$(1.3-2.1)\times10^{-8}$
$C^{18}O$	$(3.5-6.3)\times10^{14}$	$(1.8-2.3)\times10^{15}$	$(3.5-6.2)\times10^{-7}$	...
NO	4.0×10^{14}	...	1.9×10^{-9}	...
$H_2{}^f$	2.1×10^{23}	$1\times10^{22\,f}$	...	...

Notes: ^{a}Column density of the bin at 7.0 km s⁻¹, a.k.a. non-detection. ^{b}Column density of the bin at 8.0 km s⁻¹, a.k.a. tentative detection. $^c V$=7.0 km s⁻¹ component. $^d V$=8.0 km s⁻¹ component. $^e 3\sigma$ column density. ^{f}Beam averaged H_2 column density in a 44″ beam. Computed using $CO/H_2 = 10^{-4}$ and $CO/C^{18}O = 550$ (Wilson & Rood 1994).

intensity ratio of $C^{18}O$ 5–4/3–2 is equal to 0.29 for the 7.0 km s⁻¹ component. This ratio can then be analysed using the RADEX non-LTE excitation and radiative transfer program (van der Tak et al. 2007) to constrain the physical parameters. Figure 6.14 (in the Additional Materials) presents the integrated intensity ratios as function of temperature and density, obtained for optically thin conditions. The observed ratios are indicated in dash-dotted lines. Using a minimum density of ~4×10^5 cm⁻³ for the envelope within the 44″ beam (shown by the purple vertical line) implies a kinetic temperature of ~20–30 K from the 5–4/3–2 ratio, consistent with the CO sublimation temperature (gas and dust temperature are coupled at these high densities).

For these physical conditions, the absolute $C^{18}O$ 3–2 and 5–4 line intensities imply a $C^{18}O$ column density range of $(3.5-6.3)\times10^{14}$ cm⁻². The corresponding abundance ratio is $N(O_2)/N(C^{18}O)$=2.6±0.7, so $N(O_2)/N(CO)$=$(4.9\pm1.5)\times10^{-3}$ assuming $CO/C^{18}O$=550. The column densities and O_2 abundances which are associated with the protostellar source at V_{LSR} = 7.0 km s⁻¹ are summarized in Table 6.3.

The critical density for the NO transition is higher than that for O_2 or CO, so analysis requires a non-LTE excitation calculation using RADEX. For the detected NO (3) line diluted by a factor of 0.6, the inferred column density within 44″ is $N(NO)$=4×10^{14} cm⁻², assuming T_{kin}=30 K and $n(H_2)$=4×10^5 cm⁻³. For these conditions, the NO lines are optically thin. Thus, the implied NO abundance is $N(NO)/N(H_2)$=$X(NO)$=1.9×10^{-9} and $N(NO)/N(O_2)\geq0.33$. The inferred column density is nearly identical if the analysis is carried out for a 20″ beam, since the higher density at the edge of a 20″ beam (n=1.5×10^6 cm⁻³) compensates for the lack of beam dilution.

6.3.4.2 Drop abundance models

The above analysis assumes constant physical conditions along the line of sight as well as constant abundances. It is well known from multi-line observations of $C^{18}O$ that the
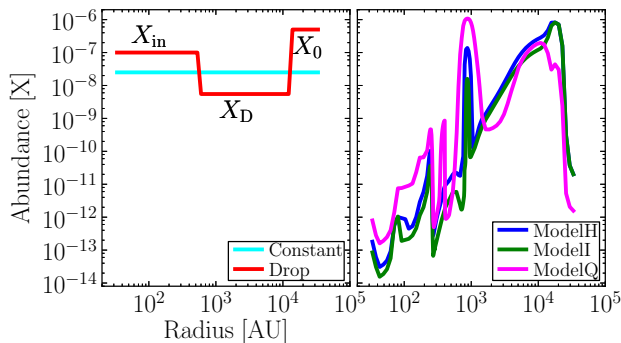
Figure 6.7 – *Left:* schematic diagram showing the best-fit drop abundance profile of O_2 following the $C^{18}O$ profile (red line) and constant abundance profile (light blue); and *right:* best-fit profiles obtained via dust-grain modeling (other colored lines).

CO abundance varies throughout the envelope, dropping by more than an order of magnitude in the cold freeze-out zone (e.g., Jørgensen et al. 2002, Yıldız et al. 2010, 2012). A more sophisticated analysis of the O_2 abundance is therefore obtained by using a model of the IRAS 4A envelope in which the density and temperature vary with position. The envelope structure presented in Fig. 6.6 has been quantified by modeling the continuum emission (both the spectral energy distribution and the submillimeter spatial extent) using the 1D spherically symmetric dust radiative transfer code DUSTY (Ivezić & Elitzur 1997). A power-law density profile is assumed with an index p, i.e., $n \propto r^{-p}$, and the fitting method is described in Schöier et al. (2002) and Jørgensen et al. (2002, 2005b), and is further discussed in Kristensen et al. (2012). The temperature is calculated as function of position by solving for the dust radiative transfer through the assumed spherical envelopes, given the luminosity of the source. The gas temperature is assumed to be equal to the dust temperature. IRAS 4A is taken to be a standalone source; the possible overlap with IRAS 4B is ignored.

The observed line intensities are used to constrain the molecular abundances in the envelope by assuming a trial abundance structure and computing the non-LTE excitation and line intensities with radiative transfer models for the given envelope structure. For this purpose, the Monte Carlo line radiative transfer program RATRAN (Hogerheijde & van der Tak 2000) is employed. The simplest approach assumes a constant O_2 abundance through the envelope. Figure 6.7 (*left*) shows different abundance profiles whereas Fig. 6.8 (*top left*) shows the resulting line intensities overplotted on the observed O_2 line. The light blue line is the maximum constant O_2 abundance that can be hidden in the noise, which is 2.5×10^{-8}. This is within a factor of 4 of the simple column density ratio estimate.

A more realistic abundance structure includes a freeze-out zone below 25 K where both O_2 and CO are removed from the gas. Such a CO 'drop' abundance profile has been determined for the IRAS 4A envelope via the optically thin $C^{18}O$ lines from 1–0 to 10–

9 in Yıldız et al. (2012). By using the best fit CO abundance structure and assuming a constant O$_2$/CO abundance ratio, a best fitting value of O$_2$/C^{18}O$\leq$1 is obtained (red line), corresponding to O$_2$/CO$< 2 \times 10^{-3}$.

In summary, both the simple column density estimate and the more sophisticated envelope models imply a maximum O$_2$ abundance of $\sim 10^{-8}$, an O$_2$/CO ratio of $\leq 5 \times 10^{-3}$.

6.4   Gas-grain models for the protostellar envelope

The next step in the analysis is to compare the upper limit for the V_{LSR}=7.0 km s^{-1} component with full gas-grain chemical models. The Ohio State University gas-grain network (Garrod et al. 2008) is used as the basis for the chemical network, which contains an extensive gas-grain chemistry. There are 590 gas phase and 247 grain surface species and 7500 reactions among them. In the subsequent sub-sections, various chemical processes that were considered in the network and are relevant for O$_2$ and NO are discussed.

6.4.1   Gas phase O$_2$ and NO formation

In the gas, O$_2$ is predominantly formed via reaction (6.1) between O atoms and OH radicals. The rate coefficient of the above reaction has been measured in the temperature range between 39 K and 142 K with the CRESU (Cinetique de Reaction en Ecoulement Supersonique Uniforme) technique by Carty et al. (2006) who found a rate coefficient of 3.5×10^{-11} cm^3 s^{-1} that is constant with temperature. However, several theoretical calculations, especially below 39 K, also exist in the literature. Using quantum mechanical calculations with the so-called *J*-shifting approximation and neglecting non-adiabatic coupling, Xu et al. (2007) obtained a rate coefficient that decreases as the temperature drops from 100 to 10 K. At 10 K, the computed rate coefficient has fallen to a value of 5.4×10^{-13} cm^3 s^{-1}, significantly lower than the 39 K experimental value. However, more recent calculations by Lin et al. (2008), in which the *J*-shifting approximation has been removed, find a rate coefficient at 10 K of 7.8×10^{-12} cm^3 s^{-1}, higher than the Xu et al. (2007) value but still only about 1/4.5 of the experimental value at 39 K. Various O$_2$ formation rates are listed in Table 6.4. We have used all three rate coefficients in order to match the observed O$_2$ abundance.

Gas-phase NO is predominantly formed through reaction (6.2). Its gas-phase reaction rate coefficient is listed in Table 6.4. This reaction is taken from the OSU database and was first determined by Smith et al. (2004).

Table 6.4 – Rate coefficients for O_2 (Equation 6.1) and NO (Equation 6.2) formation.

No.	Species	T [K]	Rate coeff. [cm^3 s^{-1}]	References
1.[a]	O_2	39–149	3.5×10^{-11}	Carty et al. (2006)
2.[b]	O_2	10	7.8×10^{-12}	Lin et al. (2008)
3.[c]	O_2	10	5.4×10^{-13}	Xu et al. (2007)
4.	O_2	…	$7.5 \times 10^{-11}(T/300)^{-0.25}$	OSU database
5.	NO	…	$7.5 \times 10^{-11}(T/300)^{-0.18}$	OSU database

Notes: [a]CRESU measurement [b]without *J*-shifting [c]with *J*-shifting

## 6.4.2 Grain chemistry specific to O_2 and NO

The grain surface chemistry formulation in the OSU code follows the general description by Hasegawa & Herbst (1993) for adsorption, diffusion, reaction, dissociation and desorption processes, updated and extended by Garrod et al. (2008). The binding energies of various species to the surface are critical parameters in the model. In most of the models, we adopt the binding energies from Garrod & Herbst (2006) appropriate for a water-rich ice surface. However, the possibility of a CO-rich ice surface is also investigated by reducing the binding energies by factors of 0.75 and 0.5, respectively (Bergin et al. 1995, Bergin & Langer 1997).

The presence of O_2 on an interstellar grain can be attributed to two different processes. First, gas phase O_2 can be accreted on the grain surface during the (pre-)collapse phase and second, atomic oxygen can recombine to form O_2 on the dust grain via the following reaction:

$$O + O \rightarrow O_2. \tag{6.4}$$

Following Tielens and Hagen (1982), 800 K is used as the binding (desorption) energy for atomic oxygen on water ice. For O_2, its binding energy on water ice is taken as 1000 K following Cuppen & Herbst (2007), which is an average value obtained from the TPD data by Ayotte et al. (2001) and Collings et al. (2004). A ratio of 0.5 between the diffusion barrier and desorption energy has been assumed for the entire calculation (Cuppen & Herbst 2007), so the hopping energy for atomic oxygen is 400 K.

For this hopping energy, one oxygen atom requires 2×10^5 seconds to hop to another site at 10 K. For comparison, the time needed for a hydrogen atom to hop to another site is around 0.35 second, which is at least a factor of 10^6 faster. Therefore, instead of forming O_2, an accreted atomic oxygen species will get hydrogenated, leading to the formation of OH and H_2O. Therefore it is most unlikely that accreted atomic oxygen will produce any significant amount of O_2 on the grain surface during the pre-collapse phase. Recent studies using the continuous time random walk (CTRW) Monte Carlo method do not produce significant O_2 on the grain surface (Cuppen & Herbst 2007). However, elevated grain temperatures ($\gtrsim$30 K), when the residence time of an H atom on the grain is very short and atomic oxygen has enhanced mobility, could be conducive to O_2 formation.
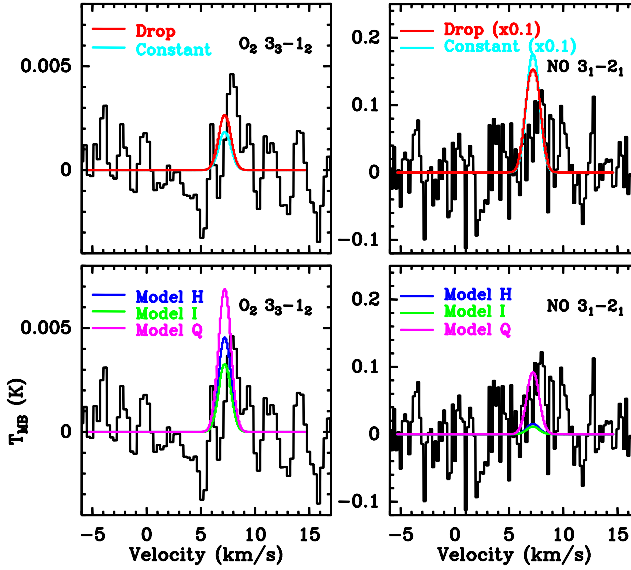
Figure 6.8 – Best-fit model spectra produced by different abundance profiles for O$_2$ 3_3–1_2 and NO (3) 3_1–2_1 are overplotted over the observed spectra. For NO, Case 2 is adopted.

What happens to the O$_2$ that is formed in the gas phase and accreted onto the dust grains? There are two major destruction pathways. First, the reaction of O$_2$ with atomic H leads to the formation of HO$_2$ and H$_2$O$_2$, which then could be converted to water following reaction pathways suggested by Ioppolo et al. (2008) and Cuppen et al. (2010):

$$O_2 \xrightarrow{H} HO_2 \xrightarrow{H} H_2O_2 \xrightarrow{H} H_2O + OH. \tag{6.5}$$
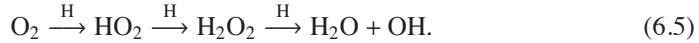
Thus, a longer cold pre-collapse phase would significantly reduce O$_2$ on the dust grains and turn it into water ice, whereas a shorter pre-collapse phase would yield a higher solid O$_2$ abundance (Roberts & Herbst 2002).

The second destruction route leads to the formation of ozone through

$$O_2 + O \rightarrow O_3. \tag{6.6}$$

This route is most effective at slightly higher grain temperatures when atomic oxygen has sufficient mobility to find an O$_2$ molecule before it gets hydrogenated. Ozone could also be hydrogenated as suggested by Tielens & Hagen (1982) and confirmed in the laboratory by Mokrane et al. (2009) and Romanzin et al. (2010):

$$O_3 \xrightarrow{H} O_2 + OH. \tag{6.7}$$
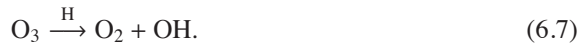
Similarly, accreted NO on the grain surface can undergo various reactions. In particular, recent laboratory experiments have shown that NO is rapidly hydrogenated to NH$_2$OH at

164

low ice temperatures (Congiu et al. 2012). A critical parameter here is the competition of the different channels for reaction of HNO + H, which can either go back to NO + H_2 or form H_2NO.

The final important ingredient of the gas-grain chemistry is the rate at which molecules are returned from the ice back into the gas phase. Both thermal and non-thermal desorption processes are considered. The first non-thermal process is reactive desorption; here the exothermicity of the reaction is channeled into the desorption of the product with an efficiency determined by a parameter a_{RRK} (Garrod et al. 2007). In these model runs, a value of 0.01 is used, which roughly translates into an efficiency of 1%. Recently, Du et al. (2012) used 7% for the formation of H_2O_2.

Second, there is desorption initiated by UV absorption. Photodissociation of an ice molecule produces two atomic or radical products, which can subsequently recombine and desorb via the reactive desorption mechanism. The photons for this process derive both from the external radiation field and from UV photons generated by ionization of H_2 due to cosmic rays, followed by the excitation of H_2 by secondary electrons. The externally generated UV photons are very effective in diffuse and translucent clouds but their role in dense clouds is limited to the edge of the core (Ruffle & Herbst 2000, Hollenbach et al. 2009). The cosmic-ray-generated internal photons can play an effective role in the dense envelope, with a photon flux of $\approx 10^4$ photons cm^{-2} s^{-1} (Shen et al. 2004). We have considered both sources of radiation in our model. In either case, the rate coefficients for photodissociation on surfaces are assumed to be the same as in the gas phase.

Photodesorption can proceed both by the recombination mechanism described above as well as by kick-out of a neighboring molecule. The combined yields for a variety of species including CO and H_2O have been measured in the laboratory (Öberg et al. 2009a,b, Muñoz Caro et al. 2010) and computed through molecular dynamics simulations for the case of H_2O by Andersson & van Dishoeck (2008) and Arasa et al. (2010). Finally, there is the heating of grains via direct cosmic ray bombardment, which is effective for weakly bound species like CO and O_2 and included following the formulae and parameters of Hasegawa & Herbst (1993).

6.4.3 Model results

Our physical models have two stages, the "pre-collapse stage" and the "protostellar stage". In the pre-collapse stage, the hydrogen density is $n_H=10^5$ cm^{-3}, visual extinction $A_V=10$ mag, the cosmic-ray ionization parameter, $\zeta= 1.3\times10^{17}$ s^{-1}, and the (gas and grain) temperature, $T=10$ K, which are standard parameters representative of cold cores. The initial elemental abundances of carbon, oxygen and nitrogen are 7.30×10^{-5}, 1.76×10^{-4} and 2.14×10^{-5}, respectively, in the form of atomic C$^+$, O and N. All hydrogen is assumed to be in molecular form initially. In the second stage, the output abundance of the first phase is used as the initial abundance at each radial distance with the density, temperature

Table 6.5 – Chemical models considered for the IRAS 4A protostellar envelope

Model	Pre-collapse stage [yr]	Protostellar stage [yr]	O_2 formation rate [cm^3 s^{-1}]	$T_{peak}(O_2)^a$ [K]	$T_{peak}(NO)^a$ [K]
A	5×10^4	10^5	7.5×10^{-11} .$(T/300)^{-0.25}$	0.119	...
B	1×10^5	10^5	7.5×10^{-11} .$(T/300)^{-0.25}$	0.102	...
C	2×10^5	10^5	7.5×10^{-11} .$(T/300)^{-0.25}$	0.085	...
D	3×10^5	10^5	7.5×10^{-11} .$(T/300)^{-0.25}$	0.073	...
E	5×10^5	10^5	7.5×10^{-11} .$(T/300)^{-0.25}$	0.042	...
F	6×10^5	10^5	7.5×10^{-11} .$(T/300)^{-0.25}$	0.024	...
G	7×10^5	10^5	7.5×10^{-11} .$(T/300)^{-0.25}$	0.011	...
H^b	8×10^5	10^5	7.5×10^{-11} .$(T/300)^{-0.25}$	0.0045	0.015
I^b	1×10^6	10^5	7.5×10^{-11} .$(T/300)^{-0.25}$	0.0032	0.011
J	8×10^4	2×10^4	3.50×10^{-11}	0.106	...
L	3×10^5	10^5	3.50×10^{-11}	0.063	...
M	3×10^5	10^5	7.84×10^{-12}	0.047	...
N	3×10^5	10^5	5.40×10^{-13}	0.018	...
O	5×10^5	10^5	3.50×10^{-11}	0.031	...
P	5×10^5	10^5	7.84×10^{-12}	0.020	...
Q^b	5×10^5	10^5	5.40×10^{-13}	0.0068	0.091

Notes: [a]RATRAN model results using a line width of 1.0 km s^{-1}. [b]Best fit models. For NO, Case 2 is tabulated.

and visual extinction parameters at each radius taken from the IRAS 4A model shown in Fig. 6.6. We assume that the transition to the protostellar phase from the pre-collapse stage is instantaneous i.e., the power-law density and temperature structure are established quickly, consistent with evolutionary models (Lee et al. 2004, Young & Evans 2005).

To explain the observed abundance profile of O_2, both the pre-collapse time and protostellar time as well as the O_2 formation rates are varied. Analysis of CO and HCO$^+$ multi-line observations in pre- and protostellar sources have shown that the high density pre-collapse stage lasts typically a few $\times10^5$ yr (e.g., Jørgensen et al. 2005b, Ward-Thompson et al. 2007). The models A to Q have different parameters and timescales which are listed in Table 6.5. Those models result in abundance profiles in the envelope at each time step and radius. These profiles are then run in RATRAN in order to compare directly with observations.

Figure 6.7 (*right*) shows examples of model abundance profiles whereas Fig. 6.8 (*bottom left*) presents the comparison between model line emission and data. Table 6.5 summarizes the resulting O_2 peak temperatures for each of the models. All models except H, I, and Q overproduce the observed O_2 emission of at most a few mK, by up to two orders of magnitude in peak temperature. The models that are consistent with the data have in common longer pre-collapse stages; in particular Model I, which has the longest pre-collapse stage of 10^6 years, best fits the 3σ O_2 limit.

For NO, the H, I, and Q models were calculated twice. In Case 1, hydrogenation of HNO leads back to NO and H_2 and in Case 2 hydrogenation of HNO leads to H_2NO as sug-
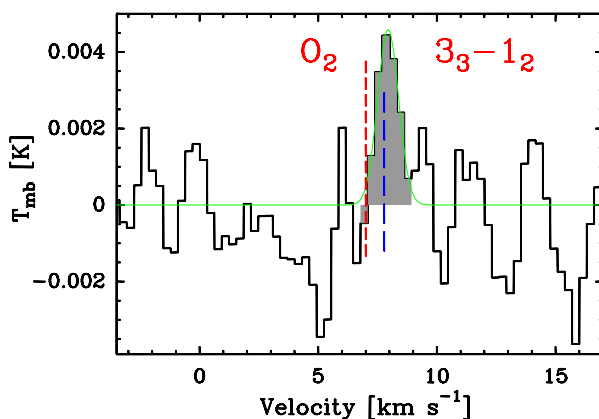
Figure 6.9 – Tentative detection of the O_2 3_3–1_2 line from the extended NGC 1333 cloud. The red line indicates the source velocity of IRAS 4A at 7.0 km s^{-1} and the blue line indicates the extended cloud V_{LSR} at 8.0 km s^{-1}. Green line indicates a Gaussian fit to the component at 8.0 km s^{-1}.

gested by Congiu et al. (2012). Comparison of the results from Case 1 with observations shows significant overproduction of the observed NO emission of 0.1 K, whereas Case 2 underproduces NO. Therefore, a combination of both reactions appears to be needed.

These results for IRAS 4A suggest that a long pre-collapse stage is characteristic of the earliest stages of star formation, in which atomic and molecular oxygen are frozen-out onto the dust grains and converted into water ice, as proposed by Bergin et al. (2000). Similarly, the rapid conversion of NO to other species on the grains limits its gas-phase abundance. It is clear that the grain surface processes are much more important than those of the pure gas-phase chemistry in explaining the O_2 and NO observations.

The model results show that the fraction of O_2 or NO left on the grains must indeed be very small, dropping to $\leq 10^{-9}$ close to the protostar (Fig. 6.8, *right*). This in turn implies that the gas and ice that enter the disk are very poor in O_2. Although IRAS 4A is the only low-mass protostar that has been observed to this depth, the conclusions drawn for IRAS 4A probably hold more generally. Thus, unless there is significant production of O_2 in the disk, the icy planetesimals will also be poor in O_2.

6.5 Tentative detection of O_2 in the 8 km s^{-1} cloud

Although there is no sign of O_2 emission at the velocity of the dense protostellar envelope (7.0 km s^{-1}), a 4.5σ tentative detection of O_2 3_3–1_2 line emission is found at V_{LSR}=8.0 km s^{-1}, the velocity of the more extended NGC 1333 molecular cloud (Fig. 6.9 Loren 1976, Liseau et al. 1988). The peak intensity of the tentative detection is T_{mb}=4.6 mK, the line width ΔV=1.3 km s^{-1}, and the integrated intensity is $\int T_{mb} dV$=6.9 mK km s^{-1}
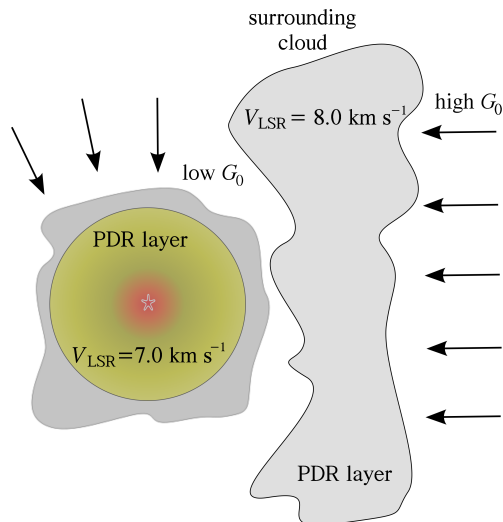
Figure 6.10 – Schematic cartoon showing the scenario of O$_2$ emission originating from the surrounding cloud.

between the velocities of 6.5 to 9.7 km s^{-1}. The large HIFI beam size of 44$''$ encompasses both the extended cloud as well as the compact envelope. Since any O$_2$ emission is optically thin, the two components cannot block each other, even if slightly overlapping in velocity. Figure 6.10 shows a possible schematic geometry for the protostar and the surrounding cloud.

The density in the surrounding cloud at 8.0 km s^{-1} is expected to be significantly lower than that in the envelope. Figure 6.14 (in the Additional Materials) includes the C^{18}O 3–2/1–0 ratio for the 8.0 km s^{-1} component. The observed value is consistent with a wide range of kinetic temperatures from 20 K to 70 K, with corresponding densities in a narrow range from 7×10^3 to 2×10^3 cm^{-3}, respectively. C^{18}O column densities from the 3–2 and 1–0 line intensities are then $(1.8–2.3)\times10^{15}$ cm^{-2} for this range of physical parameters.

For the same range of conditions, the O$_2$ column density is $(2.8 - 4.3)\times10^{15}$ cm^{-2} assuming ^{16}O/^{18}O=550. The inferred abundance ratios are $N(\text{O}_2)/N(\text{C}^{18}\text{O})$=1.2 to 2.1, and $N(\text{O}_2)/N(\text{CO})$=$(2.2–3.9)\times10^{-3}$. Assuming CO/H$_2\approx10^{-4}$ gives $N(\text{O}_2)/N(\text{H}_2)$=$(2.2–3.9)\times10^{-7}$. Interestingly, the inferred O$_2$ abundance is in between the values found for the Orion and ρ Oph A clouds (Goldsmith et al. 2011, Liseau et al. 2012).

Can such an O$_2$ column density and abundance be reproduced by chemical models? For the surrounding cloud, a large gas-grain model is not needed. Instead, the PDR models of Hollenbach et al. (2009), which include a simplified gas-grain chemistry, are adequate to analyse the emission. Figure 6.11 is a plot adapted from Melnick et al. (2012), which shows the values of G_0 required to reproduce the range of O$_2$ column densities according to the model described in Hollenbach et al. (2009). The horizontal grey band bounds the
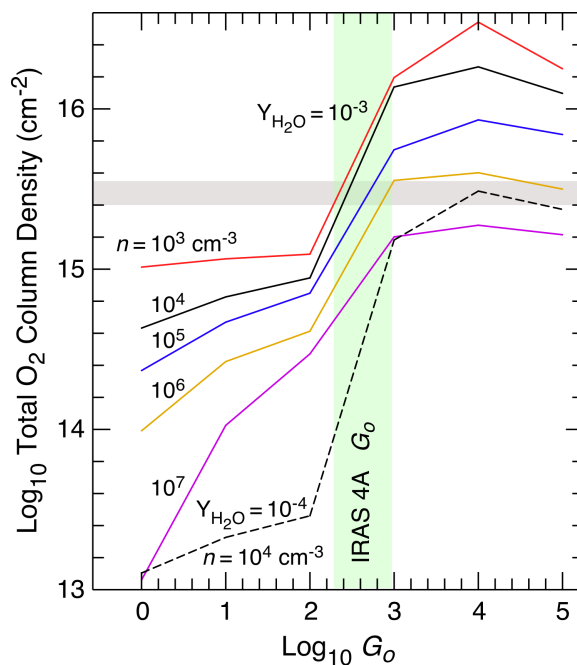
Figure 6.11 – Total O_2 column density as a function of G_o and density (adapted from Melnick et al. 2012, Hollenbach et al. 2009). The horizontal grey band shows the total O_2 column density range for the observed integrated intensity, whereas the vertical green band presents the range of G_0 values required to produce this range of O_2 column densities for gas densities between 10^3 cm^{-3} and 10^7 cm^{-3}. Y_{H_2O} is the water ice photodesorption yield.

total observed O_2 column density range of $(2.8 - 4.3) \times 10^{15}$ cm^{-2}, while the vertical green band shows the range of G_0 values required to produce this range of O_2 column densities for gas densities between 10^3 cm^{-3} and 10^7 cm^{-3}. For our low inferred densities of $< 10^4$ cm^{-3}, a high G_0 value of 300–650 fits the data. A likely scenario for the extended 8.0 km s^{-1} component would be that the UV radiation is enhanced by the nearby B9 V type main sequence star BD+30°549 (~0.5 pc away). Models with a water ice photodesorption yield $Y_{H_2O}=10^{-3}$ fit the observations well, consistent with laboratory (Öberg et al. 2009a) and theoretical work (Arasa et al. 2010).

6.6 Conclusions

We have presented the first deep 7.7 hr *Herschel*-HIFI observations of the O_2 3_3–1_2 line at 487 GHz towards a deeply embedded Class 0 protostar, NGC 1333 IRAS 4A. The results from the observations and models can be summarized as follows.

- No O$_2$ emission is detected from the protostellar envelope, down to a 3σ upper limit of $X(O_2) \lesssim 6{\times}10^{-9}$, the lowest O$_2$ abundance limit toward a protostar to date. The O$_2$/CO limit is $\leq 5 \times 10^{-3}$.

- A weak line of the chemically related NO molecule is detected at the protostellar velocity of 7.0 km s^{-1}.

- A full gas-grain chemical model coupled with the physical structure of the envelope is compared to our data consisting of two stages, a "pre-collapse stage" and "protostellar stage". Best fits to the observed upper limit of the O$_2$ line suggest a long pre-collapse stage (10^6 years), during which atomic oxygen is frozen out onto the dust grains and converted into water ice. Also, at least a fraction of NO must be converted to more complex nitrogen species in the ice.

- The low O$_2$ abundance in the gas and on the grains implies that the material entering the disk is very poor in O$_2$.

- A 4.5σ tentative O$_2$ detection is found at $V_{\mathrm{LSR}} = 8.0$ km s^{-1}, which is interpreted as emission originating from the surrounding more extended NGC 1333 cloud.

- Comparison with PDR models of Hollenbach et al. (2009) suggests a high G_0 of 300–650 in the surrounding cloud for the low inferred density of $<10^4$ cm^{-3}.

6.7 Additional materials
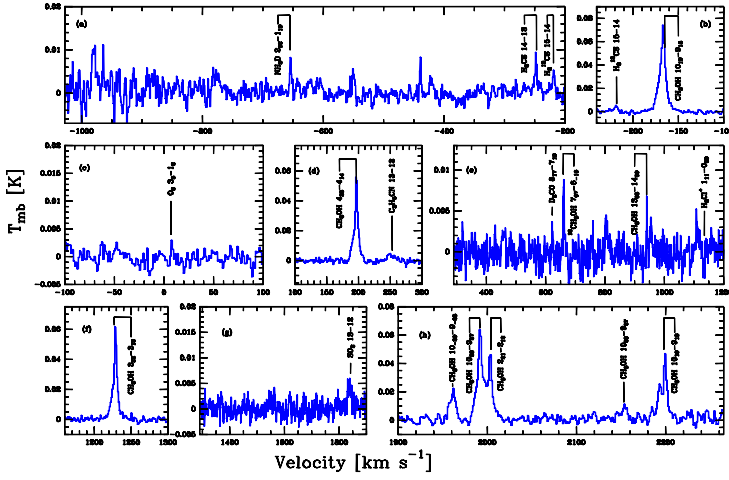
Figure 6.12 – Spectrum of Fig. 6.2 magnified over certain velocity ranges. In panel (*c*) the O_2 3_3-1_2 transition is shown. Identifications refer to the 7.0 km s^{-1} component.

Table 6.6 – Overview of the other lines observed in the same spectrum.

Mol.	Trans. J_u-J_l	E_u/k_B [K]	A_{ul} [s^{-1}]	Frequency [GHz]	$\int T_{MB}\,dV$ [K km s^{-1}]	T_{peak} [K]	FWHM [km s^{-1}]
NH$_2$D	$2_{02}-1_{10}$	47.2	1.36×10^{-4}	488.323810	0.025	0.01	3.4
H$_2$CS	14–13	188.8	1.76×10^{-3}	487.663321	0.028	0.009	3.3
H$_2^{13}$CS	15–14	200.5	1.77×10^{-3}	487.615288	0.022	0.005	3.9
CH$_3$OH	$10_{19}-9_{18}$	143.3	5.15×10^{-4}	487.531887	0.58	0.08	8.2
O$_2$	3_3-1_2	26.38	8.66×10^{-9}	487.249264	0.007	...	...
CH$_3$OH	$4_{23}-4_{14}$	60.9	5.45×10^{-4}	486.940837	0.39	0.06	7.2
C$_2$H$_5$CN	13–12	66.9	1.00×10^{-6}	486.849912	0.036	0.005	7.3
D$_2$CO	$8_{17}-7_{16}$	111.0	3.36×10^{-3}	486.248662	0.009	0.007	1.1
^{13}CH$_3$OH	$7_{07}-6_{16}$	76.5	3.02×10^{-4}	486.188242	0.039	0.01	3.9
CH$_3$OH	$13_{68}-14_{59}$	404.8	1.16×10^{-4}	485.732280	0.012	0.01	1.4
H$_2$Cl$^+$	$1_{11}-0_{00}$	...	...	485.420796	−0.005	−0.006	0.8
CH$_3$OH	$3_{22}-3_{13}$	51.6	5.02×10^{-4}	485.263263	0.401	0.071	7.3
SO$_2$	13–12	105.8	5.42×10^{-4}	484.270879	0.026	0.006	1.1
CH$_3$OH	$10_{-29}-9_{-28}$	153.6	4.88×10^{-4}	484.071775	0.17	0.02	8.4
CH$_3$OH	$10_{28}-9_{27}$	150.0	4.83×10^{-4}	484.023168	0.49	0.07	8.2
CH$_3$OH	$2_{21}-2_{12}$	44.7	3.99×10^{-4}	484.004740	0.28	0.05	4.9
CH$_3$OH	$10_{28}-9_{27}$	165.4	4.90×10^{-4}	483.761387	0.07	0.01	5.8
CH$_3$OH	$10_{19}-9_{18}$	148.7	5.13×10^{-4}	483.686308	0.21	0.05	4.2

Notes: *rms* is 1.3 mK in 0.35 km s^{-1} bin. Identifications refer to the 7.0 km s^{-1} component.
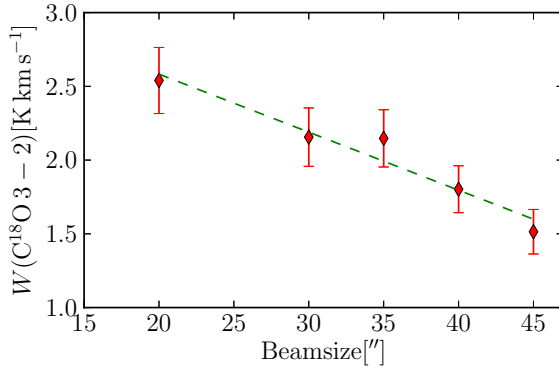
Figure 6.13 – Integrated on source C^{18}O 3–2 intensities when map is convolved to different beam sizes and corresponding intensities are measured. The intensity decreases by a factor of 0.6 with increasing beam size (20″ to 44″).
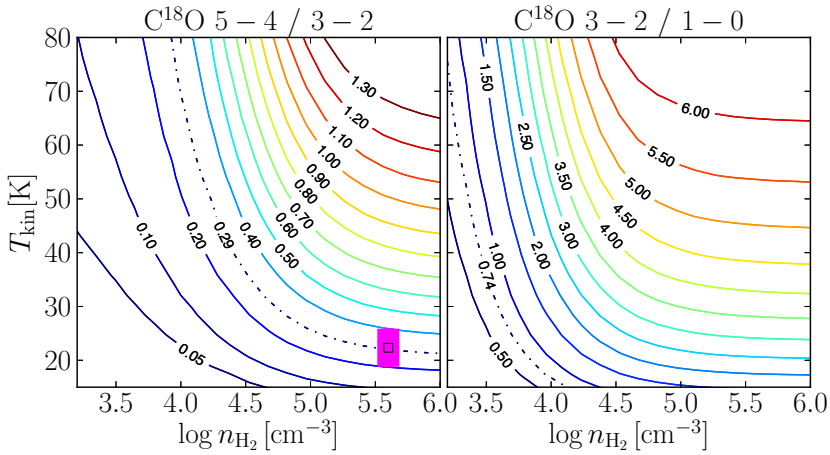
Figure 6.14 – Integrated intensity ratios calculated with RADEX, as function of temperature and density, for a C^{18}O column density of 5×10^{14} cm^{-2} (optically thin conditions). The C^{18}O 5–4/3–2 ratio is representative for the IRAS 4A envelope which is traced by the 7.0 km s^{-1} component; the C^{18}O 3–2/1–0 ratio is representative for the surrounding NGC 1333 cloud, which is traced by the 8.0 km s^{-1} component. Dash-dotted lines indicate the observed ratios of C^{18}O 5–4/3–2=0.29 and C^{18}O 3–2/1–0=0.74 for the V_{LSR}=7.0 and 8.0 km s^{-1} components, respectively. The purple bar in the left figure indicates the IRAS 4A density at the 44″/2 radius.

Acknowledgements

Central source spectra

A.1 L1448MM
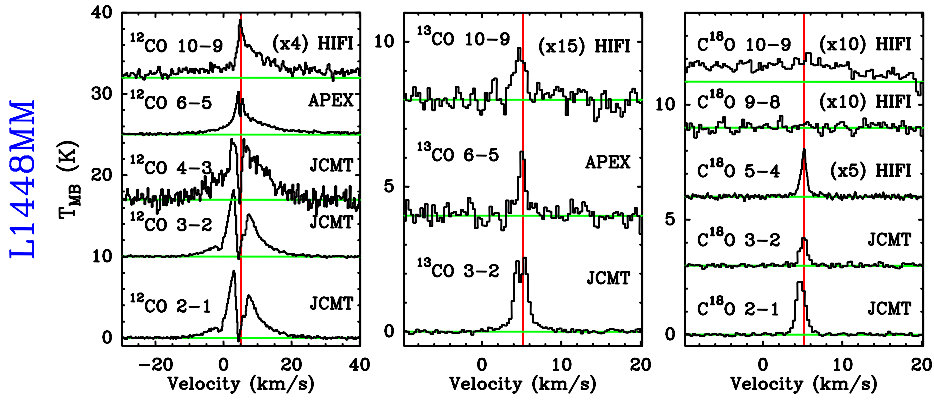
Figure A.1 – Observed ^{12}CO, ^{13}CO, and C^{18}O transitions for L1448MM

Table A.1 – Observed line intensities for L1448MM in all observed transitions.

Mol.	Transition	Telescope	Efficiency η	$\int T_{MB}dV$ [K km s^{-1}]	T_{peak} [K]	rms [K]
CO	2–1	JCMT-RxA	0.69	59.7	8.3	0.10
	3–2	JCMT-HARPB	0.63	32.1	4.2	0.09
	4–3	JCMT	0.38	87.5	7.5	0.77
	6–5[a]	APEX-CHAMP$^+$	0.46	46.1	5.7	0.12
	10–9	*Herschel*-HIFI[b]	0.64	21.5	…	0.15
^{13}CO	2–1	JCMT-RxA	0.74	9.8	6.5	0.07
	3–2	JCMT-HARPB	0.63	5.7	2.7	0.07
	6–5	APEX-CHAMP$^+$	0.48	2.9	2.7	0.34
	10–9	*Herschel*-HIFI[b]	0.74	0.3	0.1	0.02
C^{18}O	2–1	JCMT-RxA	0.69	3.5	2.4	0.06
	3–2	JCMT-HARPB	0.63	1.5	1.5	0.10
	5–4	*Herschel*-HIFI[b]	0.76	0.4	0.4	0.02
	9–8	*Herschel*-HIFI	0.74	<0.05	…	0.02
	10–9	*Herschel*-HIFI[b]	0.74	<0.06	…	0.02

[a]Gomez-Ruiz et al. in prep. [b]Only H-polarization observation is used.

A.2   IRAS2A
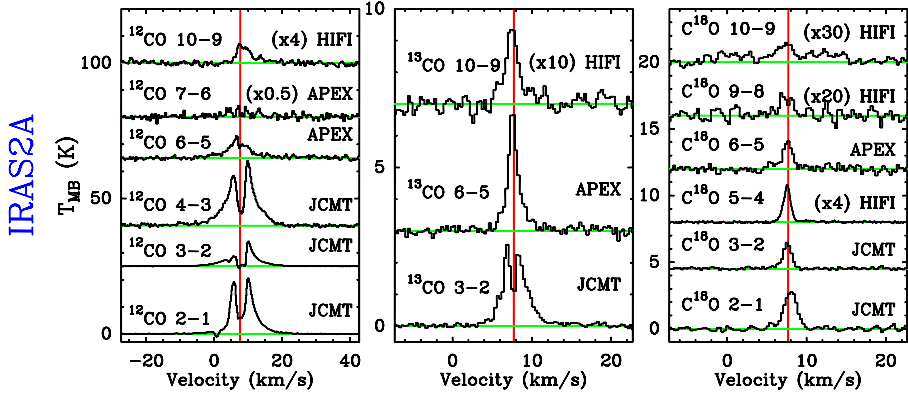
Figure A.2 – Observed ^{12}CO, ^{13}CO, and C^{18}O transitions for IRAS 2A

Table A.2 – Observed line intensities for IRAS2A in all observed transitions.

Mol.	Transition	Telescope	Efficiency η	$\int T_{MB} dV$ [K km s^{-1}]	T_{peak} [K]	rms [K]
CO	2–1	JCMT-RxA	0.69	129.7	20.5	0.08
	3–2	JCMT-HARPB	0.63	46.9	9.4	0.06
	4–3	JCMT^a	0.38	180.0	23.7	0.55
	6–5	APEX-CHAMP$^+$	0.52	55.0	8.9	0.60
	7–6	APEX-CHAMP$^+$	0.49	37.4	6.3	1.29
	10–9	*Herschel*-HIFI^b	0.64	9.2	1.8	0.14
^{13}CO	2–1	JCMT-RxA	0.69	19.3	3.9	0.10
	3–2	JCMT-HARPB	0.63	8.5	2.7	0.08
	6–5	APEX-CHAMP$^+$	0.52	7.1	3.9	0.15
	8–7	APEX-CHAMP$^+$	0.49	3.0	1.5	0.28
	10–9	*Herschel*-HIFI^b	0.74	0.6	0.3	0.03
C^{18}O	2–1	JCMT-RxA	0.69	6.0	2.8	0.15
	3–2	JCMT-HARPB	0.63	2.8	2.1	0.10
	5–4	*Herschel*-HIFI^b	0.76	0.8	0.7	0.01
	6–5	APEX-CHAMP$^+$	0.56	3.6	2.1	0.27
	9–8	*Herschel*-HIFI	0.74	0.2	0.09	0.02
	10–9	*Herschel*-HIFI^b	0.74	0.1	0.05	0.01

^{a}Taken in 11" beam. ^{b}Only H-polarization observation is used.

A.3   IRAS4A
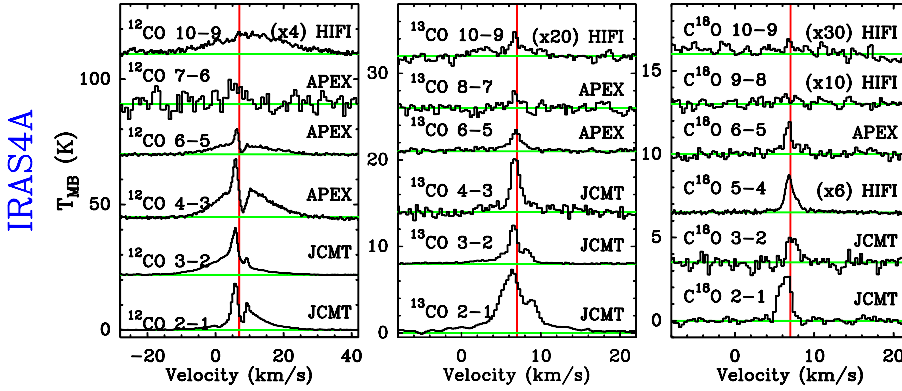
Figure A.3 – Observed ^{12}CO, ^{13}CO, and C^{18}O transitions for IRAS 4A

Table A.3 – Observed line intensities for IRAS4A in all observed transitions.

Mol.	Transition	Telescope	Efficiency η	$\int T_{MB} dV$ [K km s^{-1}]	T_{peak} [K]	rms [K]
CO	2–1	JCMT-RxA	0.69	116.5	18.4	0.11
	3–2	JCMT-HARPB	0.63	132.6	18.9	0.07
	4–3	JCMT[a]	0.38	220.0	23.4	0.92
	6–5	APEX-CHAMP$^+$	0.48	84.2	10.0	0.27
	7–6	APEX-CHAMP$^+$	0.45	55.0	17.0	4.39
	10–9	*Herschel*-HIFI[b]	0.64	52.2	2.3	0.18
^{13}CO	2–1	JCMT-RxA	0.74	39.3	7.6	0.15
	3–2	JCMT-HARPB	0.63	11.4	4.5	0.08
	4–3	JCMT[a]	0.38	15.2	7.4	0.78
	6–5	APEX-CHAMP$^+$	0.52	7.0	2.6	0.20
	8–7	APEX-CHAMP$^+$	0.49	1.9	1.0	0.42
	10–9	*Herschel*-HIFI[c]	0.74	0.7	0.2	0.02
C^{18}O	2–1	JCMT-RxA	0.69	4.9	2.7	0.23
	3–2	JCMT-HARPB	0.63	4.2	2.3	0.22
	5–4	*Herschel*-HIFI[d]	0.76	0.6	0.4	0.01
	6–5	APEX-CHAMP$^+$	0.48	3.3	2.0	0.26
	9–8	*Herschel*-HIFI	0.74	0.16	0.05	0.02
	10–9	*Herschel*-HIFI[e]	0.74	0.05	0.02	0.008

The values given here are calculated for 20" beam, therefore values are slightly different than Yıldız et al. (2012). [a]Taken in 11" beam. [b]Herschel observation corrected for the chopped emission and only H polarization observation is used. [c]H- and V-polarization observations averaged. [d]Only H-polarization observation is used. [e]Observed by open time program OT2_rvisser_2. H- and V-polarization observations averaged.

A.4   IRAS4B
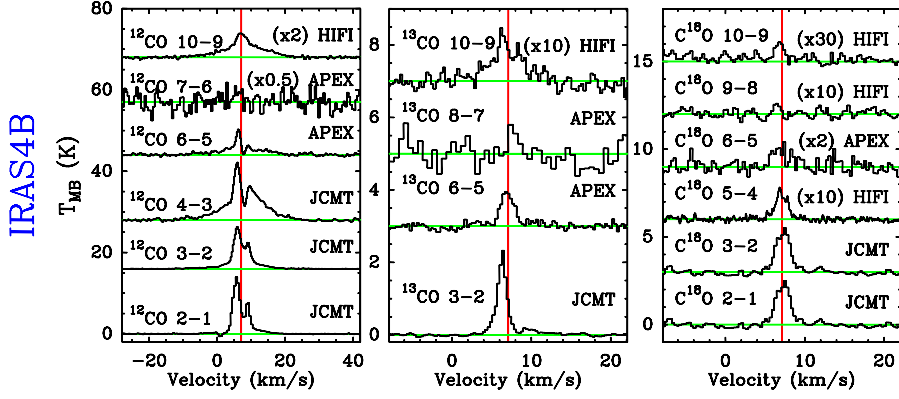
Figure A.4 – Observed ^{12}CO, ^{13}CO, and C^{18}O transitions for IRAS 4B

Table A.4 – Observed line intensities for IRAS4B in all observed transitions.

Mol.	Transition	Telescope	Efficiency η	$\int T_{MB}dV$ [K km s^{-1}]	T_{peak} [K]	rms [K]
CO	2–1	JCMT-RxA	0.69	54.7	13.9	0.07
	3–2	JCMT-HARPB	0.63	53.9	10.4	0.03
	4–3	JCMT[a]	0.38	115.2	14.4	0.26
	6–5	APEX-CHAMP$^+$	0.48	35.3	6.3	0.29
	7–6	APEX-CHAMP$^+$	0.45	<35.0	…	4.51
	10–9	*Herschel*-HIFI[b]	0.64	29.2	2.9	0.10
^{13}CO	3–2	JCMT-HARPB	0.63	5.9	2.3	0.02
	6–5	APEX-CHAMP$^+$	0.52	2.2	1.0	0.10
	8–7	APEX-CHAMP$^+$	0.42	0.8	…	0.28
	10–9	*Herschel*-HIFI[c]	0.74	0.5	0.15	0.02
C^{18}O	2–1	JCMT-RxA	0.69	5.3	2.5	0.16
	3–2	JCMT-HARPB	0.63	2.4	1.7	0.30
	5–4	*Herschel*-HIFI[d]	0.76	0.3	0.2	0.01
	6–5	APEX-CHAMP$^+$	0.48	1.3	0.8	0.22
	9–8	*Herschel*-HIFI	0.74	<0.06	…	0.02
	10–9	*Herschel*-HIFI[e]	0.74	0.06	0.04	0.009

The values given here are calculated for 20" beam, therefore values are slightly different than Yıldız et al. (2012). [a]Taken in 11" beam. [b]*Herschel* observation corrected for the chopped emission and only H polarization observation is used. [c]H- and V-polarization observations averaged. [d]Only H-polarization observation is used. [e]Observed by open time program OT2_rvisser_2. H- and V-polarization observations averaged.

A.5 L1527
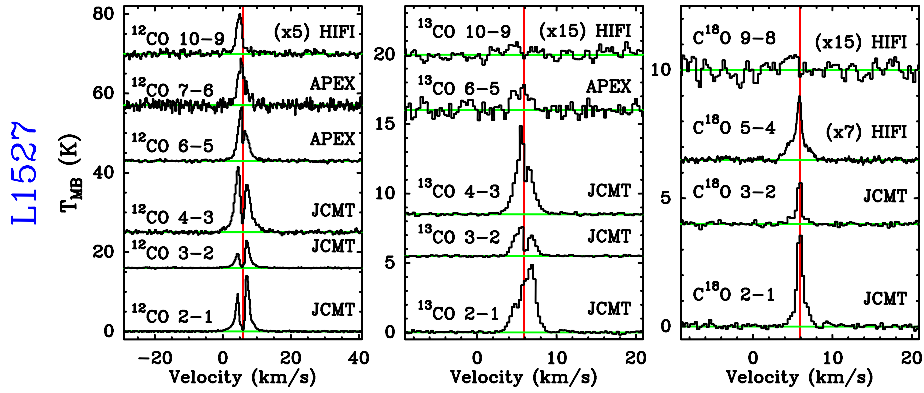
Figure A.5 – Observed ^{12}CO, ^{13}CO, and C^{18}O transitions for L1527

Table A.5 – Observed line intensities for L1527 in all observed transitions.

Mol.	Transition	Telescope	Efficiency η	$\int T_{MB} dV$ [K km s^{-1}]	T_{peak} [K]	rms [K]
CO	2–1	JCMT-RxA	0.69	38.1	14.0	0.09
	3–2	JCMT-HARPB	0.63	19.4	6.9	0.12
	4–3	JCMT[a]	0.38	63.6	16.4	0.46
	6–5	APEX-CHAMP$^+$	0.52	38.0	14.9	0.33
	7–6	APEX-CHAMP$^+$	0.49	31.9	11.8	0.85
	10–9	Herschel-HIFI[b]	0.64	5.2	2.0	0.12
^{13}CO	2–1	JCMT-RxA	0.69	12.1	4.9	0.09
	3–2	JCMT-HARPB	0.63	4.7	2.7	0.07
	4–3	JCMT[a]	0.38	12.0	6.4	0.09
	6–5	APEX-CHAMP$^+$	0.48	4.2	2.4	0.51
	10–9	Herschel-HIFI[b]	0.76	0.1	0.1	0.02
C^{18}O	2–1	JCMT-RxA	0.69	4.6	3.9	0.11
	3–2	JCMT-HARPB	0.63	1.5	1.9	0.10
	5–4	Herschel-HIFI[b]	0.76	0.5	0.3	0.01
	9–8	Herschel-HIFI	0.74	<0.05	...	0.02

[a]Taken in 11" beam. [b]Only H-polarization observation is used.

A.6 Ced110IRS4
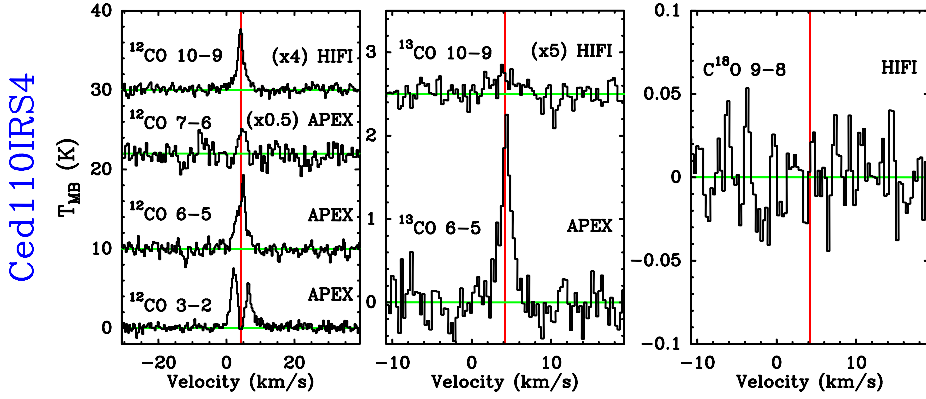
Figure A.6 – Observed ^{12}CO, ^{13}CO, and $C^{18}O$ transitions for Ced110IRS4

Table A.6 – Observed line intensities for Ced110IRS4 in all observed transitions.

Mol.	Transition	Telescope	Efficiency η	$\int T_{MB} dV$ [K km s^{-1}]	T_{peak} [K]	rms [K]
CO	3–2	APEX	0.73	31.1	7.7	0.35
	6–5	APEX-CHAMP$^+$	0.45	24.4	10.4	0.71
	7–6	APEX-CHAMP$^+$	0.42	18.2	6.8	1.49
	10–9	*Herschel*-HIFI^a	0.66	5.1	1.9	0.12
^{13}CO	6–5	APEX-CHAMP$^+$	0.45	3.0	2.7	0.30
	10–9	*Herschel*-HIFI^a	0.74	0.1	0.1	0.03
$C^{18}O$	9–8	*Herschel*-HIFI	0.74	<0.06	. . .	0.03

^{a}H- and V-polarization observations averaged.

A.7 BHR71
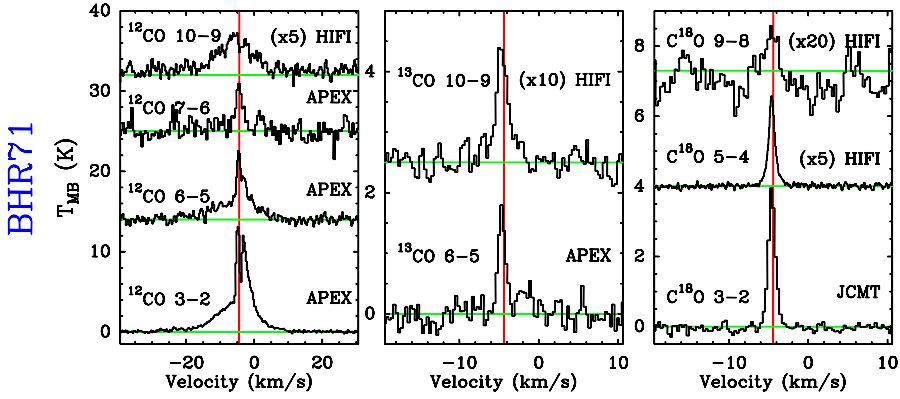
Figure A.7 – Observed ^{12}CO, ^{13}CO, and $C^{18}O$ transitions for BHR71

Table A.7 – Observed line intensities for BHR71 in all observed transitions.

Mol.	Transition	Telescope	Efficiency η	$\int T_{MB} dV$ [K km s^{-1}]	T_{peak} [K]	rms [K]
CO	3–2	APEX	0.73	96.5	14.5	0.20
	6–5	APEX-CHAMP$^+$	0.46	49.1	8.7	0.52
	7–6	APEX-CHAMP$^+$	0.49	27.3	6.8	1.31
	10–9	*Herschel*-HIFI[a]	0.64	15.1	1.0	0.15
^{13}CO	6–5	APEX-CHAMP$^+$	0.45	2.7	1.9	0.23
	10–9	*Herschel*-HIFI[b]	0.74	0.4	0.2	0.02
$C^{18}O$	3–2	APEX	0.73	4.1	4.1	0.11
	5–4	*Herschel*-HIFI[a]	0.76	0.6	0.5	0.01
	9–8	*Herschel*-HIFI	0.74	0.1	0.1	0.02

[a]Only H-polarization observation is used. [b]H- and V-polarization observations averaged.

A.8   IRAS153981
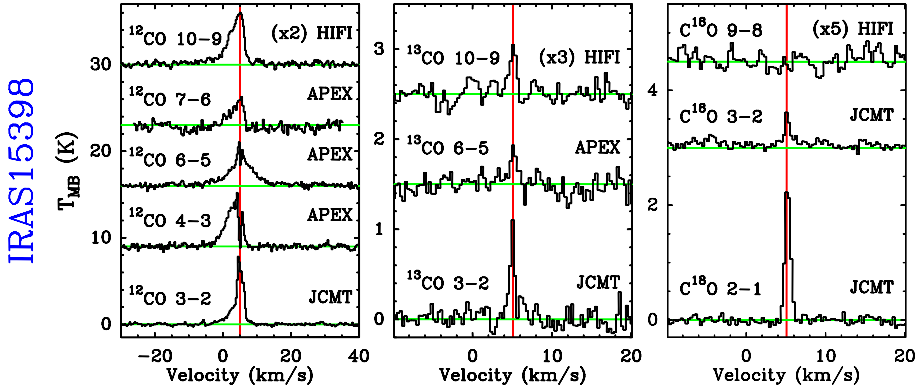
Figure A.8 – Observed ^{12}CO, ^{13}CO, and C^{18}O transitions for IRAS15398

Table A.8 – Observed line intensities for IRAS15398 in all observed transitions.

Mol.	Transition	Telescope	Efficiency η	$\int T_{MB}dV$ [K km s^{-1}]	T_{peak} [K]	rms [K]
CO	3–2	APEX	0.73	22.0	8.5	0.15
	4–3	APEX	0.60	26.3	6.8	0.32
	6–5	APEX-CHAMP$^+$	0.48	33.9	5.3	0.25
	7–6	APEX-CHAMP$^+$	0.49	16.9	3.9	0.64
	10–9	*Herschel*-HIFI[a]	0.64	17.7	3.0	0.10
^{13}CO	3–2	JCMT-HARPB	0.63	1.2	1.3	0.12
	6–5	APEX-CHAMP$^+$	0.48	0.5	0.5	0.12
	10–9	*Herschel*-HIFI[a]	0.74	0.2	0.2	0.03
C^{18}O	2–1	JCMT-RxA	0.69	2.0	2.5	0.09
	3–2	JCMT-HARPB	0.63	0.8	0.7	0.08
	9–8	*Herschel*-HIFI	0.74	<0.06	. . .	0.02

[a]H- and V-polarization observations averaged.

A.9 L483mm
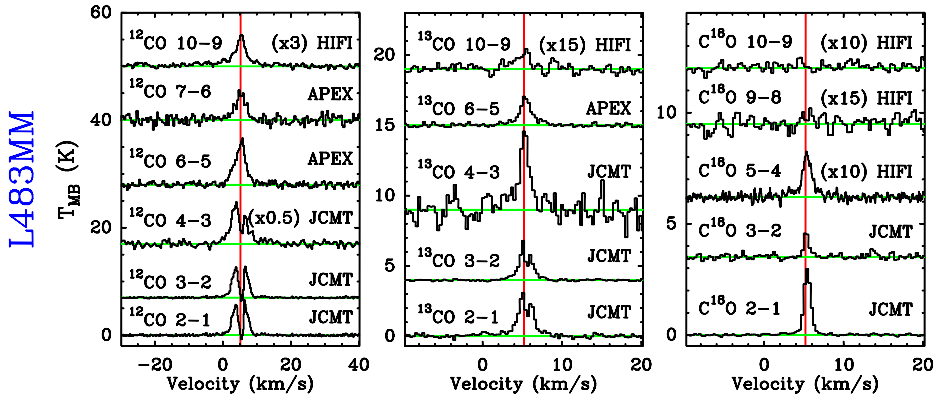
Figure A.9 – Observed ^{12}CO, ^{13}CO, and $C^{18}O$ transitions for L483mm

Table A.9 – Observed line intensities for L483mm in all observed transitions.

Mol.	Transition	Telescope	Efficiency η	$\int T_{MB}dV$ [K km s^{-1}]	T_{peak} [K]	rms [K]
CO	2–1	JCMT-RxA	0.69	22.4	6.5	0.13
	3–2	JCMT-HARPB	0.63	21.0	4.8	0.06
	4–3	JCMT	0.38	76.1	18.6	0.94
	6–5	APEX-CHAMP$^+$	0.45	32.4	8.9	0.49
	7–6	APEX-CHAMP$^+$	0.49	22.1	6.3	1.11
	10–9	*Herschel*-HIFI[a]	0.64	11.4	2.0	0.10
^{13}CO	2–1	JCMT-RxA	0.74	7.0	3.2	0.17
	3–2	JCMT-HARPB	0.63	4.3	2.9	0.07
	4–3	JCMT[b]	0.38	10.9	6.6	0.93
	6–5	APEX-CHAMP$^+$	0.46	4.2	2.2	0.13
	10–9	*Herschel*-HIFI[a]	0.74	0.2	0.1	0.02
$C^{18}O$	2–1	JCMT-RxA	0.69	3.5	3.1	0.04
	3–2	JCMT-HARPB	0.63	1.2	1.4	0.15
	5–4	*Herschel*-HIFI[c]	0.76	0.3	0.2	0.01
	9–8	*Herschel*-HIFI	0.74	<0.05	...	0.02
	10–9	*Herschel*-HIFI	0.74	<0.05	...	0.02

[a]H- and V-polarization observations averaged. [b]Taken in 11" beam. [c]Only H-polarization observation is used.

A.10   SMM1
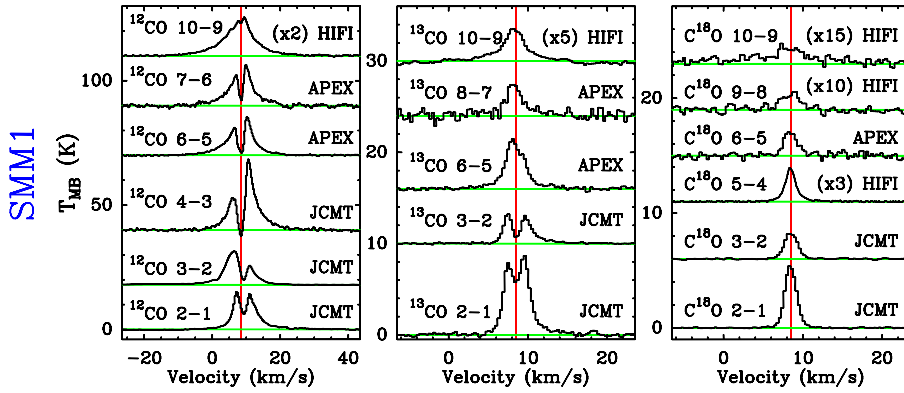
Figure A.10 – Observed ^{12}CO, ^{13}CO, and C^{18}O transitions for SMM1

Table A.10 – Observed line intensities for SMM1 in all observed transitions.

Mol.	Transition	Telescope	Efficiency η	$\int T_{MB} dV$ [K km s^{-1}]	T_{peak} [K]	rms [K]
CO	2–1	JCMT-RxA	0.69	112.5	15.1	0.19
	3–2	JCMT-HARPB	0.63	101.8	13.4	0.02
	4–3	JCMT	0.38	160.0	29.0	0.39
	6–5	APEX-CHAMP$^+$	0.52	108.4	15.5	0.17
	7–6	APEX-CHAMP$^+$	0.40	105.6	16.4	0.59
	10–9	*Herschel*-HIFI^a	0.64	82.3	7.7	0.09
^{13}CO	2–1	JCMT-RxA	0.74	31.8	8.9	0.17
	3–2	JCMT-HARPB	0.63	11.2	3.4	0.07
	6–5	APEX-CHAMP$^+$	0.46	17.5	5.6	0.18
	8–7	APEX-CHAMP$^+$	0.49	5.0	1.6	0.39
	10–9	*Herschel*-HIFI^b	0.74	3.4	0.7	0.03
C^{18}O	2–1	JCMT-RxA	0.69	10.3	5.5	0.06
	3–2	JCMT-HARPB	0.63	4.8	2.2	0.05
	5–4	*Herschel*-HIFI^b	0.76	1.8	1.0	0.01
	6–5	APEX-CHAMP$^+$	0.56	4.7	2.1	0.26
	9–8	*Herschel*-HIFI	0.74	0.4	0.02	0.02
	10–9	*Herschel*-HIFI	0.74	0.6	0.1	0.02

^{a}H- and V-polarization observations averaged. ^{b}Only H-polarization observation is used.

A.11   SMM4
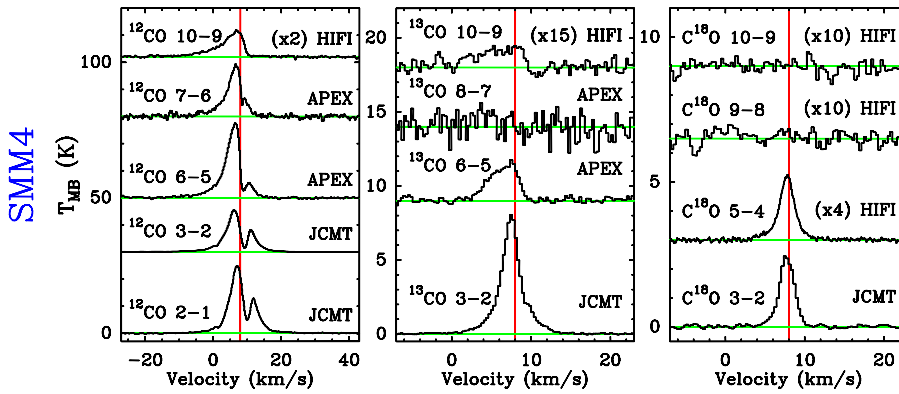
Figure A.11 – Observed ^{12}CO, ^{13}CO, and C^{18}O transitions for SMM4

Table A.11 – Observed line intensities for SMM4 in all observed transitions.

Mol.	Transition	Telescope	Efficiency η	$\int T_{MB} dV$ [K km s^{-1}]	T_{peak} [K]	rms [K]
CO	2–1	JCMT-RxA	0.69	168.4	24.8	0.10
	3–2	JCMT-HARPB	0.63	108.4	15.5	0.02
	6–5	APEX-CHAMP$^+$	0.52	159.6	27.6	0.23
	7–6	APEX-CHAMP$^+$	0.40	110.1	19.4	0.63
	10–9	*Herschel*-HIFI[a]	0.64	40.2	5.0	0.13
^{13}CO	3–2	JCMT-HARPB	0.63	26.1	8.1	0.05
	6–5	APEX-CHAMP$^+$	0.52	10.6	2.6	0.15
	8–7	APEX-CHAMP$^+$	0.49	1.6	2.6	1.00
	10–9	*Herschel*-HIFI[b]	0.74	0.5	0.1	0.02
C^{18}O	3–2	JCMT-HARPB	0.63	6.0	2.5	0.06
	5–4	*Herschel*-HIFI[b]	0.76	1.4	0.5	0.01
	9–8	*Herschel*-HIFI	0.74	<0.06	. . .	0.02
	10–9	*Herschel*-HIFI	0.74	<0.05	. . .	0.02

[a]Only H-polarization observation is used. [b]H- and V-polarization observations averaged.

A.12   SMM3
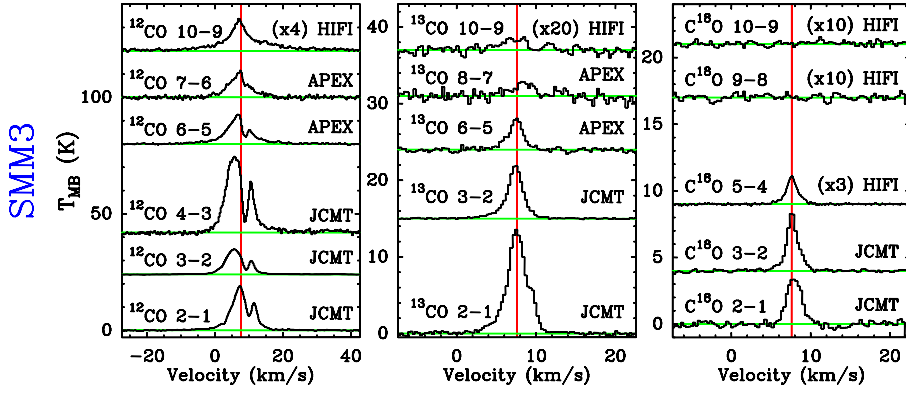
Figure A.12 – Observed ^{12}CO, ^{13}CO, and C^{18}O transitions for SMM3

Table A.12 – Observed line intensities for SMM3 in all observed transitions.

Mol.	Transition	Telescope	Efficiency η	$\int T_{MB} dV$ [K km s^{-1}]	T_{peak} [K]	rms [K]
CO	2–1	JCMT-RxA	0.69	133.0	19.1	0.11
	3–2	JCMT-HARPB	0.63	78.1	10.8	0.03
	4–3	JCMT	0.38	243.0	32.9	0.79
	6–5	APEX-CHAMP$^+$	0.52	97.6	12.7	0.22
	7–6	APEX-CHAMP$^+$	0.40	74.3	11.5	0.55
	10–9	*Herschel*-HIFI[a]	0.64	35.7	3.5	0.09
^{13}CO	2–1	JCMT-RxA	0.74	44.5	13.7	0.18
	3–2	JCMT-HARPB	0.63	18.3	7.1	0.07
	6–5	APEX-CHAMP$^+$	0.52	9.6	4.1	0.26
	8–7	APEX-CHAMP$^+$	0.49	5.6	2.3	0.61
	10–9	*Herschel*-HIFI[a]	0.74	0.3	0.09	0.02
C^{18}O	2–1	JCMT-RxA	0.69	8.0	3.4	0.32
	3–2	JCMT-HARPB	0.63	5.0	2.6	0.06
	5–4	*Herschel*-HIFI[b]	0.76	1.3	0.7	0.01
	9–8	*Herschel*-HIFI	0.74	<0.04	...	0.02
	10–9	*Herschel*-HIFI	0.74	<0.03	...	0.01

[a]H- and V-polarization observations averaged. [b]Only H-polarization observation is used.

A.13   L723mm
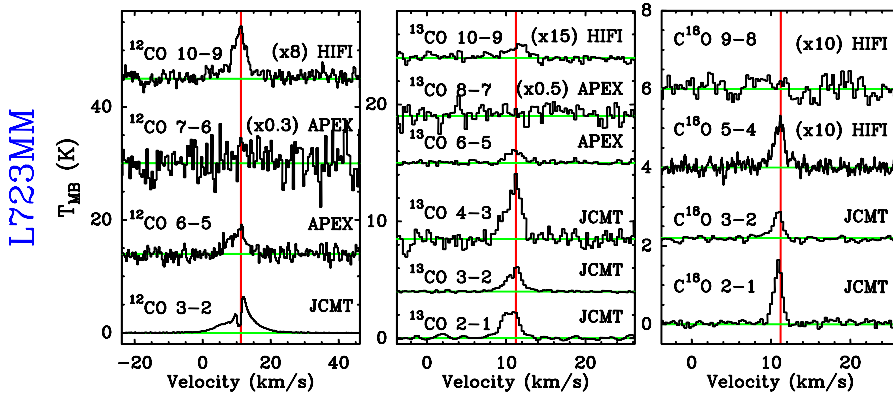
Figure A.13 – Observed ^{12}CO, ^{13}CO, and $C^{18}O$ transitions for L723mm

Table A.13 – Observed line intensities for L723mm in all observed transitions.

Mol.	Transition	Telescope	Efficiency η	$\int T_{MB} dV$ [K km s^{-1}]	T_{peak} [K]	rms [K]
CO	3–2	JCMT-HARPB	0.63	39.5	6.4	0.05
	6–5	APEX-CHAMP$^+$	0.52	22.0	5.4	1.11
	7–6	APEX-CHAMP$^+$	0.49	11.0	6.0	3.81
	10–9	*Herschel*-HIFI[a]	0.64	6.6	1.2	0.09
^{13}CO	2–1	JCMT-RxA	0.74	7.1	2.2	0.10
	3–2	JCMT-HARPB	0.63	4.8	2.2	0.08
	4–3	JCMT[b]	0.38	10.8	5.9	0.76
	6–5	APEX-CHAMP$^+$	0.45	3.3	1.3	0.18
	8–7	APEX-CHAMP$^+$	0.49	1.9	4.7	1.55
	10–9	*Herschel*-HIFI[a]	0.74	0.2	0.1	0.03
$C^{18}O$	2–1	JCMT-RxA	0.69	2.2	1.7	0.08
	3–2	JCMT-HARPB	0.63	1.0	0.7	0.09
	5–4	*Herschel*-HIFI[c]	0.76	0.2	0.1	0.02
	9–8	*Herschel*-HIFI	0.74	<0.04	. . .	0.02

[a]H- and V-polarization observations averaged. [b]Taken in 11" beam. [c]Only H-polarization observation is used.

A.14   B335
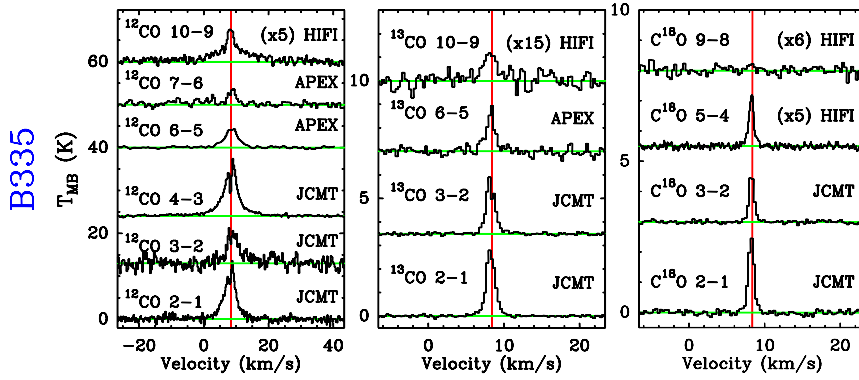
Figure A.14 – Observed ^{12}CO, ^{13}CO, and C^{18}O transitions for B335

Table A.14 – Observed line intensities for B335 in all observed transitions.

Mol.	Transition	Telescope	Efficiency η	$\int T_{MB}\,dV$ [K km s^{-1}]	T_{peak} [K]	rms [K]
CO	2–1	JCMT-RxA	0.69	56.1	13.6	0.51
	3–2	JCMT-HARPB	0.63	38.3	8.7	1.49
	4–3	JCMT	0.38	68.7	13.4	0.15
	6–5	APEX-CHAMP$^+$	0.52	25.9	4.4	0.23
	7–6	APEX-CHAMP$^+$	0.49	21.9	3.6	0.58
	10–9	*Herschel*-HIFI[a]	0.64	12.5	1.5	0.13
^{13}CO	2–1	JCMT-RxA	0.74	4.3	3.2	0.05
	3–2	JCMT-HARPB	0.63	3.4	3.0	0.07
	6–5	APEX-CHAMP$^+$	0.48	2.6	2.1	0.21
	10–9	*Herschel*-HIFI[b]	0.74	0.2	0.08	0.02
C^{18}O	2–1	JCMT-RxA	0.69	2.4	2.5	0.10
	3–2	JCMT-HARPB	0.63	1.4	1.9	0.06
	5–4	*Herschel*-HIFI[a]	0.76	0.3	0.3	0.01
	9–8	*Herschel*-HIFI	0.74	<0.05	…	0.03

[a]Only H-polarization observation is used. [b]H- and V-polarization observations averaged.

A.15   L1157
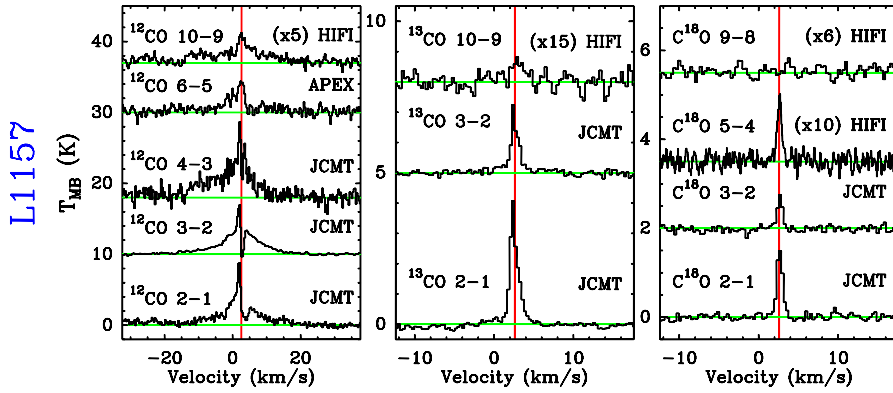
Figure A.15 – Observed ^{12}CO, ^{13}CO, and $C^{18}O$ transitions for L1157

Table A.15 – Observed line intensities for L1157 in all observed transitions.

Mol.	Transition	Telescope	Efficiency η	$\int T_{MB} dV$ [K km s^{-1}]	T_{peak} [K]	rms [K]
CO	2–1	JCMT-RxA	0.69	47.9	8.8	0.28
	3–2	JCMT-HARPB	0.63	48.2	7.4	0.10
	4–3	JCMT	0.38	78.1	10.7	0.88
	10–9	*Herschel*-HIFI[a]	0.64	8.9	0.9	0.15
^{13}CO	2–1	JCMT-RxA	0.74	5.1	4.3	0.10
	3–2	JCMT-HARPB	0.63	3.1	2.6	0.11
	10–9	*Herschel*-HIFI[b]	0.74	0.3	0.1	0.03
$C^{18}O$	2–1	JCMT-RxA	0.69	1.5	1.5	0.09
	3–2	JCMT-HARPB	0.63	0.5	0.8	0.09
	5–4	*Herschel*-HIFI[b]	0.76	0.1	0.1	0.01
	9–8	*Herschel*-HIFI	0.74	<0.05	...	0.02

[a]H- and V-polarization observations averaged. [b]Only H-polarization observation is used.

A.16   L1489
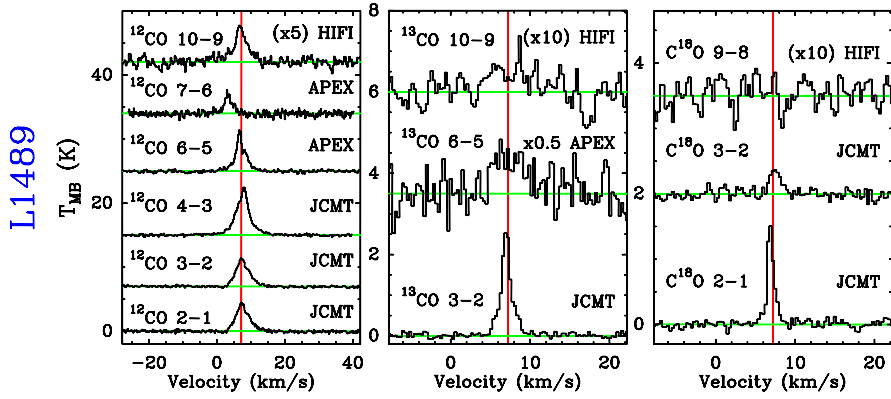
Figure A.16 – Observed ^{12}CO, ^{13}CO, and C^{18}O transitions for L1489

Table A.16 – Observed line intensities for L1489 in all observed transitions.

Mol.	Transition	Telescope	Efficiency η	$\int T_{MB}dV$ [K km s^{-1}]	T_{peak} [K]	rms [K]
CO	2–1	JCMT-RxA	0.69	19.9	4.5	0.15
	3–2	JCMT-HARPB	0.63	13.0	4.0	0.49
	4–3	JCMT	0.38	33.8	7.1	0.15
	6–5	APEX-CHAMP$^+$	0.45	20.9	6.5	0.16
	7–6	APEX-CHAMP$^+$	0.49	9.1	3.6	0.37
	10–9	*Herschel*-HIFI[a]	0.64	6.2	1.2	0.11
^{13}CO	3–2	JCMT-HARPB	0.63	4.4	2.7	0.08
	6–5	APEX-CHAMP$^+$	0.45	8.2	3.8	1.29
	10–9	*Herschel*-HIFI[a]	0.74	0.2	0.1	0.03
C^{18}O	2–1	JCMT-RxA	0.69	1.7	1.6	0.07
	3–2	JCMT-HARPB	0.63	0.7	0.4	0.10
	9–8	*Herschel*-HIFI	0.74	<0.05	…	0.02

[a]H- and V-polarization observations averaged.

A.17   L1551IRS5
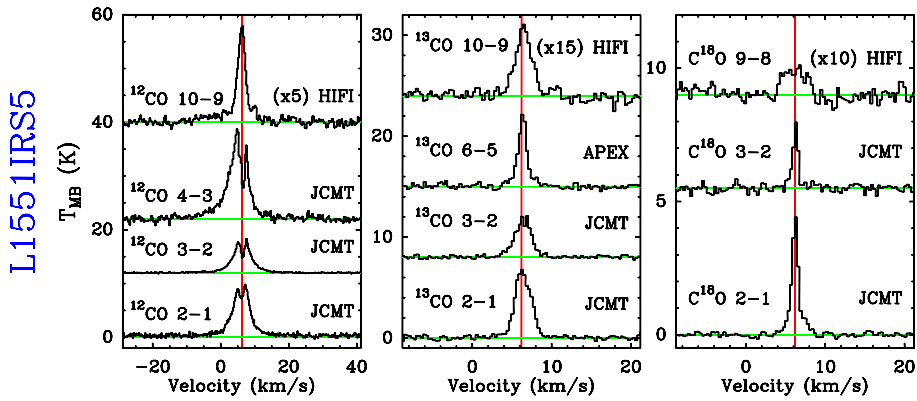
Figure A.17 – Observed ^{12}CO, ^{13}CO, and $C^{18}O$ transitions for L1551IRS5

Table A.17 – Observed line intensities for L1551IRS5 in all observed transitions.

Mol.	Transition	Telescope	Efficiency η	$\int T_{MB} dV$ [K km s^{-1}]	T_{peak} [K]	rms [K]
CO	2–1	JCMT-RxA	0.69	71.5	9.8	0.27
	3–2	JCMT-HARPB	0.63	37.5	6.7	0.11
	4–3	JCMT[a]	0.38	108.1	16.7	0.45
	10–9	*Herschel*-HIFI[b]	0.64	14.7	3.6	0.13
^{13}CO	2–1	JCMT-RxA	0.74	17.8	7.0	0.25
	3–2	JCMT-HARPB	0.63	10.2	4.8	0.18
	6–5	APEX-CHAMP$^+$	0.48	10.5	7.5	0.24
	10–9	*Herschel*-HIFI[b]	0.74	1.4	0.5	0.03
$C^{18}O$	2–1	JCMT-RxA	0.69	5.3	4.6	0.08
	3–2	JCMT-HARPB	0.63	2.3	2.6	0.18
	9–8	*Herschel*-HIFI	0.74	0.2	0.2	0.03

[a]Taken in 11" beam. [b]H- and V-polarization observations averaged.

A.18   TMR1
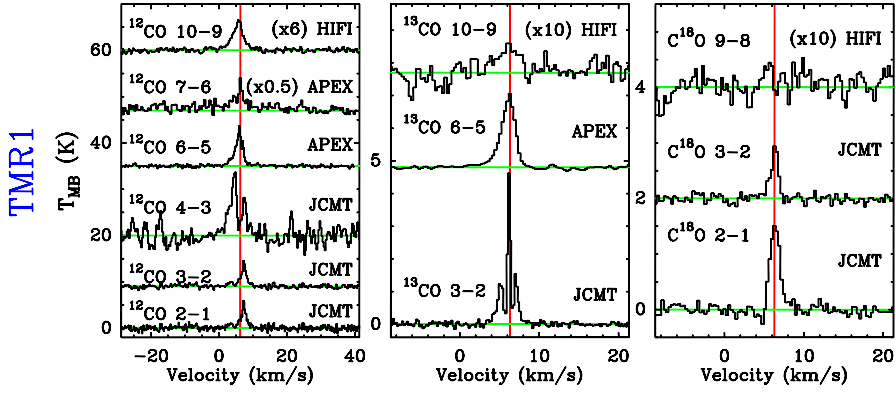
Figure A.18 – Observed ^{12}CO, ^{13}CO, and C^{18}O transitions for TMR1

Table A.18 – Observed line intensities for TMR1 in all observed transitions.

Mol.	Transition	Telescope	Efficiency η	$\int T_{MB} dV$ [K km s^{-1}]	T_{peak} [K]	rms [K]
CO	2–1	JCMT-RxA	0.69	11.9	5.9	0.41
	3–2	JCMT-HARPB	0.63	8.5	4.6	0.09
	4–3	JCMT[a]	0.38	40.8	15.2	3.26
	6–5	APEX-CHAMP$^+$	0.45	22.7	9.2	0.32
	7–6	APEX-CHAMP$^+$	0.42	21.9	8.9	0.81
	10–9	*Herschel*-HIFI[b]	0.64	9.2	2.2	0.13
^{13}CO	3–2	JCMT-HARPB	0.63	4.3	4.6	0.06
	6–5	APEX-CHAMP$^+$	0.45	4.8	2.0	0.03
	10–9	*Herschel*-HIFI[b]	0.74	0.5	0.1	0.03
C^{18}O	2–1	JCMTRxA	0.69	2.2	1.6	0.11
	3–2	JCMT-HARPB	0.63	1.1	1.2	0.09
	9–8	*Herschel*-HIFI	0.74	<0.05	…	0.02

[a]Taken in 11" beam. [b]H- and V-polarization observations averaged.

A.19 TMC1A
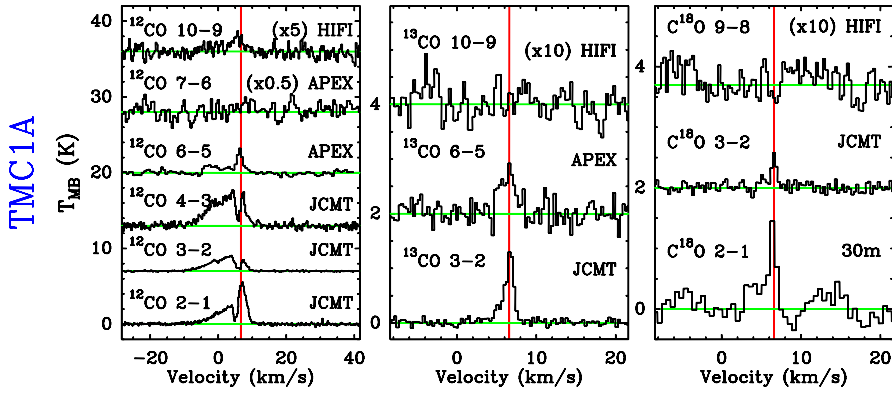
Figure A.19 – Observed ^{12}CO, ^{13}CO, and C^{18}O transitions for TMC1A

Table A.19 – Observed line intensities for TMC1A in all observed transitions.

Mol.	Transition	Telescope	Efficiency η	$\int T_{MB}dV$ [K km s^{-1}]	T_{peak} [K]	rms [K]
CO	2–1	JCMT-RxA	0.69	30.3	5.5	0.19
	3–2	JCMT-HARPB	0.63	19.1	2.1	0.09
	4–3	JCMT[a]	0.38	42.5	4.8	0.46
	6–5	APEX-CHAMP$^+$	0.52	11.7	3.2	0.24
	7–6	APEX-CHAMP$^+$	0.49	4.1	2.1	0.81
	10–9	*Herschel*-HIFI[b]	0.64	1.4	0.5	0.13
^{13}CO	3–2	JCMT-HARPB	0.63	2.2	1.4	0.07
	6–5	APEX-CHAMP$^+$	0.48	1.8	1.1	0.25
	10–9	*Herschel*-HIFI[b]	0.74	<0.1	…	0.03
C^{18}O	2–1	IRAM 30m	0.59	2.0	2.4	0.33
	3–2	JCMT-HARPB	0.63	0.6	0.6	0.11
	9–8	*Herschel*-HIFI	0.74	<0.05	…	0.02

[a]Taken in 11" beam. [b]Only H-polarization observation is used.

A.20   TMC1
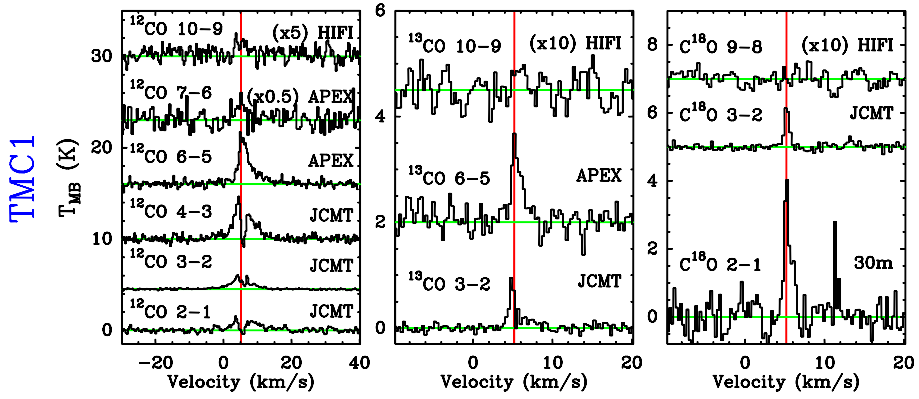
Figure A.20 – Observed ^{12}CO, ^{13}CO, and $C^{18}O$ transitions for TMC1

Table A.20 – Observed line intensities for TMC1 in all observed transitions.

Mol.	Transition	Telescope	Efficiency η	$\int T_{MB}dV$ [K km s^{-1}]	T_{peak} [K]	rms [K]
CO	2–1	JCMT-RxA	0.69	9.1	1.6	0.21
	3–2	JCMT-HARPB	0.63	9.8	2.0	0.10
	4–3	JCMT[a]	0.38	22.6	4.7	0.44
	6–5	APEX-CHAMP$^+$	0.52	26.6	6.0	0.36
	7–6	APEX-CHAMP$^+$	0.49	11.1	4.5	0.92
	10–9	*Herschel*-HIFI[b]	0.64	2.9	0.5	0.15
^{13}CO	3–2	JCMT-HARPB	0.63	1.2	1.1	0.09
	6–5	APEX-CHAMP$^+$	0.48	2.4	1.8	0.24
	10–9	*Herschel*-HIFI[c]	0.74	<0.1	...	0.03
$C^{18}O$	2–1	IRAM 30m	0.59	4.2	4.1	0.41
	3–2	JCMT-HARPB	0.63	0.9	1.3	0.12
	9–8	*Herschel*-HIFI	0.74	<0.05	...	0.02

[a]Taken in 11" beam. [b]Only H-polarization observation is used. [c]H- and V-polarization observations averaged.

A.21   HH46
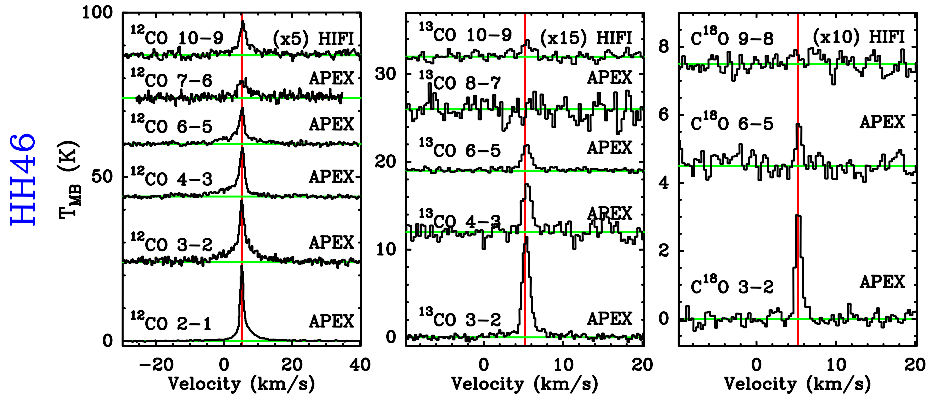
Figure A.21 – Observed ^{12}CO, ^{13}CO, and C^{18}O transitions for HH46

Table A.21 – Observed line intensities for HH46 in all observed transitions.

Mol.	Transition	Telescope	Efficiency η	$\int T_{MB}\,dV$ [K km s^{-1}]	T_{peak} [K]	rms [K]
CO	2–1	APEX	0.73	53.6	23.0	0.08
	3–2	APEX	0.73	81.9	18.8	0.72
	4–3	APEX	0.70	42.8	14.6	0.49
	6–5	APEX-CHAMP$^+$	0.45	45.2	11.8	0.47
	7–6	APEX-CHAMP$^+$	0.49	22.9	6.0	0.89
	10–9	*Herschel*-HIFI[a]	0.64	8.2	2.1	0.14
^{13}CO	3–2	APEX	0.73	17.5	11.9	0.32
	4–3	APEX[b]	0.70	8.0	6.0	1.08
	6–5	APEX-CHAMP$^+$	0.45	5.9	3.1	0.23
	8–7	APEX-CHAMP$^+$	0.42	<1.1	...	0.39
	10–9	*Herschel*-HIFI[a]	0.74	0.2	0.2	0.04
C^{18}O	3–2	APEX–2a	0.70	3.2	...	0.10
	6–5	APEX-CHAMP$^+$	0.56	1.3	1.5	0.50
	9–8	*Herschel*-HIFI	0.74	<0.05	...	0.03

[a]Only H-polarization observation is used. [b]Taken in 11" beam.

A.22   DK Cha
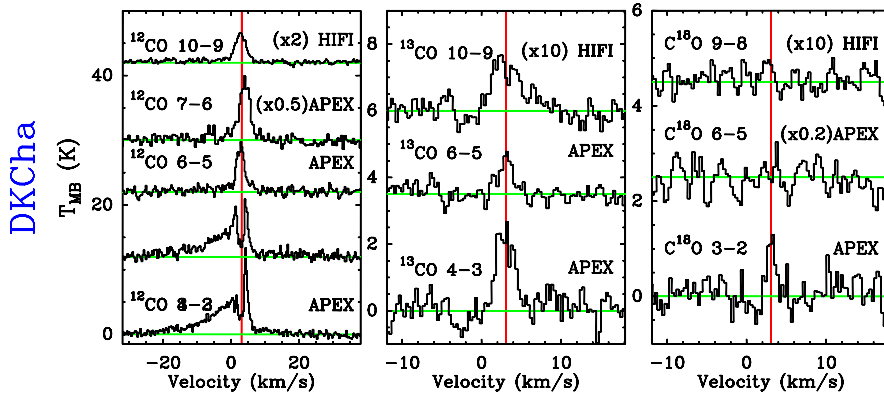
Figure A.22 – Observed ^{12}CO, ^{13}CO, and C^{18}O transitions for DK Cha

Table A.22 – Observed line intensities for DK Cha in all observed transitions.

Mol.	Transition	Telescope	Efficiency η	$\int T_{MB} dV$ [K km s^{-1}]	T_{peak} [K]	rms [K]
CO	3–2	APEX	0.73	80.0	13.3	0.38
	4–3	APEX	0.65	71.8	10.2	0.49
	6–5	APEX-CHAMP$^+$	0.45	28.0	8.2	0.57
	7–6	APEX-CHAMP$^+$	0.42	84.9	20.2	1.89
	10–9	*Herschel*-HIFI[a]	0.64	11.4	2.3	0.12
^{13}CO	3–2	APEX[b]	…	6.7	…	…
	4–3	APEX	0.65	6.5	3.0	0.44
	6–5	APEX-CHAMP$^+$	0.45	2.1	1.3	0.25
	8–7	APEX-CHAMP$^+$	0.49	0.8	…	0.90
	10–9	*Herschel*-HIFI[c]	0.74	0.8	0.2	0.03
C^{18}O	3–2	APEX	0.70	1.4	1.5	0.40
	9–8	*Herschel*-HIFI	0.74	<0.05	…	0.03

[a]H- and V-polarization observations averaged. [b]Only H-polarization observation is used. [c]van Kempen et al. (2006)

A.23 GSS30IRS1
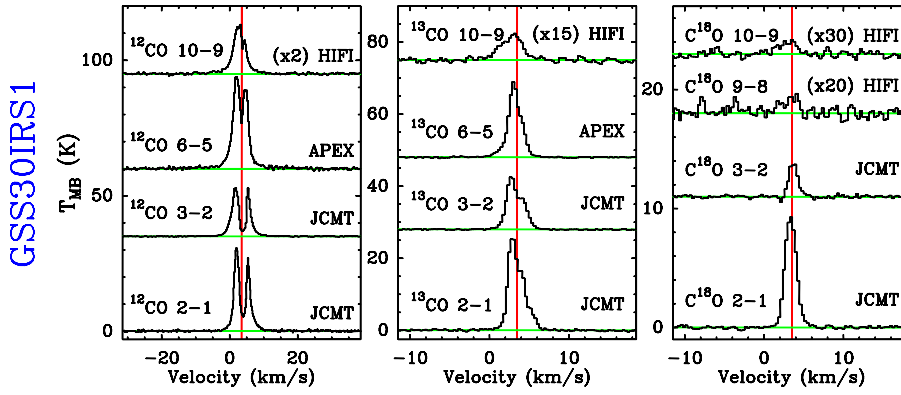
Figure A.23 – Observed ^{12}CO, ^{13}CO, and C^{18}O transitions for GSS30IRS1

Table A.23 – Observed line intensities for GSS30IRS1 in all observed transitions.

Mol.	Transition	Telescope	Efficiency η	$\int T_{MB}dV$ [K km s^{-1}]	T_{peak} [K]	rms [K]
CO	2–1	JCMT-RxA	0.69	114.8	30.8	0.23
	3–2	JCMT-HARPB	0.63	78.0	18.9	0.08
	6–5	APEX-CHAMP$^+$	0.45	172.4	34.4	0.41
	10–9	*Herschel*-HIFI[a]	0.64	41.8	9.3	0.15
^{13}CO	2–1	JCMT-RxA	0.74	58.9	26.3	0.25
	3–2	JCMT-HARPB	0.63	34.3	14.9	0.12
	6–5	APEX-CHAMP$^+$	0.48	41.6	21.4	0.13
	10–9	*Herschel*-HIFI[a]	0.74	2.1	0.5	0.03
C^{18}O	2–1	JCMT-RxA	0.69	17.1	9.4	0.12
	3–2	JCMT-HARPB	0.63	3.7	2.8	0.12
	9–8	*Herschel*-HIFI	0.74	0.2	0.09	0.02
	10–9	*Herschel*-HIFI[b]	0.74	0.09	0.04	0.009

[a]Only H-polarization observation is used. [b]H- and V-polarization observations averaged.

A.24   Elias29
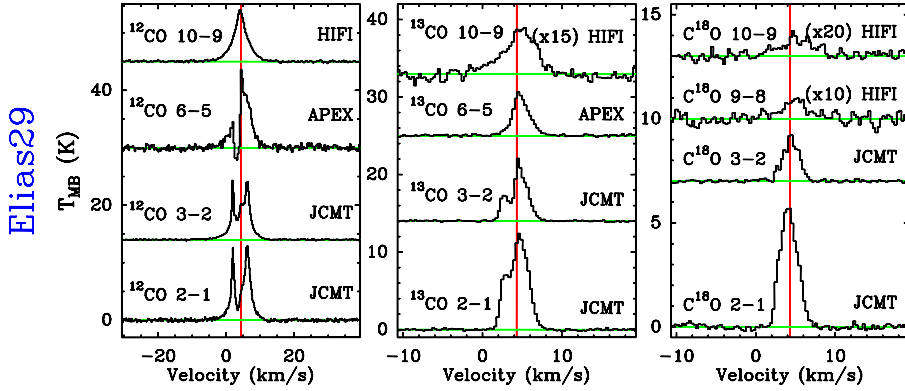
Figure A.24 – Observed ^{12}CO, ^{13}CO, and C^{18}O transitions for Elias29

Table A.24 – Observed line intensities for Elias29 in all observed transitions.

Mol.	Transition	Telescope	Efficiency η	$\int T_{MB}dV$ [K km s^{-1}]	T_{peak} [K]	rms [K]
CO	2–1	JCMT-RxA	0.69	53.7	12.9	0.18
	3–2	JCMT-HARPB	0.63	48.3	11.1	0.07
	6–5	APEX-CHAMP$^+$	0.48	45.0	14.6	0.48
	10–9	*Herschel*-HIFI^a	0.64	45.9	9.1	0.11
^{13}CO	2–1	JCMT-RxA	0.74	37.4	12.6	0.17
	3–2	JCMT-HARPB	0.63	18.7	8.3	0.10
	6–5	APEX-CHAMP$^+$	0.48	14.6	5.7	0.13
	10–9	*Herschel*-HIFI^a	0.74	1.7	0.4	0.03
C^{18}O	2–1	JCMT-RxA	0.69	15.7	5.9	0.15
	3–2	JCMT-HARPB	0.63	5.3	2.5	0.07
	9–8	*Herschel*-HIFI	0.74	0.4	0.1	0.03
	10–9	*Herschel*-HIFI^b	0.74	0.23	0.07	0.01

^{a}H- and V-polarization observations averaged. ^{b}Only H-polarization observation is used.

A.25   Oph IRS63
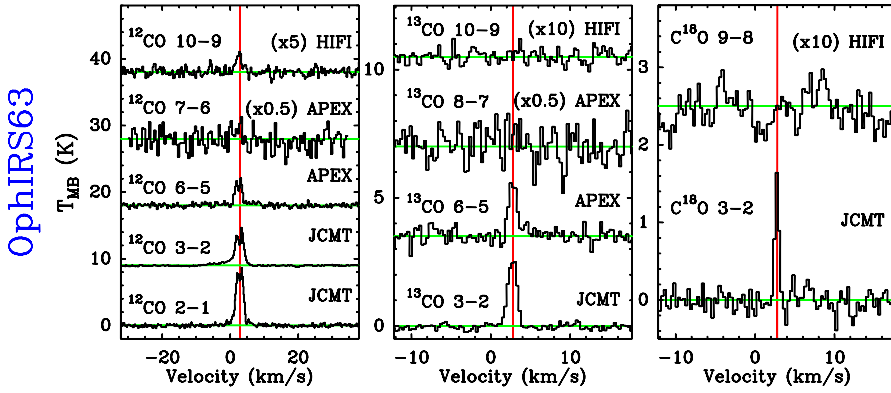
Figure A.25 – Observed ^{12}CO, ^{13}CO, and C^{18}O transitions for Oph IRS63

Table A.25 – Observed line intensities for OphIRS63 in all observed transitions.

Mol.	Transition	Telescope	Efficiency η	$\int T_{MB} dV$ [K km s^{-1}]	T_{peak} [K]	rms [K]
CO	2–1	JCMT-RxA	0.69	23.3	8.6	0.19
	3–2	JCMT-HARPB	0.63	16.5	6.1	0.09
	6–5	APEX-CHAMP$^+$	0.48	11.1	4.4	0.32
	7–6	APEX-CHAMP$^+$	0.48	8.6	4.8	1.09
	10–9	*Herschel*-HIFI[a]	0.64	1.1	0.6	0.13
^{13}CO	3–2	JCMT-HARPB	0.63	3.6	2.7	0.13
	6–5	APEX-CHAMP$^+$	0.45	3.0	2.5	0.35
	8–7	APEX-CHAMP$^+$	0.49	<4.3	...	1.68
	10–9	*Herschel*-HIFI[a]	0.74	<0.06	...	0.03
C^{18}O	3–2	JCMT-HARPB	0.63	0.9	1.7	0.17
	9–8	*Herschel*-HIFI	0.74	<0.05	...	0.02

[a]H- and V-polarization observations averaged.

A.26 RNO91
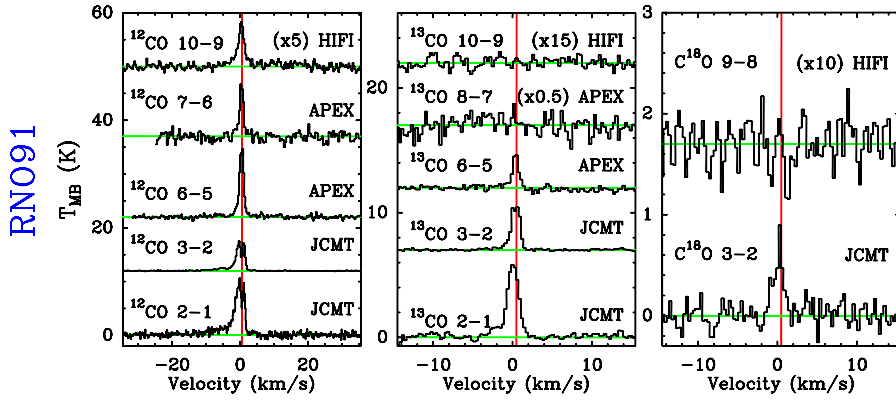
Figure A.26 – Observed ^{12}CO, ^{13}CO, and C^{18}O transitions for RNO91

Table A.26 – Observed line intensities for RNO91 in all observed transitions.

Mol.	Transition	Telescope	Efficiency η	$\int T_{\mathrm{MB}}\mathrm{d}V$ [K km s^{-1}]	T_{peak} [K]	rms [K]
CO	2–1	JCMT-RxA	0.69	40.5	10.6	0.42
	3–2	JCMT-HARPB	0.63	16.7	6.2	0.06
	6–5	APEX-CHAMP$^+$	0.48	26.0	13.5	0.33
	7–6	APEX-CHAMP$^+$	0.49	14.9	11.1	1.15
	10–9	*Herschel*-HIFI[a]	0.64	5.2	1.7	0.10
^{13}CO	2–1	JCMT-RxA	0.74	11.8	5.9	0.39
	3–2	JCMT-HARPB	0.63	5.4	3.9	0.08
	6–5	APEX-CHAMP$^+$	0.45	2.4	3.0	0.28
	8–7	APEX-CHAMP$^+$	0.49	1.6	4.6	1.77
	10–9	*Herschel*-HIFI[a]	0.74	<0.07	...	0.03
C^{18}O	3–2	JCMT-HARPB	0.63	1.1	1.1	0.14
	9–8	*Herschel*-HIFI	0.74	<0.05	...	0.02

[a]H- and V-polarization observations averaged.

Nederlandse samenvatting

Gas rond lage-massa stervorming

Waarnemingen met het Herschel Ruimte Observatorium en vanaf de aarde

Abstract

Gas- en stofdeeltjes in de omgeving van pas gevormde protosterren absorberen de straling van deze bronnen. De zogenaamde *jonge stellaire objecten* (YSO's, ~1 Zonsmassa) zijn hierdoor onmogelijk met optische of infrarood telescopen waar te nemen. Deze koude objecten kunnen echter dankzij de recente ontwikkelingen in de technologie toch waargenomen worden via lange golflengten zoals de millimeter (mm) en submillimeter (submm) golflengten. Waarnemingen op basis van moleculaire spectroscopie bij mm golflengten stelt ons in staat de moleculen te lokaliseren en hun abundanties te meten. Het is bovendien ook mogelijk om zowel de kinematische gegevens van de omliggende omhulsels als de protostellaire straalstromen te detecteren. Koolstofmonoxide (CO) staat bekend als het tweede meest abundante molecuul in het interstellaire medium (ISM) na moleculair waterstof (H_2). Met zijn simpele niveau structuur en de verschillende isotopologen (^{13}CO, $C^{18}O$, $C^{17}O$) is het met mm/submm telescopen dankzij de rotationele overgangen van CO mogelijk om relatief eenvoudig veel informatie te vergaren over deze objecten. Waar met H_2 gebieden met hoge kinetische temperaturen van een paar honderd tot een paar duizend graden Kelvin, zoals geschokt gas, waar te nemen zijn, kunnen we met CO de door protostellaire straalstromen opgeveegde gassen detecteren met een temperatuur van rond de 100 K. Mm en submm moleculaire spectroscopische waarnemingen zijn één van de belangrijkste instrumenten om koude en donkere gebieden in het heelal te observeren.

Inleiding tot stervorming

Het interstellaire medium bestaat bij benadering uit 99% gas en 1% stof in massaverhouding. Ruwweg 90% van dit gas (in deeltjes aantal) is in de vorm van waterstof (H
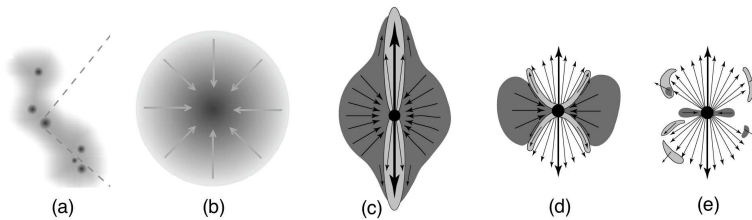
Figuur 1 – (a) Donkere moleculaire wolken. (b) Dichte kernen in moleculaire wolken beginnen ineen te storten om sterren te vormen. (c) Fase 0; de eerste van de vier stervormingsfases. Er zijn krachtige jets aanwezig. (d) Fase 1; de jets verliezen hun kracht en een accretieschijf is aan het vormen. (e) Fase 2; de jets zijn nu geheel verdwenen evenals de omhulsels en een protoplanetaire schijf is ontstaan.

of H_2), 8% is in de vorm van helium (He) en 1 á 2% bestaat uit zwaardere elementen zoals zuurstof (O), koolstof (C) en stikstof (N). Twee krachten in het heelal spelen een belangrijke rol in de geboorte en de dood van de hemelse objecten. Dit is ten eerste de zwaartekracht, die de neiging heeft om al het materiaal samen te persen en ten tweede de (thermische) druk, die ernaar streeft om al het interstellaire materiaal in de tegengestelde richting uit elkaar te drijven. Aan het begin van stervorming moet de zwaartekracht de thermische druk overwinnen opdat een gaswolk ineen kan storten. Zodra dit proces begint, zal al het materiaal naar het centrum beginnen te vloeien. Volgens de ideale gaswet kunnen we begrijpen dat dit met name gebeurt in de koudste plekken van de gaswolk. De enige gebieden die in het interstellaire medium dicht genoeg zijn voor de zwaartekracht om de relatief zwakke thermische druk (door de lage temperatuur) te overwinnen en dus het stervormingproces te starten, zijn de donkere moleculaire wolken.

De simpelste vormen van dit soort gaswolken zijn bolwolken (ook bekend als Bok globules). De temperaturen van bolwolken zijn circa 10 K, met een dichtheidsbereik van 10^3-10^4 cm^{-3} is hun massa typisch tussen de 10 en 100 Zonsmassa's. Terwijl bolwolken typische afmetingen hebben van een paar parsec, kunnen donkere wolken en wolk complexen aanzienlijk groter zijn met afmetingen van tientallen parsecs. Deze gebieden zijn de ideale locaties voor lage-massa stervorming.

Lage-massa stervorming

Lage-massa sterren worden gedefinieerd als sterren met een massa van minder dan 2 Zonsmassa's en een bolometrische helderheid minder dan 100 $L_\odot$. In Fig. 1 wordt de sequentie van lage-massa stervorming samengevat. Het koelere gas condenseert in sommige regio's tot de vorming van de iets dichtere gebieden (Fig. 1a). Gas en stofdeeltjes beginnen in de gecondenseerde gebieden ineen te storten onder de invloed van eigen zwaartekracht (Fig. 1b). De wolk van stof en gas vormt het omhulsel van waaruit accretie op de protosterren plaatsvindt. In dit stadium is de massa van het omringende omhulsel hoger dan de massa van de centrale protoster. De ineenstortende protoster zorgt voor een bipolaire mo-
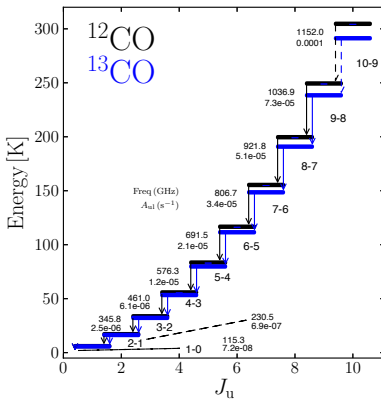
Figuur 2 – Rotatie-energie overgang diagram van koolstofmonoxide; ^{12}CO (zwart) en ^{13}CO (blauw). De stippellijnen gevn de waargenomen overgangenen met *Herschel*-HIFI. De frequentiewaarden aan de linkerkant zijn gegeven in GHz eenheden en de Einstein A coëfficiënten in s^{-1}. Zie Figuur 1.4 voor kleur versie.

leculaire straalstroom om het impulsmoment af te voeren en helpt zodoende het accretie proces (fase 0; Fig. 1c). Na verloop van tijd schakelt de straalstroom uit, maar de toevoer van materie zet door om een accretieschijf te vormen. In deze fase is de massa van het omringende omhulsel lager dan van de centrale protoster (fase 1; Fig. 1d). In de latere fasen schakelt de straalstroom helemaal uit en de resterende materie in het omringende omhulsel wordt ofwel geaccreteerd door de protoster of het vormt een circumstellaire schijf om planeten te vormen (fase 2; Fig. 1e). Deze classificatie wordt doorgaans bepaald door het meten van de spectrale energie distributie (SED) of door berekeningen van de bolometrische helderheid. Hoezeer de fasen ook op een dergelijke manier te onderscheiden zijn, er zijn nog veel vragen over het stervormingsproces.

Millimeter en submillimeter waarnemingen

Het principe achter de thermische camera is het omzetten van infrarood of submm straling in beeld. Deze straling wordt uitgezonden door verwarmde bronnen, zoals het warme stof rond jonge protosterren. Om dergelijke straling waar te kunnen nemen, moet de telescoop kouder zijn dan de bron zelf. De reden waarom moleculaire wolken donker zijn, is dat de aanwezige 1% stof zeer efficiënt is om bijna al het passerende licht te blokkeren ook al bestaat de moleculaire wolk uit 99% gas. Deze stofdeeltjes bestaan uit silicaten (zand) of grafiet (koolstofverbinding) die kleiner zijn dan 1 micrometer. Terwijl optische telescopen alleen kunnen constateren dat er een donkere wolk is, zijn submillimeter telescopen goed in staat om de thermische straling van dergelijke stoffige gebieden te observeren.

Moleculen zijn belangrijk voor de structuur van het ISM en ze spelen een belangrijke rol in de vorming van sterren en planeten door als koelmiddel voor het gas te fungeren. Door het observeren van moleculen krijgen we informatie over de fysische en chemische omstandigheden van hun verleden, heden en toekomst. Deze moleculen worden waarge-

nomen door hun discrete energie, waarbij de overgang tussen twee niveaus straling emit-teert of absorbeert die overeenkomt met een frequentie/golflengte die telescopen kunnen detecteren. Deze straling is uniek en is een soort vingerafdruk voor elk type molecuul.

Er zijn drie soorten overgangen die waargenomen kunnen worden. (*i*) Elektronische over-gangen; dit zijn de overgangen tussen de elektronische kwantumtoestanden in atomen of moleculen, wat leidt tot emissie of absorptie van straling in het zichtbare en het ultravio-lette (UV) deel van het spectrum. (*ii*) Vibrationele overgangen; deze zijn te wijten aan de vibrationele toestanden binnen elke elektronische toestand en treden op als gevolg van de oscillerende beweging van de kernen. Gassen met temperaturen rond de ~1000 K zenden straling uit bij infrarood golflengten. (*iii*) Rotationele overgangen; deze ontstaan door abrupte veranderingen in het impulsmoment van het molecuul en het koppel uitgeoefend op de moleculaire dipool. Gassen met temperaturen van <300 K zenden voornamelijk bij millimeter en submillimeter golflengten uit. In dit proefschrift worden de rotationele overgangen van de CO en O_2-moleculen gebruikt om de fysica en chemie van de protos-tellaire omgevingen te karakteriseren.

De CO-molecuul is het tweede meest voorkomende molecuul in het interstellaire medium na H_2. Het heeft een zeer eenvoudig niveau structuur (afb. 2) en verschillende observeer-bare isotopologen (^{13}CO, $C^{18}O$, $C^{17}O$). CO-moleculen zijn detecteerbaar bij mm/submm golflengten. De spectraallijnen traceren het dichte moleculaire gas in het omhulsel, dat de kinematische kenmerken van ineenstorting laat zien, en het hoge snelheid gas in de protostellaire straalstromen. Één van de belangrijkste toepassingen van de CO-molecuul is om het opgeveegde gas door de protostellaire straalstromen te karakteriseren waar de temperatuur over het algemeen relatief laag is (rond honderd graden Kelvin). CO-kaarten worden daarom veel gebruikt om de fysische eigenschappen van deze straalstromen te identificeren. $C^{18}O$ lijnen worden voornamelijk gebruikt om de sluimerende gas omhul-sels te onderzoeken, terwijl ^{13}CO een goede tracer blijkt te zijn voor het gas dat verhit is door UV straling (afb. 3).

In dit proefschrift zijn waarnemingen van verschillende grond- en ruimtetelescopen ge-bruikt om protostellaire omgevingen te bestuderen. De waarnemingen in de ruimte zijn gecentreerd rondom de Herschel Space Observatory, terwijl de grondwaarnemingen ver-richt zijn met de Atacama Pathfinder Experiment (APEX), de James Clerk Maxwell tele-scoop (JCMT), de IRAM 30m telescoop, en de Onsala 20m radiotelescoop.

De *Herschel* Space Observatory is een hoeksteenmissie van European Space Agency (ESA) die erop gericht is om het heelal bij ver-infrarood en submillimeter golflengten te bestuderen. De telescoop heeft een Cassegrain ontwerp met een primaire spiegel van 3.5 meter diameter. Dit is de grootste spiegel die ooit gebouwd en gelanceerd is naar de ruimte voor astronomische doeleinden. De drie wetenschappelijke instrumenten (HIFI, PACS en SPIRE), die de verschillende golflengten bestrijken, bevinden zich in het cryo-vacuüm van de helium container. In dit proefschrift wordt voornamelijk het HIFI-instrument ge-bruikt. HIFI (heterodyne instrument voor het ver-infrarood) is een zeer hoge resolutie heterodyne spectrometer die gevoelig is voor de frequenties in het bereik 480–1250 GHz en 1410–1910 GHz (157 tot 625 micrometer). Het is gebouwd door een consortium van

instituten onder leiding van SRON, Stichting Ruimte Onderzoek Nederland.

Het Atacama Pathfinder Experiment (APEX) is een 12 meter submillimeter telescoop op een hoogte van 5100 meter op Llano de Chajnantor in Chili. Het heeft verschillende instrumenten die werken bij frequenties vanaf ~200 GHz tot 1 THz. In dit proefschrift hebben we vooral het CHAMP$^+$ instrument gebruikt om de hoge-J CO lijnen ($J_{up} = 6$ tot 8) waar te nemen. De state-of-the-art technologie gecombineerd met de uitstekende atmosferische omstandigheden op locatie maakt het een ideaal instrument om hoogfrequente moleculaire overgangen te observeren.

De James Clerk Maxwell telescoop (JCMT) is een 15 meter submillimeter telescoop op een hoogte van 4092 meter op Mauna Kea, Hawaii. De twee instrumenten, de HARP-B 16-pixel ontvanger bij 345 GHz en de 1-pixel ontvanger A, zijn in dit proefschrift vooral gebruikt om de lage-J CO lijnen (bijv. 3–2 en 2–1) waar te nemen.

Zoals te zien is in Fig. 3 hebben lage-massa jonge stellaire objecten verschillende waarneembare componenten tijdens hun vorming. Het complex bestaat uit een bipolaire moleculaire straalstroom, zeer krachtige en sterk gebundelde stralen (jets), de centrale protoster en het omliggende omhulsel. De dichtheidsstructuur en het temperatuurprofiel van het omhulsel wordt gedefinieerd als een machtswet. Dit komt doordat bij een ineenstorting van een gaswolk zich een verloop ontwikkelt waarbij de dichtheid en temperatuur stijgen van buiten naar binnen. Zeer sterke jets en winden barsten uit vanaf beide polen van de protoster en de binnenste delen van de schijf die het materiaal in het omhulsel wegblazen in de vorm van een gecollimeerde straalstroom. Deze straalstromen zijn belangrijk bij het afvoeren van het impulsmoment en helpen de efficiëntie van het accretie proces. De interactie van de straalstroom met het omringende omhulsel verhit het materiaal welke leidt tot de vorming van vele soorten moleculen.

Warm gas

Zoals eerder vermeld wordt CO al jarenlang gezien als één van de beste tracers voor onderzoek naar de fysische structuur van jonge stellaire objecten. Doordat zeer droge locaties voor telescopen in het verleden niet beschikbaar waren en de technologie maar beperkte mogelijkheden bood, was het alleen maar mogelijk om de lagere rotatie-overgangen van CO (koud gas, < 50 K) te onderzoeken. Onlangs is het dankzij de komst van ruimtetelescopen, ontwikkelingen in hoge-technologie ontvangers en uitstekende droge waarneemlocaties mogelijk geworden om hogere-J CO rotatie-overgangen waar te nemen die hogere energieën afbakenen. Dit stelt ons in staat de temperaturen en de kolomdichtheden te kwantificeren door warm (100–150 K) en heet (>150 K) gas te karakteriseren.

Middels het gebruik van de efficiënte mapping mogelijkheden van het multi-pixel APEX-CHAMP$^+$ instrument werden de eerste grootschalige kaarten van jonge stellaire objecten gemaakt bij hoge frequenties (bijv. CO $J = 6$–5 en 7–6 overgangen). In Fig. 4 wordt de grootschalige kaart van twee nabijgelegen protosterren, NGC1333 IRAS 4A en IRAS 4B,

207
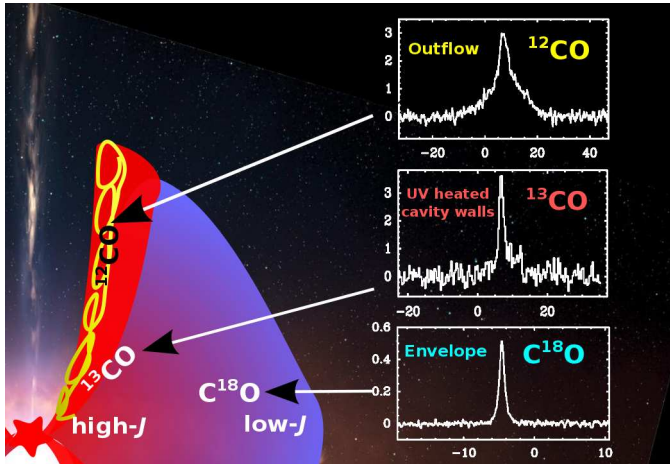
Figuur 3 – Anatomie van een protoster en zijn omgeving. In het centrum is de protoster weergegeven met jet, in paars de omhulsels van gas en stof, in rood de 'cavity walls' achter de jets. Zie Figuur 1.5 voor kleur versie.
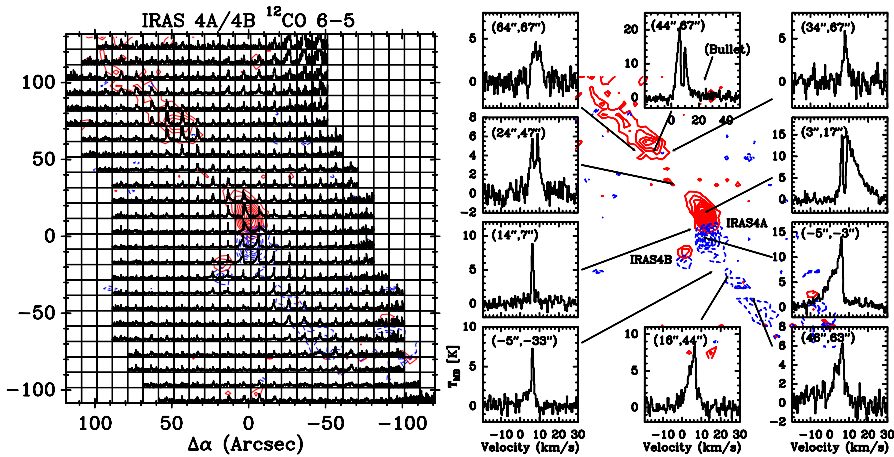
Figuur 4 – De figuur rechts toont de ^{12}CO 6–5 spectrale kaart van de NGC1333 IRAS 4A en IRAS 4B protosterren genomen met APEX-CHAMP$^+$. De figuur links toont de uitvergrote kaarten door in te zoomen op enkele van deze regio's. Zie Figuur 4.1 en 4.3 voor kleur versie.

in de ^{12}CO 6–5 overgang afgebeeld. Op de afbeelding links vertegenwoordigt elk vierkant een regio van $10'' \times 10''$ (2350 AU $\times$ 2350 AU). Het is dan ook duidelijk dat de straalstroom een afstand afgelegd heeft van zo'n 25000 AU (1 AU = afstand Zon-Aarde). Op de afbeelding rechts zijn enkele spectra van de linker afbeelding uitvergroot om de intensiteit van de CO emissie weer te geven samen met de kinematische gegevens. Veel van de spectra kunnen worden ontleed in twee onafhankelijke Gaussische profielen die verschillende fysische mechanismen van de emissie aanduiden. Spectra met lijnbreedtes
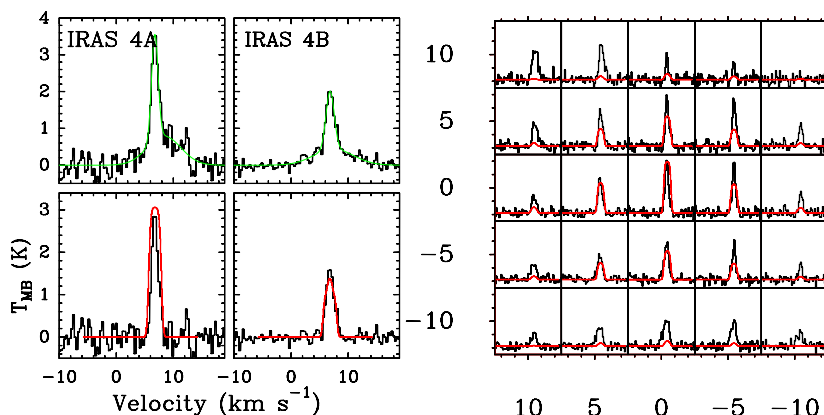
Figuur 5 – Aan de linkerkant zijn de ^{13}CO 6–5 centrum spectra van de protosterren IRAS 4A en IRAS 4B afgebeeld. De bovenpanelen tonen met de groene lijn een fit over de spectrum die is samengesteld uit twee Gaussische functies. In de onderpanelen is met de rode lijn te zien dat de modellen met de stralingstransport code van de sluimerende gas omhulsels overeenkomen met de waarnemingen. Aan de rechterkant zijn de spectra van de naaste omgeving van IRAS 4A met daaroverheen in rood de model spectra ter vergelijking weergegeven. Zie Figuur 4.18 en 4.19 voor kleur versie.

van enkele km/s duiden op straling van het gas in het sluimerende omhulsel. Daarentegen geeft een spectrum met een lijnbreedte van 15–25 km/s aan dat de emissie afkomstig moet zijn uit het hoge snelheid straalstroom gas.

De geïntegreerde intensiteit van de blauw en roodverschoven delen van de spectra worden afzonderlijk berekend om de grootte, locatie en richting van de straalstroom te vinden. In tegenstelling tot de IRAS 4A protoster die een sterk gecollimeerde straalstroom heeft, toont IRAS 4B een veel kleinere straalstroom en duidt dus op een bijna face-on inclinatie. Kortom, hoog frequente CO rotatie-overgangen zijn zeer nuttig voor het karakteriseren van het warme gas dat geassocieerd is met jonge stellaire objecten.

Belang van UV straling

Met de hoge-*J* overgangen van CO die we verkregen hebben met de hoge resolutie data, zijn we in staat om te bepalen waar elke type gas zich bevindt. Tegelijkertijd hebben we met behulp van de *J*=(6–5) overgang van de CO isotoop ^{13}CO de centrale regionen en omgevingen van de protosterren gedetecteerd met APEX. Wat vertelt deze lijn ons over de fysische processen?

In de bovenpanelen van Fig. 5 tonen we de spectra op de exacte positie van de protosterren IRAS 4A en IRAS 4B. Over de spectra heen zijn de fits met twee Gaussische functies in het groen weergegeven. Van deze spectra zijn de Gaussische fits met een wijde lijnbreedte
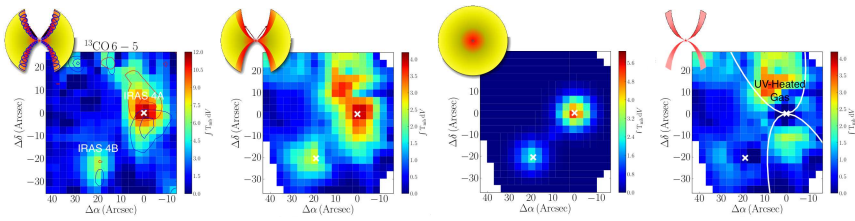
Figuur 6 – Waargenomen ^{13}CO 6–5 spectraallijn-kaarten van de NGC1333 IRAS 4A en de IRAS 4B protos-terren. (a) de waargenomen straling (b) het sluimerende gas na verwijdering van jets (c) de gemodelleerde gas omhulsels (d) bewijs van UV verwarmde 'cavity walls'. Zie Figuur 6 voor kleur versie.

die de outflows vertegenwoordigen afgetrokken (zie de zwarte lijnen in de onderpanelen van Fig. 5a). Het resterende nauwe lijn spectrum is afkomstig van de wanden van de holte die de jets en outflows in het omhulsel hebben gemaakt, de *cavity walls*. In hetzelfde onderzoek hebben we middels de veel minder abundante $C^{18}O$ lijnen ($^{12}CO/C^{18}O$)=540 vs $^{12}CO/^{13}CO$=65) de sluimerende gas omhulsels gemodelleerd. Voor deze modellen zijn de $C^{18}O$ J=(1–0) tot en met de met Herschel geobserveerde J=(9–8) en J=(10–9) lijnen gebruikt en is met de stralingstransport code `RATRAN` de hoeveelheid van het sluimerende gas en de abondantie van CO gemodelleerd.

In de onderpanelen van Fig. 5a worden in het rood de modelresultaten van het waarge-nomen gas in het omhulsel getoond. Met behulp van hetzelfde model, zie Fig. 5b, is het omhulsel in de directe omgeving van de protoster IRAS 4A te zien. Hieruit blijkt dat de intensiteit van de lijnen rond de protoster hoger ligt dan die van de modellen, m.a.w., er is nog een fysisch proces aanwezig dat tot nu toe niet is meegenomen in de modellen. We postuleren dat dit het gas is dat verwarmd wordt door UV straling in de wanden van de holte. Dit warme gas in de 'cavity walls' kan kwantitatief zichtbaar worden gemaakt door de volgende stappen toe te passen: (a) directe waarnemingen van de ^{13}CO 6–5 spec-traallijnen van het gebied, (b) de breede Gaussische fit van de spectra af te trekken, (c) de bijdrage van het omhulsel te bepalen door het $C^{18}O$ model toe te passen op ^{13}CO met het stralingstransport model `RATRAN`, en (d) deze modellen van de resterende straling af te trekken. Het blijkt dat er zich rond de wanden van de holtes die door de straalstromen zijn gevormd zich een grote hoeveelheid warm gas bevindt. Zoveel zelfs dat wanneer de massa van het gas aan de wanden berekend wordt, het blijkt dat deze bijna evenveel is als de massa van het opgeveegde gas door de straalstromen. Aan de hand van deze waarnemingen hebben we de eerste directe bewijzen geleverd van het door UV straling verwarmde gas in de 'cavity walls'.

Conclusie

In dit proefschrift hebben we dankzij de technologische ontwikkelingen antwoorden kun-nen geven op een aantal vragen, maar stervorming blijft nog steeds een onvolledig opge-

lost probleem. Door de technische verbeteringen in het mm/submm regime die nodig zijn om het binnenste van koude, donkere moleculaire wolken door te dringen en de productie van arrays van telescopen (interferometers zoals ALMA), zullen de huidige vragen ongetwijfeld op zijn tijd weer plaats maken voor nieuwere vragen. In deze studie hebben we geprofiteerd van de hoogfrequente CO waarnemingen die we met de Herschel ruimtetelescoop en de op een hoogte van 5100 meter bevindende hoge resolutie mapping APEX telescoop verkregen hebben. Door middel van ^{12}CO waarnemingen waren we in staat de locatie en de intensiteit van outflows te identificeren. We hebben met onze ^{13}CO waarnemingen de eerste directe bewijzen geleverd van door UV straling verwarmde 'cavity walls' van het gas gelegen rond de jets en via C^{18}O de abondantie van CO in het omhulsel bepaald.

Türkçe özet

Düşük Kütleli Yıldız Oluşumunda Gaz[1]

## *Herschel Uzay Gözlemevi ve Yer Tabanlı Gözlemsel Taramalar*

Özet

Henüz yeni oluşmakta olan ilkel yıldızların (protostars) çevresinde bulunan çok miktardaki soğuk gaz ve toz parçacıkları, gelen ışınımın soğurulmasına neden olur. Bu nedenle düşük kütleli ($\sim 1\,\mathrm{M}_\odot$) ilkel yıldızları optik veya kırmızı-ötesi dalgaboylarında tespit etmek imkansızdır. Ancak, bu tür soğuk cisimleri daha uzun dalga boylarında yani milimetre veya milimetre-altı (mm-/altı) dalga-boylarında gözlemek ancak son birkaç on yıldır gelişmekte olan teknoloji ile mümkün olmuştur. Mm-/altı bölgede yapılan molekül tayf gözlemleri bu bölgelerdeki yoğun gaz moleküllerinin var-lığını ve bolluğunu tespit etmemize yardımcı olur. Bununla beraber, ilkel yıldız çevresinde bulunan zarfın yıldız üzerine hareketi ile ilgili kinematik bilgilerin yanı sıra, bu sırada meydana gelen ilkel yıldız fışkırmalarını gözlemlememizi sağlar. Örneğin, CO molekülü yıldızlararası ortamda H_2'den sonra en yüksek bolluğa sahip molekül olarak bilinir. Basit yapısıyla ve izotopologlarıyla birlikte ($^{13}CO, C^{18}O, C^{17}O$) rotasyonel geçişlerinin de kolayca uyarılması sonucu mm–/altı bölgelerde göz-lemlenip bu tür soğuk bölgeler hakkında geniş bilgi verir. H_2 molekülü sıcaklıkları binlerce Kelvin derecede bulunan şoklanmış gazı ölçerken, CO ilkel yıldızlardaki moleküler fışkırmalar neticesiyle süpürülen, sıcaklığı çok daha az olan gazı (~ 100 K) incelememize olanak sağlar. Mm-/altı molekül tayf gözlemleri böylelikle evrendeki soğuk ve karanlık bölgelerin araştırılmasında en önemli araç olarak öne çıkmaktadır.

Yıldız oluşumu

Yıldızlar arasında bulunan bölgeye yıldızlararası ortam (Interstellar Medium - ISM) adı verilir. Bu ortamda bulunan madde kütlesel olarak karşılaştırıldığında yaklaşık %99'u gaz

---

[1] Bu Türkçe özet 18. Ulusal Astronomi Kongresi'nde (Malatya, 27-31 Ağustos 2012) gerçekleştirilen davetli konuşmanın bildirisi olarak yayınlanmıştır ancak birkaç düzeltme de içerir. Detayları *Publications* bölümünde bulabilirsiniz.
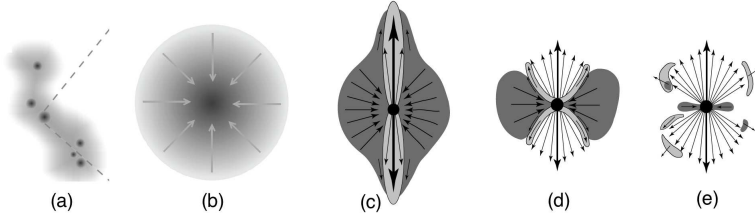
Şekil 1 – (a) Karanlık molekül bulutları. (b) Bulutun içerisinde bir yoğunlaşma bölgesi yıldız oluşturmak üzere çökmeye başlıyor. (c) Class 0 denen ilk gömülü safha; yüksek şiddette fışkırmalar var (d) Class I safhası; fışkırmaların gücü azalıp birikim (accretion) diski oluşmaya başlar. (e) Fışkırmalar artık tamamen durur ve gezegen oluşturan disk meydana gelir.

ve %1'i toz halindedir. Bu gazın da sayıca %90'ı Hidrojen (H veya H_2), %8'i Helyum (He) ve ~%1-2'si ağır elementlerden oluşur. Yıldızların doğumunu, yaşamını ve ölümünü belirleyen iki kuvvetten birincisi maddeyi merkeze doğru çökmeye zorlayan kütleçekim kuvveti ve diğeri de yıldızlararası maddeyi dışarı doğru itmeye zorlayan basınç kuvvetidir. Yıldız oluşumunun ilk safhalarında, yıldızın çökebilmesi için kütleçekiminin basınçtan daha baskın olması gerekir. Böyle olduğunda madde yoğun merkeze doğru akmaya başlar. İdeal gaz yasasına göre düşük basınca sahip bölgeler olabildiğince soğuk bölgelerdir. Yıldızlararası ortamda yıldız oluşumunu başlatacak denli yoğunluğa ve çok düşük sıcaklığa sahip bölgelere karanlık molekül bulutlar (dark molecular clouds) adı verilir. Bu tür bulutların en basiti Bok bulutlarıdır ve buralarda sıcaklıklar ~10 K, yoğunluklar 10^3-10^4 cm^{-3} olup, kütleleri de 10 $M_\odot$ ile 100 $M_\odot$ arasında değişim gösterebilir. Bok bulutları birkaç parsek büyüklüğünde olabilirken, karanlık molekül bulutlar da birkaç on parsek genişliğinde olabilir. Bu tür bölgeler yıldız oluşumu için en uygun bölgelerdir.

Düşük kütleli yıldız oluşumu

Düşük kütleli yıldızlar, kütlesi 5 $M_\odot$'den ve bolometrik parlaklığı 100 $L_\odot$'den az olan yıldızlar olarak tanımlanır. Şekil 1'de küçük kütleli yıldız oluşum (low-mass star formation) süreci özetlenmiştir. Karanlık moleküler bulut içerisinde madde, bazı bölgelerde kümelenerek ortama göre biraz daha yoğun bölgeler meydana getirir (Şekil 1a). Bulutta bulunan gaz ve toz parçacıkları kütleçekimi vasıtasıyla bu küme bölgelerde çökmeye başlarlar (Şekil 1b). Bu gaz ve toz bulutu aynı zamanda merkezdeki ilkel yıldıza madde aktarılan zarfı da oluşturur. Bu zarfın kütlesi henüz merkezindeki ilkel yıldızın kütlesinden daha fazladır. Çökmekte olan merkezdeki ilkel yıldız, üzerindeki fazla açısal momentumdan kurtulmak için çift kutuplu moleküler fışkırma meydana getirir (Class 0, Şekil 1c). Zamanla madde aktarımı bir birikim (accretion) diski vasıtasıyla devam eder ve fışkırmalar azalır. Bu safhada artık zarfın kütlesi merkezdeki ilkel yıldızın kütlesinden daha düşüktür (Class I, Şekil 1d). Daha ileri safhada artık fışkırmalar tamamen durur, çevresindeki zarf ya ilkel yıldıza aktarılır ya da birikim diskinde gezegenleri oluşturmak üzere dönmeye devam eder (Class II, Şekil 1e). Class 0, I, II şeklinde sınıflandırma biçimi
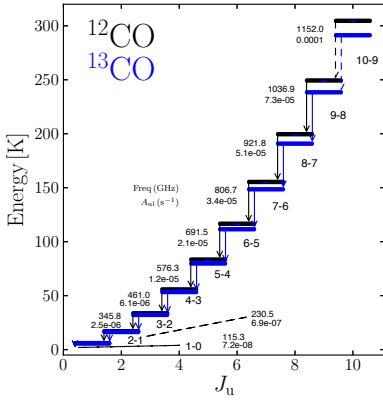
Şekil 2 – Karbonmonoksit molekülünün ^{12}CO (siyah) ve ^{13}CO (mavi) için gösterilen rotasyonel enerji geçişi diyagramı. Kesikli çizgi ile gösterilen geçişler *Herschel*-HIFI tarafından gözlemlenmiştir. Solda görülen frekans değerleri GHz ve Einstein *A* katsayıları da sn^{-1} cinsinden verilmiştir. Değerler JPL, CDMS ve LAMDA veritabanlarından alınmıştır. Bu resmin renkli versiyonunu Resim 1.4'te bulabilirsiniz.

Lada (1999) tarafından yüzlerce ilkel yıldızın tayfsal enerji dağılımı incelenerek oluşturulmuştur. Bu şekilde birkaç farklı safha tanımlanmış olsa da yıldız oluşumu hala tam olarak açıklanamamış bir problem olmaya devam etmektedir.

Milimetre ve milimetre-altı gözlemler

Bilindiği üzere termal kameralar kırmızı-ötesi ışınımı görüntüye dönüştürerek çalışır. Kırmızı-ötesi ışınım da aslında ısıdan kaynaklanan bir ışınımdır. Özellikle bu ışınımı gözlemek istiyorsak teleskobumuz gözlemek istediğimiz cisimden daha soğuk olmalıdır. Moleküler bulutların karanlık görünmesinin nedeni, %99 oranında gazdan meydana gelmesinden ziyade bu ortamda toz parçacıklarının etkin olmasındandır. Bu toz parçacıkları 1 mikrondan çok daha küçük olan silikatlar (kum) veya karbon bileşikleri olan grafitten ibarettir. Her ne kadar yıldızlararası ortamın sadece %1'ini meydana getirse de toz, optik dalgaboyundaki bütün ışınımı soğurma konusunda yeteneklidir. Milimetre-altı ışınım da boyutları yaklaşık 0.1 mikrometre olan bu toz parçacıklarından yayılır.

Atom ve moleküllerde üç çeşit enerji geçişi gerçekleşir ve her bir geçiş belli bir frekansa ve enerjiye karşılık gelir. Bunlar; optik dalgaboylarında görülen elektronik geçişler, yakın kırmızı-ötesi dalgaboylarında görülen titreşimsel (vibrasyonel) geçişler ve milimetre ve milimetre-altı dalgaboylarında görülen dönme (rotasyonel) geçişleridir. Moleküllerin rotasyonel geçişlerinde diğer geçiş türlerine göre enerji çok az olduğundan, sıcaklığı 10 ile 250 K arasında değişen çok soğuk bölgeleri gözlemek mümkündür. Bu geçişler de optik bölgede olduğu gibi salınım ve soğurma çizgi tayfları oluşturarak yıldızlararası ortamın fiziksel ve kimyasal yapısı hakkında önemli bilgiler verirler.

Bu çizgilerin enerjisi çok düşük olduğundan bize gelen sinyal de bir o kadar zayıftır. Bu frekans aralığının astronomide önemli bir ihtiyaç olduğu anlaşıldığı sıralarda gökcisimlerinden gelen zayıf sinyalleri güçlendirip bize sunacak bir teknoloji mevcut değildi.
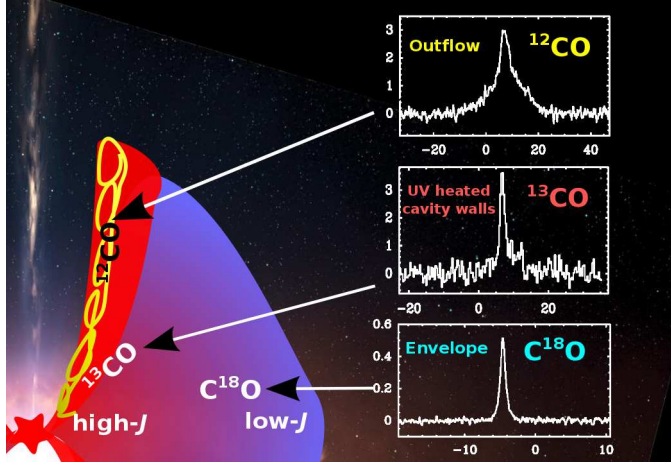
215

Yakın-kırmızı-öte (near-IR) dalgaboyları bile optik teleskoplarla gözlenebiliyorken, uzak-kırmızı-öte (far-IR) ve milimetre-altı (0.1–1 mm) için geliştirilmiş bir teknoloji yoktu. Ancak radyo bölgesinde yıllardan beri süren gelişmelerin sonucunda çok güçlü alıcılar yapılabilmişti. Milimetre-altı tam bu iki bölgenin arasında yer aldığından dolayı optik ve radyoyu birleştirip melez teknoloji (heterodyne technique) meydana getirildi. Teleskop aynası aynı optikteki gibi pürüzsüz olmakla beraber teleskoba gelen sinyaller bir radyo dalgası gibi yükseltilebildi. Yapılan şey, gökcisminden gelen sinyalin teleskoptaki dedektörden yayınlanan sabit bir sinyal ile çarpılıp radyo dalgalarının bulunduğu bölgeye karşılık getirilmesiydi. Böylece elde edilen sinyal düşük frekansta ancak gökcisminden gelen tüm bilgiler de korunarak işleme hazır hale getirildi.

Yıldız oluşumunun ilk sahneleri soğuk ve karanlık moleküler bulutlardaki gaz ve tozun içerisine gömülü olduğundan ancak uzun dalga boyunda çalışan teleskoplar tarafından çeşitli molekülleri kullanarak dolaylı olarak gözlemlenir. Bu ortamlardaki moleküller de ortamın ısınması ve/veya soğumasında büyük öneme sahiptir. Biz de bu molekülleri gözleyerek bu ortamlardaki fiziksel ve kimyasal yapı hakkında bilgi sahibi olabiliyoruz. Yıldızlararası ortamda bugüne kadar 170'den fazla molekül keşfedilmiştir. Her bir molekül, sahip olduğu kendine özgü enerji geçişleri sonucu oluşan tayflar yoluyla bize farklı bilgiler verir. Örneğin siyanür (CN ve HCN) bu bölgelerdeki UV ışınımı hakkında bilgi verirken, karbonmonosülfid (CS) ortamın yoğunluğu hakkında bilgi verir. Silisyumoksit (SiO) özellikle yüksek hızlı jetleri bulmamıza yardım ederken, karbonmonoksit (CO veya HCO, HCO$^+$) farklı sıcaklıklardaki bölgeleri bulmamıza yardım eder.

Özellikle CO yıllardır yıldızların ilk doğum anları olan ilkel yıldızları araştırmak için kullanılıyor. CO'nun en önemli özelliği yıldızlararası ortamda hidrojen gazından sonra ikinci en çok bolluğa sahip molekül olmasının yanında (her CO molekülüne karşılık 10 000 H$_2$ molekülü) rotasyonel geçiş enerjileri 5 K (J=1–0) gibi çok düşük bir değerden başlar. Milimetre-altı astronomlarının enerji birimi olarak Kelvin kullanması buraya önemli bir not olarak düşülebilir. Karbonmonoksitin her bir geçişi farklı bir bilgi verdiğinden neredeyse her bir geçiş için ayrı bir teleskop yapılmış durumdadır. Örneğin J=(1–0) geçişi İsveç'teki Onsala Radyoteleskobuyla, J=(2–1) İspanya'daki IRAM 30 metre teleskobuyla, J=(2–1), (3–2), (4–3) için Hawaii'deki James Clerk Maxwell Teleskoplarıyla gözlenebiliyor. Daha yüksek geçişler için daha yüksek ortamlara çıkmak gerekiyor. J=(6–5) ve (7–6) için Şili'deki APEX teleskobu kullanılırken daha sonrası için artık atmosfer dışına yada uzaya gidilmesi gerekiyor. İşte bu noktada *Herschel*-HIFI imdadımıza yetişiyor ve yüksek-J'ye sahip geçişleri ve dolayısıyla daha yüksek sıcaklıkları gözlemleyebiliyoruz.

Bu çalışmada kullanılan mm-/altı teleskopları aşağıda sıralanmıştır; *Herschel* Uzay Gözlemevi (*Herschel* Space Observatory) bir ESA/NASA görevi olup, 3.5 metrelik ayna çapıyla bugüne kadar uzaya gönderilen en büyük aynaya sahip uzay teleskobudur. Toplam 3.5 yıl ömür biçilen *Herschel*, 14 Mayıs 2009 yılında fırlatılmış olup Dünya'dan yaklaşık 1.5 milyon km uzaklıkta L2 Lagrange noktasında yer alır ve Dünya ile eşzamanlı olarak Güneş çevresinde hareketini sürdürür. Gözlem dalgaboyu uzun-kırmızı-öte (far-IR) ile milimetre-altı dalgaboyu arasındadır. Bu çalışmada kullanılan *Herschel*'in içerisinde yer alan 3 dedektörden biri olan HIFI, 476 GHz ile 1910 GHz arası gözlem yapma ye-

Şekil 3 – Bir ilkel yıldız ve çevresinin anatomisi. Merkezde jet fışkırtan ilkel yıldız (protostar), kırmızı-mavi ile gösterilen gaz ve tozdan meydana gelen zarfı, kırmızı ile gösterilen fışkırmaların ardında kalan kavite duvarları. Bu resmin renkli versiyonunu Resim 1.5'de bulabilirsiniz.

teneğine sahiptir. Atacama Pathfinder Experiment (APEX) teleskobu, Şili'nin Atacama Çölü'nde 5100 metre yükseklikte kurulmuş olup 12 metrelik çanak çapına sahiptir. Teleskopta bulunan CHAMP$^+$ adlı enstrüman 650/850 GHz arası yüksek frekans alıcısı, 2x7 piksel çözünürlüğü ve haritalama kabiliyeti ile dünyanın bu frekanslarda gözlem yapan en etkin dedektörlerinden biridir.

Gömülü Class 0 safhası

Şekil 3'te görüldüğü gibi küçük kütleli ilkel yıldızlar farklı fiziksel yapılardan meydana gelir. Bunlar arasında, çift kutuplu moleküler fışkırmalar, fışkırmayı sağlayan jetler, merkezde oluşmakta olan ilkel yıldız, çevresinde bulunan ilkel yıldıza madde sağlayan zarf ve onu da çevreleyen moleküler bulut ile kompleks bir yapıya sahiptir. İlkel yıldız zarfını merkezinden dışına doğru tanımlayan sıcaklık ve yoğunluk yapısı Güç Yasası (Power Law) ile ifade edilir (Jørgensen et al. 2002). Böylelikle sıcaklık ve yoğunluk çökme devam ettikçe dışarıdan içeriye doğru sürekli artma gösterir. İlkel yıldızın merkezine yakın bir bölgede geniş açılı ve yüksek hızlı rüzgarlar oluşmasıyla fazla olan açısal momentum taşınır. Bunun sonucu olarak da çift kutuplu moleküler fışkırmalar, akresyon diskine dik olarak yayıldığından merkezdeki ilkel yıldızın düzenli bir şekilde dönmesini ve akresyonun artmasını sağlar. Fışkırmaların yönünü Doppler yasası gereği bir kutbu maviye, diğer kutbu da kırmızıya kayma ile tespit edebiliriz. Fışkırmalar çok yüksek hızlarda olduğundan ortamı ısıtıp çevresindeki maddeyi etkiler ve çeşitli kimyasal tepkimeler vasıtasıyla yeni yeni moleküllerin oluşmasını sağlarlar (Snell et al. 1980, Bachiller & Tafalla 1999).

217
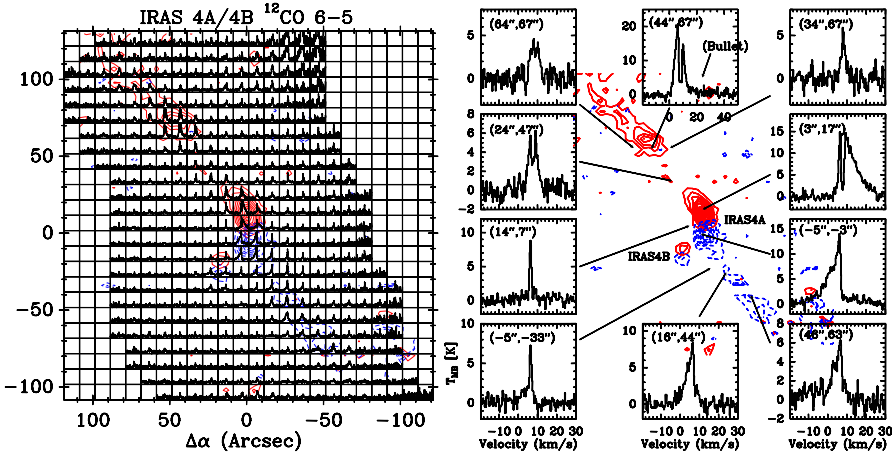
Şekil 4 – Sağda, NGC1333 IRAS 4A ve IRAS 4B ilkel yıldızlarının ^{12}CO 6–5 gözlemleri ile hazırlanan tayfsal haritası görülüyor. Solda, aynı haritadan bazı bölgelerin tayflarının büyütülmüş hali görülüyor (Yıldız et al. 2012). Bu resmin renkli versiyonunu Resim 4.1 ve 4.3'de bulabilirsiniz.

Sıcak gaz

Daha önceden belirtildiği üzere CO, yıllardır ilkel yıldızların fiziksel yapısını incelemek için çok iyi bir araç olarak kullanılıyor. Teknolojinin ve ideal gözlem merkezlerinin elverdiği ölçüde günümüze kadar yapılan tüm araştırmalar genelde CO'nun düşük rotasyonel geçişleri ($J_{up} \leq 3$) ile yapılan gözlemler neticesinde elde edilmişti (Blake et al. 1995, Shirley et al. 2002). Böylelikle soğuk gaz (<50 K) içeren bölgeler incelenebiliyordu. Ancak günümüzde yerden yada uzaydan yeni yeni gerçekleştirilen yüksek frekans gözlemleri, CO'nun yüksek rotasyonel geçişlerini gözlememize olanak sağladı. Bununla beraber, soğuk gazın yanında artık ılık (100 K–150 K) veya sıcak gazın (>150 K) da karakterize edilmesiyle bu tür cisimlerin sıcaklık ve kolon yoğunlukları çok daha iyi tespit edilebilir oldu.

APEX teleskobunun CHAMP$^+$ dedektörünün hızlı ve etkin harita yapabilme kabiliyeti ile ilk defa ilkel yıldız çevrelerinin yüksek frenkanslarda (CO'nun J=6–5 ve 7–6 geçişlerinin) haritaları elde edilmeye başlandı (van Kempen et al. 2009b, Yıldız et al. 2012). Şekil 4'de bize uzaklığı 235 parsek olan NGC 1333 IRAS 4A ve IRAS 4B adlı iki ilkel yıldızın bu teleskoptan ^{12}CO 6–5 geçişi ile gözlenmiş haritası sunulmuştur. Burada her bir karecik yaklaşık 10"×10" yaysaniyesi genişliğinde olup dolayısıyla 2350 AB×2350 AB (AB: Astronomik Birim) büyüklüğünde bir bölgeyi temsil eder. Böylelikle fışkırmaların boyutlarının yaklaşık 20 000 - 30 000 AB kadar çok geniş bir bölgeyi kapladığını görebiliriz. Tek çanak (single dish) milimetre teleskoplarından bugün itibariyle bu frekanslarda elde edilen en iyi çözünürlüğü APEX teleskobu sunar ve bir pikselin boyutu 8" mertebesindedir. Şekil 4 solda verilen tayfsal haritada ilkel yıldızın etrafındaki CO ışınımını niceliksel olarak bölge bölge ölçebilme olanağına kavuşuyoruz. Elde edilen

tayfların yüksek çözünürlüğü vasıtasıyla belli bölgelerdeki tayflara bir yada birkaç Gauss fiti yaparak çözümleyebiliyoruz. Bu fitler ilkel yıldıza ait ortamda farklı fiziksel bileşenleri incelemeye olanak tanır. Çizgi genişliği birkaç km/s olan bileşenler düşük hıza sahip durgun gazı (quiescent envelope gas) tespit etmeye olanak sağlarken, genişlikleri 15-25 km s^{-1} olan bileşenler yüksek hızlı fışkırmalar neticesinde ilerleyen gazı (outflowing gas) gösterir.

Elde edilen salınım tayfının ayrı ayrı maviye veya kırmızıya kayan bölgelerinin altında kalan alanı (integrated intensity) hesapladığımızda yüksek hıza sahip fışkırmaların boyutunu ve yönünü tespit edebiliriz. Şekil 4 *sağda* da bazı özel bölgelerin tayflarının büyütülmüş hali verilmiştir.

IRAS 4A ilkel yıldızı çok yüksek kolimasyona sahip fışkırmalar oluştururken, IRAS 4B ilkel yıldızı bundan çok daha az fışkırma gösteriyor. CO'nun düşük-J'ye sahip çizgilerinde çözünürlük çok daha düşük olduğundan ancak bu yeni gözlemler ile IRAS 4B ilkel yıldız fışkırmalarının yönünün bize doğru olduğunu (face-on inclination) tespit edebildik.
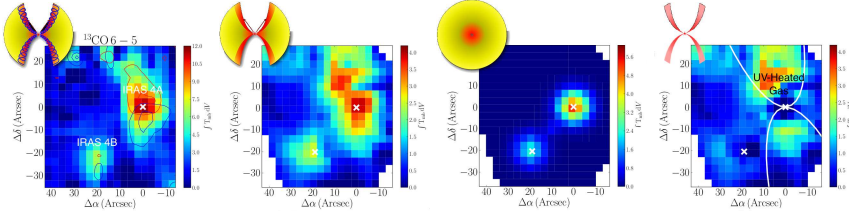
UV ile ısınan kavite duvarları

Elde edilen yüksek çözünürlüklü veri ile CO'nun yüksek geçişleri bize hangi tür gazın nerede bulunduğunu tespit etmemize olanak sağlar. APEX ile aynı zamanda CO'nun izotopologu olan ^{13}CO $J=(6–5)$ sayesinde aynı ilkel yıldızların merkez bölgelerini ve yakın çevresinin de gözlemleri yapılabildi (Şekil 6a). ^{12}CO/^{13}CO bolluk oranı 65'tir. Şekil 5'te üst hücrelerde IRAS 4A ve IRAS 4B ilkel yıldızlarının tam merkezlerinden alınan tayflar verilmiştir. Tayflar üzerinde iki Gauss fiti yeşil ile gösterilmiştir. Bunlardan geniş çizgi genişliğine sahip Gauss fiti fışkırmaları temsil ettiğinden dolayı gözlenen tayftan çıkarılmıştır (Şekil 5a'da alt hücrelerde siyah olarak gösterilen). Geriye kalan dar çizgi genişliğine sahip tayf, ilkel yıldız zarfından ve fışkırmaların ardında kalan kavite duvarlarından gelen ışıma neticesinde oluşmuştur. Aynı çalışmada bolluğu çok daha düşük olan C^{18}O çizgileri ($X(^{12}$CO$)/X($C^{18}O$)=540$) kullanılarak durgun zarf gazının modellemesi yapılmıştır. Modelleme için C^{18}O çizgilerinin $J=(1–0)$'dan, *Herschel* ile gözlenen $J=(9–8)$ ve (10–9)'a kadar olan çizgileri kullanılmış ve RATRAN (Hogerheijde & van der Tak 2000) ışınım transfer model kodu (radiative transfer code) kullanılarak durgun gazın miktarı modellenmiştir.

Şekil 5a'da alt hücrelerde gözlemlenen durgun gaza ait tayfın üzerinde kırmızı ile modelleme sonuçları gösterilmiştir. Şekil 5b'de aynı model kullanılarak IRAS 4A ilkel yıldızının yakın çevresindeki durgun gazın dağılımı görülüyor. Burada ilkel yıldızın çevresindeki tayfın yeğinliğinin modelden daha fazla olduğu dikkat çekiyor. Buradan hareketle Şekil 6'da aslında bir nevi matematiksel bir işlem yaparak, fışkırmaların ardında kalan kavite duvarlarında bulunan gazı niceliksel olarak ölçebildik. (6a) Bölgenin ^{13}CO 6–5 ile direk gözlemlerinden, (6b) yukarıda açıklandığı üzere bütün tayflardan geniş çizgi genişliğine sahip Gauss fitleri çıkarılıp arta kalan ışınım bulunmuştur. (6c) RATRAN ile yapılan ışınım transferi modeli, (6d) de 6c'den çıkarıldığında arta kalan ışınımı verir. Görüldüğü
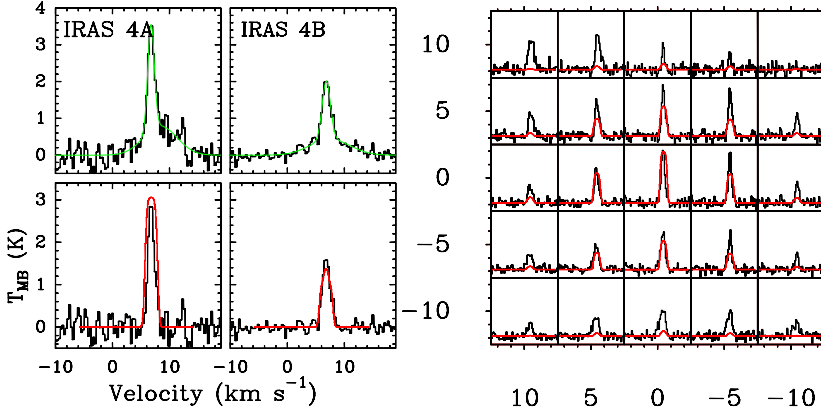
Şekil 5 – Solda, IRAS 4A ve IRAS 4B ilkel yıldızlarının merkezlerinden alınan ^{13}CO 6–5 tayfı. Üstte yeşil ile tayfa yapılan iki Gauss fiti görülüyor. Altta ise ışınım transfer kodu ile modellenen zarfın gözlemlerle uygunluğu görülüyor. Sağda ise sadece IRAS 4A'nın yakın çevresinin tayfı ve model tayfı üst üste konarak karşılaştırılıyor (Yıldız et al. 2012). Bu resmin renkli versiyonunu Resim 4.18 ve 4.19'de bulabilirsiniz.

Şekil 6 – NGC1333 IRAS 4A ve IRAS 4B ilkel yıldızlarının ^{13}CO 6–5 ile gözlemlenmiş haritası. (a) Gözlenen ışınım, (b) fışkırmalar çıkarılıp kalan durgun gaz, (c) zarfın modellenmiş görüntüsü, (d) UV ile ısınan kavite duvarlarının ilk gözlemsel kanıtı elde edildi.

üzere fışkırmaların kavite duvarlarında (outflow cavity walls) çok yüksek oranda gazın kaldığı ortaya çıkmaktadır. Hatta bu gazın kütlesi hesaplandığında, fışkırmalarla itilen gazın kütlesi ile neredeyse aynı olduğu bulundu. Bu gözlemler sonucu UV ışınımı ile ısınan gazın ilk direk gözlemsel kanıtını elde etmiş olduk.

Sonuç

Gelişen teknoloji ile birlikte birçok yeni sorulara ve cevaplara ulaştığımız yıldız oluşumu hala tam olarak açıklanamamış bir problem olmaya devam etmektedir. Soğuk ve karanlık moleküler bulutlarının içerisine ancak uzun dalga boyları ile ulaşılabildiğinden milimetre ve milimetre-altı teknolojisindeki gelişmeler, uygun gözlem yerlerinin bulunması ve dizge teleskoplarının (interferometre) üretilmesiyle bu sorular kuşkusuz zamanla yerini daha yeni sorulara bırakacaktır. Bu çalışmada, uzay-konuşlu *Herschel* Gözlemevinden ve 5100

metre yükseklikte bulunmasının avantajı ile yüksek çözünürlüklü haritalama kabiliyetini birleştiren APEX teleskobundan alınan yüksek frekans CO gözlemlerinden faydalandık. ^{12}CO gözlemleri ile fışkırmaların yerlerini ve miktarını tespit edebildik. ^{13}CO gözlemleri ile fışkırmaların ardında kalan kavite duvarlarında bulunan UV ışınımı ile ısınan gazın ilk direk gözlemsel kanıtını elde etmiş olduk.

Bibliography

Acharyya, K., Fuchs, G. W., Fraser, H. J., van Dishoeck, E. F., & Linnartz, H. 2007, A&A, 466, 1005

Alonso-Albi, T., Fuente, A., Crimier, N., et al. 2010, A&A, 518, A52

Andersson, S. & van Dishoeck, E. F. 2008, A&A, 491, 907

André, P. & Montmerle, T. 1994, ApJ, 420, 837

André, P., Ward-Thompson, D., & Barsony, M. 2000, Protostars & Planets IV, 59

Arasa, C., Andersson, S., Cuppen, H. M., van Dishoeck, E. F., & Kroes, G.-J. 2010, J. Chem. Phys., 132, 184510

Arce, H. G., Borkin, M. A., Goodman, A. A., Pineda, J. E., & Halle, M. W. 2010, ApJ, 715, 1170

Arce, H. G. & Sargent, A. I. 2006, ApJ, 646, 1070

Arce, H. G., Shepherd, D., Gueth, F., et al. 2007, Protostars and Planets V, 245

Ayotte, P., Scott, S. R., Stevenson, K. P., et al. 2001, J. Geophys. Res., 106, 33387

Bachiller, R., Liechti, S., Walmsley, C. M., & Colomer, F. 1995, A&A, 295, L51

Bachiller, R., Martin-Pintado, J., Tafalla, M., Cernicharo, J., & Lazareff, B. 1990, A&A, 231, 174

Bachiller, R. & Perez Gutierrez, M. 1997, ApJ, 487, L93

Bachiller, R. & Tafalla, M. 1999, in NATO ASIC Proc. 540: The Origin of Stars and Planetary Systems, ed. C. J. Lada & N. D. Kylafis, 227

Benedettini, M., Busquet, G., Lefloch, B., et al. 2012, A&A, 539, L3

Bergin, E. A. & Langer, W. D. 1997, ApJ, 486, 316

Bergin, E. A., Langer, W. D., & Goldsmith, P. F. 1995, ApJ, 441, 222

Bergin, E. A., Melnick, G. J., Stauffer, J. R., et al. 2000, ApJ, 539, L129

Bergin, E. A. & Snell, R. L. 2002, ApJ, 581, L105

Bergin, E. A. & Tafalla, M. 2007, ARA&A, 45, 339

Bjerkeli, P., Liseau, R., Larsson, B., et al. 2012, A&A, 546, A29

Black, J. H. & Smith, P. L. 1984, ApJ, 277, 562

Blake, G. A., Sandell, G., van Dishoeck, E. F., et al. 1995, ApJ, 441, 689

Bontemps, S., André, P., Terebey, S., & Cabrit, S. 1996, A&A, 311, 858

Bottinelli, S., Ceccarelli, C., Williams, J. P., & Lefloch, B. 2007, A&A, 463, 601

Bourke, T. L., Garay, G., Lehtinen, K. K., et al. 1997, ApJ, 476, 781

Brown, D. W. & Chandler, C. J. 1999, MNRAS, 303, 855

Buckle, J. V., Hills, R. E., Smith, H., et al. 2009, MNRAS, 399, 1026

Cabrit, S. & Bertout, C. 1990, ApJ, 348, 530

Cabrit, S. & Bertout, C. 1992, A&A, 261, 274

Carty, D., Goddard, A., Kohler, S., Sims, I., & Smith, I. 2006, J. Phys. Chem. A, 110, 3101

Caselli, P. & Ceccarelli, C. 2012, A&A Rev., 20, 56

Ceccarelli, C., Caselli, P., Herbst, E., Tielens, A. G. G. M., & Caux, E. 2007, Protostars and Planets V, 47

Chen, H., Myers, P. C., Ladd, E. F., & Wood, D. O. S. 1995, ApJ, 445, 377

Chiang, H., Looney, L. W., Tassis, K., Mundy, L. G., & Mouschovias, T. C. 2008, ApJ, 680, 474

Choi, M., Kang, M., Tatematsu, K., Lee, J.-E., & Park, G. 2011, PASJ, 63, 1281

Collings, M. P., Anderson, M. A., Chen, R., et al. 2004, MNRAS, 354, 1133

Collings, M. P., Dever, J. W., Fraser, H. J., McCoustra, M. R. S., & Williams, D. A. 2003, ApJ, 583, 1058

Congiu, E., Fedoseev, G., Ioppolo, S., et al. 2012, ApJ, 750, L12

Cuppen, H. M. & Herbst, E. 2007, ApJ, 668, 294

Cuppen, H. M., Ioppolo, S., Romanzin, C., & Linnartz, H. 2010, Phys. Chem. Chem. Phys., 12, 12077

Curtis, E. I., Richer, J. S., & Buckle, J. V. 2010a, MNRAS, 401, 455

Curtis, E. I., Richer, J. S., Swift, J. J., & Williams, J. P. 2010b, MNRAS, 408, 1516

de Graauw, T., Helmich, F. P., Phillips, T. G., et al. 2010, A&A, 518, L6

Dent, W., Duncan, W., Ellis, M., et al. 2000, in Astronomical Society of the Pacific Conference Series, Vol. 217, Imaging at Radio through Submillimeter Wavelengths, ed. J. G. Mangum & S. J. E. Radford, 33

Desmurs, J.-F., Codella, C., Santiago-García, J., Tafalla, M., & Bachiller, R. 2009, A&A, 498, 753

Di Francesco, J., Johnstone, D., Kirk, H., MacKenzie, T., & Ledwosinska, E. 2008, ApJS, 175, 277

Downes, T. P. & Cabrit, S. 2007, A&A, 471, 873

Drouin, B. J., Yu, S., Miller, C. E., et al. 2010, J. Quant. Spectrosc. Rad. Trans., 111, 1167

Du, F., Parise, B., & Bergman, P. 2012, A&A, 538, A91

Dunham, M. M., Arce, H. G., Allen, L. E., et al. 2013, ArXiv: 1301.4416

Dunham, M. M., Evans, II, N. J., Terebey, S., Dullemond, C. P., & Young, C. H. 2010, ApJ, 710, 470

Enoch, M. L., Evans, II, N. J., Sargent, A. I., & Glenn, J. 2009, ApJ, 692, 973

Evans, N. J., Dunham, M. M., Jørgensen, J. K., et al. 2009, ApJS, 181, 321

Franklin, J., Snell, R. L., Kaufman, M. J., et al. 2008, ApJ, 674, 1015

Fuente, A., Caselli, P., McCoey, C., et al. 2012, A&A, 540, A75

Fuller, G. A. & Ladd, E. F. 2002, ApJ, 573, 699

Garrod, R. T. & Herbst, E. 2006, A&A, 457, 927

Garrod, R. T., Wakelam, V., & Herbst, E. 2007, A&A, 467, 1103

Garrod, R. T., Weaver, S. L. W., & Herbst, E. 2008, ApJ, 682, 283

Giannini, T., Nisini, B., & Lorenzetti, D. 2001, ApJ, 555, 40

Goicoechea, J. R., Cernicharo, J., Karska, A., et al. 2012, A&A, 548, A77

Goldsmith, P. F., Liseau, R., Bell, T. A., et al. 2011, ApJ, 737, 96

Goldsmith, P. F., Melnick, G. J., Bergin, E. A., et al. 2000, ApJ, 539, L123

Goldsmith, P. F., Snell, R. L., Erickson, N. R., et al. 1985, ApJ, 289, 613

Goldsmith, P. F., Snell, R. L., Hemeon-Heyer, M., & Langer, W. D. 1984, ApJ, 286, 599

Green, J., Evans, N., Jørgensen, J., et al. 2013; subm., ApJ

Greene, T. P., Wilking, B. A., André, P., Young, E. T., & Lada, C. J. 1994, ApJ, 434, 614

Gregersen, E. M., Evans, II, N. J., Zhou, S., & Choi, M. 1997, ApJ, 484, 256

Griffin, M. J., Abergel, A., Abreu, A., et al. 2010, A&A, 518, L3

Gueth, F., Guilloteau, S., & Bachiller, R. 1996, A&A, 307, 891

Güsten, R., Baryshev, A., Bell, A., et al. 2008, in SPIE Conference Series, Vol. 7020

Gutermuth, R. A., Myers, P. C., Megeath, S. T., et al. 2008, ApJ, 674, 336

Habart, E., Dartois, E., Abergel, A., et al. 2010, A&A, 518, L116

Harsono, D., Visser, R., Bruderer, S., et al. subm., A&A

Hasegawa, T. I. & Herbst, E. 1993, MNRAS, 261, 83

Hatchell, J. & Fuller, G. A. 2008, A&A, 482, 855

Hatchell, J., Fuller, G. A., & Richer, J. S. 2007, A&A, 472, 187

Hatchell, J., Richer, J. S., Fuller, G. A., et al. 2005, A&A, 440, 151

Hayashi, C., Hoshi, R., & Sugimoto, D. 1962, Progress of Theoretical Physics Supplement, 22, 1

Hayashi, M., Hasegawa, T., Ohashi, N., & Sunada, K. 1994, ApJ, 426, 234

Herbst, E. & Klemperer, W. 1973, ApJ, 185, 505

Herbst, E. & van Dishoeck, E. F. 2009, ARA&A, 47, 427

Herczeg, G. J., Karska, A., Bruderer, S., et al. 2012, A&A, 540, A84

Hirota, T., Bushimata, T., Choi, Y. K., et al. 2008, PASJ, 60, 37

Ho, P. T. P. & Barrett, A. H. 1980, ApJ, 237, 38

Hogerheijde, M. R. & van der Tak, F. F. S. 2000, A&A, 362, 697

Hogerheijde, M. R., van Dishoeck, E. F., Blake, G. A., & van Langevelde, H. J. 1997, ApJ, 489, 293

Hogerheijde, M. R., van Dishoeck, E. F., Blake, G. A., & van Langevelde, H. J. 1998, ApJ, 502, 315

Hollenbach, D., Kaufman, M. J., Bergin, E. A., & Melnick, G. J. 2009, ApJ, 690, 1497

Ioppolo, S., Cuppen, H. M., Romanzin, C., van Dishoeck, E. F., & Linnartz, H. 2008, ApJ, 686, 1474

Ivezić, Z. & Elitzur, M. 1997, MNRAS, 287, 799

Jennings, R. E., Cameron, D. H. M., Cudlip, W., & Hirst, C. J. 1987, MNRAS, 226, 461

Johnstone, D., Boonman, A. M. S., & van Dishoeck, E. F. 2003, A&A, 412, 157

Johnstone, D., Hendricks, B., Herczeg, G. J., & Bruderer, S. 2013, ArXiv: 1301.7341

Jørgensen, J. K., Bourke, T. L., Myers, P. C., et al. 2007, ApJ, 659, 479

Jørgensen, J. K., Bourke, T. L., Myers, P. C., et al. 2005a, ApJ, 632, 973

Jørgensen, J. K., Schöier, F. L., & van Dishoeck, E. F. 2002, A&A, 389, 908

Jørgensen, J. K., Schöier, F. L., & van Dishoeck, E. F. 2004, A&A, 416, 603

Jørgensen, J. K., Schöier, F. L., & van Dishoeck, E. F. 2005b, A&A, 437, 501

Jørgensen, J. K., Schöier, F. L., & van Dishoeck, E. F. 2005c, A&A, 435, 177

Jørgensen, J. K., van Dishoeck, E. F., Visser, R., et al. 2009, A&A, 507, 861

Karska, A., Herczeg, G. J., van Dishoeck, E. F., et al. 2013, ArXiv: 1301.4821

Kasemann, C., Güsten, R., Heyminck, S., et al. 2006, in SPIE Conference Series, Vol. 6275

Kauffmann, J., Bertoldi, F., Bourke, T. L., Evans, II, N. J., & Lee, C. W. 2008, A&A, 487, 993

Kennicutt, R. C. & Evans, N. J. 2012, ARA&A, 50, 531

Kenyon, S. J., Hartmann, L. W., Strom, K. M., & Strom, S. E. 1990, AJ, 99, 869

Klein, B., Philipp, S. D., Krämer, I., et al. 2006, A&A, 454, L29

Knee, L. B. G. & Sandell, G. 2000, A&A, 361, 671

Kristensen, L. E. & van Dishoeck, E. F. 2011, Astronomische Nachrichten, 332, 475

Kristensen, L. E., van Dishoeck, E. F., Bergin, E. A., et al. 2012, A&A, 542, A8

Kristensen, L. E., van Dishoeck, E. F., Tafalla, M., et al. 2011, A&A, 531, L1

Kristensen, L. E., Visser, R., van Dishoeck, E. F., et al. 2010, A&A, 521, L30

Lacy, J. H., Knacke, R., Geballe, T. R., & Tokunaga, A. T. 1994, ApJ, 428, L69

Lada, C. J. 1987, in IAU Symposium, Vol. 115, Star Forming Regions, ed. M. Peimbert & J. Jugaku, 1–17

Lada, C. J. 1999, in NATO ASIC Proc. 540: The Origin of Stars and Planetary Systems, ed. C. J. Lada & N. D. Kylafis, 143

Lada, C. J. & Wilking, B. A. 1984, ApJ, 287, 610

Langer, W. D. & Penzias, A. A. 1990, ApJ, 357, 477

Larsson, B., Liseau, R., Pagani, L., et al. 2007, A&A, 466, 999

Lay, O. P., Carlstrom, J. E., & Hills, R. E. 1995, ApJ, 452, L73

Lee, C.-F., Mundy, L. G., Stone, J. M., & Ostriker, E. C. 2002, ApJ, 576, 294

Lee, J.-E., Bergin, E. A., & Evans, II, N. J. 2004, ApJ, 617, 360

Lefloch, B., Cabrit, S., Codella, C., et al. 2010, A&A, 518, L113

Lefloch, B., Castets, A., Cernicharo, J., & Loinard, L. 1998, ApJ, 504, L109

Lemke, D. 2008, Sterne und Weltraum, January, p36

Lin, S. Y., Guo, H., Honvault, P., Xu, C., & Xie, D. 2008, J. Chem. Phys., 128

Lique, F. 2010, J. Chem. Phys., 132, 044311

Liseau, R., Goldsmith, P. F., Larsson, B., et al. 2012, A&A, 541, A73

Liseau, R., Sandell, G., & Knee, L. B. G. 1988, A&A, 192, 153

Lommen, D., Jørgensen, J. K., van Dishoeck, E. F., & Crapsi, A. 2008, A&A, 481, 141

Looney, L. W., Mundy, L. G., & Welch, W. J. 2000, ApJ, 529, 477

Loren, R. B. 1976, ApJ, 209, 466

Loren, R. B. 1989, ApJ, 338, 902

Maloney, P. & Black, J. H. 1988, ApJ, 325, 389

Manoj, P., Watson, D. M., Neufeld, D. A., et al. 2013, ApJ, 763, 83

McKellar, A. 1940, PASP, 52, 187

Melnick, G. J., Stauffer, J. R., Ashby, M. L. N., et al. 2000, ApJ, 539, L77

Melnick, G. J., Tolls, V., Goldsmith, P. F., et al. 2012, ApJ, 752, 26

Micono, M., Davis, C. J., Ray, T. P., Eisloeffel, J., & Shetrone, M. D. 1998, ApJ, 494, L227

Mokrane, H., Chaabouni, H., Accolla, M., et al. 2009, ApJ, 705, L195

Muñoz Caro, G. M., Jiménez-Escobar, A., Martín-Gago, J. Á., et al. 2010, A&A, 522, A108

Müller, H. S. P., Schlöder, F., Stutzki, J., & Winnewisser, G. 2005, Journal of Molecular Structure, 742, 215

Myers, P. C., Evans, II, N. J., & Ohashi, N. 2000, Protostars and Planets IV, 217

Myers, P. C. & Ladd, E. F. 1993, ApJ, 413, L47

Neininger, N., Guélin, M., Ungerechts, H., Lucas, R., & Wielebinski, R. 1998, Nature, 395, 871

Neufeld, D. A. & Dalgarno, A. 1989, ApJ, 340, 869

Nisini, B., Benedettini, M., Codella, C., et al. 2010, A&A, 518, L120

Nisini, B., Santangelo, G., Antoniucci, S., et al. 2013, A&A, 549, A16

Nordh, H. L., von Schéele, F., Frisk, U., et al. 2003, A&A, 402, L21

Öberg, K. I., Linnartz, H., Visser, R., & van Dishoeck, E. F. 2009a, ApJ, 693, 1209

Öberg, K. I., van Broekhuizen, F., Fraser, H. J., et al. 2005, ApJ, 621, L33

Öberg, K. I., van Dishoeck, E. F., & Linnartz, H. 2009b, A&A, 496, 281

Ossenkopf, V. & Henning, T. 1994, A&A, 291, 943

Ott, S. 2010, in Astronomical Society of the Pacific Conference Series, Vol. 434, Astronomical Data Analysis Software and Systems XIX, ed. Y. Mizumoto, K.-I. Morita, & M. Ohishi, 139

Pagani, L., Langer, W. D., & Castets, A. 1993, A&A, 274, L13

Pagani, L., Olofsson, A. O. H., Bergman, P., et al. 2003, A&A, 402, L77

Parise, B., Belloche, A., Leurini, S., et al. 2006, A&A, 454, L79

Pickett, H. M., Poynter, R. L., Cohen, E. A., et al. 2010, Journal of Quantitative Spectroscopy & Radiative Transfer, 111, 1617

Pilbratt, G. L., Riedinger, J. R., Passvogel, T., et al. 2010, A&A, 518, L1

Plume, R., Bergin, E. A., Phillips, T. G., et al. 2012, ApJ, 744, 28

Poglitsch, A., Waelkens, C., Geis, N., et al. 2010, A&A, 518, L2

Ridge, N. A., Di Francesco, J., Kirk, H., et al. 2006, AJ, 131, 2921

Roberts, H. & Herbst, E. 2002, A&A, 395, 233

Robitaille, T. P., Whitney, B. A., Indebetouw, R., Wood, K., & Denzmore, P. 2006, ApJS, 167, 256

Roelfsema, P. R., Helmich, F. P., Teyssier, D., et al. 2012, A&A, 537, A17

Romanzin, C., Arzoumanian, E., Es-Sebbar, E., et al. 2010, Planet. Space Sci., 58, 1748

Ruffle, D. P. & Herbst, E. 2000, MNRAS, 319, 837

San José-García, I., Mottram, J. C., Kristensen, L. E., et al. 2013, ArXiv e-prints

Sandell, G., Aspin, C., Duncan, W. D., Russell, A. P. G., & Robson, E. I. 1991, ApJ, 376, L17

Sandell, G. & Knee, L. B. G. 2001, ApJ, 546, L49

Santangelo, G., Nisini, B., Giannini, T., et al. 2012, A&A, 538, A45

Saraceno, P., Andre, P., Ceccarelli, C., Griffin, M., & Molinari, S. 1996, A&A, 309, 827

Schöier, F. L., Jørgensen, J. K., van Dishoeck, E. F., & Blake, G. A. 2002, A&A, 390, 1001

Schöier, F. L., Jørgensen, J. K., van Dishoeck, E. F., & Blake, G. A. 2004, A&A, 418, 185

Schöier, F. L., van der Tak, F. F. S., van Dishoeck, E. F., & Black, J. H. 2005, A&A, 432, 369

Shen, C. J., Greenberg, J. M., Schutte, W. A., & van Dishoeck, E. F. 2004, A&A, 415, 203

Shirley, Y. L., Evans, II, N. J., & Rawlings, J. M. C. 2002, ApJ, 575, 337

Shirley, Y. L., Evans, II, N. J., Rawlings, J. M. C., & Gregersen, E. M. 2000, ApJS, 131, 249

Shu, F. H., Adams, F. C., & Lizano, S. 1987, ARA&A, 25, 23

Smith, H., Buckle, J., Hills, R., et al. 2008, in SPIE Conference Series, Vol. 7020

Smith, I. W. M., Herbst, E., & Chang, Q. 2004, MNRAS, 350, 323

Snell, R. L., Loren, R. B., & Plambeck, R. L. 1980, ApJ, 239, L17

Spaans, M., Hogerheijde, M. R., Mundy, L. G., & van Dishoeck, E. F. 1995, ApJ, 455, L167

Swings, P. & Rosenfeld, L. 1937, ApJ, 86, 483

Tachihara, K., Onishi, T., Mizuno, A., & Fukui, Y. 2002, A&A, 385, 909

Tafalla, M., Liseau, R., Nisini, B., et al. 2013, ArXiv: 1301.5322

Tafalla, M., Myers, P. C., Caselli, P., & Walmsley, C. M. 2004, A&A, 416, 191

Tafalla, M., Myers, P. C., Mardones, D., & Bachiller, R. 2000, A&A, 359, 967

Tafalla, M., Santiago-García, J., Hacar, A., & Bachiller, R. 2010, A&A, 522, A91

Tielens, A. G. G. M. & Hagen, W. 1982, A&A, 114, 245

Tobin, J. J., Hartmann, L., Calvet, N., & D'Alessio, P. 2008, ApJ, 679, 1364

Černis, K. 1990, Ap&SS, 166, 315

van der Marel, N., Kristensen, L. E., Visser, R., et al. 2013; subm., A&A

van der Tak, F. F. S., Black, J. H., Schöier, F. L., Jansen, D. J., & van Dishoeck, E. F. 2007, A&A, 468, 627

van der Werf, P. P., Isaak, K. G., Meijerink, R., et al. 2010, A&A, 518, L42

van Dishoeck, E. F. & Black, J. H. 1988, ApJ, 334, 771

van Dishoeck, E. F. & Blake, G. A. 1998, ARA&A, 36, 317

van Dishoeck, E. F., Kristensen, L. E., Benz, A. O., et al. 2011, PASP, 123, 138

van Dishoeck, E. F., van Kempen, T. A., & Güsten, R. 2009, in Astronomical Society of the Pacific Conference Series, Vol. 417, Submillimeter Astrophysics and Technology: a Symposium Honoring Thomas G. Phillips, ed. D. C. Lis, J. E. Vaillancourt, P. F. Goldsmith, T. A. Bell, N. Z. Scoville, & J. Zmuidzinas, 203

van Kempen, T. A., Green, J. D., Evans, N. J., et al. 2010a, A&A, 518, L128

van Kempen, T. A., Hogerheijde, M. R., van Dishoeck, E. F., et al. 2006, A&A, 454, L75

van Kempen, T. A., Kristensen, L. E., Herczeg, G. J., et al. 2010b, A&A, 518, L121

van Kempen, T. A., van Dishoeck, E. F., Güsten, R., et al. 2009a, A&A, 507, 1425

van Kempen, T. A., van Dishoeck, E. F., Güsten, R., et al. 2009b, A&A, 501, 633

van Kempen, T. A., van Dishoeck, E. F., Hogerheijde, M. R., & Güsten, R. 2009c, A&A, 508, 259

van Kempen, T. A., van Dishoeck, E. F., Salter, D. M., et al. 2009d, A&A, 498, 167

Vasta, M., Codella, C., Lorenzani, A., et al. 2012, A&A, 537, A98

Visser, R. & Dullemond, C. P. 2010, A&A, 519, A28

Visser, R., Kristensen, L. E., Bruderer, S., et al. 2012, A&A, 537, A55

Visser, R., van Dishoeck, E. F., Doty, S. D., & Dullemond, C. P. 2009, A&A, 495, 881

Vladilo, G., Centurion, M., & Cassola, C. 1993, A&A, 273, 239

Volgenau, N. H., Mundy, L. G., Looney, L. W., & Welch, W. J. 2006, ApJ, 651, 301

Walawender, J., Bally, J., Francesco, J. D., Jørgensen, J., & Getman, K. . 2008, NGC 1333: A Nearby Burst of Star Formation (Handbook of Star Forming Regions, Volume I: The Northern Sky ASP Monograph Publications, Vol. 4.), 346

Walter, F. M. 1987, PASP, 99, 31

Ward-Thompson, D., André, P., Crutcher, R., et al. 2007, Protostars and Planets V, 33

Weiss, A., Downes, D., Neri, R., et al. 2007a, A&A, 467, 955

Weiss, A., Downes, D., Walter, F., & Henkel, C. 2007b, in Astronomical Society of the Pacific Conference Series, Vol. 375, From Z-Machines to ALMA: (Sub)Millimeter Spectroscopy of Galaxies, ed. A. J. Baker, J. Glenn, A. I. Harris, J. G. Mangum, & M. S. Yun , 25

Wilson, R. W., Jefferts, K. B., & Penzias, A. A. 1970, ApJ, 161, L43

Wilson, T. L. & Rood, R. 1994, ARA&A, 32, 191

Woodall, J., Agúndez, M., Markwick-Kemper, A. J., & Millar, T. J. 2007, A&A, 466, 1197

Wright, E. L., Mather, J. C., Bennett, C. L., et al. 1991, ApJ, 381, 200

Xu, C., Xie, D., Honvault, P., Lin, S. Y., & Guo, H. 2007, Journal of Chemical Physics, 127

Yang, B., Stancil, P. C., Balakrishnan, N., & Forrey, R. C. 2010, ApJ, 718, 1062

Yıldız, U., Kristensen, L., van Dishoeck, E., et al. 2013; subm., A&A; DOI: 10.1051/0004-6361/201220849

Yıldız, U. A., Kristensen, L. E., van Dishoeck, E. F., et al. 2012, A&A, 542, A86

Yıldız, U. A., van Dishoeck, E. F., Kristensen, L. E., et al. 2010, A&A, 521, L40

Young, C. H. & Evans, II, N. J. 2005, ApJ, 627, 293

Publications

Refereed Publications

34. **Yıldız U. A.**; Kristensen, L. E.; van Dishoeck, E. F.; Belloche, A.; van Kempen, T. A.; Hogerheijde, M. R.; Guesten, R.; van der Marel, N.; *APEX-CHAMP$^+$ high-J CO observations of low–mass young stellar objects: III. NGC 1333 IRAS 4A/4B envelope, outflow and UV heating*; 2012, Astronomy & Astrophysics, Vol. 542, A86 [ADS]

33. **Yıldız, U. A.**; van Dishoeck, E. F.; Kristensen, L. E.; Visser, R.; Jørgensen, J. K.; Herczeg, G. J.; van Kempen, T. A.; Hogerheijde, M. R.; Doty, S. D.; Benz, A. O.; Bruderer, S.; Wampfler, S. F.; Deul, E.; Bachiller, R.; Baudry, A.; Benedettini, M.; Bergin, E.; Bjerkeli, P.; Blake, G. A.; Bontemps, S.; Braine, J.; Caselli, P.; Cernicharo, J.; Codella, C.; Daniel, F.; di Giorgio, A. M.; Dominik, C.; Encrenaz, P.; Fich, M.; Fuente, A.; Giannini, T.; Goicoechea, J. R.; de Graauw, Th.; Helmich, F.; Herpin, F.; Jacq, T.; Johnstone, D.; Larsson, B.; Lis, D.; Liseau, R.; Liu, F.-C.; Marseille, M.; McCoey, C.; Melnick, G.; Neufeld, D.; Nisini, B.; Olberg, M.; Parise, B.; Pearson, J. C.; Plume, R.; Risacher, C.; Santiago-García, J.; Saraceno, P.; Shipman, R.; Tafalla, M.; Tielens, A. G. G. M.; van der Tak, F.; Wyrowski, F.; Dieleman, P.; Jellema, W.; Ossenkopf, V.; Schieder, R.; Stutzki, J.; *Herschel/HIFI observations of high-J CO lines in the NGC 1333 low-mass star-forming region*; 2010, Astronomy & Astrophysics, Vol. 521, L40 [ADS]

32. **Yıldız, Umut A.**; Kristensen, L. E.; van Dishoeck, E. F.; San José-García, I.; Karska, A.; Harsono, D.; Tafalla, M.; Fuente, A.; Visser, R.; Jørgensen, J.; Hogerheijde, M.; *Water in low-mass star-forming regions with Herschel: High-J CO survey observed with HIFI*; submitted to Astronomy & Astrophysics (Chapter 3 in this thesis)

31. **Yıldız, Umut A.**; Acharyya, K.; Goldsmith, P. F.; van Dishoeck, E. F.; Melnick, G.; Liseau, R.; Chen, J-H.; Pagani, L.; Bergin, E.; Caselli, P.; Herbst, E.; Visser, R.; Gerin, M.; *Deep observations of O$_2$ toward a low-mass protostar with Herschel-HIFI*, To be submitted (Chapter 6 in this thesis).

30. San José-García, I; Mottram, J. C.; Kristensen L. E.; van Dishoeck E. F.; **Yıldız, U. A.**; van der Tak, F. F. S.; Herpin, F.; Visser, R.; McCoey, C.; Wyrowski, F.; Braine, J.; and Johnstone, D.; *Herschel-HIFI observations of high-J CO and isotopologues in star-forming regions: from low- to high-mass*; 2013, Astronomy & Astrophysics, in press [ADS]

29. Tafalla, M.; Liseau, R.; Nisini, B.; Bachiller, R.; Santiago-Garcia, J.; van Dishoeck, E. F.; Kristensen, L. E.; Herczeg G. J.; and **Yıldız, U. A.**; *High-pressure water in bipolar outflows, Results from a Herschel-WISH survey*; 2013, Astronomy & Astrophysics, in press [ADS]

28. Karska, A.; Herczeg, G. J.; van Dishoeck, E. F.; Wampfler, S. F.; Kristensen, L. E.; Goicoechea, J. R.; Visser, R.; Nisini, B.; San-Jose Garcia, I.; Bruderer, S.; Sniady, P.; Doty, S.; Fedele, D.; **Yıldız, U. A.**; Benz, A. O.; Bergin, E.; Caselli, P.; Herpin, F.; Hogerheijde, M. R.; Johnstone, D.; Jorgensen, J. K.; Liseau, R.; Tafalla, M.; van der Tak, F.; Wyrowski, F.; *Water in star forming regions with Herschel (WISH) III. Far-infrared cooling lines in low-mass young stellar objects* 2013, Astronomy & Astrophysics, in press [ADS]

27. Caselli, Paola; Keto, Eric; Bergin, Edwin A.; Tafalla, Mario; Aikawa, Yuri; Douglas, Thomas; Pagani, Laurent; **Yıldız, Umut A.**; van der Tak, Floris F. S.; Walmsley, C. Malcolm; Codella, Claudio; Nisini, Brunella; Kristensen, Lars E.; van Dishoeck, Ewine F.; *First detection of water vapor in a pre-stellar core*; The Astrophysical Journal Letters, 2012, Vol. 759, 37 [ADS]

26. Kristensen, L. E.; van Dishoeck, E. F.; Bergin, E. A.; Visser, R.; **Yıldız, U. A.**; San José-García, I.; Jørgensen, J. K.; Herczeg, G. J.; Johnstone, D.; Wampfler, S. F.; Benz, A. O.; Bruderer, S.; Cabrit, S.; Caselli, P.; Doty, S. D.; Harsono, D.; Herpin, F.; Hogerheijde, M. R.; Karska, A.; van Kempen, T. A.; Liseau, R.; Nisini, B.; Tafalla, M.; van der Tak, F.; Wyrowski, F.; *Water in star-forming regions with Herschel (WISH): II. Evolution of 557 GHz 1_{10}-1_{01} emission in low-mass protostars*; 2012, A&A, Vol. 542, A8 [ADS]

25. Fuente, A.; Caselli, P.; McCoey, C.; Cernicharo, J.; Johnstone, D.; Fich, M.; van Kempen, T.; van Dishoeck, E.; **Yıldız, U.**; Visser, R.; Kristensen, L.; Alonso-Albi, T.; Herpin, F.; Tisi, S.; *The abundance of $C^{18}O$ and HDO in the envelope and hot core of the intermediate mass protostar NGC 7129 FIRS 2*; 2012, A&A, Vol. 540, A75 [ADS]

24. Liseau, R.; Goldsmith, P. F.; Larsson, B.; Pagani, L.; Bergman, P.; Le Bourlot, J.; Bell, T. A.; Benz, A. O.; Bergin, E. A.; Bjerkeli, P.; Black, J. H.; Bruderer, S.; Caselli, P.; Caux, E.; Chen, J.-H.; de Luca, M.; Encrenaz, P.; Falgarone, E.; Gerin, M.; Goicoechea, J. R.; Hjalmarson, Å.; Hollenbach, D. J.; Justtanont, K.; Kaufman, M. J.; Le Petit, F.; Li, D.; Lis, D. C.; Melnick, G. J.; Nagy, Z.; Olofsson, A. O. H.; Olofsson, G.; Roueff, E.; Sandqvist, Aa.; Snell, R. L.; van der Tak, F. F. S.; van Dishoeck, E. F.; Vastel, C.; Viti, S.; **Yıldız, U. A.**; *Multi-line detection of O_2 toward ρ Oph A*; 2012, A&A, Vol. 541, A73 [ADS]

230

23. Herczeg, G. J.; Karska, A.; Bruderer, S.; Kristensen, L. E.; van Dishoeck, E. F.; Jørgensen, J. K.; Visser, R.; Wampfler, S. F.; Bergin, E. A.; **Yıldız, U.**; Pontoppidan, K. M.; Gracia-Carpio, J.; *Water in star-forming regions with Herschel: highly excited molecular emission from the NGC 1333 IRAS 4B outflow*; 2012, A&A, Vol. 540, A84 [ADS]

22. Roelfsema, P. R.; Helmich, F. P.; Teyssier, D.; Ossenkopf, V.; Morris, P.; Olberg, M.; Shipman, R.; Risacher, C.; and 90 co-authors incl.**Yıldız, U.**; *In-orbit performance of Herschel-HIFI*; 2012, Astronomy & Astrophysics, Vol. 537, A17 [ADS]

21. Hogerheijde, Michiel R.; Bergin, Edwin A.; Brinch, Christian; Cleeves, L. Ilsedore; Fogel, Jeffrey K. J.; Blake, Geoffrey A.; Dominik, Carsten; Lis, Dariusz C.; Melnick, Gary; Neufeld, David; Panić, Olja; Pearson, John C.; Kristensen, Lars; **Yıldız, Umut A.**; van Dishoeck, Ewine F.; *Detection of the Water Reservoir in a Forming Planetary System*; 2011, **Science**, Vol. 334 no. 6054 pp. 338-340 [ADS]

20. Goldsmith, Paul F.; Liseau, René; Bell, Tom A.; Black, John H.; Chen, Jo-Hsin; Hollenbach, David; Kaufman, Michael J.; Li, Di; Lis, Dariusz C.; Melnick, Gary; Neufeld, David; Pagani, Laurent; Snell, Ronald; Benz, Arnold O.; Bergin, Edwin; Bruderer, Simon; Caselli, Paola; Caux, Emmanuel; Encrenaz, Pierre; Falgarone, Edith; Gerin, Maryvonne; Goicoechea, Javier R.; Hjalmarson, Åke; Larsson, Bengt; Le Bourlot, Jacques; Le Petit, Franck; De Luca, Massimo; Nagy, Zsofia; Roueff, Evelyne; Sandqvist, Aage; van der Tak, Floris; van Dishoeck, Ewine F.; Vastel, Charlotte; Viti, Serena; **Yıldız, Umut**; *Herschel Measurements of Molecular Oxygen in Orion*; 2011, The Astrophysical Journal, Vol. 737, A96 [ADS]

19. Kristensen, L. E.; van Dishoeck, E. F.; Tafalla, M.; Bachiller, R.; Nisini, B.; Liseau, R.; **Yıldız, U. A.**; *Water in low-mass star-forming regions with Herschel (WISH-LM). High-velocity H_2O bullets in L1448-MM observed with HIFI*, 2010, A&A, Vol. 531, L1 [ADS]

18. van Dishoeck, E. F.; Kristensen, L. E.; Benz, A. O.; Bergin, E. A.; Caselli, P.; Cernicharo, J.; Herpin, F.; Hogerheijde, M. R.; Johnstone, D.; Liseau, R.; Nisini, B.; Shipman, R.; Tafalla, M.; van der Tak, F.; Wyrowski, F.; and 57 co-authors incl. **Yıldız, U. A.**; *Water in Star-forming Regions with the Herschel Space Observatory (WISH). I. Overview of Key Program and First Results*; 2011, PASP, 123, 138V [ADS]

17. Kristensen, L. E.; Visser, R.; van Dishoeck, E. F.; **Yıldız, U. A.**; Doty, S. D.; Herczeg, G. J.; Liu, F.-C.; Parise, B.; Jørgensen, J. K.; van Kempen, T. A.; Brinch, C.; Wampfler, S. F.; Bruderer, S.; Benz, A. O.; Hogerheijde, M. R.; Deul, E.; and the WISH Team; *Water in low-mass star-forming regions with Herschel: HIFI spectroscopy of NGC1333*; 2010, A&A, Vol. 521, L30 [ADS]

231

16. Caselli, P.; Keto, E.; Pagani, L.; Aikawa, Y.; **Yıldız, U. A.**; van der Tak, F. F. S.; Tafalla, M.; Bergin, E. A.; Nisini, B.; Codella, C.; van Dishoeck, E. F.; and the WISH Team; *Water vapor toward starless cores: the Herschel view*; 2010, A&A, Vol. 521, L29 [ADS]

15. Bergin, E. A.; Hogerheijde, M. R.; Brinch, C.; Fogel, J.; **Yıldız, U. A.**; Kristensen, L. E.; van Dishoeck, E. F.; Bell, T. A.; and the WISH Team; *Sensitive limits on the abundance of cold water vapor in the DM Tau protoplanetary disk*; 2010, A&A, Vol. 521, L33 [ADS]

14. Wampfler, S. F.; Herczeg, G. J.; Bruderer, S.; Benz, A. O.; van Dishoeck, E. F.; Kristensen, L. E.; Visser, R.; Doty, S. D.; Melchior, M.; van Kempen, T. A.; **Yıldız, U. A.**; Dedes, C.; Goicoechea, J. R.; Baudry, A.; Melnick, G.; and the WISH Team; *Herschel observations of the hydroxyl radical (OH) in young stellar objects*; 2010, A&A, Vol. 521, L36 [ADS]

13. Bruderer, S.; Benz, A. O.; van Dishoeck, E. F.; Melchior, M.; Doty, S. D.; van der Tak, F.; Stäuber, P.; Wampfler, S. F.; Dedes, C.; **Yıldız, U. A.**; Pagani, L.; Giannini, T.; de Graauw, Th.; and the WISH Team; *Herschel-HIFI detections of hydrides towards AFGL 2591 (Envelope emission versus tenuous cloud absorption)*; 2010, A&A, Vol. 521, L44 [ADS]

12. Johnstone, D.; Fich, M.; McCoey, C.; van Kempen, T. A.; Fuente, A.; Kristensen, L. E.; Cernicharo, J.; Caselli, P.; Visser, R.; Plume, R.; Herczeg, G. J.; van Dishoeck, E. F.; Wampfler, S.; and 48 co-authors incl. **Yıldız, U. A.**; *Herschel/HIFI spectroscopy of the intermediate mass protostar NGC 7129 FIRS 2*; 2010, A&A, Vol. 521, L41 [ADS]

11. Chavarría, L.; Herpin, F.; Jacq, T.; Braine, J.; Bontemps, S.; Baudry, A.; Marseille, M.; van der Tak, F.; Pietropaoli, B.; Wyrowski, F.; Shipman, R.; Frieswijk, W.; van Dishoeck, E. F.; Cernicharo, J.; and 48 co-authors incl. **Yıldız, U. A.**; *Water in massive star-forming regions: HIFI observations of W3 IRS5*; 2010, A&A, Vol. 521, L37 [ADS]

10. Benz, A. O.; Bruderer, S.; van Dishoeck, E. F.; Stäuber, P.; Wampfler, S. F.; Melchior, M.; Dedes, C.; Wyrowski, F.; Doty, S. D.; van der Tak, F.; and 59 co-authors incl. **Yıldız, U. A.**; *Hydrides in Young Stellar Objects: Radiation tracers in a protostar-disk-outflow system*; 2010, A&A, Vol. 521, L35 [ADS]

 9. Wyrowski, F.; van der Tak, F.; Herpin, F.; Baudry, A.; Bontemps, S.; Chavarría, L.; Frieswijk, W.; Jacq, T.; Marseille, M.; Shipman, R.; van Dishoeck, E. F.; and 54 co-authors incl. **Yıldız, U. A.**; *Variations in H_2O^+/H_2O ratios toward massive star-forming regions*; 2010, A&A, Vol. 521, L34 [ADS]

8. Marseille, M. G.; van der Tak, F. F. S.; Herpin, F.; Wyrowski, F.; Chavarría, L.; Pietropaoli, B.; 65 co-authors incl. **Yıldız, U. A.**; *Water abundances in high-mass protostellar envelopes: Herschel observations with HIFI*; 2010, A&A, Vol. 521, L32 [ADS]

7. Sturm, B.; Bouwman, J.; Henning, Th.; Evans, N. J.; Acke, B.; Mulders, G. D.; Waters, L. B. F. M.; van Dishoeck, E. F.; Meeus, G.; Green, J. D.; Augereau, J. C.; Olofsson, J.; Salyk, C.; Najita, J.; and 29 co-authors incl. **Yıldız, U. A.**; *First results of the Herschel key program "Dust, Ice and Gas In Time" (DIGIT): Dust and gas spectroscopy of HD 100546*; 2010, A&A, Vol. 518, L129 [ADS]

6. van Kempen, T. A.; Green, J. D.; Evans, N. J.; van Dishoeck, E. F.; Kristensen, L. E.; Herczeg, G. J.; MerŠn, B.; Lee, J.-E.; Jørgensen, J. K.; Bouwman, J.; and 35 co-authors incl. **Yıldız, U. A.**; *Dust, Ice, and Gas In Time (DIGIT) Herschel program first results. A full PACS-SED scan of the gas line emission in protostar DK Chamaeleontis*; 2010, A&A, Vol. 518, L128 [ADS]

5. van Kempen, T. A.; Kristensen, L. E.; Herczeg, G. J.; Visser, R.; van Dishoeck, E. F.; Wampfler, S. F.; Bruderer, S.; Benz, A. O.; Doty, S. D.; Brinch, C.; Hogerheijde, M. R.; Jørgensen, J. K.; Tafalla, M.; Neufeld, D.; and 41 co-authors incl. **Yıldız, U. A.**; *Origin of the hot gas in low-mass protostars. Herschel-PACS spectroscopy of HH 46*; 2010, A&A, Vol. 518, L121 [ADS]

4. Nisini, B.; Benedettini, M.; Codella, C.; Giannini, T.; Liseau, R.; Neufeld, D.; Tafalla, M.; van Dishoeck, E. F.; and 47 co-authors incl. **Yıldız, U. A.**; *Water cooling of shocks in protostellar outflows. Herschel-PACS map of L1157*; 2010, A&A, Vol. 518, L120 [ADS]

3. van der Tak, F. F. S.; Marseille, M. G.; Herpin, F.; Wyrowski, F.; and 54 co-authors incl. **Yıldız, U. A.**; *Water abundance variations around high-mass protostars: HIFI observations of the DR21 region*; 2010, A&A, Vol. 518, L107 [ADS]

2. Fich, M.; Johnstone, D.; van Kempen, T. A.; McCoey, C.; Fuente, A.; Caselli, P.; Kristensen, L. E.; Plume, R.; Cernicharo, J.; Herczeg, G. J.; van Dishoeck, E. F.; Wampfler, S.; Gaufre, P.; Gill, J. J.; Javadi, H.; Justen, M.; Laauwen, W.; Luinge, W.; Ossenkopf, V.; Pearson, J.; and 41 co-authors incl. **Yıldız, U. A.**; *Herschel-PACS spectroscopy of the intermediate mass protostar NGC 7129 FIRS 2*; 2010, A&A, Vol. 518, L86 [ADS]

1. Toloba, E.; Boselli, A.; Gorgas, J.; Peletier, R. F.; Cenarro, A. J.; Gadotti, D. A.; Gil de Paz, A.; Pedraz, S.; **Yıldız U.**; *Kinematic Properties as Probes of the Evolution of Dwarf Galaxies in the Virgo Cluster*; 2009, ApJ, Vol. 707, L17 [ADS]

For publication links, please follow ADS `http://bit.ly/adsumut`.

Papers in preparation

1. **Yıldız, Umut A.**; et al. *APEX-CHAMP$^+$ high-J CO observations of low–mass young stellar objects: IV. Survey of Low-mass Protostars*, To be submitted (Chapter 5 in this thesis).

Conference Proceedings & Abstracts

19. **Yıldız, Umut A.**; van Dishoeck, Ewine F.; Kristensen, Lars E.; *Star Formation with sub-/mm Astronomy - Milimetre/milimetre-alti Astronomisi ile Yıldız Oluşumu*; 18th Turkish National Astronomy Congress, Malatya, Turkey, Aug 27-31, 2012

18. **Yıldız, Umut A.**; Solmaz, Arif; Önal, Özgecan; Mirahmetoğlu, Halit; Saygaç, A. Talat; Güneş, Mikail; Yıldız, Mustafa K.; Özyar, Ümit F.; Şahin, Özge; Tuğral, M. Raşid; Atmaca, Gökhan; Kayhan, Cenk; Yeşilyaprak, Cahit; Dağtekin, Nazlı D.; Yaşar, Ekrem; Çoban, Mutlu; Canımkurbey, Betül; Öztürk, Pelin; Tokalı, Songül; Salman, Gonca; Zor, Hatice; Şensoy, Aslı; İnam, Sıtkı Ç.; Koçak, Fırat; Özdemir, Tuncay; Erdoğdu, Çağrı; Akı, Fatma Nur; Ekinci, Mustafa; Dönmez, Çağatay K.; Nasıroğlu, İlham; Aykutalp, Ayçin; Höçük, Seyit; Engin, M. Fatih; Aliş, Sinan; Yelkenci, Korhan; Yelkenci, Ayşegül T.; Özeren, Ferhat F.; Çabuk, Senem; Ataman, Erkan; Akkuş, Tuba; Tuncel, Efe; Bucakhan, Fehmi; Taşkın, Sevda; Öztürk, Fahri; Şahin, Timur; Baltacı, Neşever; Başpınar, Saniye; Uzunyayla, Pınar; Konak, Nermin D.; Etli, Özgür; Yılmaz, Figen; Dönmez, Orhan; Topal, Selçuk; Kalkan, Selami; Sonbaş, Eda; Küpçü-Yoldaş, Aybüke; *Journey of Turkish Membership to ESO - Turkiye'nin ESO'ya uyelik yolculuğu*; 18th Turkish National Astronomy Congress, Malatya, Turkey, Aug 27-31, 2012

17. **Yıldız, Umut A.**; Küçük, İbrahim; Öztürk, Fahri; Topal, Selçuk; Akgiray, Ahmed; Beklen, Elif; Gürkan-Uygun, Gülay; Ünal, Oktay; Ergin, Tülün; *Turkish National Radiotelescope Project - Ulusal Radyoteleskop Projesi*; 18th Turkish National Astronomy Congress, Malatya, Turkey, Aug 27-31, 2012

16. San José-García, I.; Mottram, J. C.; Kristensen, L. E.; van Dishoeck, E. F.; **Yıldız, U. A.** and the WISH team; *Studying the star-formation across the mass spectrum with Herschel-HIFI observations of CO*; Galactic Scale Star Formation, Heidelberg, 30 July-3 August 2012

15. San José-García, I.; Mottram, J. C.; Kristensen, L. E.; van Dishoeck, E. F.; **Yıldız, U. A.** and the WISH team; *Studying the star-formation across the mass spectrum with Herschel-HIFI observations of CO*; European Week of Astronomy and Space Science (EWASS), Symposium 2, Rome, -6 July 2012 [pdf]

14. Hogerheijde, Michiel R.; Bergin, Edwin A.; Brinch, Christian; Cleeves, L. Ilsedore; Fogel, Jeffrey K. J.; Blake, Geoffrey A.; Dominik, Carsten; Lis, Dariusz C.; Melnick, Gary; Neufeld, David; Panić, Olja; Pearson, John C.; Kristensen, Lars; **Yıldız, Umut A.**; van Dishoeck, Ewine F.; *Cold water and ammonia vapor in protoplanetary disks*; European Week of Astronomy and Space Science (EWASS), Symposium 2, Rome, -6 July 2012 [pdf]

13. **Yıldız, U. A.**; van Dishoeck, E. F.; Kristensen, L. E.; Ramchandani, J.; San José-García, I.; Mottram, J. C.; Jørgensen, J. K.; and the WISH Team; *High-J CO survey of low-mass protostars observed with Herschel-HIFI and LOMASS database*; From atoms to pebbles, Herschel's view of Star and Planet Formation Symposium held in Grenoble, France, March 20-23, 2012 [pdf]

12. Kristensen, L. E.; van Dishoeck, E. F.; Visser, R.; Mottram, J. C.; Herczeg, G. J.; Jørgensen, J. K.; Bruderer, S.; Harsono, D.; Hogerheijde, M. R.; Karska, A.; San José-García, I.; Wampfler, S.; **Yıldız U. A.**; and the WISH team; *Feedback from low-mass protostars onto their surroundings: some like it hot*; From atoms to pebbles, Herschel's view of Star and Planet Formation Symposium held in Grenoble, France, March 20-23, 2012 [ADS]

11. Hogerheijde, Michiel R.; Bergin, Edwin A.; Brinch, Christian; Cleeves, L. Ilsedore; Fogel, Jeffrey K. J.; Blake, Geoffrey A.; Dominik, Carsten; Lis, Dariusz C.; Melnick, Gary; Neufeld, David; Panić, Olja; Pearson, John C.; Kristensen, Lars; **Yıldız, Umut A.**; van Dishoeck, Ewine F.; *Herschel observations of cold water vapor and ammonia in protoplanetary disks*; From atoms to pebbles, Herschel's view of Star and Planet Formation Symposium held in Grenoble, France, March 20-23, 2012 [ADS]

10. Hogerheijde, Michiel R.; Bergin, Edwin A.; Brinch, Christian; Cleeves, L. Ilsedore; Fogel, Jeffrey K. J.; Blake, Geoffrey A.; Dominik, Carsten; Lis, Dariusz C.; Melnick, Gary; Neufeld, David; Panić, Olja; Pearson, John C.; Kristensen, Lars; **Yıldız, Umut A.**; van Dishoeck, Ewine F.; *Detecting cold water vapor in a planet-forming disk*; Star Formation through Spectroimaging at High Angular Resolution Workshop, Taipei, Taiwan, June 20-24, 2011 [pdf]

9. **Yıldız, U. A.**; Kristensen, L. E.; van Dishoeck, E. F.; Jørgensen, J. K.; Visser, R.; San José-García, I.; Herschel WISH Team *High-J CO survey of low-mass protostars observed with Herschel-HIFI*; The Molecular Universe, Proceedings of the 280th Symposium of the International Astronomical Union held in Toledo, Spain, May 30-June 3, 2011, #388 [ADS]

8. San José-García, I.; Kristensen, L. E.; **Yıldız, U. A.**; van Dishoeck, E. F.; Herschel WISH Team; *Linking high-J CO emission from low- to high-mass protostars with Herschel-HIFI*; The Molecular Universe, Proceedings of the 280th Symposium of the International Astronomical Union held in Toledo, Spain, May 30-June 3, 2011, #326 [ADS]

7. Herczeg, G. J.; Karska, A.; Kristensen, L. E.; van Dishoeck, E. F.; Visser, R.; Jorgensen, J.; Bruderer, S.; **Yıldız, U.**; Herschel Wish Team; *Warm water in Herschel/PACS observations of NGC 1333 IRAS 4B: the outflow, not the disk!*; "The Molecular Universe, Proceedings of the 280th Symposium of the International Astronomical Union held in Toledo, Spain", May 30-June 3, 2011, [#]195 [ADS]

6. Hogerheijde, M.; Bergin, E. A.; Brinch, C.; Cleeves, L.; Fogel, J.; Blake, G.; Cernicharo, J.; Dominik, C.; Lis, D. C.; Melnick, G.; Neufeld, D.; Panic, O.; Pearson, J.; Kristensen, L.; **Yıldız, U.**; van Dishoeck, E.; *Detecting the cold water reservoir in a protoplanetary disk*; "The Molecular Universe, Proceedings of the 280th Symposium of the International Astronomical Union held in Toledo, Spain", May 30-June 3, 2011, [#]16 [ADS]

5. Kristensen, L. E.; van Dishoeck, E.; **Yıldız, U.**; Visser, R.; Herczeg, G.; Jorgensen, J.; van Kempen, T.; Hogerheijde, M.; WISH Team; *WISHes coming true: low-mass protostars as chemical fountains*; "The Molecular Universe, Proceedings of the 280th Symposium of the International Astronomical Union held in Toledo, Spain", May 30-June 3, 2011, [#]10 [ADS]

4. **Yıldız, U.**; van Dishoeck, E. F.; Kristensen, L. E.; Visser, R.; Herczeg, G.; van Kempen, T. A.; Jørgensen, J. K.; Hogerheijde, M. R.; Wish Team; *"Energetic processes revealed by spectrally resolved high-J CO lines in low-mass star-forming regions with Herschel-HIFI"*, 2011, Zermatt 5th ISM Symposium "Conditions and impact of star formation: New results with Herschel and beyond", September 19-24, 2010 [ADS]

3. Kristensen, L. E.; Visser, R.; van Dishoeck, E. F.; **Yıldız, U.**; Herczeg, G. J.; Doty, S.; Jørgensen, J. K.; van Kempen, T. A.; Brinch, C.; Wampfler, S.; Bruderer, S.; Benz, A. O.; *Wishes Coming True: Water in low-mass star-forming regions with Herschel*; 2011, Proceedings of 5th Zermatt ISM Symposium "Conditions and impact of star formation: New results with Herschel and beyond", September 19-24, 2010 [ADS]

2. Wampfler, S. F.; Herczeg, G. J.; Bruderer, S.; Benz, A. O.; van Dishoeck, E. F.; Kristensen, L. E.; van Kempen, T. A.; Doty, S. D.; Visser, R.; **Yıldız, U.**; and the WISH Team; *"Probing the Water Chemistry in Young Stellar Objects with Hydroxyl Observations'*, 2011, Zermatt 5th ISM Symposium "Conditions and impact of star formation: New results with Herschel and beyond", September 19-24, 2010 [pdf]

1. **Yıldız, U.**; van Dishoeck, E. F.; Kristensen, L. E.; van Kempen, T. A.; Belloche, A.; Guesten, R.; *The shocking truth about star formation as revealed by warm CO CHAMP[+] Mapping*; 64th Nederlandse Astronomen Conferentie (NAC) held in Rolduc, Kerkrade, May 13-15, 2009 [pdf]

POPULAR ARTICLES

2. Efe Tuncel, **Umut A. Yıldız**, *APEX Telescope: First Precursor to ALMA, (APEX Teleskobu: ALMA'nın ilk Öncüsü) in Turkish*, Tübitak Bilim ve Teknik Dergisi, Aralık 2012, Sayı: 541, Sayfa: 38-42

1. **Umut A. Yıldız**, *Science with ALMA, (ALMA ile Bilim) in Turkish*, Tübitak Bilim ve Teknik Dergisi, Ekim 2011, Sayı: 527, Sayfa: 30-35 [pdf]

Curriculum Vitae

I was born in February 28, 1980 in Istanbul, Turkey, however, my parents' hometown is Ordu. My father was a chief-policeman, therefore I have lived in many cities and attended many different schools within Turkey; İstanbul, Bingöl, Karabük, Zonguldak, then Çanakkale where I have gotten my high school diploma from Çanakkale Milli Piyango Anatolian High School in 1998.

Then, I found the opportunity to follow my life ambition to become an astronomer and won the nationwide university entrance examination to study at the Ankara University, Department of Astronomy and Space Sciences. I was quite active in my early years, including being the president of the Amateur Astronomy Club (ASART) of Ankara University. At the end of the first semester of my third year, I decided to improve my English and found myself at the London Heathrow Airport, 10 days later. My plan was to stay there for the next semester and summer –6-7 months–, but after the summer, I decided to apply to British universities to study astronomy. In September 2001, I was accepted by University College London for an astronomy diploma program. One year after, I decided to go back to Turkey because a degree from a UK university is very expensive and my old university was a lot cheaper. After two years of UK experience, I went back to Ankara University. Reregistering to the university was quite painful, because many of the second year classes were either abolished or the lecture code had changed. I was by now a fifth year student but finished only the first year lectures. However, I was quite motivated to finish my university, so I took as many courses as possible. In my sixth (final) year, I passed 24 lectures which is probably still a record at the Faculty of Science, and also finished a Minor in Mathematics and become within the top 5% of the peer students. If I could have taken three more lectures, I would have finished a Physics Minor as well, but I simply did not have time.

In September 2005, I started my Masters study at the University of Groningen, Kapteyn Astronomical Institute. I studied within the *Stellar Populations Group* led by Reynier F. Peletier, who is now the director of the Kapteyn Institute. The project was based on the data from MAGPOP-ITP *(Multiwavelength Analysis of Galaxy Populations - International Time Programme)* training network, which is funded by the European Union with the Kapteyn Institute as the Associated-Node. I joined the group in February 2007 to work on the project called "Stellar Populations of Dwarf Galaxies: Optical and Near-IR Surface Photometry of Quiescent Dwarf Galaxies". We obtained H & K band near-IR images of 55 dwarf galaxies by using the William Herschel Telescope (WHT), Telescopio Nazionale Galileo (TNG), and the Nordic Optical Telescope (NOT) at La Palma, Canary Islands in 13 nights. During my research, I have reduced and calibrated the images to study the surface photometry of each dwarf galaxy. Close to the completion of the project, I was

fortunate to receive a 3-months research fellowship from the MAGPOP project in order to continue my activities in the IAC *(Instituto de Astrofisica de Canarias)*, Tenerife. I guess the life in Tenerife matured me and prepared me for the future. The experience from this research led me to find another great project with more substantial data from *Herschel* Space Observatory.

In December 2008, I was accepted to the Ph.D. position at Leiden University, Leiden Observatory, in the *Molecular Astrophysics Group* led by Prof. Dr. Ewine van Dishoeck in order to work with the WISH (Water In Star-forming regions with *Herschel*) guaranteed-time key program to conduct research on star formation. Delays of the launch of *Herschel* and a cosmic ray hit to the HIFI instrument six month after launch, led me to study some ground-based APEX and JCMT observations and better prepare for *Herschel* data, which started to pour down in March 2010. I was very lucky to participate in three large *Herschel* consortiums (WISH, HOP, DIGIT), which gave me the opportunity to collaborate with more than 100 great astronomers. Key discoveries of our teams include the first detection of water and oxygen molecules in prestellar cores and protostellar disks. I also had the opportunity to have hands-on experience with sub-/mm observations via several observing trips to APEX (Chile), JCMT (Hawaii), and IRAM 30m (Spain). During my thesis research, I really enjoyed working on large-scale observational data. Particularly, I also got a chance to participate in the *Herschel*-HIFI calibration group in SRON-Groningen, which also added another direction for my future to join future instrumentation projects.

What next? Well, since childhood, I lived and traveled in many different cities in many different countries. Therefore I am not attached to one specific city, but I am only interested in great projects that I can contribute to and work. The plan is to continue to pursue a career in astronomical research and instrumentation. I will continue in Pasadena, California, (USA) as a postdoctoral researcher at the NASA Jet Propulsion Laboratory and California Institute of Technology with Prof. Dr. Paul Goldsmith.

So, who is Umut A.?

OK, it is still me. In my legal documents, I do not have a middle name. But since Yıldız is a very common surname in Turkey and even there are more than 500 Umut Yıldız on Facebook, I decided to create a bogus middle name —actually just a letter— **A.**, in order reduce the chances for having the same name and surname in astronomical papers. Even though sometimes I forget to add A., I am always trying to use this letter in every of my scientific papers. If you wonder what A. stands for, well, I have not decided yet, but it fits with **A**stronomy, right (what a geek) :).

Acknowledgments

" - Knowledge is to understand.
- To understand who you are
- If you not know who you are
- What's the use of learning?"

– Yunus Emre (ca.1238-ca.1320) - Turkish Scholar

CO, al, et, de, IRAS, van, sources, envelope, line, observations, abundance, data, observed, km, 13CO, O2, Class, 12CO, Fig, spectra, lines, outflow, JCMT, Herschel, HIFI, C18O, emission, APEX, gas, temperature, transitions, Dishoek, low-mass, APEX-CHAMP+, density, Yıldız, Table, model, mass, 4A, GHz, map, NGC, WISH, ApJ, protostars, Chapter, Figure, velocity, component, temperatures, beam, intensities, profiles, outflows, range, H2O, H2, Kristensen, JCMT-HARPB, Telescope, obtained, source, presented, higher, used, models, column, narrow, e.g, rotational, excitation, show, parameters, protostellar, radius, respectively, protostar, molecular, een, het, ve, Kempen, FCO, high-J, whereas, different, positions, toward, structure, resolution, components, calculated, ratios, red, high, maps, densities, also, physical, lower, heating, intensity, Observed, Observatory, cloud, formation, regions, value, low, blue, Blue, Red, broad, AU, UV, 2A, ile, rms, order, results, Netherlands, Space, Jørgensen, JCMT-RxA, Herschel-HIFI, dust, spectrum, shown, shows, using, values, integrated, evolution, factor, force, profile, taken, position, cm, te, inner, found, well, fit, two, 4B, Kristensen